Multi-Scale Multi-Phase field model for Shrinkage Performance of Concrete

A thesis presented for the degree of

Doctor of Philosophy in Civil and Structural Engineering

at The University of Sheffield

By

Songsong Meng

The Department of Civil and Structural Engineering

October 2024

Abstract

Concrete, as a porous composite material, is susceptible to moisture loss, which can initiate degradation mechanisms such as autogenous and drying shrinkage. These shrinkage phenomena lead to crack initiation and propagation, compromising structural safety and durability. Therefore, understanding concrete shrinkage under varying hydric conditions is critical for extending the service life of concrete structures. However, existing research lacks the precision needed to accurately predict moisture loss, crack development, and shrinkage behaviour.

This study introduces innovative mesoscale numerical models to simulate moisture diffusion, mechanical properties, and shrinkage in concrete, aiming to assess its long-term performance. The inclusion of a pore phase in the model enables accurate monitoring and solution derivation. Autogenous shrinkage is modelled through chemical shrinkage in the matrix phase (mortar), while drying shrinkage is attributed to moisture loss in the pore phase during hydration. The latter is described via capillary stress evolution induced by moisture evaporation.

To develop and calibrate the proposed model, extensive experiments were conducted to characterize concrete's physical properties at the mesoscale, including moisture transport, mechanical degradation, crack propagation, and shrinkage. The approach integrates numerical modelling with laboratory testing to monitor early-age moisture content, temperature, and strain in concrete elements. Mechanical behaviour and crack propagation in mortar and concrete specimens were also experimentally evaluated.

A novel micro–meso model is presented, utilizing random packing and Voronoi tessellation to generate aggregates, the interfacial transition zone (ITZ), and pore structure. The Rayleigh–Ritz and Brunauer–Skalny–Bodor (BSB) models are employed to simulate pore distribution and calculate moisture diffusion coefficients for both vapor and liquid water. This diffusion model considers critical variables such as the water-to-cement (w/c) ratio, concrete maturity, and environmental conditions.

Crack development is simulated using an elasto-plastic phase-field model, which is calibrate through compressive and bending tests, as well as comparative data from the literature. For mechanical performance, a multi-phase-field model is developed to predict fracture and energy dissipation behaviour. Calibration against experimental data confirms its accuracy. Additionally, a potential energy correction parameter is proposed, reflecting the influence of aggregate volume and mortar potential energy on elastic modulus and peak load capacity.

By integrating moisture diffusion and mechanical behaviour across four phases—aggregate, mortar, ITZ, and pores—a comprehensive coupled system is proposed to predict shrinkage behaviour and mechanical performance. Given that shrinkage is primarily driven by moisture loss, accurate modelling of moisture diffusion is essential, as it governs the drying process and controls the development of shrinkage-induced strains. These strains, in turn, affect both short- and long-term deformation and cracking in structural elements.

This study addresses these challenges by using common variables such as the w/c ratio and concrete maturity to assess the effects of pore relative humidity and ambient temperature on concrete diffusivity through inverse numerical analysis. Results show strong agreement between the model and experimental data, confirming the model's capability to capture the influence of mix design and environmental conditions on moisture evolution in drying concrete.

Acknowledgement

I would like to express my deepest appreciation and gratitude to my supervisors, Professor Kypros Pilakoutas, Dr Maurizio Guadagnini, Professor Iman Hajirasouliha, and Dr Giacomo Torelli, for their continued support, guidance, patience and encouragement during my research work.

My sincere appreciation to the technical staff of the Concrete and Heavy Structures Laboratory, in particular Kieran Nash, Shaun Waters, Paul Bentley and Samuel J Gibson, for their great technical support.

I would also like to thank former and current researchers of the Concrete and Earthquake research group for our excellent time together. Specially Shanker Lal Meghwar, Yifan Li, Ahmad Mahmoud Kobeiter Abiad, Talal O Alshammari, Geyu Dong, Xiao Zhao and Kajanan Selvaranjan for helping me with experiments and numerical modelling.

Finally, I offer immense thanks and gratitude to my immediate family and parents for supporting and encouraging me during my complete research.

Table of Contents

List of Symbols and Abbreviations

Technical Terms:

1-D: One dimensional

2-D: Two dimensional

3-D: Three dimensional

RH: Relative humidity

ITZ: Interfacial transition zone between aggregate and cement paste

Mesoscale: Mesoscale level of concrete, including aggregate, cement paste and ITZ

Microscale: Microscale level of concrete for pores, including gel pores, small capillary pores, large capillary pores and micro cracks

BEI: Backscattered electron imaging

MIP: Mercury intrusion porosimetry

C-S-H: Calcium-silicate-hydrate

Ink-bottle: The ink bottle-shaped pore composed of large and small pores

Ink-bottle effect: In standard MIP tests, the pressurization procedure forces mercury to intrude a pore system through throat pores to reach interior ink-bottle pores. In the subsequent depressurization procedure, mercury in the throat pores can be freely extruded out while mercury in the interior ink-bottle pores is irreversibly entrapped.

MiMe model: Micro-meso scale model

R-R: Rayleigh-Ritz distribution model

LB: Lattice Boltzmann

BSB: Brunauer-Skalny-Bodor model

W/C ratios: Water/Cement ratio

DP: Drucker-Prager yield criterion

PTM: Point tracking method

MT: Mori-Tanaka scheme

Multi-scale: Multi-scale level of concrete, including mesoscale and microscale levels

HPC: high-performance concrete

LWC: lightweight concrete

Symbols:

J_L**:** flow rate of liquid water

K_L**:** diffusion coefficient of liquid water

p_c**:** capillary pressure

h**:** relative humidity

M_w**:** molar mass of water

ρ_L**:** density of liquid water

R**:** universal gas constant

T**:** temperature

J_V**:** diffusion flux of vapour water

K_V**:** diffusion coefficient of vapour water

p_{VS}**:** saturated vapour pressure

ϕ_t**:** total porosity

ϕ_i**:** volume ratio between the porosity of pore type *i* and the overall porosity

B_i**:** the peak of the differential porosity for each pore type on a logarithmic scale

f_d**:** density distribution of pores

S_r**:** saturated degree

r_c**:** critical radius

r_k**:** the sum of capillary condensate radius

t_a**:** the thickness of absorbed water layer

k_V**:** vapour water diffusion coefficient of single pore

D_{va}**:** permeability of vapour water in air

l_m**:** mean free path of water molecules

r_e: actual pore radius

τ: the representative pore tortuosity, pore tortuosity is calculated by the ratio of the length of curve to the distance between of pores

η: viscosity of vapour water

h_b: relative humidity on the concrete surface

h_e: ambient relative humidity

δ: the effective thickness of the concrete boundary

γ: the crack volume

d: the damage state

g_c: the release rate of critical energy

σ: the stress tensor

ε: the strain tensor

ε^+: the tensile strain

ε^-: the compressive strain

Π: the total potential energy

Π^u: the total potential energy of displacement field

Π^{ext}: the external energy

Π_M: the total potential energy of mortar phase

Π_{ITZ}: the total potential energy of ITZ phase

Π_A: the total potential energy of aggregate phase

V_M: the volume fraction of mortar phase

V_{ITZ}: the volume fraction of ITZ phase

V_A: the volume fraction of aggregate phase

E: the elastic modulus

v: the Poisson's ratio

K: the stiffness matrix

K_M: the stiffness matrix of mortar

K_{ITZ}: the stiffness matrix of ITZ

K_A: the stiffness matrix of aggregate

$E(u,d)$: the elastic energy

$P(u,d)$: the plastic energy

$W(u,d)$: the crack energy

ψ_{ε}^{el}: the elastic energy

ψ_{0}^{el}: the initial elastic energy

ψ_{ε}^{el+}: the tensile energy

ψ_{ε}^{el-}: the compressive energy

ψ_{ε}^{pl}: the plastic energy

ψ_{0}^{pl}: the initial plastic energy

α: the hydration degree

$H(t)$: the cumulative heat generation

H^0: the total cumulative heat generation

$CS(t)$: the chemical shrinkage

CS^0: the total chemical shrinkage

ε_{cs}: the autogenous shrinkage

ε_{ds}: the drying shrinkage

Chapter 1: Introduction

This chapter outlines the research's context and importance. It details the primary aims, objectives, and methodology, and provides an overview of each chapter in the thesis.

1.1 Background

1.1.1 Shrinkage

Concrete, as a typical composite material, finds widespread application in the construction of most civil engineering structures (Chen and Feng, 2022). The serviceability and durability of concrete structures are important due to their exposure to various adverse impacts (Briffaut et al., 2016). According to literature, self-induced material deformations rather than external loading induce 80% of concrete damage and degradation (Chen et al., 2015). Concrete shrinkage is the most important self-induced deformation and is affected by the mix composition, member dimensions, and ambient conditions (Larrard, 1990). Shrinkage is mostly induced by moisture loss from inside the concrete, causing crack initiation and propagation (Shen et al., 2022). Therefore, moisture loss (self-desiccation and drying process) and any resulting damage and degradation mechanisms are necessary to be understood and quantified. However, moisture loss inside concrete is complex to predict due to the non-linear diffusion and complex geometric properties of concrete (Huang et al., 2015). Due to its heterogeneous nature, concrete exhibits complex damage and degradation mechanisms at the mesoscale, necessitating precise and efficient prediction of mesoscale models, stress redistribution, energy dissipation and crack propagation (Naderi et al., 2021a).

Autogenous (or basic) shrinkage in concrete normally as a result of cement hydration. Throughout the cement hydration process, the cement particles gradually enlarge and merge with neighbouring cement particles by consuming the surrounding water (Ding et al., 2019). With persistent hydration of cement, autogenous shrinkage is induced as a result of the volume reduction in the cement paste (Ding et al., 2019) and drop in temperature created by the heat of hydration. The volume reduction is the result of both self-desiccation and chemical shrinkage. As any remaining water from capillary pores is extracted by unhydrated binder particles (Tazawa, 1999) the pores begin to empty resulting in internal capillary stresses (Thomas et al., 2012).

Drying shrinkage refers to the volume reduction in an unloaded hydrated cement paste or concrete caused by a decrease in RH within the partially saturated porous matrix during the drying process (Rezvani et al., 2019). Due to the moisture diffusion evolution, drying shrinkage is a time-dependent volume change in the cementitious matrix caused by water loss (Hansen, 1987). Because of the evaporation of bleeding water, surface tension of water is also induced before hardening (Feldman and Sereda, 1970, Parrott and Young, 1982), which results in capillary stress (Feldman and Sereda, 1970,

Coussy et al., 1998, Bentz et al., 1998) and disjoining pressure near the surface of concrete leading to plastic shrinkage (Bažant and Research, 1972, Jennings and Research, 2008). Drying shrinkage in concrete is predominantly caused by capillary stress (Powers, 1960).

1.1.2 Moisture Diffusion

Concrete, as a porous material, is susceptible to moisture transport, enabling aggressive chemical agents to infiltrate and potentially trigger degradation mechanisms (Liu and Zhang, 2023). These degradation processes can include chloride penetration (Ye et al., 2016, Zhu et al., 2016), alkali-silica reaction (Léger et al., 1996, Multon and Sellier, 2016), and carbonation (Ye et al., 2016). In this context, concrete's transport properties are crucial in determining its durability (Basheer et al., 2001, Hussain and Ishida, 2010). Moisture diffusivity, a fundamental property that governs the rate at which moisture propagates within the material, is a key parameter in assessing not only shrinkage strains but also concrete's resistance to the deleterious effects of moisture-related phenomena. A robust understanding of moisture diffusivity enables the development of strategies and materials that can mitigate or even prevent these mechanisms of degradation, ultimately extending the lifespan of concrete structures. Therefore, a more accurate prediction of moisture diffusion can be achieved by a model that couples microstructure with diffusion properties in cementitious materials. This can be accomplished by converting the different micro-scale pore types into a homogeneous mesoscale phase. Examples of this include, the Maxwell model (Nielsen et al., 2003), the differential medium model (Garboczi and Bentz, 1998, Pivonka et al., 2004), and the self-consistent model (Bary and Béjaoui, 2006).

1.1.3 Damage and Degradation Mechanisms

Crack initiation and propagation is unavoidable in structures made of cementitious materials like mortar and concrete. Cracks can form as a result of mechanical and thermal loads, as well as shrinkage, and have significant implications on structural durability and safety (Jia et al., 2022). Therefore, understanding, describing and predicting concrete's degradation and failure mechanisms by crack evolution is crucial. Moreover, concrete materials display intricate damage and degradation mechanisms at the mesoscale, necessitating precise and efficient prediction of mesoscale models, stress redistribution, energy dissipation, and crack propagation. In mesoscopic modelling, concrete is typically considered as a material with four phases, including aggregates, mortar matrix, ITZ and pores (Van Mier, 2012).

1.1.4 A multi-scale model

It is widely employed that concrete's microstructure is categorized into four fundamental levels, as illustrated in Fig.1.1.

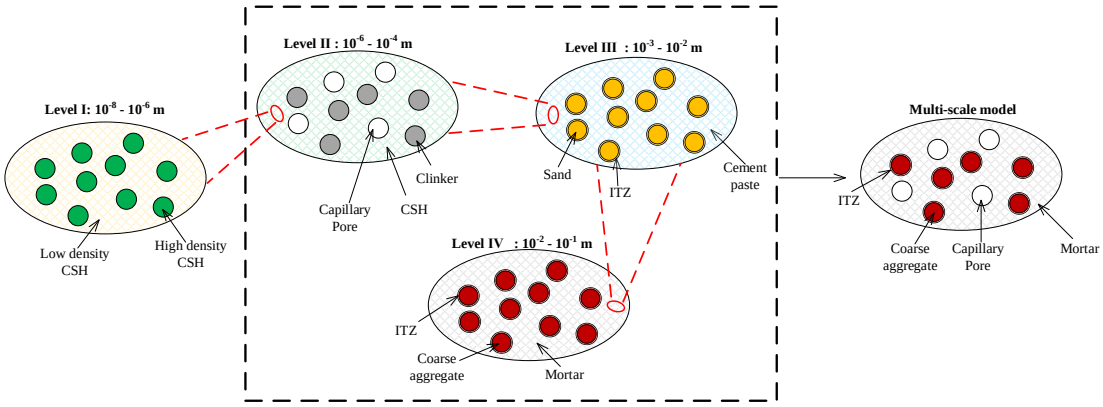

Fig.1.1. Multi-scale model of concrete

CSH scale (10^{-8} - 10^{-6} m, level I): At this scale, calcium-silicate-hydrate (C-S-H) is primary product of cementitious materials. According to differences in densities C-S-H can be categorized into low density (LD) C-S-H and high density (HD) C-S-H. In normal concrete, HD C-S-H occupies space within the phase for LD C-S-H. Therefore, when calculating elastic properties of C-S-H, LD C-S-H is considered as a main phase and is viewed as matrix, while HD C-S-H is treated as inclusion.

Cement solid scale (10^{-6} - 10^{-4} m, level II): The hardened cement solid consists of the C-S-H phase, calcium hydroxide (CH), residual clinker (CL), and capillary pores. As for this level, the C-S-H phase is considered matrix material, while other phases are treated as inclusions. Therefore, CH, CL, pores are typically treated as phases included within CSH matrix for determining elastic parameters of the cement solid phase.

Mortar scale (10^{-3} - 10^{-2} m, level III): At this level, mortar phase includes cement particles, ITZ and fine aggregates. The cement phase is considered matrix to include ITZ and fine aggregate.

Concrete scale (10^{-2} - 10^{-1} m, level IV): At meso-scale, concrete material is considered a mixture including mortar, coarse aggregate, as well as ITZ around coarse aggregates. Therefore, mortar is the matrix phase to contain the inclusion parts of coarse aggregate and ITZ.

In this study, level II, III and IV are examined to calculate elastic parameters for different phases, such as mortar, coarse aggregate, ITZ and pores. The elastic parameters for pore phase is determined and decomposed from homogenous mortar phase into mortar and pore phase using mortar experiments and the MT scheme

1.2 Significance

Shrinkage is a significant cause of distress in concrete structures, often resulting in high repair and maintenance costs for critical infrastructure. Understanding the factors influencing shrinkage and integrating them into predictive models can help mitigate these issues (Menu et al., 2020). Therefore, it

is essential to investigate and assess shrinkage-induced deformation under varying environmental conditions, such as temperature and RH. However, a multi-scale, multi-phase coupling system that involves moisture diffusion, crack propagation, shrinkage and shrinkage-induced cracking, mechanical failure, and degradation is challenging to achieve as all of these phenomena are highly coupled. In addition, there is also a lack of understanding of the shrinkage and mechanical behaviour of concrete at the mesoscale level, including mortar, ITZ, aggregate, and pores.

This research will address these gaps by performing experimental tests and numerical simulations. The experimental part of this project will measure the moisture diffusion and mechanical properties of concrete, including relative humidity inside concrete, ambient relative humidity, autogenous shrinkage, drying shrinkage, elastic modulus, Poisson's ratio, as well as compressive and tensile strength of concrete. Simultaneously, a numerical framework will be developed for a comprehensive analysis of multi-coupling phase-field, including moisture diffusion, self-desiccation, crack propagation, energy dissipation, shrinkage, mechanical degradation at the mesoscale model with four phases (aggregate, ITZ, mortar and pores).

1.3 Problem Statements

Traditional methods for evaluating shrinkage, treat concrete as a homogenous material for moisture diffusion and shrinkage development. These methods do not directly reflect the influence of non-linear and non-uniform moisture diffusion, distribution and evolution due to the spatial distribution of aggregate, ITZ, mortar and pores, resulting in inaccurate results. Furthermore, the crack propagation, mechanical degradation and failure mechanism are not considered to predict the shrinkage and long-term effects on concrete structures.

To address these issues, several researchers have introduced empirical equations to quantitatively evaluate their effects. However, these empirical relations are hard to consider how:

1) moisture diffusion and evolution change over time depending on temperature, relative humidity, network and tortuosity of pore structure.
2) crack initiation, stiffness degradation and crack propagation due to external or internal load affect different phases of concrete at a mesoscale level.
3) energy dissipation is distributed between different phases with different volume fractions.
4) to obtain the representative elastic and crack properties for ITZ and pores to describe the contribution of pores to crack propagation.
5) shrinkage develops due to hydration or drying processes.

1.4 Aims and Objectives

This research seeks to study crack development and shrinkage deformation caused by moisture diffusion at a mesoscale model and to propose more accurate numerical models. The objectives to achieve this aim are as follows:

1. To assess and propose the governing equations for moisture diffusion in normal concrete within a mesoscale framework (pores and ITZ).
2. To study the impact of porosity, temperature, ambient RH and tortuosity on moisture diffusion. To calibrate the proposed moisture transport model with experimental data.
3. To introduce a mechanical constitutive model and numerical method to describe the crack initiation, propagation and energy dissipation within a mesoscale model.
4. To introduce the energy dissipation theory among different parts (aggregate, ITZ, mortar and pores) of concrete to describe the accurate degradation properties of concrete.
5. To employ the representative volume element method to determine the representative elastic properties of pore phase, and combine the energy dissipation theory to calculate the representative energy release rate and parameters of crack to describe the contribution of pores in crack propagation.
6. To calibrate the proposed model using a) mechanical tests including: compressive tests on concrete and mortar, three-point bending tests for concrete, and b) shrinkage tests: including autogenous and drying shrinkage.
7. To simulate autogenous shrinkage using numerical models and calibrate using experimental results.
8. To predict drying shrinkage using a numerical model that combines mechanical stresses with moisture drying and drying shrinkage.

1.5 Thesis Layout

This thesis is comprised of eight chapters, with six chapters (Chapters 2 through 7) presented as independent research journal papers, while the remaining two chapters (Chapters 1 and 8) follow a traditional thesis structure. Chapter 1 provides an introduction to this research; Chapter 2 proposes a meso-micro model to predict the moisture diffusion inside concrete; Chapter 3 introduces a complex phase-field model to describe the crack development of a mesoscale model of concrete; Chapter 4 proposes an energy dissipation theory to describe the energy development in the different components of concrete; Chapter 5 studies the representative mechanical properties of pore phases based on previous research, Mori-Tanaka scheme and theory proposed in Chapter 4; Chapter 6 studies the autogenous shrinkage and crack propagation of concrete and includes an experimental study and numerical modelling that combines the models from Chapter 2 and Chapter 4; Chapter 7 studies drying shrinkage

and crack propagation of concrete with experimental studies and numerical models. An overall discussion, summarised conclusions and recommendations are presented in Chapter 8.

Chapter 2: *"An Innovative Method for Mesoscale Modelling of Moisture Diffusion in Concrete"* proposes a new mesoscale modelling to simulate the moisture diffusion inside concrete, to address **Objectives 1 and 2**. It introduces a novel micro-meso (MiMe) model for concrete, employing random packing and Voronoi tessellation to generate the aggregates, ITZ and pore structure. To simulate pore distribution and determine the radius and fraction of various pore types, the Rayleigh-Ritz (R-R) pore distribution model is combined with the Brunauer-Skalny-Bodor (BSB) model. The moisture diffusion coefficient is then calculated for vapour water and liquid water, implementing a non-steady state to simulate moisture diffusion within the pores. Using this model, the impact of ambient RH, temperature and tortuosity on moisture diffusion is investigated. By comparing numerical predictions with experiments, it is demonstrated that the proposed methodology can be effectively implemented to capture the RH distribution across various scenarios, encompassing early age concrete, hardened concrete and concretes with varying W/C ratios.

Chapter 3: *"Phase field Modeling of Meso-scale Framework for Predicting Fracture Propagation of Concrete: Numerical Calibration and Experimental Calibration"* proposes an elasto-plastic phase-field model based on the Drucker-Prager yield criterion, to address **Objectives 3 and 6**. To model the asymmetric tension-compression behaviour of porous materials, the strain energy contribution to crack propagation is analysed using spectral decomposition. To calibrate the proposed model, compressive and three-point bending tests are conducted on concrete and mortar specimens, utilizing the 2D point tracking method (PTM) to record crack propagation. Furthermore, three experiments from literature are utilized to calibrate the model. The predictions align well with the experimental results, calibrating that the proposed methodology effectively captures crack propagation across concrete.

Chapter 4: *"Multiple-phase-field Modelling for Fracture and Damage Behaviour of Concrete"* proposes an energy dissipation theory for concrete with different component contents for homogenous and mesoscale model, to address **Objective 4**. This model can capture crack propagation within concrete with varying components and studies the effect of different volume fractions of components. Three experiments from the literature, including three-point bending and wedge splitting tests with varying notch depths, are utilized to investigate the impact of the volume fraction of concrete composites and to calibrate this theory.

Chapter 5: *"A Multi-scale Poro-elasto-plastic Model for Concrete Damage and Failure Behaviour"* investigates the influence of pores on failure mechanisms, to address **Objective 5**. The representative mechanical properties of the pore phase are obtained by combining the energy dissipation theory from Chapter 4 and the Mori-Tanaka scheme to avoid discontinuities in concrete. To calibrate and calibrate this model, various specimens are subjected to compressive and three-point bending tests. A comparison

between numerical predictions and experimental observations shows that the proposed methodology effectively captures crack propagation in concrete.

Chapter 6: *"A Multi-scale Phase-field Model for Autogenous Shrinkage for Concrete"* investigates autogenous shrinkage and its resulting crack propagation in concrete by combining the model from Chapter 1 and Chapter 5, to address **Objective 7**. The elasto-plastic phase-field model is applied to simulate autogenous shrinkage and crack propagation in concrete using a micro-meso model. The spatial distribution of aggregates is combined with the Monte Carlo method and Voronoi tessellation to determine the geometric properties of the concrete. To calibrate and calibrate this model, various specimens are subjected to autogenous shrinkage with different scales and water/cement ratios. By comparing numerical predictions with experimental observations, the proposed methodology effectively predicts autogenous shrinkage and captures crack propagation across concrete.

Chapter 7: *"A Multi-scale Phase-field Model for Drying Shrinkage for Concrete"* investigates the drying shrinkage and the resulting cracks, to address **Objective 8**. The open microstructure of concrete presents significant challenges in understanding moisture diffusion, capillary stress, drying shrinkage, failure mechanisms, and predicting crack propagation paths. Therefore, this section introduces a multi-coupled model that integrates a moisture diffusion model with an elasto-plastic phase-field model to simulate drying shrinkage and crack propagation in concrete using a micro-meso model. The geometric properties of concrete are determined by integrating the spatial distribution of aggregates with the Monte Carlo method and Voronoi tessellation. Various specimens are subjected to drying shrinkage at different depths and with varying water/cement ratios to calibrate and calibrate the model. The comparison between numerical predictions and experimental observations demonstrates that the proposed methodology effectively predicts drying shrinkage and crack propagation in concrete.

Chapter 8: *"Conclusions and Discussion for Future Research"* summarizes the main conclusions of this thesis. Recommendations for future research are proposed and discussed.

Chapter 2: An Innovative Method for Mesoscale Modelling of Moisture Diffusion in Concrete

Abstract

Moisture diffusion influences the durability and the long-term behaviour of concrete and whilst it predominantly occurs via cement matrix and Interfacial Transition Zone, most existing models consider concrete to be homogeneous. This paper introduces a novel micro-meso model that employs random packing and Voronoi tessellation. Rayleigh-Ritz pore distribution and Brunauer-Skalny-Bodor models are combined to determine the radius and fraction of various pores. The results indicate that relative humidity (RH) diffuses faster with increasing temperature, decreasing ambient RH and tortuosity. Ambient relative humidity (RH) has a stronger impact on diffusion compared to temperature and tortuosity. Numerical and experimental comparisons demonstrate that the proposed methodology effectively captures RH distribution across various scenarios. Furthermore, explicit pore network modelling incorporates key parameters for a more accurate analysis. Integrating the proposed methodology into a fully coupled hygro-mechanical framework can potentially yield more accurate predictions of mechanical behaviour; enhancing the reliability of long-term performance assessments and enabling more durable concrete design.

Keywords: Pore structure, Brunauer-Skalny-Bodor (BSB) model, Rayleigh-Ritz model, Voronoi diagram, Moisture diffusion, Relative humidity distribution

2.1 Introduction

Durability is of paramount importance for achieving a long service life in concrete structures. Concrete, inherently porous in nature, is susceptible to moisture transport, enabling aggressive chemical agents to infiltrate and potentially trigger degradation mechanisms (Liu and Zhang, 2023). These degradation processes can include chloride penetration (Ye et al., 2016, Zhu et al., 2016), alkali-silica reaction (Léger et al., 1996, Multon and Sellier, 2016), and carbonation (Ye et al., 2016). In this context, concrete's transport properties are crucial in determining its durability (Basheer et al., 2001, Hussain and Ishida, 2010) . Moisture diffusivity, a critical property that governs the rate of moisture movement within the material, is an essential parameter in assessing concrete's resistance to deleterious effects of moisture-related phenomena. A robust understanding of moisture diffusivity enables the development

of strategies and materials that can mitigate or even prevent these mechanisms of degradation, ultimately extending the lifespan of concrete structures.

Several numerical models have been developed to predict moisture movement in cementitious materials (Martın-Pérez et al., 2001, Samson and Marchand, 2007, Teixeira de Freitas et al., 2017). At a mesoscale model, diffusivity of the various constituents (phases) of concrete (aggregates, cement matrix and ITZ) is required to predict global moisture transport (Li and Song, 2022). For this purpose, theoretical equations for liquid and vapour water, derived from Darcy's law and Fick's second law, are commonly used to express the relationships between moisture diffusion coefficient, water saturation degree and relative humidity (RH) (Baroghel-Bouny et al., 1999, Mounajed et al., 2004, Qin et al., 2009, Baker et al., 2009). Building upon these principles, Caré and Hervé (Caré and Hervé, 2004) proposed a mesoscale model to predict the moisture diffusivity in concrete with varying coarse aggregate volume fractions, while Sun et al. (Sun et al., 2011) introduced a multi-phase model that explicitly accounts for the individual phases, including mortar, ITZ and aggregates, as well as a homogenization phase. Huang et al. (Huang et al., 2015) developed a multi-scale model that accounts for pore size distribution and fraction to study moisture diffusion. Moreover, Dehwah and Xi (Dehwah et al., 2024) studied the moisture diffusion mechanisms whilst considering different pore sizes by employing molecular, Knudsen and surface diffusions. A generalized self-consistent model was introduced to predict moisture diffusion in concrete including influence of coarse aggregates (Christensen, 2012). Nevertheless, these theoretical models still necessitate the use of empirically calibrated moisture diffusion coefficients, based on experimentally determined parameters (e.g. time, RH, distance, temperature), to express their relationship with moisture saturation and RH. Moreover, the measurement of these parameters is affected by material variability and the precision of the instrumentation (Tada and Watanabe, 2005, Nizovtsev et al., 2008, Terheiden, 2008, Anderberg and Wadsö, 2008).

Wang and Ueda (Wang et al., 2009) employed both macro and meso models to derive a theoretical solution for diffusivity by phase, assuming that most diffusion occurs in the mortar and ITZ. However, as 2-D models do not account for porosity and tortuosity of pore structures, these are unlikely to provide accurate predictions for 3-D problems. Furthermore, most models focus on the diffusivity of the phases, treating them as homogeneous, thus making it challenging to capture the impact of pore structure on diffusion process (Huang et al., 2015).

In contrast to mesoscale models, microscale models focus on modelling diffusivity based on microstructure characteristics of pore structures, which include volume fraction and size distribution. Experimental techniques employed to obtain the pore structure features include: micro imaging generated by X-rays (micro-CT), backscattered electron imaging (BEI) and mercury intrusion porosimetry (MIP). The MIP method can detect a broad spectrum of pore sizes, ranging from 2.5 nm to 10^5 nm. On the other hand, BEL and micro-CT offer two-dimensional and three-dimensional images of

pores, along with their spatial distribution. Results show that concrete contains a diverse array of pores, predominantly falling into four categories: (i) C-S-H gel pores (calcium-silicate-hydrate), (ii) small capillaries, (iii) large capillaries and (iv) voids (Pipilikaki and Beazi-Katsioti, 2009).

Zhang and Ye (Zhang and Ye, 2019) introduced a micro-model to predict moisture diffusion in non-saturated cementitious materials, accounting for different pore radii based on MIP measurements. However, the precision of measured pore radii derived from the MIP method can be compromised by the "ink-bottle" effect (Diamond and research, 2000). To address this limitation, a cylindrical pore model, coupled with thermodynamic theories, can be employed to more accurately predict moisture diffusion (Ranaivomanana et al., 2011, Ranaivomanana et al., 2013a, Espinosa and Franke, 2006, Pollmann et al., 2021). Furthermore, the pore size distribution can be characterized through a multi-Rayleigh-Ritz (R-R) model encompassing various pore types (Ranaivomanana et al., 2013a). This pore distribution model uses the pore type fraction and radii to represent the pore density distribution.

Zhang et al. (Zhang et al., 2012b) proposed a "Lattice Boltzmann" (LB) model for moisture transport to investigate the water-gas diffusion in porous materials. However, they did not account for the gel pores in mortar, despite other studies emphasizing their critical role in moisture diffusion (Hou et al., 2018, McDonald et al., 2010, Patel et al., 2018).

A more accurate prediction of moisture diffusion can thus be achieved by a model that links microstructural features to the diffusion properties of cementitious materials. This can be accomplished by converting the different micro-scale pore types into a homogeneous mesoscale phase. Examples of this include applications of the Maxwell model (Nielsen et al., 2003), the differential medium model (Garboczi and Bentz, 1998, Pivonka et al., 2004), and the self-consistent model (Bary and Béjaoui, 2006). However, these models do not consider coarse aggregates and, hence, are more suited to model mortar rather than concrete.

This chapter introduces the development of a mesoscopic model to describe moisture diffusion in concrete using the Rayleigh-Ritz pore size distribution model. A Voronoi diagram is used to generate a mesh for pores, ITZ surrounding randomly positioned impermeable aggregate, and mortar, resulting in a 2-D concrete mesoscale model. A time-dependent model is employed to account for non-steady state diffusion and predict the moisture transport through the pores and ITZ. The introduced model is calibrated using experimental results. Based on this model, the specific phases of pores and ITZ will contribute towards more precise descriptions of the RH distribution and evolution in concrete. Because of its enhanced predictive capabilities, the model derived herein can be used to study multi-phase coupled problems, such as thermo-hygral, hygro-mechanical, or thermo-hygro-mechanical problems. Integrating the proposed methodology into existing mechanical frameworks will lead to an increased accuracy in predicting the material's mechanical response, including shrinkage, creep and crack

development effects. This in turn will enhance the reliability of long-term performance assessments and facilitate the design of more durable concrete structures.

2.2 Geometric properties of mesoscale model

The approach adopted combines the mesoscale geometry and microscale theory to develop the micro-meso (MiMe) model to simulate moisture diffusion. The following sections describe the parameters that are necessary to define the geometry of all concrete constituents e.g., mortar, aggregate, ITZ and pores, and presents the methodology used to develop the mesoscale model.

2.2.1 Distribution and shapes of aggregate

The Monte Carlo method is employed to locate centroid and diameter of each aggregate and to generate their in-plane spatial distribution (Rajamani et al., 1986, Huang et al., 2022), which is expressed as:

$$\begin{cases} x = x_{\min} + i(x_{\max} - x_{\min}) \\ y = y_{\min} + j(y_{\max} - y_{\min}) \end{cases} \tag{2.1}$$

where, x_{min}, x_{max}, y_{min}, y_{max} are the lower and upper limit of the concrete domain in x direction and y direction, respectively; and i and j are random numbers sampled between 0 and 1.

Specific rules regarding the judgement of interaction between aggregates are imposed to avoid overlap of individual aggregates and ensure that each aggregate is located within the boundaries of the specimen, which is expressed as:

$$\sqrt{(x-x')^2 + (y-y')^2} \geq \frac{(d+d')}{2} \tag{2.2}$$

where, x', y' and d' are the coordinates of previous aggregates and diameters, respectively.

Based on the mix design (in kg/m^3: water 168, OPC 420, river sand 718 and crushed granite aggregate 1127; and the density of the aggregate (2700 kg/m^3) a volume ratio of 42 % aggregate is determined and used to generate the aggregate mesh) (Huang et al., 2015). Three size groups are considered based on the grading curve of Mora's sample (Mora et al., 1998) to create a reasonable aggregate size distribution (4.75 to 9.5 mm -28.4 %, 9.5 to 12.5 mm - 63.6 % and 12.5 to 16 mm 8 %).

Polygonal aggregates with a diameter ranging from 4.75 to 16 mm are created by employing the Fuller distribution (Xia et al., 2021) to generate the number of edges and angles of polygon (α). A typical two-dimensional random polygon aggregate model is shown in Fig. 2.1.

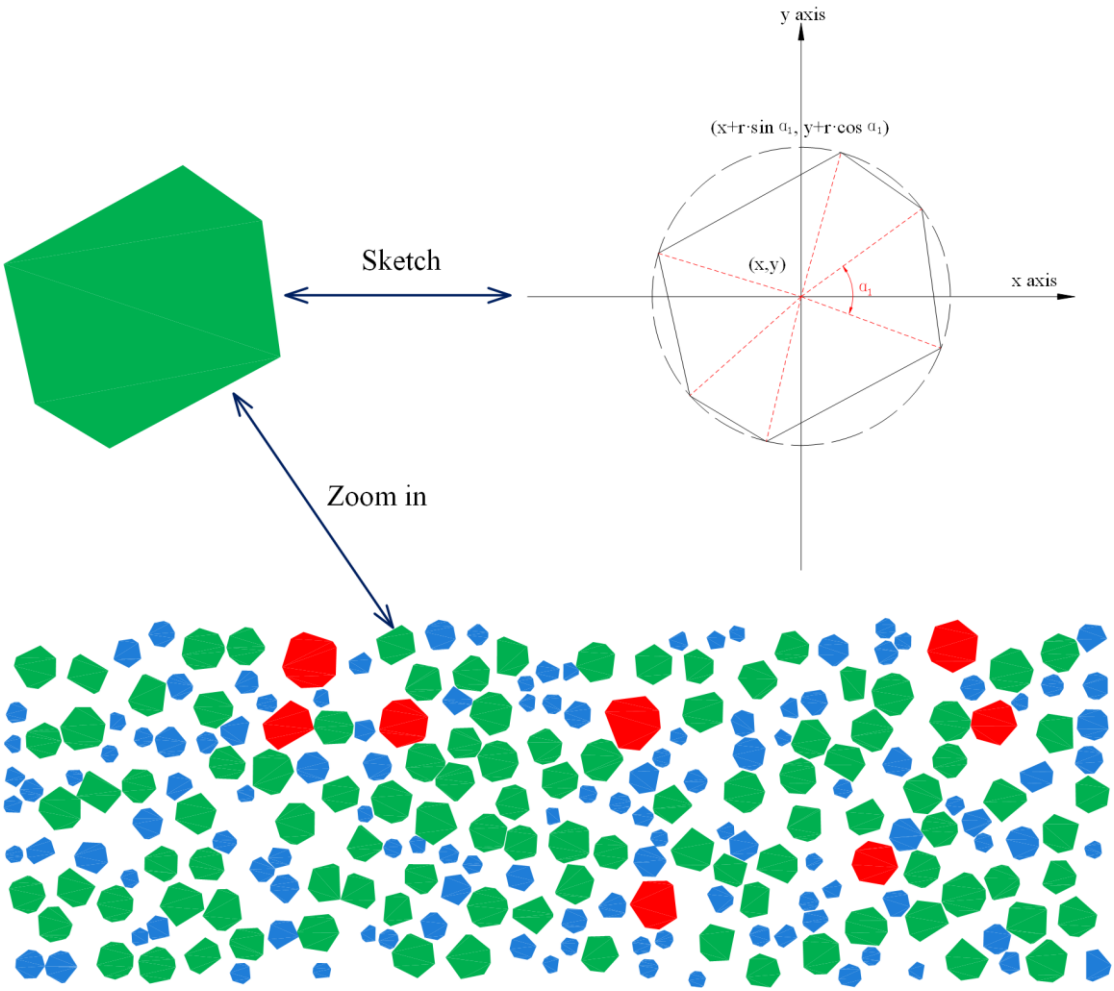

Fig. 2.1 2-D random distribution of polygonal aggregates

2.2.2 Geometric properties of the ITZ

Although the ITZ enhances the pore network connectivity, it also affects the overall tortuosity and complicates the diffusion process in ways that cannot be easily quantified. As a result, diffusion within the ITZ is often treated similarly to diffusion within the pore network (Delagrave et al., 1997).

The diffusion properties of ITZ are dominated by total pore volume within this zone. Moisture transport is assumed to occur exclusively within the ITZ, which can be visualised as the zone surrounding the aggregates with a thickness *"t"* (see Fig. 2.2), and does not occur through the interfaces with mortar and aggregates. The ITZ thickness is generally considered to be around 0.05 mm (Huang et al., 2015), hence this value is adopted in the present study.

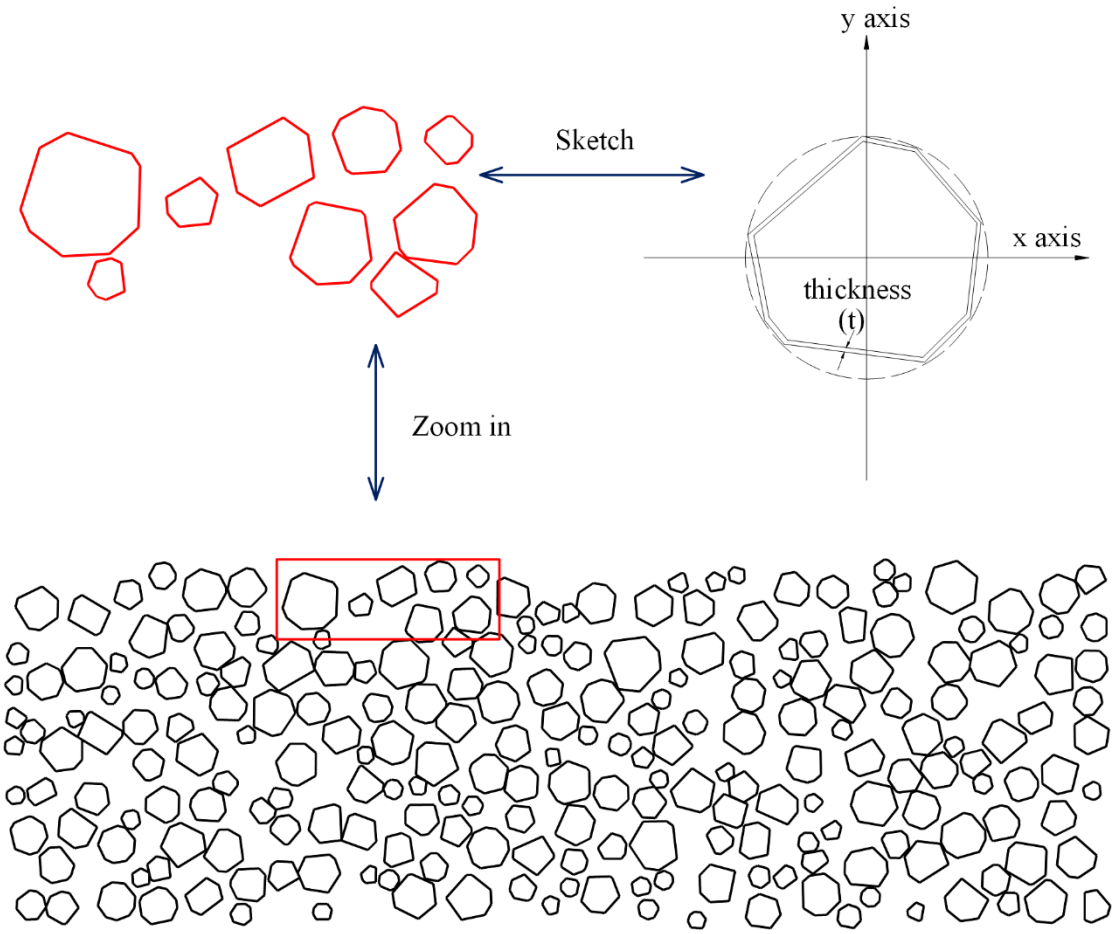

Fig. 2.2. 2-D random distribution of polygonal ITZ

2.2.3 Mortar pore structure

In this study, the bulk of the mortar matrix is considered to be impermeable, akin to aggregates. Therefore, the diffusion process through a network of interconnected pores, capillaries, and ITZ.

To create the capillary structure, the Voronoi tessellation method for polygonal geometrical elements (Idiart, 2009) is adopted. This method generates an array of randomly allocated nodes, located at the centroid of the Voronoi regions within the mortar. These nodes are interconnected via equidistant segments that either intersect or meet at the ITZ, as depicted in Fig. 2.3(a) and (b). The nominal width of these capillary segments is set at 0.3 mm and the total area of the capillary network is determined on the experimentally derived porosity from MIP or other methods.

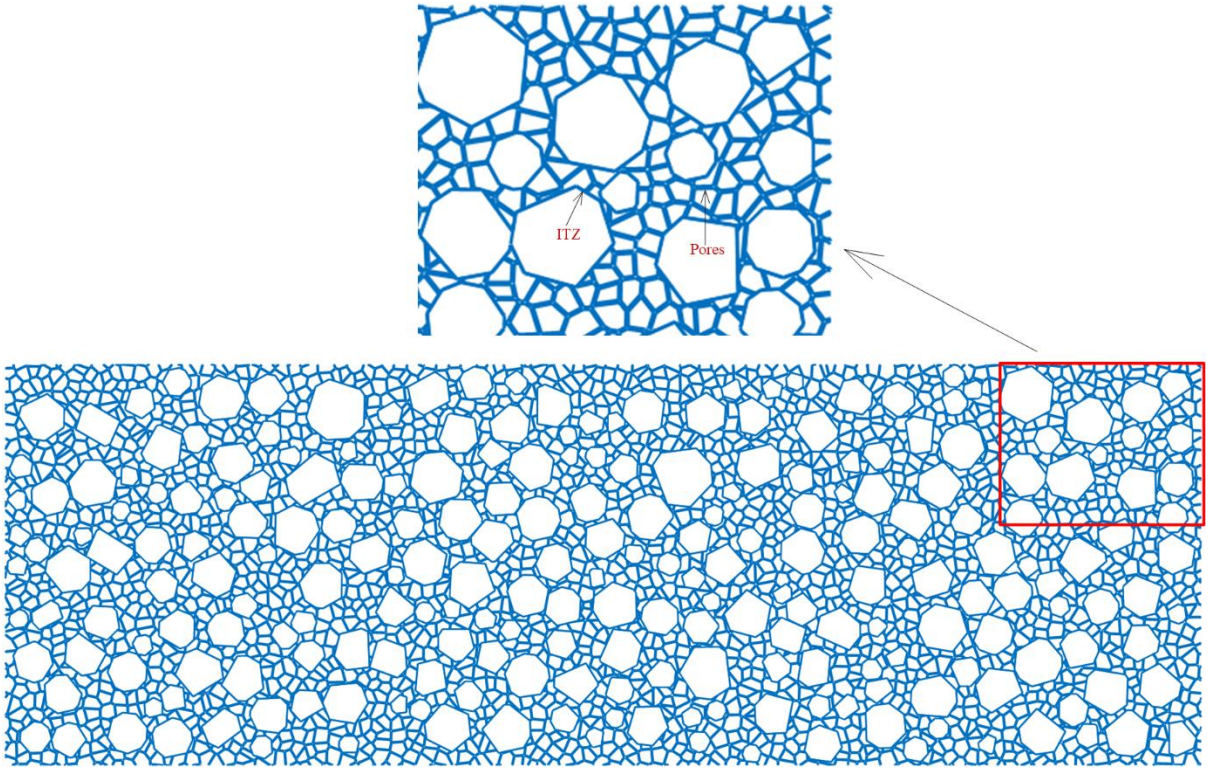

(a)

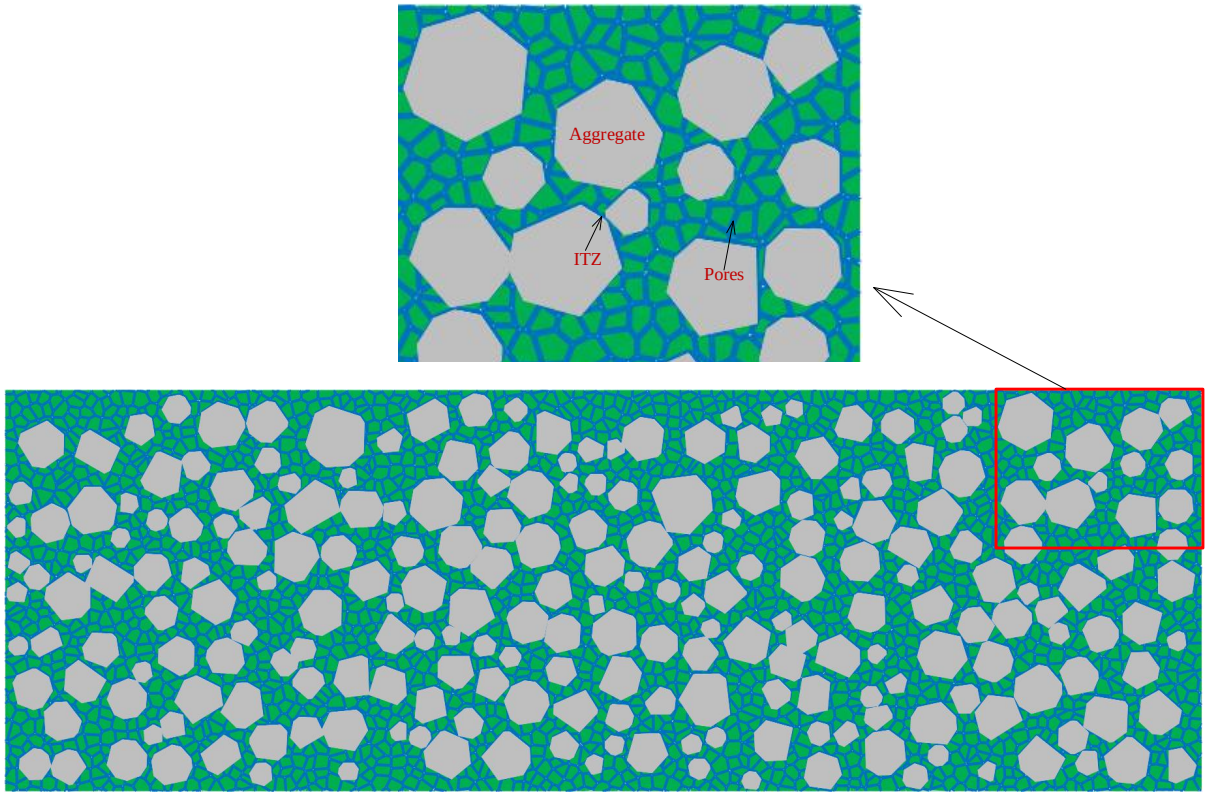

(b)

Fig. 2.3. (a) capillary structure, and (b) overall network

2.3 Theoretical framework for diffusion through capillary structure

Moisture transport in concrete is driven by flow potential, resulting in both diffusion (for water and vapour) and permeation (for liquid water) that lead to desorption and adsorption (Damrongwiriyanupap et al., 2013, Caré, 2003, Ye et al., 2006). Desorption occurs when concrete is exposed to an environment with relatively low RH. Liquid water diffuses due to capillary stress, whilst vapour water diffuses through pores that are partially unoccupied (by liquid) due to gas pressure differential.

Based on the extended Darcy's equation, the flow rate of liquid water (J_L (kg·m^{-2}s^{-1})) can be represented as follows:

$$J_L = -K_L(h)\frac{\partial p_c}{\partial x} \tag{2.3}$$

where K_L (s) represents the diffusion coefficient of liquid water as a function of h (RH %), p_c (Pa) refers to the capillary pressure.

The relationship between RH and capillary stress is obtained using Kelvin's equation and expressed as follows:

$$p_c = -\frac{\rho_L RT \ln h}{M_w} \tag{2.4}$$

where M_w is the molar mass of water (kg/mol), ρ_L is the density of liquid water (kg/m^3), R is the universal gas constant (J·K^{-1}mol^{-1}), and T represents the temperature at the point under consideration (K).

Fick's law is used to express the flux balance of water mass during vapour diffusion:

$$J_V = -K_V(h)\frac{\partial p_v}{\partial x} \tag{2.5}$$

where J_V is the diffusion flux of water vapour (kg·m^{-2}s^{-1}), K_V is the diffusion coefficient of vapour water varying with h (RH %). Vapour relative humidity is defined as the ratio of vapour pressure to saturated vapour pressure, $h = p_V / p_{VS}$. Thus, the diffusion of vapour water is expressed as:

$$J_V = -K_V(h)\, p_{VS}\frac{\partial h}{\partial x} \tag{2.6}$$

where J_V is the vapour flow rate (kg·m^{-2}s^{-1}), p_V (Pa) is the vapour pressure, p_{VS} (Pa) is the saturated vapour pressure.

For mass balance, the rate of water mass change per unit volume is equal to the difference of moisture flux J across the boundaries of an infinitesimal control volume, which is expressed as:

$$-\frac{\partial w}{\partial t} = \nabla \cdot J \tag{2.7}$$

By combining Eqs. (2.3) to (2.7), the diffusion process including liquid and vapour water is obtained as:

$$\frac{\partial w}{\partial h}\frac{\partial h}{\partial t} = \frac{\partial}{\partial x}\left(K_L \frac{\rho_L RT}{M_W h}\frac{\partial h}{\partial x} + K_V p_{VS}\frac{\partial h}{\partial x}\right) \tag{2.8}$$

where $\partial w/\partial h$ is the slope of the adsorption or desorption isotherm, w and h are the water content and RH due to moisture diffusion ($w = w_a - \Delta w_s$, $h = h_a - \Delta h_s$), w_a and h_a are total water content and RH in concrete, Δw_s water loss by hydration process, Δh_s is the RH reduction due to hydration process.

To predict the moisture diffusion, both vapour and liquid permeability of concrete (in Eq. (2.8)) are needed. These diffusion coefficients, which make up the total diffusivity, depend on the pore radius and distribution and can be obtained using the Rayleigh-Ritz model.

2.3.1 Rayleigh-Ritz (R-R) distribution for pores

To determine the diffusion coefficients for vapour and liquid water, the diameter and portion of each type of pores needs to be considered. Huang et al. (Huang et al., 2015) categorize pores based on their diameters into the following types: 1) C-S-H gel pores (less than 2.5 nm), 2) small capillaries (ranging from 2.5 nm to 50 nm), 3) large capillaries (50 to 105 nm), and 4) voids (exceeding 105 nm). However, the larger voids (>105 nm) are normally closed pores that lack connectivity and do not affect the diffusion processes. Moreover, the presence of microcracks (width more than 1 μm) also impacts moisture transport and should be incorporated into the pore size distribution model.

The R-R model can be employed to disaggregate the MIP curve to determine the distribution of each type of pore (Maekawa et al., 2008). The proportion of each pore type by volume (ϕ_i) and their representative radius (r) are used to delineate the distribution of each type of pores, expressed as:

$$\phi = \phi_t \sum_1^4 \phi_i \left(1 - \exp\left(-\frac{r}{B_i}\right)\right) \tag{2.9}$$

where ϕ_t is the total porosity of concrete, and ϕ_i is volume ratio between the porosity of pore type i and the overall porosity. B_i is the pore radius at the peak of the differential porosity for each pore type on a logarithmic scale.

A random connection of tubular geometry capillaries is adopted to simulate the entire pore structure (Maekawa et al., 2008). Thus, the pore size distribution is connected to the density distribution of pores f_d, which is defined as the derivative of porosity with respect to pore radius r:

$$f_d = \phi_t \sum_{1}^{4} \frac{\phi_i}{B_i} \exp\left(-\frac{r}{B_i}\right) \tag{2.10}$$

From Fig. 2.4, the saturation degree S_r can be determined by integrating the pore-specific surface area and the thickness of water molecules along the radial direction:

$$S_r = \frac{1}{\phi} \int_0^{r_c} f_d(r)\, dr \tag{2.11}$$

where r_c is the critical radius (i.e. the pore radius below which capillary condensation can occur), and it is defined as the sum of capillary condensate radius r_k and the thickness of absorbed water layer on the pore wall t_a, as shown in Fig. 2.4.

Fig. 2.4. Moisture sorption within a capillary with saturated flow

To obtain the analytical solution for the R-R model, the well-establisehd water saturation degree solution model by Brunauer-Skalny-Bodor is employed along with empirical functions introduced by Xi et al. (Xi et al., 1994) to calculate the saturation degree. The Brunauer-Skalny-Bodor model thus reduces to a two-parameter (C and k) formula shown in Eq. (2.12):

$$S_r = \frac{h(1-k)\left[1+(C-1)k\right]}{(1-kh)\left[1+(C-1)kh\right]} \tag{2.12}$$

The parameters, ϕ_i and B_i, can be obtained by combining Eqs. (2.10), (2.11) and Eq. (2.12) and implementing a curve-fitting method (Mualem, 1976).

2.3.2 Diffusivity of vapour and liquid water

In concrete, vapour water flows through capillaries into the pores and this movement depends on the flow potential due to difference in RH. The Knudsen's theory is applied to explain the collision between molecules and their interactions with pore walls of vapor water diffusion. The vapour water diffusion coefficient, k_v, can be described using the equation (Quenard et al., 1992):

$$k_V = \frac{D_{va}}{1 + l_m / 2r_e}\left(\frac{M_w}{RT}\right) \tag{2.13}$$

where l_m denotes the mean free path of water molecules, while r_e is actual pore radius, equivalent to r_k (shown in Fig. 2.4), D_{va} represents the permeability of vapour water in air as given below (Quenard et al., 1992):

$$D_{va} = D_0 \frac{P_0}{P}\left(\frac{T}{T_0}\right)^{1.88} \tag{2.14}$$

where D_0 represents the vapour water diffusion coefficient at a pressure of P_0 and temperature of T_0 (D_0 = 21.6 × 10-6 m^2/s, P_0=11325 Pa, T_0=273.16 K) (Quenard et al., 1992).

The diffusion coefficient of unsaturated concrete, K_v, is obtained using Eq. (2.15) by integrating over the pore size range (Maekawa et al., 2008):

$$K_V = \int_{r_c}^{\infty} \frac{k_V}{\tau}\left(\frac{r - t_a}{r}\right)^2 f_d(r)\,dr \tag{2.15}$$

where τ is a parameter representing pore tortuosity and it is taken as $\tau = (\pi/2)^2$ (Maekawa et al., 2008, Ishida et al., 2007).

As developed by Ishida et.al. (Ishida et al., 2007), permeability of liquid water can be expressed as a function of moisture flux balance based on the Hagen-Poiseuille equation (Ishida et al., 2007), and the diffusion coefficient of liquid water can be determined as:

$$K_L = \frac{\rho_L}{8\tau^2\eta}\left(\int_0^{r_c} r f_d(r)\,dr\right)^2 \tag{2.16}$$

where ρ_L represents the density of the liquid water, and η denotes its viscosity.

For concrete, the convective process at the surface also needs to be considered. According to the mass balance between ambient air and concrete, the diffusion flux to air can be expressed by (Roy, 2004):

$$J = -\frac{D_{va} M_w p_{vs}}{RT} \cdot \frac{h_b - h_e}{\delta} \tag{2.17}$$

where h_b and h_e denote the relative humidity on the concrete surface and the ambient relative humidity, respectively. The parameter δ represents the effective thickness of the concrete boundary, which can be taken to be about 25 mm (Xi et al., 1994).

2.3.3 Discretization and numerical implementation

The finite element method (FEM) is utilized to describe the moisture diffusion at the pore structure by using a specially formulated User Defined Element (UEL) subroutine in Abaqus. In FEM implementation, $\Omega \subset H^D$ is the domain representing the moisture diffusion region, with D being the spatial dimension (D = 2) and $\partial\Omega$ representing the boundary.

Starting from Eq. (2.8), multiplying by an arbitrary variational field that satisfies the essential boundary conditions δh and by integrating over Ω, the following weak form function of diffusion process can be obtained:

$$\begin{cases} \dfrac{\partial h}{\partial t} = \dfrac{\partial \delta h}{\partial t} \\ \dfrac{\partial f(h)}{\partial x} = \dfrac{\partial \delta h}{\partial x} f(h) \\ \displaystyle\int_\Omega \left\{ \frac{\partial w}{\partial h} \frac{\partial \delta h}{\partial t} \right\} d\Omega = \int_\Omega \left\{ \frac{\partial \delta h}{\partial x} K_L \frac{\rho_L RT}{M_W h} \frac{\partial h}{\partial x} + \frac{\partial \delta h}{\partial x} K_V p_{VS} \frac{\partial h}{\partial x} \right\} d\Omega \end{cases} \tag{2.18}$$

To solve the Eq. (2.18), the format of the weak form function is described as:

$$\int_\Omega \left\{ \frac{\partial \delta h}{\partial x} K_L \frac{\rho_L RT}{M_W h} \frac{\partial h}{\partial x} + \frac{\partial \delta h}{\partial x} K_V p_{VS} \frac{\partial h}{\partial x} - \frac{\partial w}{\partial h} \frac{\partial \delta h}{\partial t} \right\} d\Omega = 0 \tag{2.19}$$

Taking into account boundary condition outlined in Eq. (2.17), Knudsen number is employed to describe the collision between molecules and their interactions with pore walls of vapor water diffusion, whilst the Hagen-Poiseuille theory is employed to obtain the performance of liquid water diffusion, hence, the adsorption and desorption moisture diffusion function is obtained as follows:

$$\int_{\Omega}\left\{\frac{\partial\delta h}{\partial x}K_L\frac{\rho_L RT}{M_W h}\frac{\partial h}{\partial x}+\frac{\partial\delta h}{\partial x}K_V p_{VS}\frac{\partial h}{\partial x}-\frac{\partial w}{\partial h}\frac{\partial\delta h}{\partial t}\right\}d\Omega-\int_{\partial\Omega}\delta h\left\{\frac{D_{va}M_w p_{vs}}{RT}\cdot\frac{h-h_e}{d}\right\}d\partial\Omega=0 \tag{2.20}$$

The Galerkin approach assumes that the variational field, δh, can be expressed by the following function:

$$\delta h = N_T \delta h^N \tag{2.21}$$

where δh^N is the nodal RH, N_T refers to the matrix of shape functions derivatives for the scalar fields ($N_T = [N_1, N_2, N_3, N_4]$).

Substituting Eq. (2.21) into Eq. (2.20), the following is obtained:

$$\delta h^N\left\{\begin{array}{l}\int_{\Omega}\left\{\frac{\partial N_T}{\partial x}K_L\frac{\rho_L RT}{M_W h}\frac{\partial h}{\partial x}+\frac{\partial N_T}{\partial x}K_V p_{VS}\frac{\partial h}{\partial x}-\frac{\partial w}{\partial h}\frac{\partial N_T}{\partial t}\right\}d\Omega\\ -\int_{\partial\Omega}N_T\left\{\frac{D_{va}M_w p_{vs}}{RT}\cdot\frac{h-h_e}{d}\right\}d\partial\Omega\end{array}\right\}=0 \tag{2.22}$$

Since the δh^N is arbitrarily chosen, the weak form function of moisture diffusion can be described as:

$$\left\{\begin{array}{l}\int_{\Omega}\left\{\frac{\partial N_T}{\partial x}K_L\frac{\rho_L RT}{M_W h}\frac{\partial h}{\partial x}+\frac{\partial N_T}{\partial x}K_V p_{VS}\frac{\partial h}{\partial x}-\frac{\partial w}{\partial h}\frac{\partial N_T}{\partial t}\right\}d\Omega\\ -\int_{\partial\Omega}N_T\left\{\frac{D_{va}M_w p_{vs}}{RT}\cdot\frac{h-h_e}{d}\right\}d\partial\Omega\end{array}\right\}=0 \tag{2.23}$$

The discretization of this diffusion system at element level is followed:

$$\left\{\begin{array}{l}\nabla h = B_T h^N\\ \tilde{h} = N_T \tilde{h}^N\end{array}\right. \tag{2.24}$$

where $\tilde{h}^N$ is nodal incremental relative humidity. B_T is the matrix of shape function derivatives for the tensor fields ($B_T = [\partial N_1/\partial x, \partial N_2/\partial x, \partial N_3/\partial x, \partial N_4/\partial x]$).

Using the Galerkin method (Nguyen et al., 2019), the solution equation for FEM is proposed by combining Eq. (2.23) and Eq. (2.24):

$$\int_{\Omega} N_T^T \frac{\partial h}{\partial t}\frac{\partial w}{\partial h} d\Omega + \int_{\Omega} B_T^T K_L \frac{\rho_L RT}{M_W h}\frac{\partial h}{\partial x} d\Omega + \int_{\Omega} B_T^T K_V p_{VS} \frac{\partial h}{\partial x} d\Omega - \int_{\partial\Omega} N_T^T \frac{D_{va} M_w p_{vs}}{RT}\frac{(h_s - h_e)}{\delta} dS = 0 \quad (2.25)$$

A modified Newton-Raphson approach is utilized to obtain solution for this non-linear diffusion equation (Nguyen et al., 2019), which is expressed as:

$$\left[\int_{\Omega} N_T^T \frac{N_T}{\Delta t}\frac{\partial w}{\partial h} d\Omega + \int_{\Omega} B_T^T K_L \frac{\rho_L RT}{M_W h} B_T d\Omega + \int_{\Omega} B_T^T K_V p_{VS} B_T d\Omega - \int_{\partial\Omega} N_T^T \frac{D_{va} M_w p_{vs}}{RT}\frac{N_T}{\delta} dS\right] h^N = \int_{\Omega} N_T^T \frac{\partial h}{\partial t}\frac{\partial w}{\partial h} d\Omega + \int_{\Omega} B_T^T K_L \frac{\rho_L RT}{M_W h}\frac{\partial h}{\partial x} d\Omega + \int_{\Omega} B_T^T K_V p_{VS} \frac{\partial h}{\partial x} d\Omega - \int_{\partial\Omega} N_T^T \frac{D_{va} M_w p_{vs}}{RT}\frac{(h_s - h_e)}{\delta} dS \quad (2.26)$$

2.4 Calibration of model

2.4.1 Parameters of model

This proposed model was verified using experimental observations by Huang et al. (Huang et al., 2015). Prismatic specimens (100 mm × 150 mm × 300 mm) (Fig. 2.5) were placed inside a chamber at 23 °C and 100 % RH for 90 days. It was assumed that the hydration process was substantially complete by this stage. After curing, the perimeter of the specimens was sealed and removed into a chamber at 23 °C and 18 % relative humidity for 30 days.

Table 2.1 shows the R-R pore distribution parameters as obtained by Huang et al. (Huang et al., 2015), whilst Fig. 2.6 shows the moisture diffusivity based on the methodology discussed in Section 2.3.2.

It is important to note that when pore distribution parameters are not determined experimentally, their values can be estimated as discussed in Section 2.3.1.

Table 2.1: Parameters for R-R pore distribution model.

	ϕ_1	B_1 (nm)	ϕ_2	B_2 (nm)	ϕ_3	B_3 (nm)	ϕ_4	B_4 (nm)
Sample	0.042	1.01	0.056	5.00	0.020	32.05	0.012	571.80

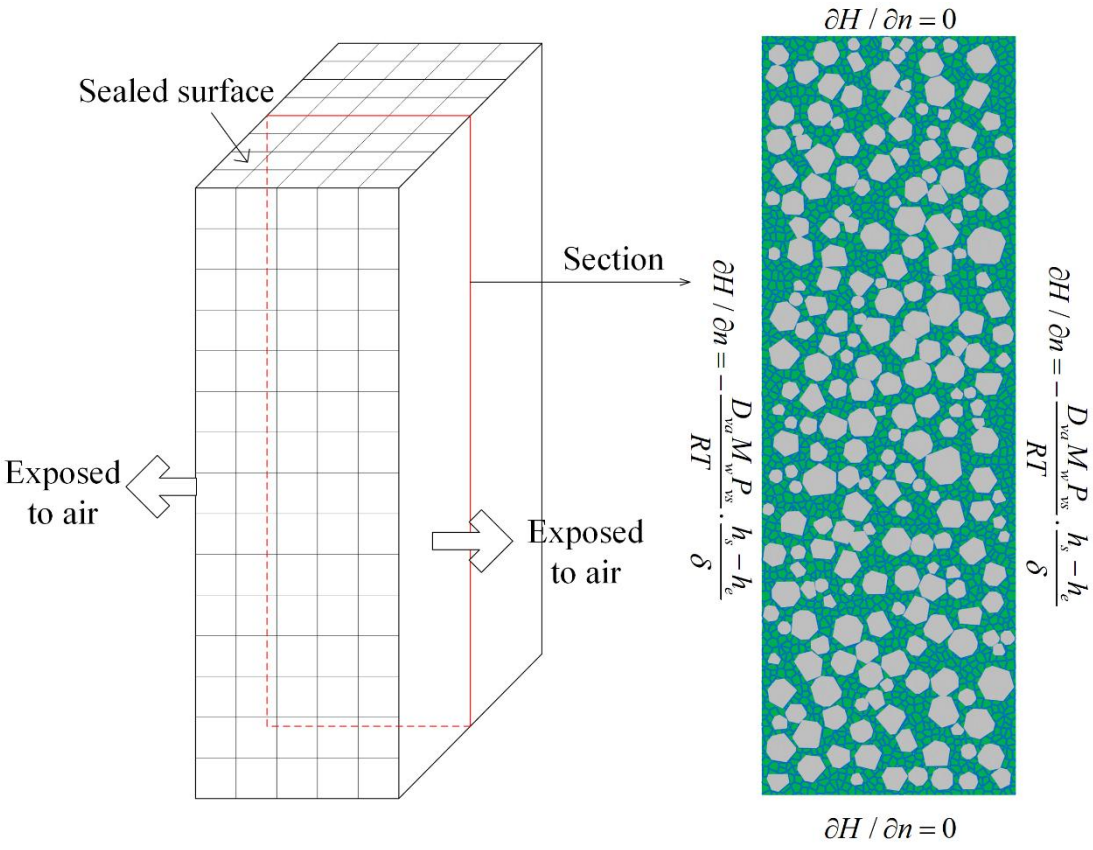

(a) (b)

Fig. 2.5. (a) Sealing conditions of sample, and (b) FEM model of sample

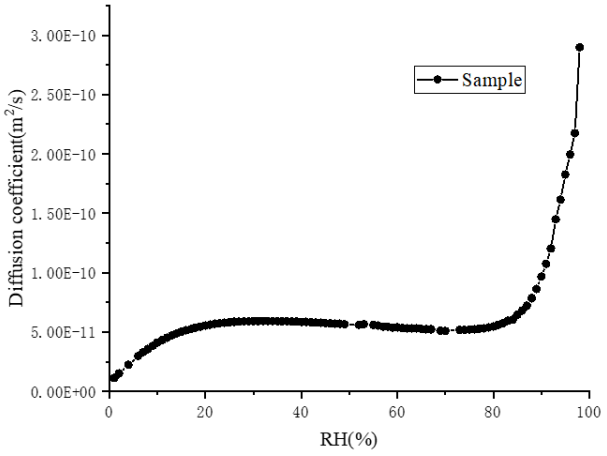

(a)

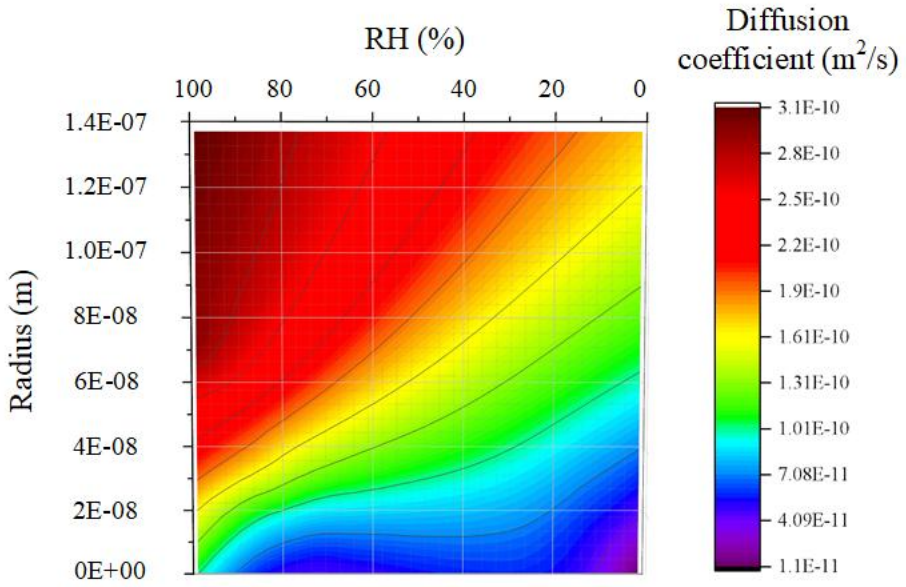

(b)

Fig. 2.6. Diffusion coefficient dependent on (a) RH, and (b) RH and radius

2.4.2 Comparison between experimental data and numerical results

RH distribution in sample can be predicted by the MiMe scale model, introduced above, by using the data and parameters given in Section 2.4.1. Fig. 2.5 (b) shows the FEM model developed for the cement matrix, aggregate, and ITZ pore structures; using the method developed at Section 2.2 as well as initial boundary condition. RH evolution in pore network for the top and bottom 20 mm at different times (i.e., 7, 14 and 30 days) is shown in Fig. 2.7.

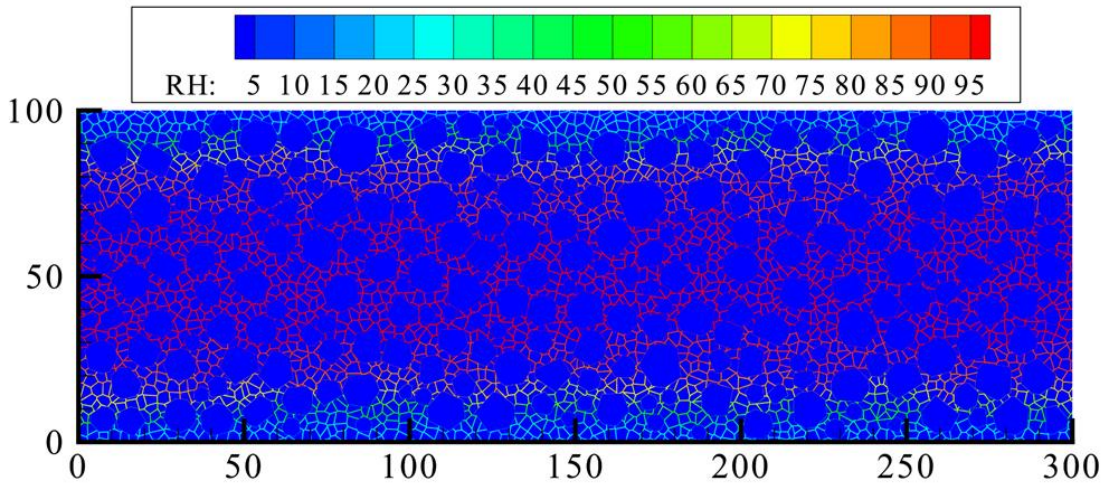

(a)

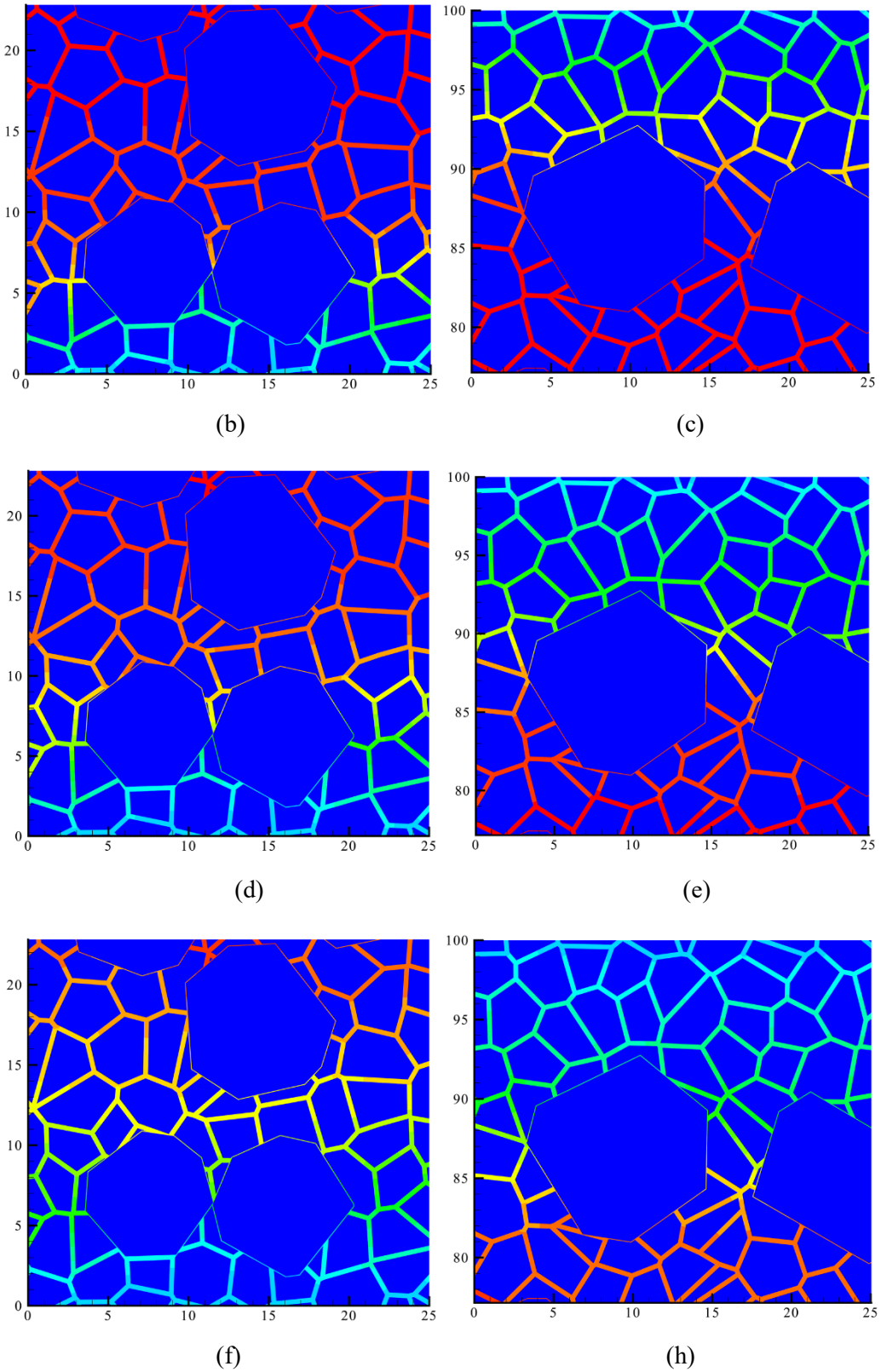

Fig. 2.7. RH evolution along time, (a) RH distribution at 30th day, (b) Bottom-left corner at 7th day, (c) Top-left corner at 7th day, (d) Bottom-left corner at 14th day, (e) Top-left corner at 14th day, (f) Bottom-left corner at 30th day, and (h) Top-left corner at 30th day

Fig. 2.8 presents a comparison between the predictions and the experimental data at 30 days. Overall, the results are in good agreement. However, due to the impact of pores tortuosity, the RH distribution along length of specimen at each depth is not perfectly uniform as for a homogeneous material (see Fig. 2.9). Fig. 2.10 (a) shows the RH distribution in pore structure in the sample, and the variation of RH with depth at five changed sections along the length of the specimen. As expected, the RH drops rapidly near the boundaries, but is still almost fully saturated in the middle (98 %).

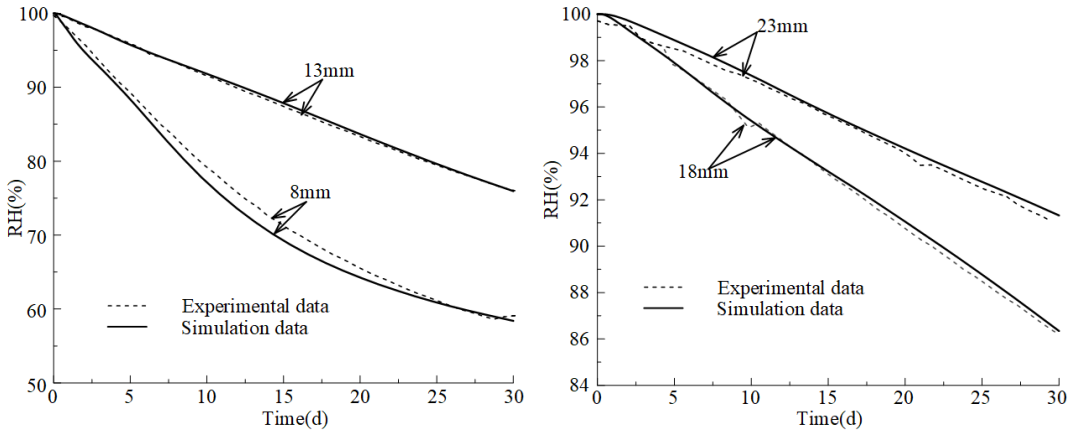

(a) (b)

Fig. 2.8. Comparison between experimental data and simulation results at different depth, (a) 8 mm and 13 mm, and (b) 18 mm and 23 mm

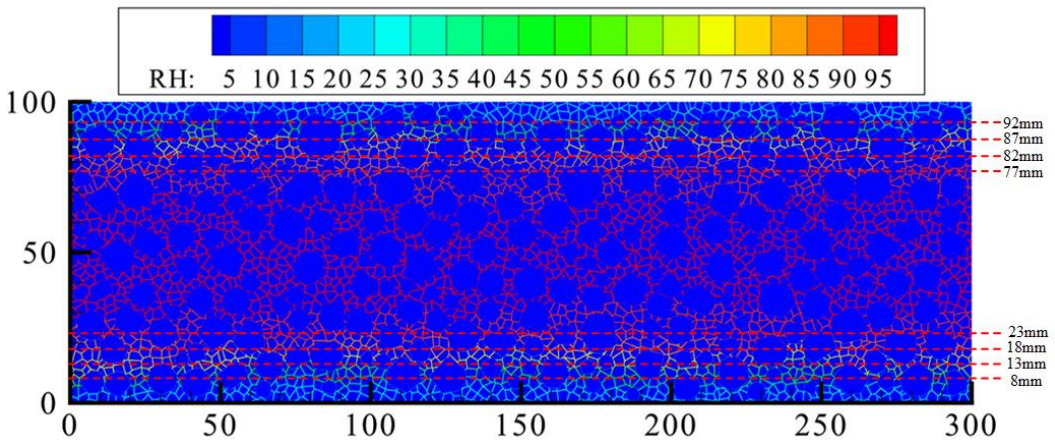

(a)

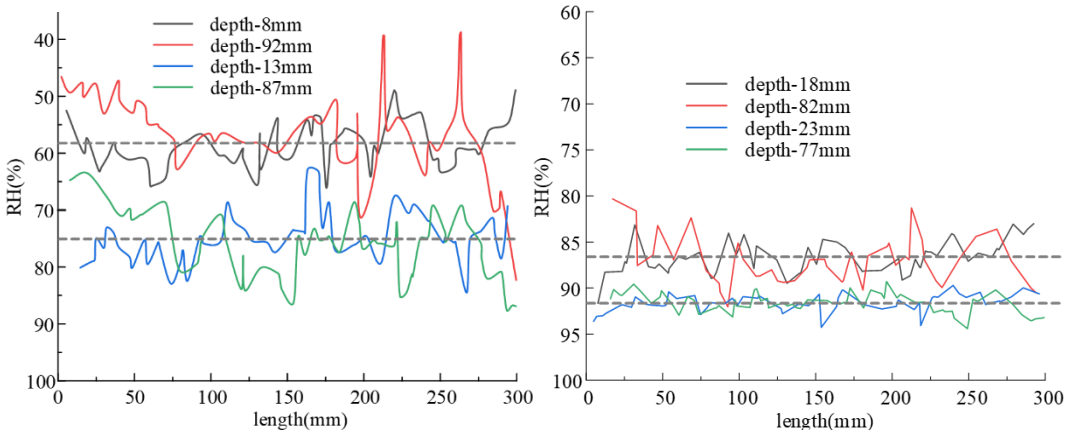

(b) (c)

Fig. 2.9. (a) RH distribution within the pore network and location of measuring depths, (b) RH distribution at depths of 8 mm and 13 mm from top and bottom, and (c) RH distribution at depths of 18 mm and 23 mm from top and bottom

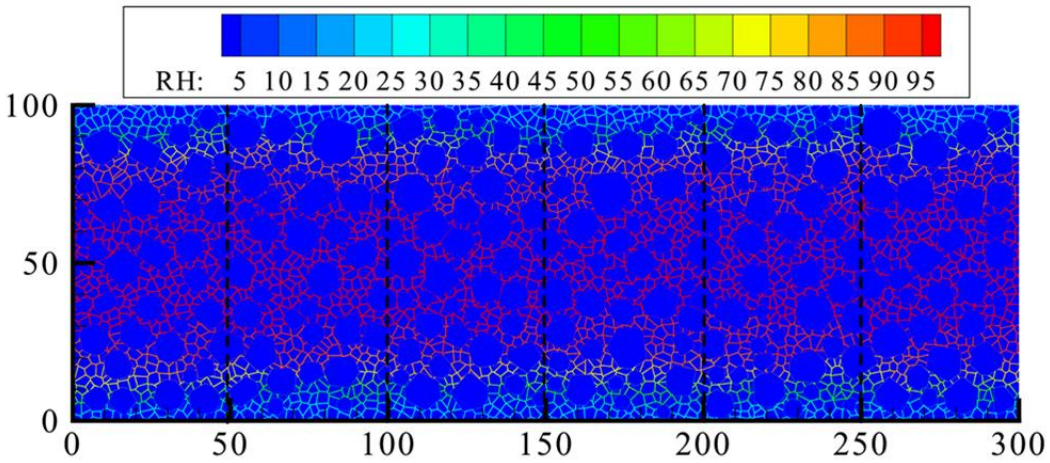

(a)

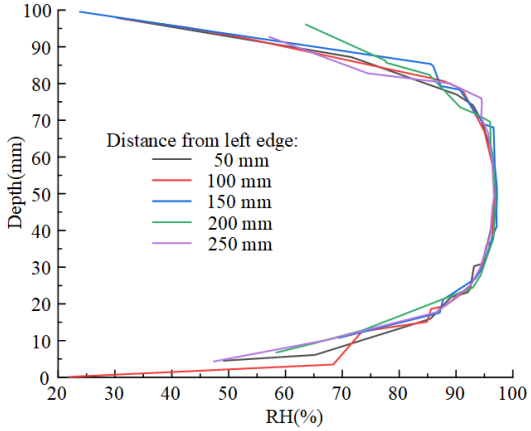

(b)

Fig. 2.10. (a) RH distribution within the pore network and location of measuring sections, and (b) RH distribution along the specimen depth at various sections

2.4.3 Parametric investigation

The impacts of ambient relative humidity, temperature, and tortuosity to diffusivity of concrete are described in Fig. 2.11 (a), (b) and (c), respectively. Depth of 8 mm is used for these results. As expected, moisture transport increases with a decrease in ambient RH (see Fig. 2.11 (a)) since this creates a higher flow potential at the concrete-air boundary, increasing the evaporation rate at the concrete surface. The effect of increasing temperature in 20°C increments is shown in Fig. 2.11 (b). As temperature increases, RH drops faster to a small extent the diffusion ability of concrete (Quenard et al., 1992). On the contrary, increased tortuosity slows down moisture diffusion by extending the diffusion paths.

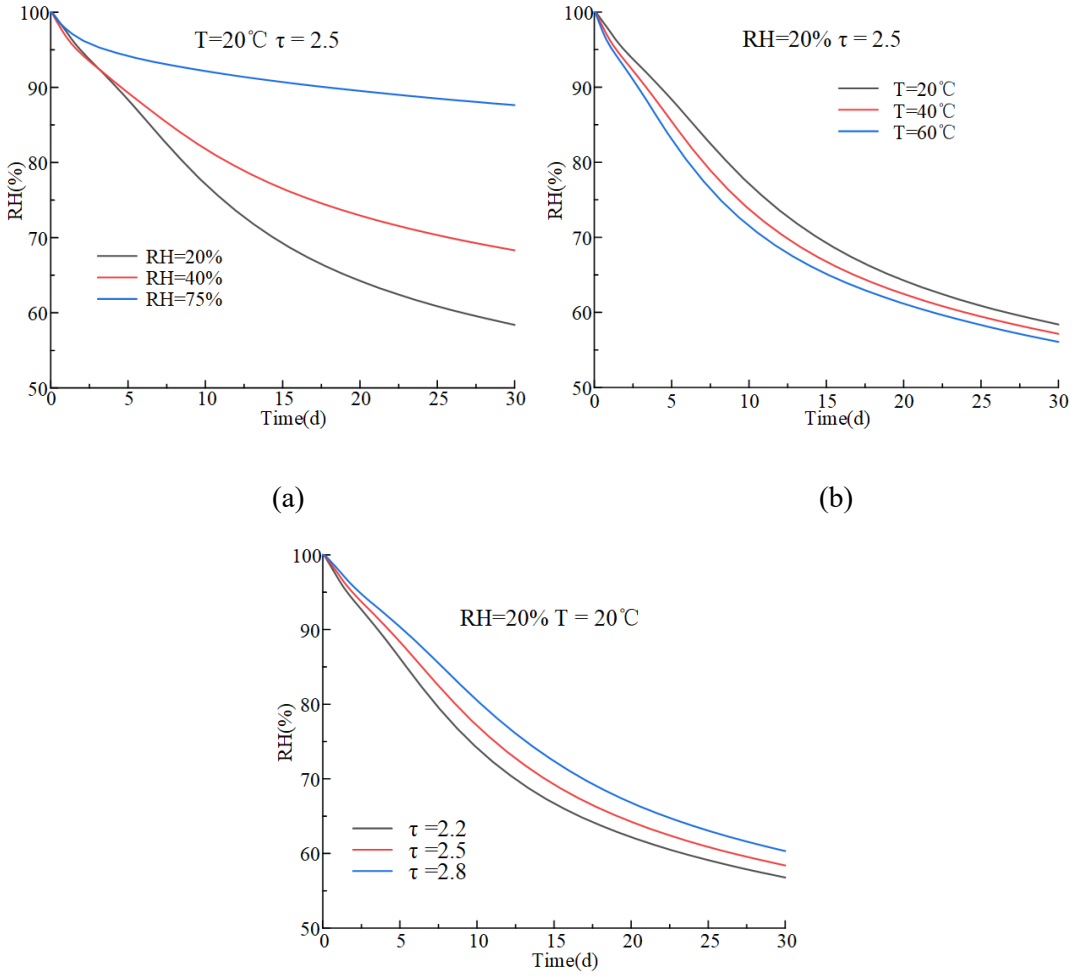

Fig. 2.11. Effects of parameters on moisture diffusion: (a) Ambient RH, (b) Temperature, and (c) Tortuosity

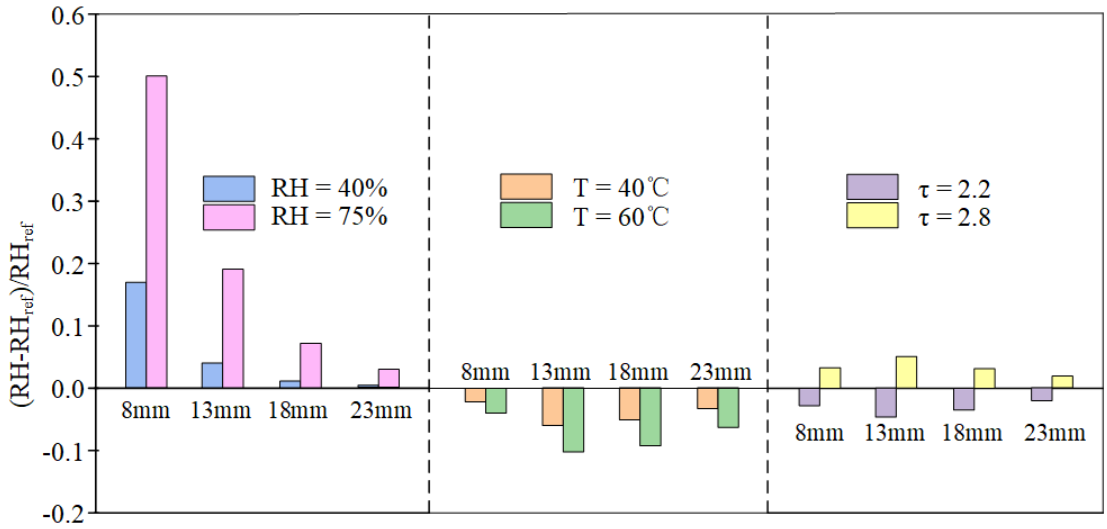

Fig. 2.12. Sensitivity of RH change to different parameters

Sensitivity of diffusion model with main investigated parameters is shown in Fig. 2.12. In the figure, RH_{ref} is defined as the reference environment characterized by T = 20 °C, RH = 20 % and, assuming a tortuosity τ = 2.5. The relative change in RH resulting from exposure to different environmental conditions and values of tortuosity is presented. Increasing the temperature by 20 °C or 40 °C, decreases RH by about 3 % and 10.8 %, respectively. Increasing the ambient RH by 20 % or 75 % results in an increase in RH by about 20 % and 50 %, respectively. A change in tortuosity from 2.5 to 2.2 and 2.8, results in changes in RH that vary from -4.8 % and 5.5 %, respectively.

2.5 Influence of mesostructural characteristics on moisture diffusion

Concrete, as a typical multi-phase composite material, can be viewed as a heterogeneous material with a highly complex composite structure at mesoscopic level. Based on previous models, key characteristics of concrete include heterogeneities introduced by adding coarse aggregate and fine aggregate to the mortar matrix, leading to the formation of ITZ, and a porous component comprising of mortar. Therefore, the influence of ITZ thickness, fine aggregate volume fraction, and shape of coarse aggregate are investigated.

2.5.1 ITZ thickness effect of model

According to previous literature, the ITZ can be represented as a thin bonding layer between the aggregate and cement matrix, typically having a thickness ranging from 10 to 50 μm (Shuguang et al., 2015). To study the impact of ITZ thickness, thicknesses of 10, 20, 30 and 40 μm are considered. The same distribution, shape and size of aggregate, and pore structure are employed to minimize the effect of other geometric features. It is important to note, however, that ITZ thickness affects the porosity of

the ITZ phase, an in turn the total porosity, albeit slightly, as shown in Table 2.2. The RH evolution at 8mm depth with different ITZ thickness is shown in Fig. 2.13.

Table 2.2: Porosity for different phases with varying ITZ thickness.

Model	Porosity (%)		
	ITZ	Pores	Total
ITZ-50	1.02	11.9	12.92
ITZ-40	0.82	11.9	12.72
ITZ-30	0.61	12.0	12.61
ITZ-20	0.41	12.0	12.41
ITZ-10	0.2	12.05	12.25

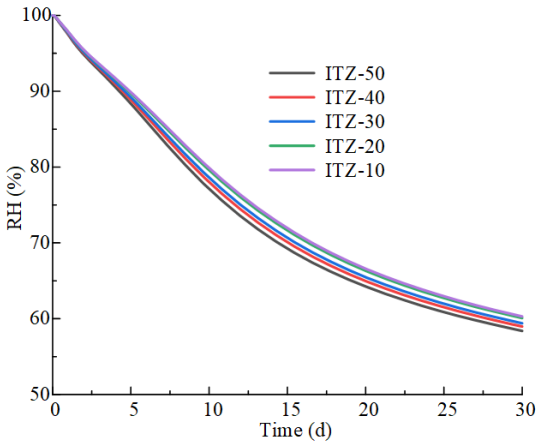

Fig. 2.13. RH evolution with different ITZ thickness

From Fig. 2.13, the RH evolution (at 8mm) slightly increases from 58.4% to 60.3%, which shows that a decrease in ITZ thickness reduces moisture diffusion. This is because a reduction in ITZ thickness increases the representative tortuosity of the pore phase, thereby reducing the overall porosity.

2.5.2 Fine aggregate effect

To analyse the influence of fine aggregate to moisture diffusion, different volume fractions (3%, 6% and 9%) are considered. As the inclusion of higher volume fractions of fine aggregates would prove

computationally costly, and was not deemed to provide any further insights, only these three cases were examined. The resulting aggregate distributions are shown in Fig. 2.14. The other geometric features, such as volume content and spatial distribution of coarse aggregate, and pore structure remain the same. However, the porosity changes slightly with the inclusion of fine aggregate, as shown in Table 2.3. The RH evolution at 8mm depth with the different fine aggregate contents is shown in Fig. 2.15.

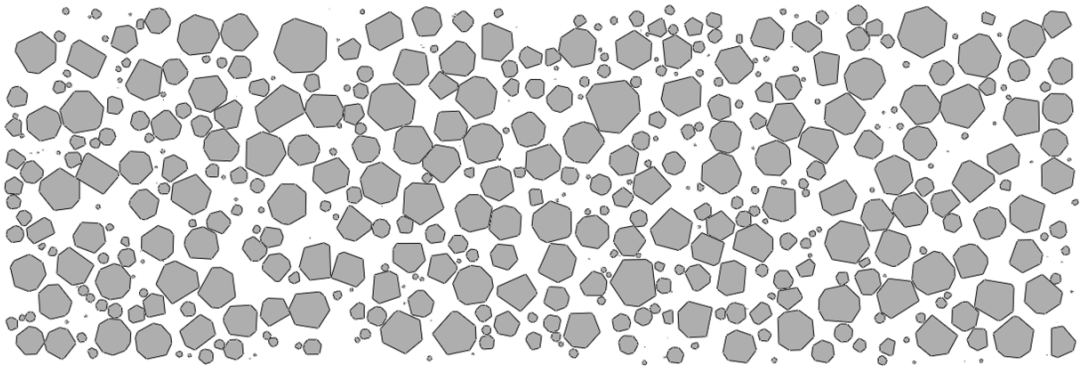

(a)

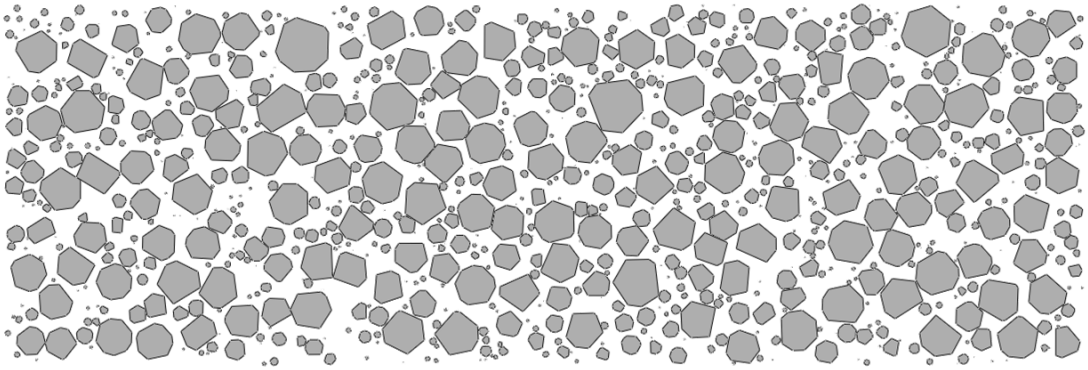

(b)

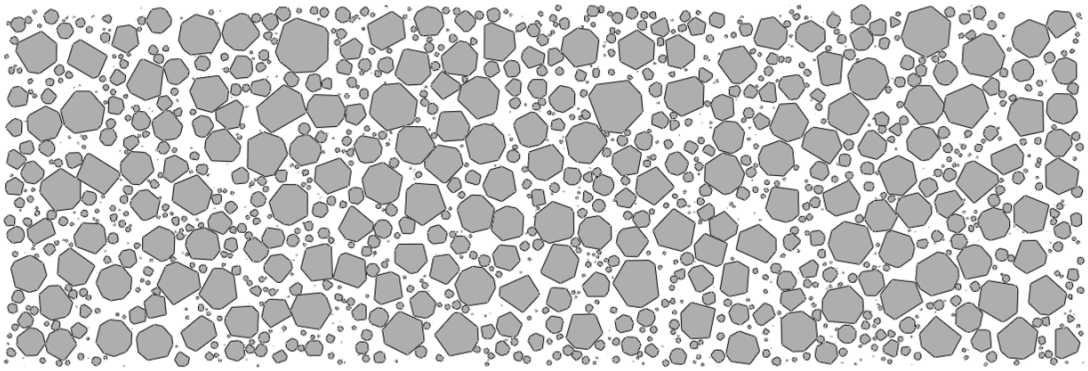

(c)

Fig. 2.14. Distribution of aggregate with various fraction of fine aggregate: (a) 3%, (b) 6% and (c) 9%

Table 2.3: Porosity for different contents of fine aggregate

Model	Porosity (%)		
	ITZ	Pores	Total
Sand-0%	1.02	11.90	12.92
Sand-3%	1.28	11.27	12.55
Sand-6%	1.58	10.65	12.23
Sand-9%	1.93	10.01	11.94

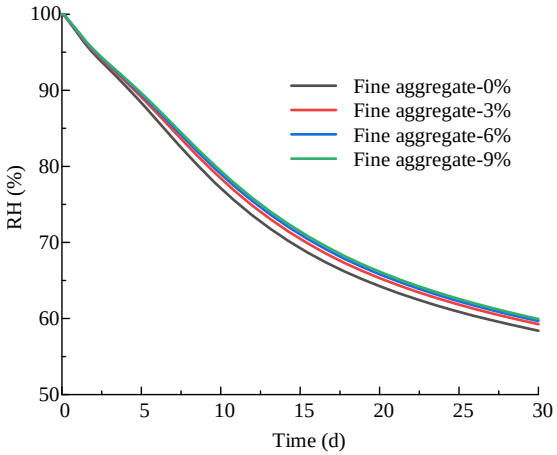

Fig. 2.15. RH evolution with different fine aggregate fractions

From Fig. 2.15, the RH evolution (at 8mm) is found to slightly increase, from 58% to 60%, with the inclusion of fine aggregates. This shows that an increase in volume fraction of fine aggregates slightly reduces the moisture diffusion inside concrete. This results from the decrease in the representative tortuosity of the pore phase, as well as total porosity of specimens. However, this effect is marginal and, given the high computational costs associated with the generation of the higher number of aggregates, a simplified model only including the coarse aggregated can be adopted.

2.5.3 Shape effect

To study the impacts of coarse aggregate shape, two types of aggregate with spherical and ellipsoidal shapes are examined. To minimize the effect of other geometric features, the same pore structure is employed. The models are shown in Fig. 2.16. Porosity details for different phases are shown in Table 2.4. RH evolution at 8mm depth with different aggregate shapes is shown in Fig. 2.17.

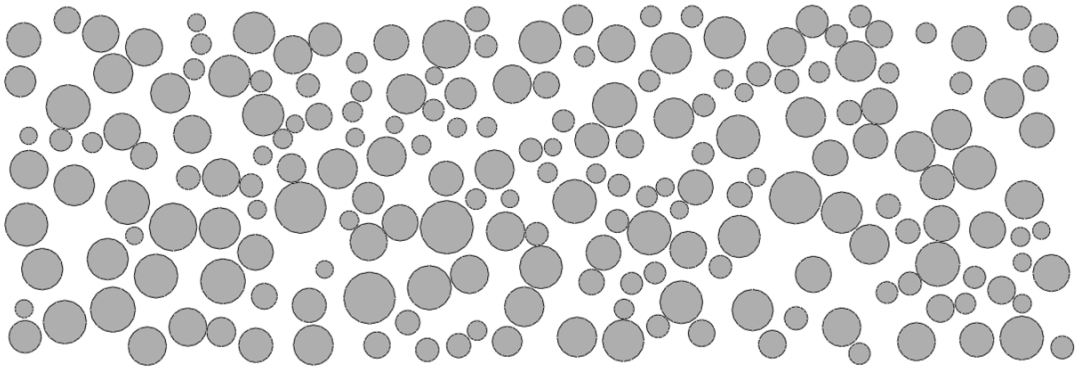

(a)

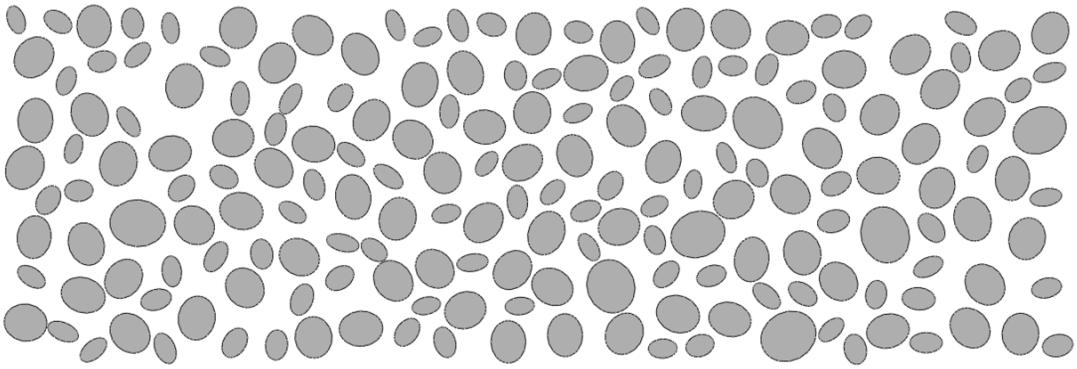

(b)

Fig. 2.16. Distribution of aggregate with different shape of coarse aggregate: (a) spherical aggregate and (b) ellipsoidal aggregate

Table 2.4: Porosity for different phases with different shape of aggregate.

Model	Porosity (%)		
	ITZ	Pores	Total
Polygonal aggregate	1.02	11.90	12.92
Spherical aggregate	0.91	11.86	12.77

Ellipsoidal aggregate	0.90	11.89	12.79

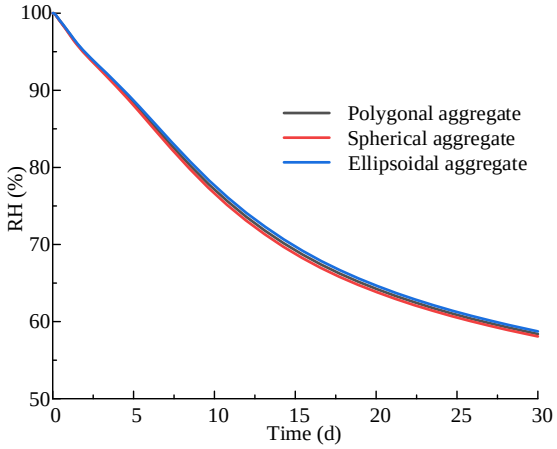

Fig. 2.17. RH evolution with different shape of coarse aggregate

From Fig. 2.17, it can be observed that RH evolution (at 8mm) changes slightly with different shapes of coarse aggregate, ranging from 58.1% for spherical aggregate to 58.4% for polygonal aggregate and 58.8% for ellipsoidal aggregate. However, again this change is marginal and a correction is needed only if the aggregates are substantially flaky or fibre like.

2.6 Calibration of MiMe model

2.6.1 RH distribution in hardened concrete

This model is verified using experimental data by Jin et al. (Jin et al., 2022). One hundred mm cubes were stored inside a chamber with 22 ± 2 ℃ and 95 ± 5 % RH for 60 days. It was assumed that the hydration process was substantially complete by this stage. After curing, 5 surfaces of samples were sealed by epoxy resin while only top side was left exposed. Specimens were subsequently stored inside a chamber with 30 ℃, 30 % RH and RH measurements inside the specimen with two depths (5mm and 30mm) were taken for 30 days. Table 2.5 shows the parameters of the R-R pore distribution model, determined by procedures mentioned in Section 2.3.1. Drying moisture diffusion obtained from the implementation of the introduced model for the entire cube is shown in Fig. 2.18.

Table 2.5: Parameters for R-R pore distribution model of harden concrete

	ϕ_1	B_1 (nm)	ϕ_2	B_2 (nm)	ϕ_3	B_3 (nm)	ϕ_4	B_4 (nm)
PC1	0.0512	0.681	0.0498	2.17	0.0154	11.4	0.0064	571.8
PC2	0.0432	0.657	0.0421	2.01	0.0129	10.2	0.0054	562.4

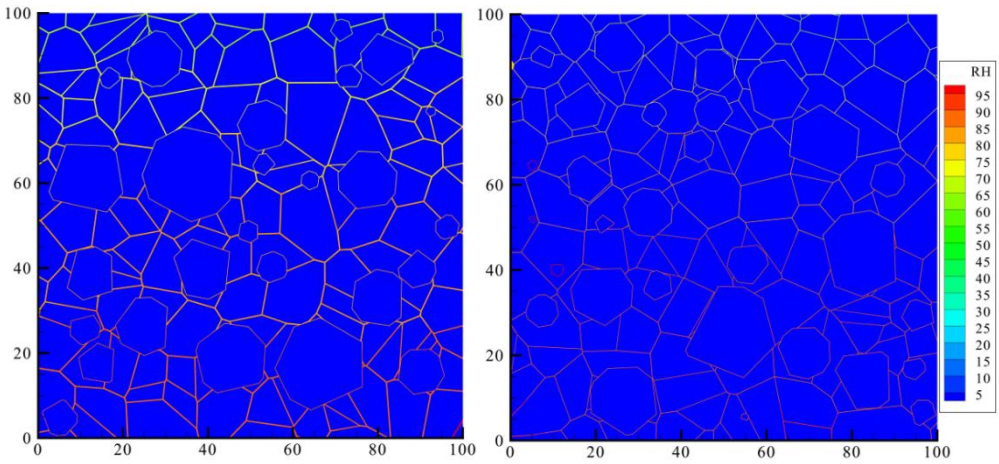

(a) (b)

Fig. 2.18. FEM model for (a) PC1, and (b) PC2 samples

The RH evolution in the pore network for the top 5 and 30 mm sections is shown in Fig. 2.19 versus time up to 2800 hours. Overall, the predictions align well with the experimental results, which confirms ability of MiMe for predicting RH distribution in hardened concrete.

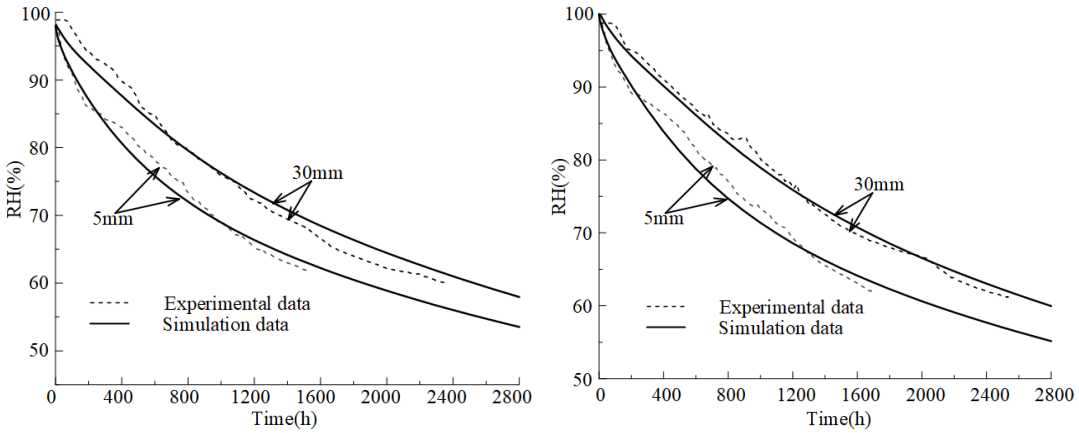

(a) (b)

Fig. 2.19. Comparison between experimental data and simulation results for (a) PC1, and (b) PC2 samples

2.6.2 RH distribution of early-age concrete

This MiMe model is further verified for early age concrete using experimental data by Wei et al. (Wei et al., 2019). Three beam specimens (1000 mm × 100 mm × 38 mm) were molded and sealed completely before being placed inside a chamber with a temperature of 23 ± 2 ℃, 40 ± 5 % RH. The specimens were then unsealed from the top surface at different times (7, 28 and 50 days) so as to measure the RH changes induced by self-desiccation and the drying process. In this sample, the change in RH result from self-desiccation is directly obtained from RH evolution of sealed samples. As for hydration heat of small samples, any temperature increase is transient and its effect was ignored in this analysis.

Table 2.6 lists the parameters for R-R pore distribution model determined by procedures mentioned in Section 2.3.1. FEM simulated drying moisture diffusion for the entire beam is shown in Fig. 2.20.

Table 2.6: Parameters for R-R pore distribution model of early age concrete

	ϕ_1	B_1 (nm)	ϕ_2	B_2 (nm)	ϕ_3	B_3 (nm)	ϕ_4	B_4 (nm)
sample	0.04	1.06	0.06	6.32	0.012	73.8	0.008	571.80

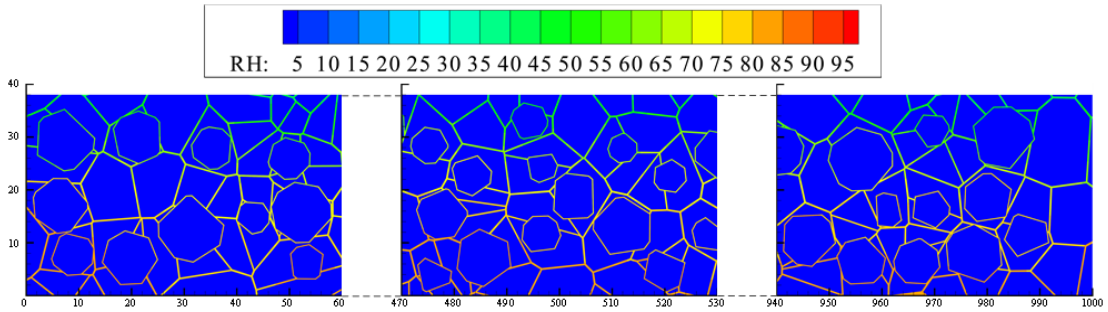

Fig. 2.20. FEM model for beam sample

The RH time history at mid-height (19 mm) is shown for all three beams in Fig. 2.21. The predictions align well with the experimental results, confirming the accuracy with MiMe in predicting RH distribution in early age concrete.

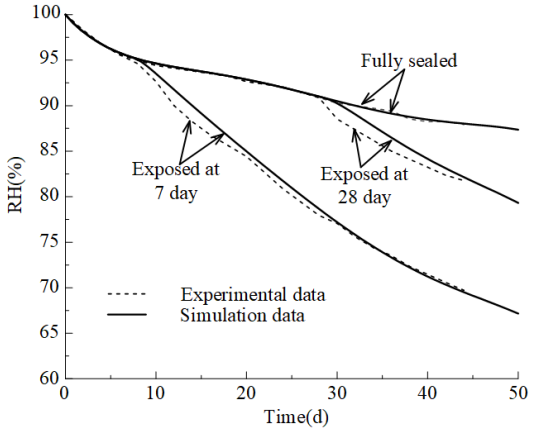

Fig. 2.21. Comparison of experimental data with simulation results for specimens exposed to unidirectional drying at different ages

2.6.3 RH distribution in concrete with varying water-cement ratios

This model was further verified using experimental data for concrete with varying W/C ratios (0.28, 0.4 and 0.68) by Kim and Lee (Kim et al., 1999). Prismatic specimens (100 mm × 100 mm × 200 mm) were submerged in water for 3 days. After water-curing, some specimens were subjected to a stable temperature with 20 ± 1 ℃, RH 50 ± 2 %. Fully sealed specimens were also examined to consider the RH evolution of self-desiccation.

Table 2.7 lists the parameters for R-R pore distribution model determined by procedures mentioned in Section 3.1. FEM simulated drying moisture diffusions for the three prisms are shown in Fig. 2.22.

Table 2.7: Parameters for R-R pore distribution model of different W/C concrete

W/C	ϕ_1	B_1 (nm)	ϕ_2	B_2 (nm)	ϕ_3	B_3 (nm)	ϕ_4	B_4 (nm)
0.28	0.055	0.99	0.036	7.26	0.017	65.2	0.017	551.7
0.4	0.045	1.01	0.04	6.94	0.025	72.1	0.032	553.2
0.68	0.037	1.04	0.05	6.32	0.035	73.8	0.041	557.80

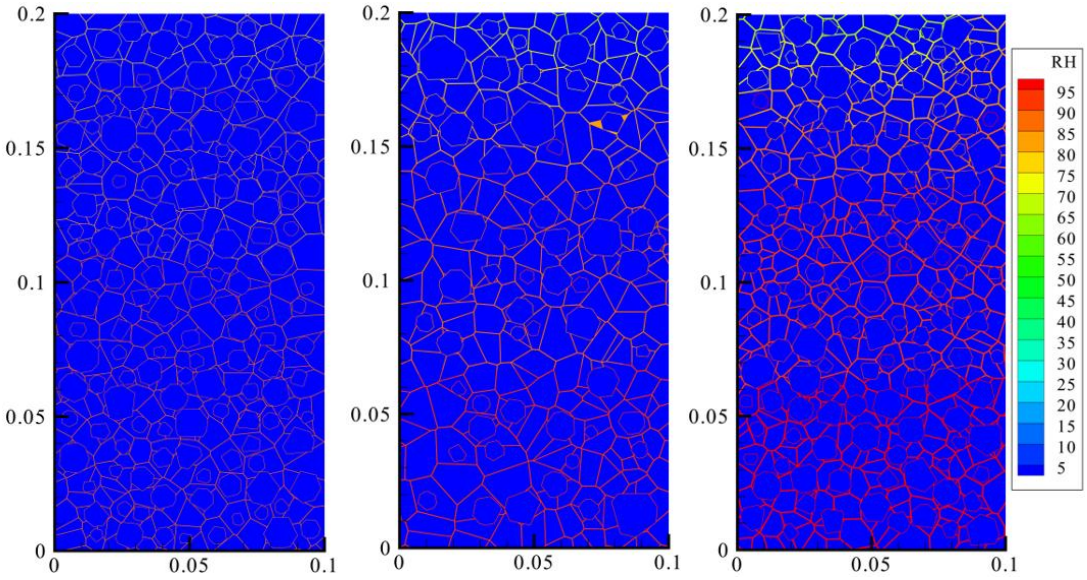

(a) (b) (c)

Fig. 2.22. FEM model for samples with W/C equal to: (a) 0.28, (b) 0.4, and (c) 0.68

The RH time evolution in the pore network for the top 120 mm up to 60 days is given in Fig. 2.23. The predictions obtained using the MiMe model align well with the experimental results, thus confirming the ability of this proposed model to account for the impact of different W/C ratios on RH distribution.

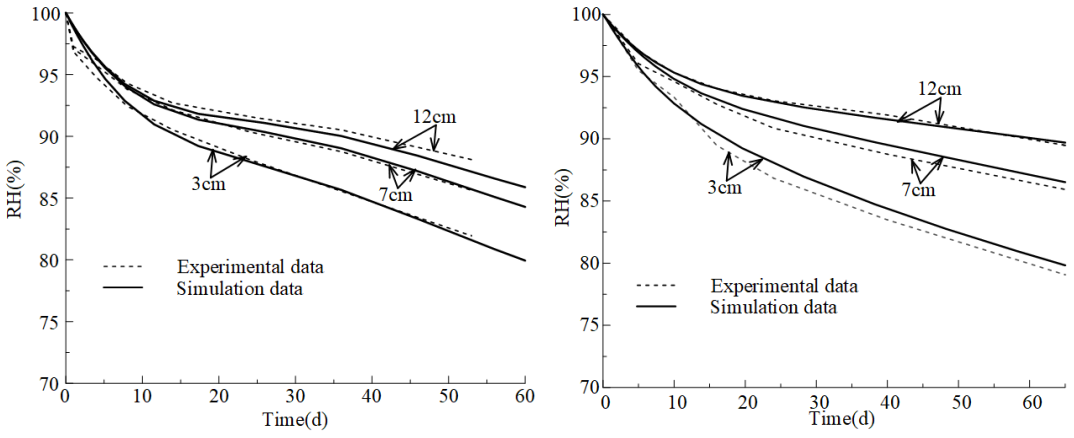

(a) (b)

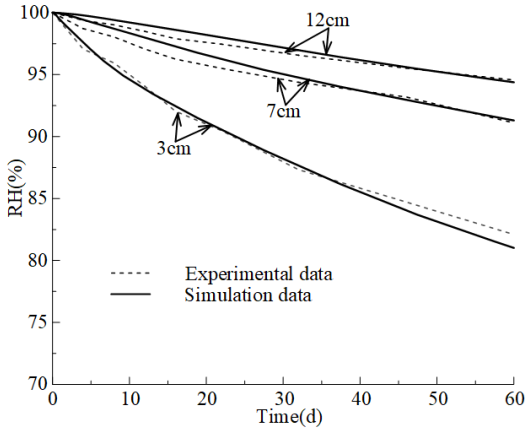

(c)

Fig. 2.23. Comparison of experimental data and numerical predictions for specimens with W/C equal to: (a) 0.28, (b) 0.4, and (c) 0.68

2.6.4 Precision of the numerical model

The absolute average error (AAE) (Eq. (27)) (Thermou and Hajirasouliha, 2018) between the experimental results and simulation predictions of the different case studies discussed in the previous sections are summarized in Table 2.8.

$$AAE = \frac{\sum_{i=1}^{N} \left| \frac{(x)_i^{sim} - (x)_i^{\exp}}{(x)_i^{\exp}} \right|}{N} \tag{27}$$

where $(x)_i^{sim}$ are the numerical results and $(x)_i^{\exp}$ are experimental values, N represents total number of RH data along with time.

Table 2.8: AAE between simulation and experiments

Model	AAE (%) at different depths (mm)								
	5	8	13	18	19	23	30	70	120
Huang Q (Huang et al., 2015)	-	1.38	0.27	0.21	-	0.26	-	-	-
PC1 (Mora et al., 1998)	1.64	-	-	-	-	-	1.94	-	-
PC2 (Mora et al., 1998)	1.56	-	-	-	-	-	1.10	-	-

Exposed at 7th day (Wei et al., 2019)	-	-	-	-	0.81	-	-	-	-
Exposed at 28th day (Wei et al., 2019)	-	-	-	-	0.66	-	-	-	-
Full sealed (Wei et al., 2019)	-	-	-	-	0.25	-	-	-	-
W/C-0.28 (Kim et al., 1999)	-	-	-	-	-	-	0.70	0.46	0.61
W/C-0.4 (Kim et al., 1999)	-	-	-	-	-	-	0.79	0.49	0.15
W/C-0.68 (Kim et al., 1999)	-	-	-	-	-	-	0.59	0.54	0.34

It can be seen that the AAE values for all examined cases are below 2 %, which confirms that the developed MiMe model can effectively model diffusion and drying process in concrete.

2.7 Conclusions

To predict moisture diffusion in concrete, a MiMe (micro-meso) model based on Voronoi tessellation and Monte Carlo approach is proposed. This model utilizes Rayleigh-Ritz (R-R) pore distribution to obtain diffusion coefficient of concrete, considering vapour water diffusion and liquid water permeability. The primary conclusions drawn from this study are:

(1) Using Monte Carlo method and Voronoi tessellation to generate the geometry and spatial distribution of aggregate, ITZ, and pores, serves as an adaptable and viable method that enables the direct consideration of concrete tortuosity in the modelling process.

(2) The correct determination of the diffusion coefficient (vapour and liquid water) and pore size distribution (using the R-R model) at the micro level is essential for developing accurate meso-scale models. In the present study moisture diffusion in concrete was described with a maximum error 1.64%.

(3) Moisture diffuses faster with increasing ambient temperature (RH diffusion increase from 2% to 10%), decreasing RH (RH diffusion increase from 1% to 50%), and decreasing tortuosity (RH diffusion increase from -2% to 5%). The parametric analysis shows that the ambient RH has a more substantial impact on moisture diffusion compared to temperature and tortuosity.

(4) The RH distribution at a given depth is significantly affected by the assumed tortuosity.

(5) Moisture diffuses slightly faster with decreasing ITZ thickness and decreasing fine aggregate fractions. The various shape of coarse aggregates causes a minor effect on moisture transport.

(6) Comparisons between experimental data and numerical predictions show that RH evolution can be adequately predicted for early age concrete, hardened concrete and concretes with different W/C ratios.

Integrating the proposed methodology into a fully coupled hygro-mechanical framework will allow for more accurate predictions of the mechanical behaviour under load. This in turn will enhance the reliability of long-term performance assessments and facilitate the design of more durable concrete structures. As shown above, parameters such as shape, size of aggregate and ITZ thickness do not show an important influence on moisture diffusion. However, the effect of pores distribution requires further investigation.

Chapter 3: Phase field Modelling of Meso-scale Framework for Predicting Fracture Propagation of Concrete: Numerical Calibration and Experimental Calibration

Abstract

Capturing crack development in cementitious materials at the mesoscopic level is crucial for analysing crack patterns and failure mechanisms. This paper introduces a meso-scale model for concrete that utilizes random packing to generate the geometry and spatial distribution of aggregate, interfacial transition zone (ITZ) and mortar. The Drucker-Prager yield criterion is introduced in this phase-field model to account for the elasto-plastic behaviour of the mortar and the ITZ. The spectral decomposition of the strain tensor is employed to model the asymmetric tension and compression damage behaviour of porous materials. The parameters of the proposed model are calibrated on experimental data obtained from compressive and flexural tests of concrete and mortar specimens, including detailed information on crack initiation and propagation. Furthermore, three experiments from the literature are utilized to calibrate this model. The predictions show strong agreement with the experimental results, confirming that the proposed methodology effectively captures crack propagation in concrete. This work will lead to more accurate predictions of concrete cracking mechanisms and long-term behaviour.

Keywords: Concrete, Elasto-plastic phase-field model, Mesoscale model, Compressive test, Three-point bending test, Parameter investigation

3.1 Introduction

Crack initiation and propagation is unavoidable in structures made of cementitious materials like mortar and concrete. Cracks can develop from mechanical and thermal loads, as well as shrinkage, and have significant implications on structural durability and safety (Jia et al., 2022). Therefore, it is crucial to understand, describe, and simulate concrete degradation and failure due to crack evolution. Unlike conventional homogeneous models, at the mesoscopic scale, concrete is typically considered as a four-phase material comprising mortar, coarse aggregates, interfacial transition zone (ITZ) and pores (Van Mier, 2012), and its behaviour is controlled by stress redistribution between the different phases in the fracture zones (Naderi et al., 2021a). However, the use of accurate and reliable models to characterize

the heterogeneity of the multiple phases is essential to predict the intricate degradation mechanisms resulting from stress redistribution, energy dissipation, and crack propagation.

To achieve this, extensive experiments have been conducted to obtain the microscopic and mesoscopic features of concrete (Song et al., 2019, Georget et al., 2021, Gallucci et al., 2007, Kim et al., 2021, Yang et al., 2019). X-ray computed tomography (XCT) is commonly utilized to record the mesoscopic spatial distribution of materials inside concrete (Coleri et al., 2013, Yang et al., 2017), with a realistic sizes, volume content, shapes and spatial location of aggregate (Huang et al., 2016a, Yang et al., 2019). However, the precision of XCT is limited by image accuracy, and its implementation can be very expensive and time-consuming for high resolution images (Yang et al., 2013), or when large volumes need to be scanned to adequately capture material variability. Consequently, a quantitative understanding of how concrete's mesoscale properties influence cracking still remains elusive.

The use of simulation models comprising multiple phases can serve as an effective alternative to study the development of damage mechanisms in concrete. Indirect and direct algorithms are commonly employed to construct a mesoscale model for concrete. When using indirect algorithms, the material properties (aggregate, mortar and ITZ) are assigned to pre-generated elements to describe the spatial randomness of the different phases. However, the geometric properties of aggregate, mortar and ITZ cannot be explicitly described (Yang et al., 2009). In contrast, direct algorithms first generate the geometry of the individual constituents, which are then randomly located within the domain to model the meso-structure of concrete explicitly. Subsequently, these components are meshed and their material properties are assigned (Huang et al., 2016c, Ma et al., 2016). Compared with indirect algorithms, direct algorithms make allowance for the description of material geometric characteristics, making them attractive for mesoscale numerical simulations. Additionally, the low computational cost of direct algorithms makes them feasible to analyse large-scale structures (Wang et al., 2015, Wu et al., 2019).

The implementation of an appropriate numerical approach is also essential for studying the failure mechanisms of concrete. Commonly employed methods include the discrete element method (DEM) and the smeared element method (SEM). In DEM, crack development is modelled by inserting irregular displacement elements along the edges of solid elements (López et al., 2008, Huang et al., 2016c, Naderi et al., 2021b, Guo et al., 2019) or inside elements (Du et al., 2014, Patil et al., 2019, Oliver et al., 2015). However, the discrete method requires pre-inserting cohesive meshes along each edge, leading to high computational costs. Conversely, to capture the crack propagation using the smeared method, a priori knowledge is necessary to define mesh functions and crack initiation and development criteria (Zhang et al., 2018b, Zhang and Mang, 2020, Zeng et al., 2019, Zhang et al., 2021, Zhang et al., 2020). Approaches such as tracking element methods (Zhang et al., 2018b, Zhang and Mang, 2020, Zeng et al., 2019, Zhang et al., 2021, Zhang et al., 2020) and cracking particle methods (Rabczuk and Belytschko, 2004, Rabczuk et al., 2010), however, show promise in efficiently dealing with embedded

strong discontinuities. In contrast, continuum degradation functions are more effective at simulating diffusive degradation, ranging from undamaged to complete damaged conditions, than capturing sharp cracks (Wriggers et al., 2006, Markou et al., 2013, Pulatsu et al., 2019, Huang et al., 2016b, Liu et al., 2019, Kim et al., 2011). The parameter length scale is normally introduced for regularizing non-local microcrack interactions, either through integral (Pijaudier-Cabot and Bažant, 1987, Zhang et al., 2019) or gradient enhancement (Peerlings et al., 1996, Simone et al., 2004, Nguyen et al., 2018).

According to Griffith (Griffith, 1921), Irwin (Irwin et al., 1967) and Barenblatt (Barenblatt, 1962) classical theory of brittle fracture in solids, crack evolution takes place when the energy release rate reaches its critical value. Additionally, variational methods (Francfort et al., 1998, Bourdin et al., 2008) based on minimization of energy and regularized settings (Tortorelli and Ambrosio, 1990, Mumford et al., 1989) based on a Γ-convergent have been proposed.

Building upon these theories, Bourdin et al. developed a numerical phase-field model to describe brittle fracture (Bourdin et al., 2000). This numerical model enables automatic handling of multiple fracture processes, including opening, evolution, integration and branching for cracks of 2-D or 3-D solids, without requiring additional strategies (Bourdin et al., 2008). However, the isotropic nature of this phase-field model (Bourdin et al., 2000) predicts identical tensile and compressive fracture behaviour, resulting in the formation of unnatural cracks under compressive loads. To consider this behaviour, a common method involves decomposing the stored elastic energy into a positive (tensile energy) and negative (compressive energy) component.

Various methods of decomposition have been proposed, such as volumetric-deviatoric decomposition (Amor et al., 2009) of elastic energy and the spectral decomposition (Miehe et al., 2010b) of the strain tensor. However, the energy decomposition of the elastic phase-field fails to capture the plastic fracture response of concrete. To address this limitation, complex non-linear models have been proposed to predict the elasto-plastic mechanical behaviour, along with stiffness degradation in both tension and compression (Alessi et al., 2018, Choo et al., 2018, Pise et al., 2019, Späth et al., 2021, Jiang et al., 2023, Molnár et al., 2020). The introduction of such models provide flexibility and enables phase-field models to efficiently describe plastic cracking. These models, however, while following the variational framework, would cause a loss of reliability issues because of the adjustments required in the parameters governing failure mechanisms and damage criteria. The Drucker-Prager (Drucker and Prager, 1952) yield criterion is typical employed in phase-field models to explicitly account for plastic energy and predict the crack propagation in brittle materials.

In this paper, a phase-field model is introduced to analyse crack propagation in cementitious composites at the mesoscale. The unsymmetric tension and compression behaviour of mortar and concrete is modelled by employing the continuous, stepwise linear approximations to solve the degradation functions. The proposed model is implemented within the commercial software ABAQUS using the

user defined element (UEL), and it is calibrated and calibrated on experimental data available in the literature. Through the proposed modelling approach, the effect of mesoscopic features (e.g. aggregate distribution) and key model parameters (e.g. mesh size and length scale parameter) on fracture propagation and failure mechanisms of cementitious materials are examined in depth. The framework can be easily extended to include the effect of time-dependent phenomena, such as shrinkage and creep, to predict the long-term performance of concrete structures.

3.2 Phase-field model for diffusive crack problems

This section summarizes the key concepts of the phase-field damage theory. Additional information can be found in the literature (Miehe et al., 2010a).

3.2.1 Regularized representation of crack topology

Let $\Omega \subset \mathbb{R}^D$ ($D = 1, 2, 3$ being the space dimension) be a domain representing a cracking solid, and $\partial\Omega$ its boundaries (Fig. 3.1). The topology of a sharp crack, Γ, which is considered as a solid subjected to a distributed traction F (Fig. 3.a), is defined by the damage state variable d ($0 \leq d \leq 1$) representing the damage condition ($d = 0$ indicates the undamaged state and $d = 1$ indicates a fully damaged state). Fig. 3.1b defines the normalised representation for the diffusive crack surface to describe crack width.

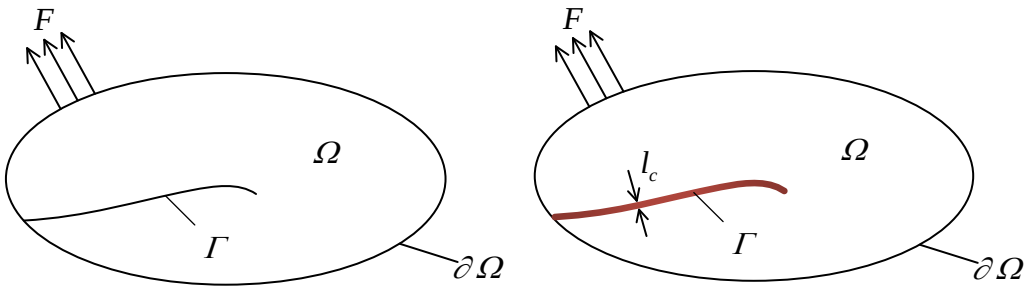

(a) (b)

Fig. 3.1. Normalised representation for the crack surface: (a) sharp topology, (b) diffusive topology

By smearing the crack over the solid domain, Ω, the continuous and diffusive method can be utilized to describe the crack and simulate the discontinuous discrete properties, and a continuous dimensionless field can be used to characterize the crack topology. The crack density for the unit volume, γ, can be described using the following equation (Miehe et al., 2010a):

$$\gamma\left(d,\nabla d\right)=\frac{d^2}{2l_c}+\frac{l_c}{2}\left|\nabla d\right|^2 \tag{3.1}$$

where, l_c is the parameter of length scale of diffusive crack.

Therefore, the normalised area or volume of the crack is expressed as:

$$\Gamma\left(d\right)=\int_\Omega \gamma\left(d,\nabla d\right)d\Omega \tag{3.2}$$

3.2.2 Energy function in the cracking solid

To link crack development to displacement, the total potential energy, *Π,* of the cracked domain, *Ω,* is defined as the sum of crack and strain energy, resulting in the following equation:

$$\Pi=E\left(u,d\right)+P\left(u,d\right)+W\left(d\right)=\int_\Omega \psi_\varepsilon\left(\varepsilon\left(u\right),d\right)d\Omega+\int_\Gamma g_c d\Gamma \tag{3.3}$$

where, *E(u,d)* represents the elastic energy, *P(u,d)* represents the plastic energy, *W(d)* is the fracture energy, u is the displacement field, $\varepsilon\ (u)$ is the tensor of strain fields, ψ_ε is the strain energy, and g_c is the critical energy release rate.

The strain energy density, $\psi_\varepsilon\ (\varepsilon\ (u),\ d)$, is described as:

$$\psi_\varepsilon\left(\varepsilon\left(u\right),d\right)=\psi_\varepsilon^{el}\left(\varepsilon\left(u\right),d\right)+\psi_\varepsilon^{pl}\left(\varepsilon\left(u\right),d\right) \tag{3.4}$$

where, $\psi_\varepsilon^{el}(\varepsilon(u),\ d)$ is the elastic strain energy density, $\psi_\varepsilon^{pl}(\varepsilon(u),\ d)$ is the plastic strain energy density.

The total strain tensor $\varepsilon(u)$ can be described utilizing the symmetric displacement gradient, $\nabla_s u$, as:

$$\varepsilon=\nabla_s u=\frac{1}{2}\left[\nabla u+\nabla^T u\right] \tag{3.5}$$

With the description of fracture surface density using phase-field variables, the crack energy can be described using a domain integral (Liu et al., 2016) according to:

$$\int_\Gamma g_c d\Gamma\approx\int_\Omega g_c\left[\frac{d^2}{2l_c}+\frac{l_c}{2}\left|\nabla d\right|^2\right]d\Omega=w^0\left(d\right) \tag{3.6}$$

To define the fracture energy in the staggered algorithm, Miehe (Miehe et al., 2016) provides the formulation described as:

$$W(d)=\int_{\Omega} t(d)+w^{0}(d)\,d\Omega \tag{3.7}$$

where, *t(d)* is the threshold energy, and are defined as follows:

$$\begin{cases} t(d)=\psi_c-g(d)\psi_c \\ w^{0}(d)=2l_c\psi_c\left[d^2+l_c^2\left|\nabla d\right|^2\right] \end{cases} \tag{3.8}$$

where, ψ_c is the specific critical fracture energy, $\psi_c = g_c/2l_c$, *g(d)* is a degradation function: $g(d) = (1 - d)^2 + k$, and k represents a small number responsible for the stability of the solution.

Therefore, the total potential energy is described as:

$$\Pi=\int_{\Omega}\left[\psi_{\varepsilon}^{el}\left(\varepsilon(u),d\right)+\psi_{\varepsilon}^{pl}\left(\varepsilon(u),d\right)+W(d)\right]d\Omega \tag{3.9}$$

3.2.3 Elastic strain energy degradation

When considering quasi-brittle materials, it is widely acknowledged that only tensile stresses lead to fracture initiation and propagation, whereas compressive stresses facilitate crack closure and inhibit crack growth. Therefore, crack evolution and damage development are primarily associated with tensile strain energy (Zhou et al., 2018).

The spectral decomposing of the strain tensor is employed to separate the strain energy into its positive (tensile) and negative (compressive) components (Miehe et al., 2010b):

$$\varepsilon_{el}=\varepsilon^{+}+\varepsilon^{-} \tag{3.10}$$

And the strain of positive and negative is described as:

$$\varepsilon^{\pm}=\sum_{i=1}^{D}\left\langle\varepsilon_i\right\rangle^{\pm}n_i\otimes n_i \tag{3.11}$$

where, ε_i and n_i represent the eigenvalues and eigenvectors of ε, D is the spatial dimensions, in Eq. (3.11) $\varepsilon^{+}=\left(\varepsilon+\left|\varepsilon\right|\right)/2$ and $\varepsilon^{-}=\left(\varepsilon-\left|\varepsilon\right|\right)/2$.

Subsequently, the energy density function of elastic strain is described as (Liu et al., 2016):

$$\psi_0^{el\pm}=\frac{\lambda}{2}\left\langle tr(\varepsilon)\right\rangle_{\pm}^{2}+\mu tr\left(\varepsilon_{\pm}^{2}\right) \tag{3.12}$$

where, ψ_0^{el+} and ψ_0^{el-} are the tensile and compressive strain energy functions, respectively. λ and μ are the Lame's constants, *tr* (ε) is the trace of strain.

The elastic energy function is expressed:

$$\psi_\varepsilon^{el}\left(\varepsilon(u),d\right)=g(d)\cdot\psi_0^{el+}(\varepsilon)+\psi_0^{el-}(\varepsilon) \tag{3.13}$$

The definition of the positive and negative energy components can vary based on the implementation. The brittle materials is analysed in this case, it is as follows:

$$\psi_\varepsilon^{el}\left(\varepsilon(u),d\right)=\mu\sum_{i=1}^{3}\left[\langle\varepsilon_i\rangle_-^2+g(d)\langle\varepsilon_i\rangle_+^2\right]+\frac{\lambda}{2}\left[g(d)\langle tr(\varepsilon)\rangle_+^2+\langle tr(\varepsilon)\rangle_-^2\right] \tag{3.14}$$

When the damage is considered to occur under shear during both compression and tension (Amor et al., 2009, Freddi et al., 2010):

$$\psi_\varepsilon^{el}\left(\varepsilon(u),d\right)=g(d)\left[\mu\sum_{i=1}^{3}\varepsilon_i^2+\frac{\lambda}{2}\langle tr(\varepsilon)\rangle_+^2\right]+\frac{\lambda}{2}\langle tr(\varepsilon)\rangle_-^2 \tag{3.15}$$

Assuming a plane strain state (ε_3 = 0), the elastic energy function can be expressed in terms of its eigenvalues as follows (Moës et al., 2011):

$$\begin{aligned}\psi_\varepsilon^{el}\left(\varepsilon(u),d\right)=&\frac{vE\left(\left(1-\alpha d\right)^2+k\right)}{2(1-2v)(1+v)}\left(\varepsilon_1+\varepsilon_2\right)^2\\&+\frac{E}{2(1+v)}\left(\left(\left(1-\alpha_1 d\right)+k\right)\varepsilon_1^2+\left(\left(1-\alpha_2 d\right)+k\right)\varepsilon_2^2\right)\end{aligned} \tag{3.16}$$

where, α, α_1 and α_2 are employed to evaluate the negative or positive strain, if $\varepsilon_i < 0$, $\alpha_i = 0$, else $\alpha_1 = 1$, and if $\varepsilon_1 + \varepsilon_2 < 0$, $\alpha = 0$, else $\alpha = 1$. The eigenstresses are derived from the eigenstrains by taking the derivative of Eq. (3.16):

$$\begin{pmatrix}\sigma_1\\\sigma_2\end{pmatrix}=\underbrace{\frac{E}{1+v}\begin{pmatrix}\left(\left(1-\alpha_1 d\right)^2+k\right)+\beta\left(\left(1-\alpha d\right)^2+k\right) & \beta\left(\left(1-\alpha d\right)^2+k\right)\\ \beta\left(\left(1-\alpha d\right)^2+k\right) & \left(\left(1-\alpha_2 d\right)^2+k\right)+\beta\left(\left(1-\alpha d\right)^2+k\right)\end{pmatrix}}_{L}\begin{pmatrix}\varepsilon_1\\\varepsilon_2\end{pmatrix} \tag{3.17}$$

where, $\beta = v/(1-2v)$, v is the Poisson's ratio, E is the Young's modulus.

Eq. (3.17) can also be described as:

$$\tilde{\sigma} = L\tilde{\varepsilon} \tag{3.18}$$

where, $\tilde{\sigma}$ represents the eigenstress and $\tilde{\varepsilon}$ represents the eigenstrain.

The stress is determined as the derivative of the potential and the tangent stiffness, K, as the derivative of stress.

$$\sigma = \frac{\partial \psi}{\partial \varepsilon} = \frac{\partial \psi}{\partial \tilde{\varepsilon}} \frac{\partial \tilde{\varepsilon}}{\partial \varepsilon} = \tilde{\varepsilon}^T L \frac{\partial \tilde{\varepsilon}}{\partial \varepsilon} \tag{3.19}$$

$$K = \frac{\partial \sigma}{\partial \varepsilon} = \left(\frac{\partial \tilde{\varepsilon}}{\partial \varepsilon} \right)^T L \frac{\partial \tilde{\varepsilon}}{\partial \varepsilon} + \tilde{\varepsilon} L \frac{\partial^2 \tilde{\varepsilon}}{\partial \varepsilon^2} \tag{3.20}$$

3.2.4 Plastic strain energy degradation

The total strain field is separated into elastic and plastic components:

$$\varepsilon = \varepsilon_{el} + \varepsilon_{pl} \tag{3.21}$$

The energy density of plastic part is defined as:

$$\psi_{\varepsilon}^{pl}\left(\varepsilon(u), d\right) = g(d)\psi_0^{pl}(\varepsilon) \tag{3.22}$$

where, $\psi_0^{pl}(\varepsilon)$ is the initial plastic strain energy.

To describe the nonlinear mechanical behaviour of concrete under compressive and tensile loads, this implementation supports the Drucker-Prager (Drucker and Prager, 1952) yield criterion:

$$f(I_1, J_2) = \sqrt{J_2} + \beta I_1 - g(d)\left[\sigma^{\lim} + H\varepsilon_{eq}^{pl}\right] \tag{3.23}$$

where, I_1 is the first invariant of the Cauchy stress tensor, J_2 is the second invariant of the deviatoric part of the Cauchy stress tensor, $\sigma^{\lim}$ is the yield stress, H is hardening modulus and ε_{eq}^{pl} is the energy-equivalent plastic strain.

Yield stress and energy-equivalent plastic strain is combined to describe the plastic energy history:

$$\psi_0^{pl}\left(\varepsilon_{eq}^{pl}(u)\right) = \varepsilon_{eq}^{pl}(u)\left[\sigma^{\lim} + \frac{1}{2}H\varepsilon_{eq}^{pl}(u)\right] \tag{3.24}$$

The plastic energy function is based on Drucker-Prager (Drucker and Prager, 1952) yield criterion, which can be described by flow rules as follows (Krabbenhøft, 2002):

$$\psi_{\varepsilon}^{pl} = g(d)\psi_0^{pl} = g(d)\left(\varepsilon_{eq}^{pl}\right)^T K_0 \varepsilon_{eq}^{pl}$$
$$K_0 = \left(K - \frac{K\dfrac{\partial g}{\partial \sigma}\left(\dfrac{\partial f}{\partial \sigma}\right)^T K}{H + \left(\dfrac{\partial f}{\partial \sigma}\right)^T D \dfrac{\partial g}{\partial \sigma}} \right) \tag{3.25}$$

where, K is elastic constitutive matrix, K_0 is elasto-plastic constitutive matrix, g and f are plastic potential energy.

Total potential energy function is constructed by combining elastic energy, plastic energy and fracture energy, which is followed as:

$$\prod = \int_{\Omega} \left\{ g(d)\left[\psi_0^{el+}(\varepsilon) + \psi_0^{pl}(\varepsilon) - \psi_c\right] + \psi_0^{el-}(\varepsilon) + \psi_c + 2l_c\psi_c\left[d^2 + l_c^2\left|\nabla d\right|^2\right] \right\} d\Omega \tag{3.26}$$

3.3 Staggered algorithm with FEM

3.3.1 Staggered time-integration algorithm

The governing equations of phase-field model results in a coupled problem with two fields of the phase and displacement fields (d and u), enabling numerical solutions necessary for capturing crack evolution branches. This coupled system can be addressed using either a fully coupled "monolithic" method or a sequentially coupled "staggered" method (Miehe et al., 2010b). As for the monolithic algorithm, the functions for this coupled problem are solved simultaneously at every time increment. However, the equations of displacement field exhibit complex non-linear behaviour, leading to numerous iterations and suffering from poor convergence. Conversely, the staggered algorithm separates this problem into two independent minimization processes. First, the sharp fracture is normalised by the phase field variable, which is computed based on the energy history. Then, the damage variable of phase field is utilized to update the displacement results.

With a fixed d, the displacement field is defined as follows:

$$\prod^{u} = \int_{\Omega}\left[\psi_{\varepsilon}^{el}\left(\varepsilon(u), d\right) + \psi_{\varepsilon}^{pl}\left(\varepsilon(u), d\right)\right] d\Omega - \prod^{ext} \tag{3.27}$$

where, Π^{ext} is the external energy induced by body force and surface force, which is formulated as follows:

$$\prod^{ext} = \int_{\Omega} \bar{\gamma} \cdot u d\Omega + \int_{\partial\Omega} \bar{t} \cdot u d\partial\Omega \tag{3.28}$$

where, $\bar{\gamma}$ and $\bar{t}$ are volume force and surface force, respectively.

By varying both energies ($\delta\Pi^u = 0$), the corresponding Eulerian functions (strong form) for the displacement can be expressed as follows:

$$\begin{aligned} &\delta\prod{}^u = 0 \quad \forall \delta u \rightarrow \quad \nabla\sigma - \bar{\gamma} = 0 && in \quad \Omega \\ &\sigma \cdot n = \bar{t} && on \quad \Gamma_N \\ &u = \bar{u} && on \quad \Gamma_D \end{aligned} \tag{3.29}$$

Similarly, when potential energy from the displacement field is described by history energy field, Lagrangian equation for the phase field problem is expressed as:

$$\prod^d = \int_{\Omega} \left[g_c \gamma\left(d, \nabla d\right) + g\left(d\right) H \right] d\Omega \tag{3.30}$$

And the history field is described as:

$$\begin{aligned} &H_0 = 0 \\ &H_{n+1} = \max \begin{Bmatrix} \psi_0^{el+} + \psi_0^{pl} - \psi_c \\ H_n \end{Bmatrix} \end{aligned} \tag{3.31}$$

where, H_n is the previously obtained energy history at step n.

Furthermore, this formulation enforces irreversibility of the damage ($\dot{d} \geq 0$). Thus, the corresponding strong form is given as:

$$\begin{aligned} &\delta\prod{}^d = 0 \quad \forall \delta d \rightarrow \quad \frac{g_c}{2l_c}\left(d - l_c^2 \Delta d\right) = \left(1 - d\right) H \quad in \quad \Omega \\ &\nabla d \cdot n = 0 \quad in \quad \Gamma \end{aligned} \tag{3.32}$$

3.3.2 Finite element discretization in ABAQUS

Using the general FEM framework, phase (d) and displacement (u) field can be clearly obtained. The discretized formulations for the phase field are established using FEM. According to the quantities at step time t_n, the new phase-field variable can be determined at step time t_{n+1}:

$$d_{n+1} = Arg\left\{ \inf_d \int_{\Omega} \left[g_c \gamma\left(d, \nabla d\right) + g\left(d\right) H \right] d\Omega \right\} \tag{3.33}$$

where, history energy field (H) is computed based on Eq. (3.31). The relevant linear solution can be calculated by utilizing the Newton-Raphson nonlinear solver:

$$K_n^d d_{n+1} = -r_n^d \tag{3.34}$$

where, d_{n+1} is unknow variable for new phase field variable. r_n^d is the residual vector and K_n^d is tangent stiffness matrix at step time t_n.

The phase-field variable of an element is determined by interpolating the variable of phase field at the nodes using the shape function,

$$d = N_i d_i \tag{3.35}$$

where, N_i represent shape function for the variable of phase field ($N_i = [N_1 \ldots N_a]$cc, a = 3 or 4 for 2D with triangle or element quadrilateral), d_i represents the variable of phase field on node i.

The phase field gradient within the element is a represents as a matrix containing the spatial derivatives, given as:

$$\nabla d = B_i d_i \tag{3.36}$$

where, B_i represents the derivative matrix of the shape function for the phase field variable.

According to Eq. (3.33), the corresponding residue vector for the phase-field variable is formulated as:

$$r^d = \int_\Omega \left\{ \left[\frac{g_c}{l_c} - 2(1-d)H \right] (N_i)^T + g_c l_c (B_i)^T \nabla d \right\} d\Omega \tag{3.37}$$

And the tangent stiffness matrix is obtained as follows:

$$K^d = \int_\Omega \left\{ \left[\frac{g_c}{l_c} - 2H \right] (N_i)^T N_i + g_c l_c (B_i)^T B_i \right\} d\Omega \tag{3.38}$$

As for the variable of displacement field for an element, this is calculated from similarly function, and internal and external components are used to describe: $r^u = f^{int} - f^{ext}$, and the vector of external force includes body and surface forces:

$$f^{ext} = \int_\Omega (N_i)^T \cdot \bar{\gamma} d\Omega + \int_{\partial\Omega} (N_i)^T \cdot \bar{t} d\partial\Omega \tag{3.39}$$

The internal part is described as:

$$r^u = \int_\Omega \left\{ \left[(1-d)^2 + k \right] (B_i)^T \sigma_0^{eq} \right\} d\Omega \tag{3.40}$$

The displacement tangent matrix is computed as:

$$K^u = \int_\Omega \left\{ \left[(1-d)^2 + k \right] (B_i)^T K_0 B_i \right\} d\Omega \tag{3.41}$$

where, K_0 is the elasto-plastic constitutive matrix based on the flow rule.

3.3.3 Model Calibration

To verify this algorithm for phase field model, different standard benchmark simulations are performed, including tensile test and shear test of the notched plate, as well as three-point bending test on a plate containing three pre-existing holes. The benchmark simulations are shown in Section 3.8. The simulated crack evolution branches from these simulations show good alignment with other experimental data or simulation results, demonstrating the feasibility and reliability of the phase-field modelling scheme. This approach is additional extended to simulate crack behaviour in mesoscopic models, particularly concerning multiple phases composite materials like cementitious materials.

3.4 Experimental program

To verify this numerical model, experiments for crack development were conducted, including compressive and three-point bending tests of mortar and concrete. 2D point tracking method (PTM) was used during loading application to track fracture propagation with a rate of one image per second.

3.4.1 Materials and compositions

The aim of the test program was to identify the mechanical properties for numerical modelling. To obtain parameters for meso-scale model (aggregate, ITZ, mortar), different specimens were cast, including mortar cubes (50 mm × 50 mm × 50 mm), concrete cubes (75 mm × 75 mm × 75 mm) and concrete prisms (285 mm × 75 mm × 75 mm). The concrete mix design was based on earlier researches (Hu et al., 2019), with Portland cement type CEM II 32.5R (335 kg/m3). The water/cement ratio was 0.55, and a dosage of 2 lt/m^{3}of superplasticizer was used. Two size ranges (diameter) of river gravel were utilized, with 491 kg/m^3 for diameter of 5-10 mm, 532 kg/m^3 for diameter of 10-14 mm. Additionally, river sharp sand was used as fine aggregate with 847 kg/m^3. After casting, the concrete and mortar specimens were placed in the chamber (75% RH and 20 ℃) using the saturated salt method for 28 days. At the testing day, porosity, compressive test and three-point bending test were conducted for the concrete and mortar specimens.

To prepare samples for porosity calculation, specimens were dried in an oven at 70 ℃ until reaching constant mass, as the decomposition of non-evaporable water in the C-S-H gel and ettringite begins at 75 ℃, and then immersed in water until constant mass was obtained, which allowed for the porosity calculation of mortar and concrete (Liu et al., 2021).

3.4.2 Three-point bending tests of prisms: setup and testing

Based on EN 14651:2005 (CEN, 2005), a notch mearing 5 mm in width and 25 mm in depth was sawn at the mid-span of each specimen on the day of testing. The specimen was tested under a three-point bending arrangement with Crack Mouth Opening Displacement (CMOD) measurements. Deflections and CMOD were recorded utilizing two Linear Variable Differential Transducers (LVDTs), with length 3 mm and 5 mm, respectively. LVDTs were fixed on bottom and side of specimen on glued blocks across the notch, while crack propagation was measured by the digital camera, see Fig. 3.2. For the flexural tests, the load was applied at a constant rate of 0.045 mm/min ($\varepsilon=10^{-5}$) by a SHIMADZU universal testing machine.

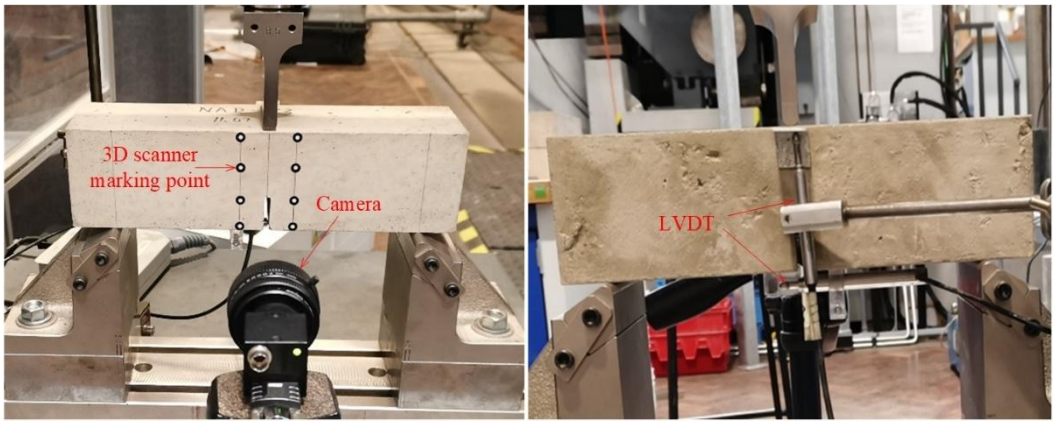

(a) (b)

Fig. 3.2. Experimental arrangement of prism tests: (a) Camera and 2D marking points setting, (b) LVDTs setting

3.4.3 Compressive tests

Compressive tests on mortar and concrete specimens were performed using a cube crusher to determine Young's modulus (E), Poisson's ratio (v) and Yield stress (σ_y). Mortar specimens were prepared by removing the coarse aggregate from concrete with the same mix batch. To minimize the effect of aggregate variability, the same mix of concrete was used for both flexural and compressive tests. After the flexural tests, cubic concrete specimens (75 mm × 75 mm × 75 mm) were prepared from the prismatic specimens.

Based on BS EN 12390-3: 2009 (Standard, 2009), the plain concrete and mortar cubes were subjected to uniaxial compressive loading at a constant rate of 0.6 N/mm^2/s. To obtain the load-displacement curve, 2D scanner marking points and camera were used to monitor and record the movement of marking points, see Fig. 3.33.

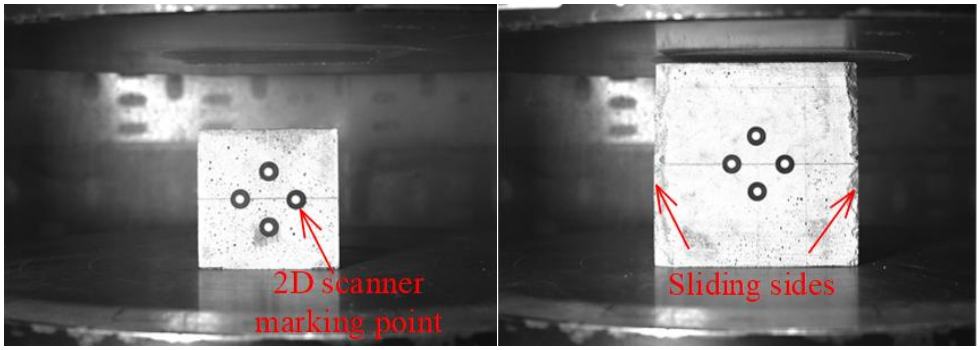

(a) (b)

Fig. 3.3. Experimental arrangement of compressive tests: (a) mortar specimen, (b) concrete specimen

3.4.4 Results of compressive and flexural tests

Table 3.1 shows the mean compressive strength of cube specimens, peak loads, porosity. The mortar and concrete compressive strength for this batch was approximately 40 MPa, and it gradually decreased with increasing porosity.

Table 3.1: Mechanical parameters of mortar and concrete

Specimen	Compressive strength (MPa)	Peak load (kN)	Porosity (%)
Mortar A	40.9	102.3	16.8
Mortar B	40.6	101.5	17.0
Mortar C	40.3	100.8	17.2
Concrete A	41.2	231.5	11.4
Concrete B	39.4	221.6	11.0

Using PTM images (see Fig. 3.4 and Fig. 3.5), the movement of 2D marking points and overall dimensions of the specimens were determined using ImageJ to calculate the strain and displacements during testing over time. The change in distance between the top and bottom points was used to obtain

vertical strain, while the left and right distance was used for horizontal strains. The cube crusher provided the data of stress and load over time. The Poisson's ratio was determined by employing vertical and horizontal strains. The curves of load-displacement were calculated by combining data from ImageJ and the cube crusher, as shown in Fig. 3.6 and Fig. 3.7. The crack propagation during the three-point bending test is depicted in Fig. 3.8, while the load-displacement and CMOD data of flexural test is shown in Fig. 3.9.

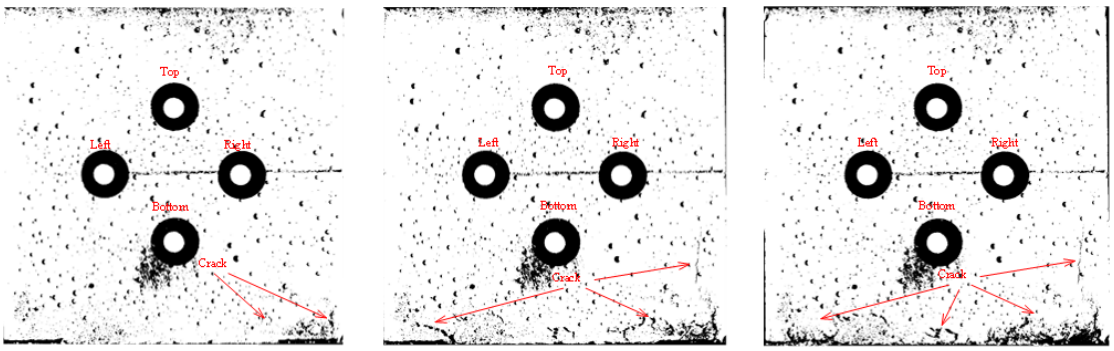

Fig. 3.4. Compressive test of mortar at different load: (a) 0.22 mm, (b) 0.232 mm, and (c) 0.24 mm

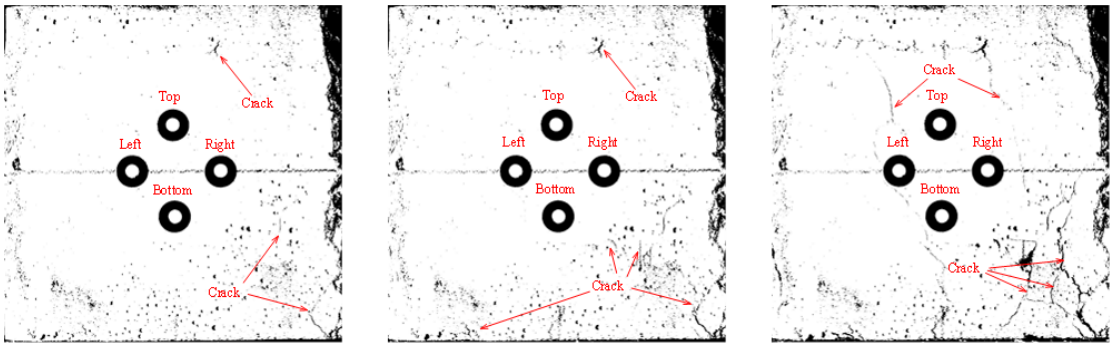

Fig. 3.5. Compressive test of concrete at different load: (a) 0.264 mm, (b) 0.3 mm, and (c) 0.315mm

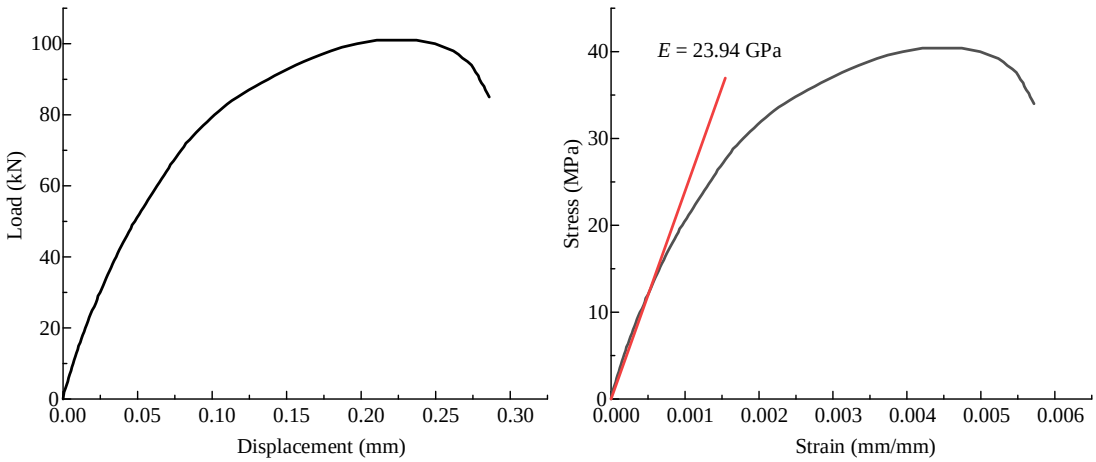

(a) (b)

Fig. 3.6. Compressive results of mortar specimen: (a) load-displacement, (b) stress-strain

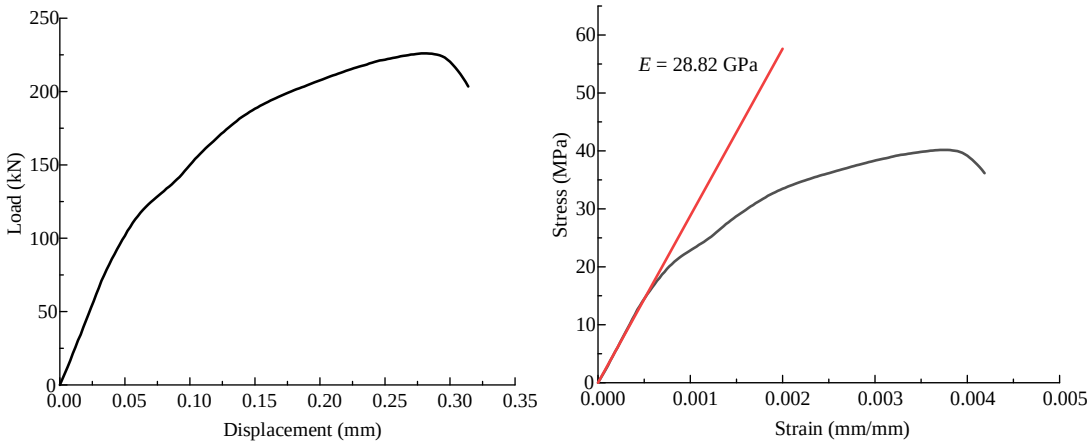

(a) (b)

Fig. 3.7. Compressive results of concrete specimen: (a) load-displacement, (b) stress-strain

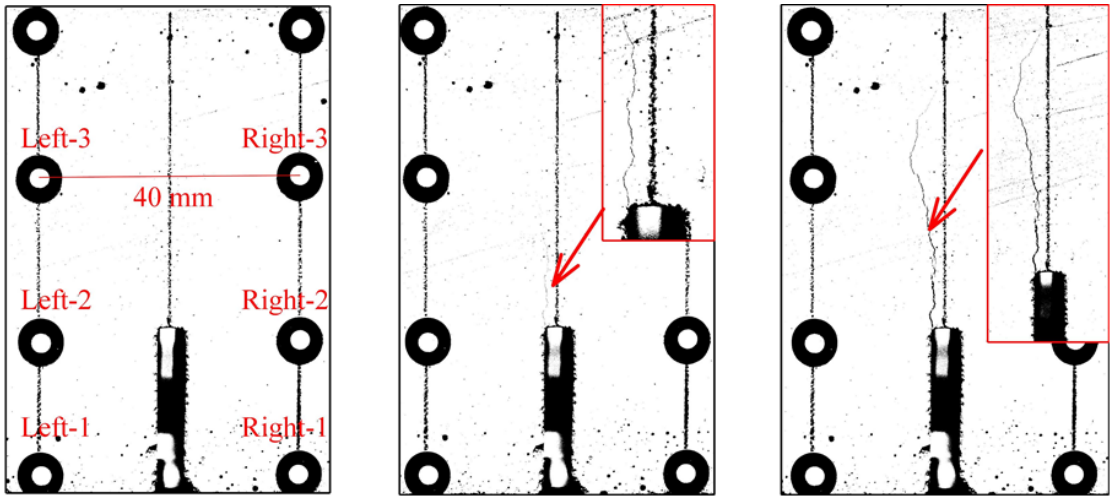

(a) (b) (c)

Fig. 3.8. Flexural test of concrete at different load: (a) 0.036mm, (b) 0.072mm, and c) 0.111 mm

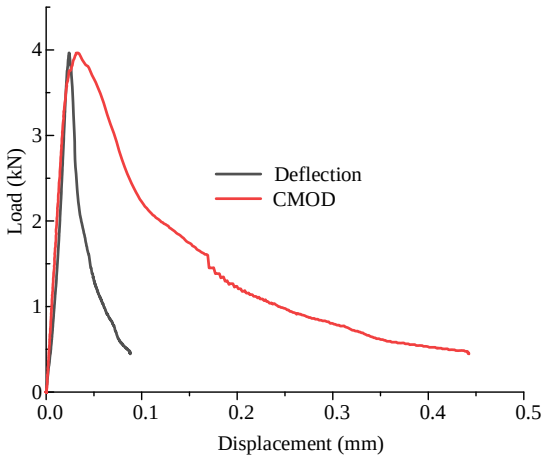

Fig. 3.9. Load-displacement curve of flexural test

To determine the crack propagation, the CMOD obtained from PTM at different depths is used. These were at 0mm depth (left-1 and right-1), 25mm depth (left-2 and right-2), and 50mm depth (left-3 and right-3), as shown in Fig. 3.8. A comparison between LVDT and PTM is used initially for calibration purposes. Based on the strains from PTM, the displacement change at the bottom surface with the same distance as the LVDT (50mm) is determined, as shown in Fig. 3.10.

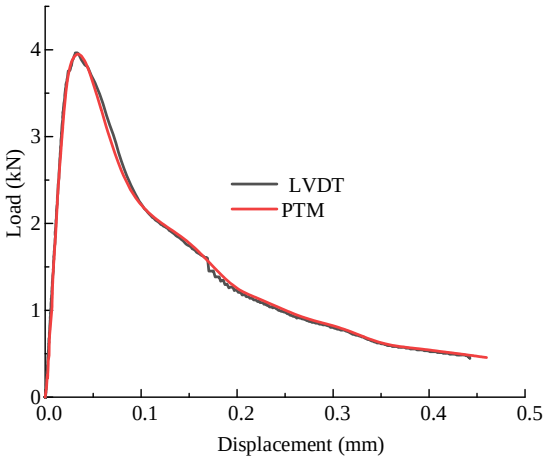

Fig. 3.10. CMOD comparison between LVDT and PTM

The CMOD obtained from PTM is also used to capture the crack evolution over depth, with a typical example shown in Fig. 3.11.

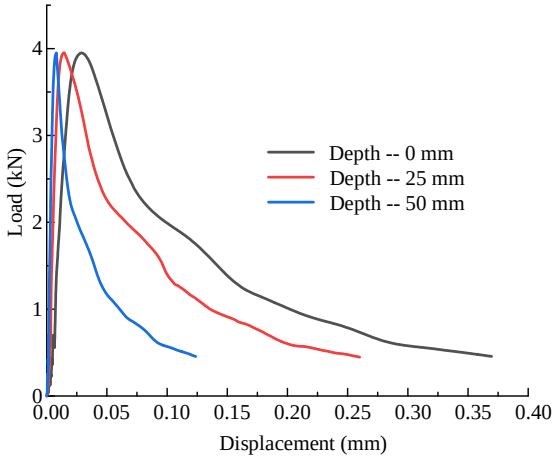

Fig. 3.11. CMOD from PTM at different depth

3.5 Calibration of mechanical properties of multiple phases

To simulate the crack development in concrete using a mesoscopic model, it is essential to obtain parameters for different phases. The governing equations of phase-field model utilizes two fields coupling system, including phase and mechanical fields (d and u), related to the equivalent parameters such as Elastic modulus (E), Poisson's ratio (v), the length scaler parameter (l_c) and the specific critical fracture energy (ψ_c). Considering the different concrete's performance of compression and tension, two critical fracture energy parameters (ψ_c^c and ψ_c^t) and appropriate yielding stresses need to be adopted to describe mechanical behaviour of concrete and mortar. From experimental results, both mortar and concrete exhibit softening behaviour during the plastic stage, which induces two yield stresses (σ_{y1}^c and σ_{y2}^c) and Harding modulus (H_1 and H_2) in compression. According to literature (Taerwe and Matthys, 2013), initial yielding occurs at the same value of tensile stress σ_y^t within the range $0.9\, f_t < \sigma_y^t \leq f_t$ obtained from uniaxial tension loading. For the uniaxial compressive tests of concrete, the yielding stress was obtained from Fig. 3.6 and Fig. 3.7. As for the yield stress in tension, this was adopted from the authors' previous research (Hu et al., 2019). The parameter of Drucker-Prager can be determined by putting yield stresses into Eq. (3.23). Subsequently, two different critical fracture energy parameters for tension ψ_c^c and compression ψ_c^t are obtained based on experimental data. This enables numerical models to track the fracture evolution path.

3.5.1 Uniaxial compressive simulation of mortar

To calibrate this phase-field model, mortar specimens were simulated to predict crack propagation with uniaxial compressive load. In this simulation, a square domain (with length L = 50 mm) was used, and the load was applied on top surface in y-direction. The bottom surface is fixed as shown in Fig. 3.12. The same element size of mortar model was employed with h = 0.3 mm and includes 61299 triangle elements. The parameters used for mortar are shown in Table 3.2.

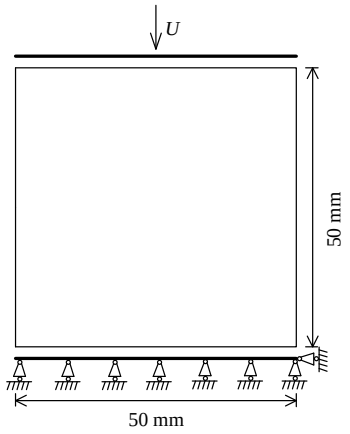

Fig. 3.12. Geometric and boundary conditions of mortar specimens

Table 3.2: Parameters for mortar specimens of phase field

	E GPa	v	σ_{y1}^{c} MPa	H_1 GPa	σ_{y2}^{c} MPa	H_2 GPa	σ_{y}^{t} MPa	l_c mm	β	ψ_c^c MPa	ψ_c^t MPa
Mortar	24	0.2	16	13	30	4.6	3.6	1	0.37	1.1	0.0105

Compressive load is applied in increments $\Delta u = 7.5 \times 10^{-4}$ mm ($\varepsilon = 10^{-5}$) for 800 steps. Fig. 3.13 shows the crack propagation path, whilst experimental data is presented in Fig. 3.4. This Numerical model shows crack propagation at right bottom side, but there is no further crack development in the simulation. This is a result of the numerical model treating the mortar specimen as a homogenous material without considering the effect of meso-structures such as pores, river sand. Fig. 3.14 indicates a comparison of load-displacement between the elasto-plastic phase-field model and experimental data, which demonstrates a great agreement.

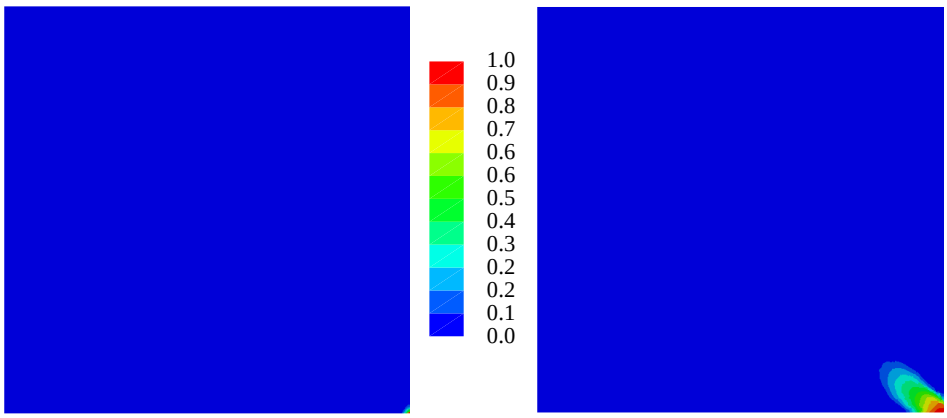

(a) (b)

Fig. 3.13. Crack propagation process over displacement, (a) $U = 0.14$ mm, (b) $U = 0.22$ mm

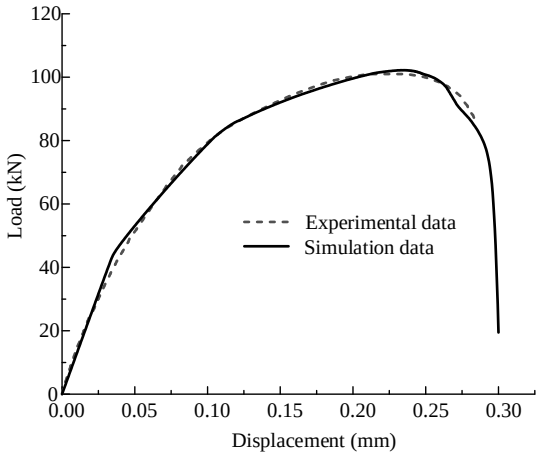

Fig. 3.14. Comparison of load-displacement curve of mortar specimens

3.5.2 Uniaxial compressive simulation of concrete

In this simulation, the direct algorithm was adopted to generate the mesoscopic model within a square domain (75mm × 75mm). Based on the concrete mix, polyhedral shaped aggregates were generated with two diameter sizes ranging from 5-10 mm and 10-14 mm, with a volume fraction ratio of 0.48: 0.52, and the volume fraction of aggregate being about 40%, determined by the mix design and density (2590kg/m^3) of aggregate.

To obtain the in-plane spatial distribution of different particles for a section of size 75 mm × 75 mm, the Monte Carlo method and Fuller were adopted to locate the centre point, diameters, edges, and angles of polygon, respectively. The ITZ phase is represented as a thin layer between the aggregates and the cement matrix, typically having a thickness ranging from 10-50 μm (Shuguang et al., 2015). In this case, a thickness of 30 μm was used.

In this simulation, the boundary and loading conditions are the same as in mortar simulation, (see Fig. 3.15). The same mesh size of concrete model was employed with $h = 0.3$ mm for all particles (aggregate, ITZ and mortar) and includes 81952 triangle elements. The mesoscopic modelling is displayed in Fig. 3.15 and parameters used for concrete are listed in Table 3.3. To compare and calibrate the theoretical model and experiments, crack evolution branches and load-displacement are compared, as shown in Fig. 3.16 and Fig. 3.17. Again, it can be observed that a very good agreement is found.

Table 3.3: Parameters for concrete specimens of phase field

	E GPa	v	σ_{y1}^{c} MPa	H_1 GPa	σ_{y2}^{c} MPa	H_2 GPa	σ_{y}^{t} MPa	l_c mm	β	ψ_c^c MPa	ψ_c^t MPa
Aggregate	40	0.2	-	-	-	-	-	-	-	-	-
Mortar	24	0.2	16	13	30	4.6	3.6	1	0.37	1.1	0.0105
ITZ	12	0.2	16	5.8	30	2.1	3.6	1	0.37	0.55	0.005

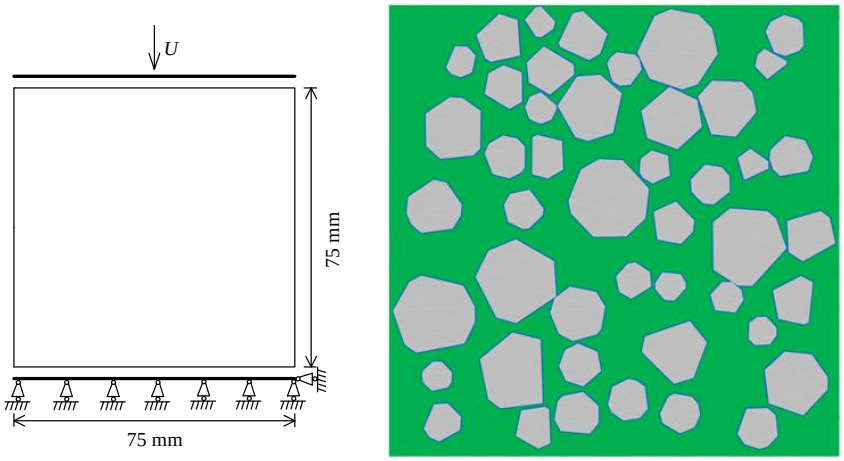

(a) (b)

Fig. 3.15. Properties of concrete specimens: (a) boundary conditions, (b) geometric details of concrete

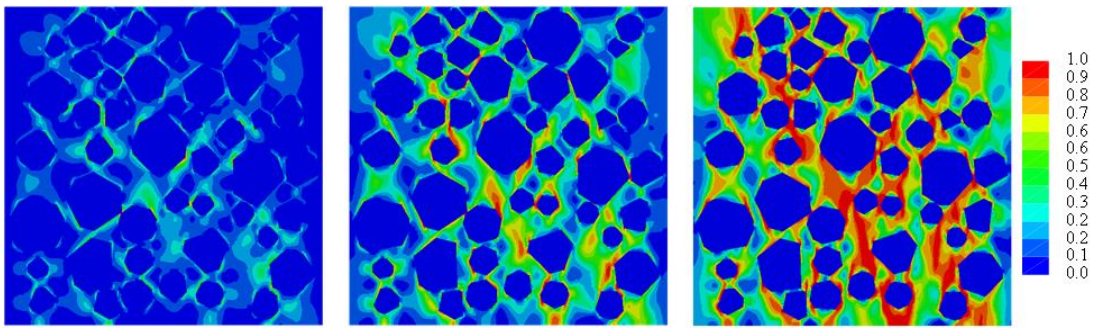

(a) (b) (c)

Fig. 3.16. Crack propagation process over displacement, (a) U = 0.21 mm, (b) U = 0.29 mm, (c) U = 0.35 mm

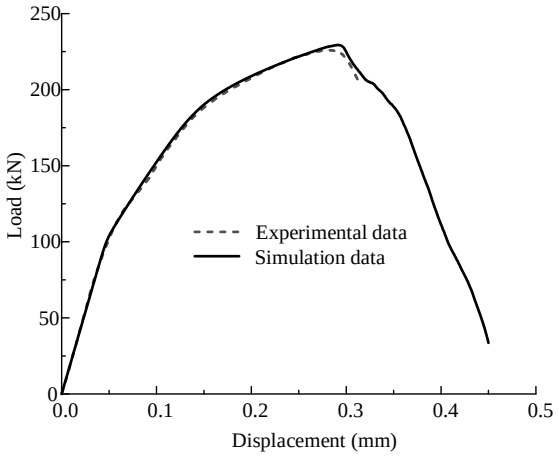

Fig. 3.17. Comparison of load-displacement curve of concrete specimens

3.5.3 Three-point bending simulation for concrete

As for this simulation, a rectangular specimen (285 mm × 75 mm) was used. Mesostructural elements with polyhedral shaped aggregate are generated in the rectangle domain, and the geometric characterises of coarse aggregates and ITZ (size, volume) are consistent with those used in compressive test. In this simulation, the load was applied at the top side in y-direction using a rate of 0.045 mm/min ($\varepsilon=10^{-5}$/s). The left support at the bottom side is fixed in both x-direction and y-direction, and the right support is fixed in y-direction. For computational efficiency, specimens' sides are considered elastic. This and the boundary conditions are shown in Fig. 3.18. To study and evaluate the effect of aggregate distribution, three mesoscopic models of concrete were generated to capture crack propagation. The geometric properties of one of these models are shown in Fig. 3.19. The element size for elastic part is 1 mm and the nonlinear part and for all phases (aggregate, ITZ and mortar) is 0.3 mm, and the specimen includes 133354 triangular elements. The parameters used are shown in Table 3.3. To compare and calibrate the theoretical model and experiments, the fracture evolution path is compared to the same displacement obtained (0.036 mm, 0.072 mm and 0.111 mm) from experiments, as shown in Fig. 3.20. The load-displacement curves are compared in Fig. 3.21, whilst the comparison of load-CMOD curves is shown in Fig. 3.22.

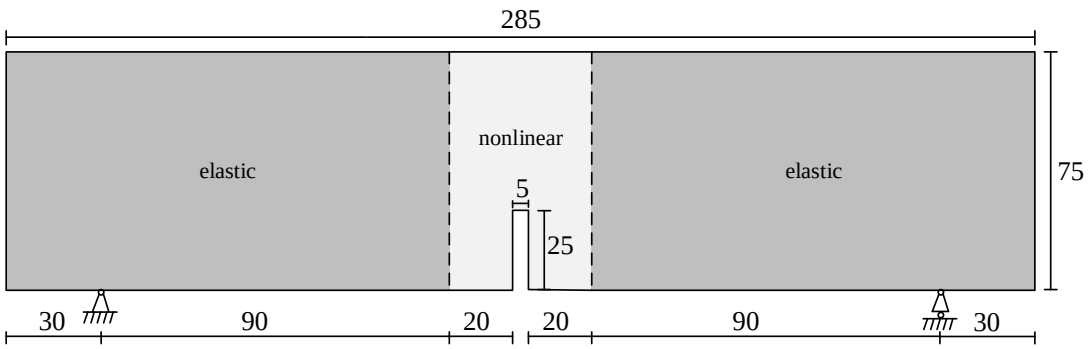

Fig. 3.18. Boundary conditions and dimension details of concrete specimen

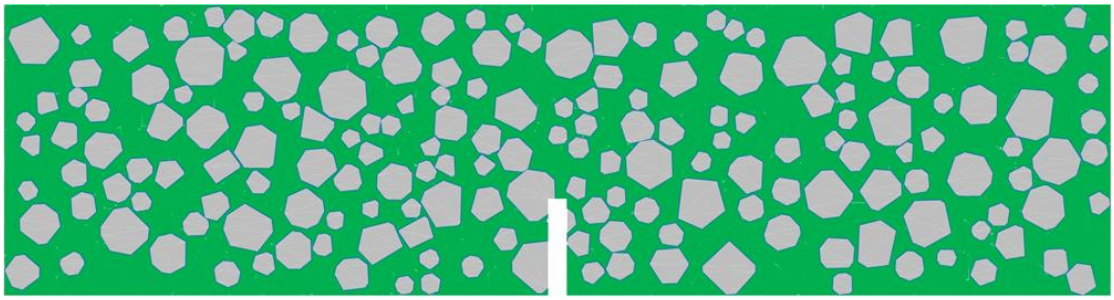

Fig. 3.19. Geometric details of meso-model of concrete specimen of Model A

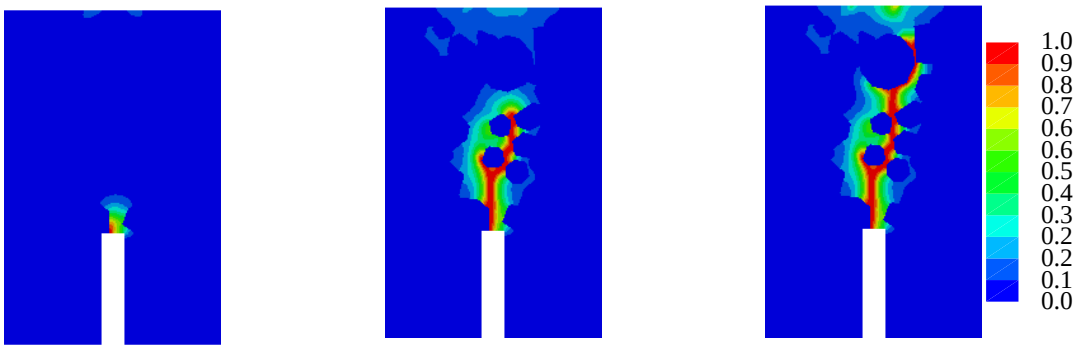

(a)

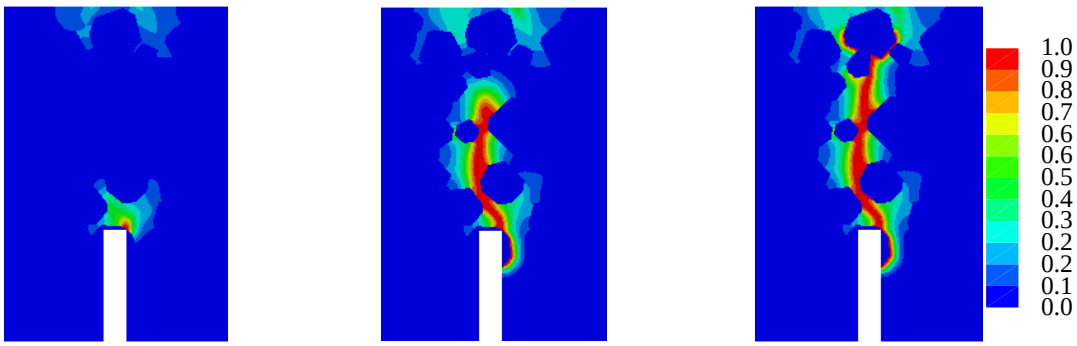

(b)

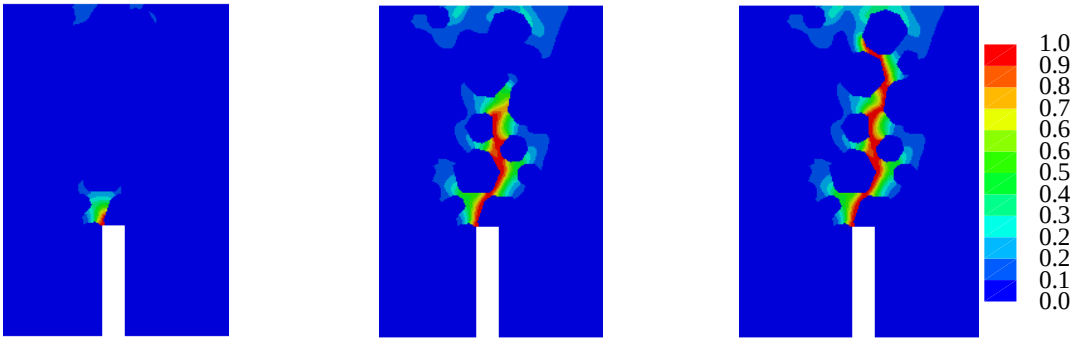

(c)

Fig. 3.20. Crack propagation process of three models: (a) Model A, (b) Model B, and (c) Model C

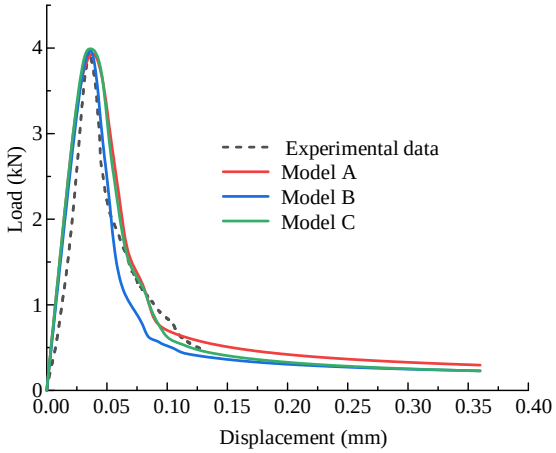

Fig. 3.21. Comparison of load-displacement curve of concrete specimens

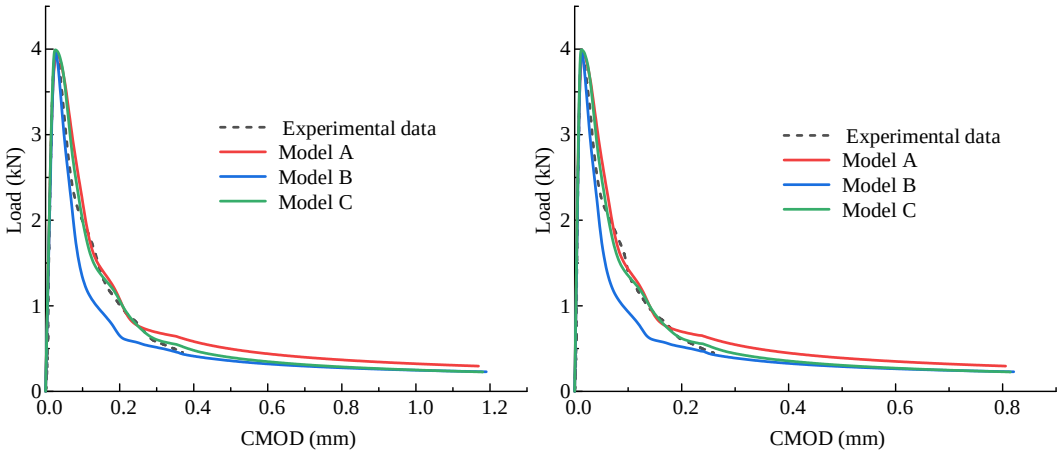

(a) (b)

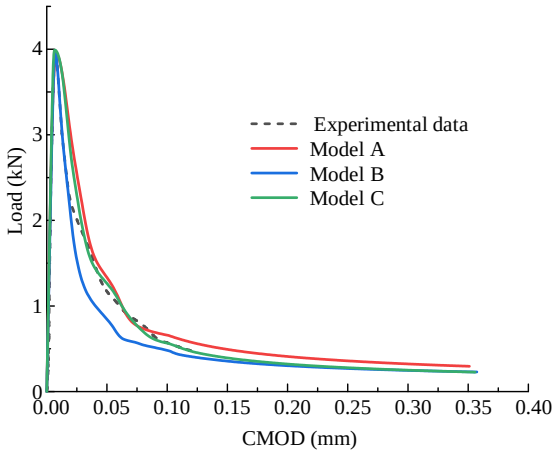

(c)

Fig. 3.22. Comparison of load-CMOD curve at different depths: (a) 0 mm, (b) 25 mm, (c) 50 mm

From the results, all numerical models show good alignment before crack propagation stage. However, the crack paths, crack openings and load-displacement curves deviate after cracking, influenced by the distribution of aggregate. By combining the load-displacement curve and crack propagation results it is observed that load develops differently when cracks propagate along the aggregate horizontally. Since ITZ is more prone to breakage compared to mortar, cracks trend to penetrate along the ITZ when other weak points of the ITZ are distant. Despite the variability in the results arising from the variability in the location of aggregates, it is observed that overall this elasto-plastic phase-field model can effectively simulate and predict the crack evolution from mesoscopic level of concrete. However, the 2D model still has limitations for representing 3-D crack propagation.

3.5.4 Effect of element size and length scale parameter

To analyse the influence of element size on the simulation results, crack development in the three-point bending test is simulated in model C (0.3mm mesh size) with four different mesh sizes for the region around crack: 0.2mm, 0.6 mm, 1.5 mm and 3 mm. The material properties used in Section 3.5.2 are used in the mesh size analysis.

The results for load versus deflection are displayed in Fig. 3.23 (a). It can be observed that the numerical results are not important mesh size sensitive.

To effect of the parameter of length scale l_c was also examined parametrically with four different values: 0.5mm, 2 mm and 3mm and the results are shown in Fig. 3.23 (b). It can be observed that length scaler significantly affects the results and as l_c increases, the peak load decreases.

The mesh size does not significantly affect the load-displacement response; however, it influences the crack paths and branching due to mesh resolution accuracy. In contrast, the length scale parameter, which represents the crack width in this simulation, has a substantial impact on the crack energy. Consequently, changes in the length scale significantly influence the load-displacement behaviours, as well as the crack path and its evolution.

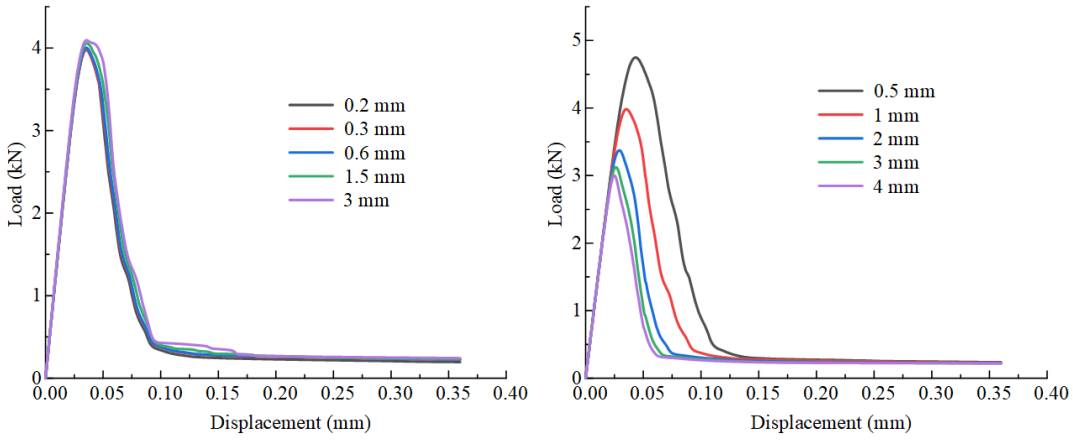

(a) (b)

Fig. 3.23. Comparison of load-displacement curve with different parameters: (a) mesh size, (b) length scaler

3.6 Experimental calibration of numerical model

The proposed phase field model was calibrated against additional experimental data obtained from flexural tests available in the literature (Ren et al., 2023, Yang et al., 2023, Hu et al., 2018). "Model-V1" simulates concrete prisms with dimensions 400 mm × 100 mm × 100 mm as tested by Ren et al. (Ren et al., 2023). These specimens were stored in a chamber at 20°C and 95% RH for 28 days and notched at midspan before testing (the notch was 25 mm deep and 0.5 mm wide). "Model-V2" simulates concrete prisms with dimensions 400 mm × 100 mm × 100 mm as tested by Yang et al. (Yang et al., 2023). These specimens were cured at a temperature of 20°C and 95% RH for 60 days. After curing, the specimens were notched at midspan for a depth of 30 mm and a width of 3mm. "Model-V3" simulates concrete prisms with dimensions 550 mm × 150 mm × 150 mm as tested by Hu et al. (Hu et al., 2018). The specimens were stored in laboratory conditions (22 ± 3 °C) and covered with wet hessian fabric and plastic sheets to maintain high moisture levels during the curing process. After 28days of curing, all covered sheets were removed and the specimens were exposed to drying until 90 days. Before testing, a 25 mm deep and 5 mm wide notch was cut at their midspan. All specimens were tested in displacement control at a rate of 0.05 mm/min (Model-V1 and model-V3) and 0.02 mm/min (Model-V2). The model parameters used in the simulations are calibrated based on experimental data and summarised in Table 3.4, while a comparison with the relevant experimental data confirming the accuracy of the numerical analyses is shown in Fig. 3.24.

Table 3.4: Parameters for calibration models of phase field

Model	Components	E (GPa)	v	H (GPa)	σ_y^t (MPa)	l_c (mm)	β	ψ_c^t (MPa)
Model-V1	Aggregate	35	0.2	-	-	-	-	-
	Mortar	21	0.2	6	4.19	1	0.38	0.0152
	ITZ	10	0.2	3	4.19	1	0.38	0.0076
Model-V2	Aggregate	40	0.2	-	-	-	-	-
	Mortar	30	0.2	8	4.17	1	0.37	0.0108

	ITZ	15	0.2	4	4.17	1	0.37	0.0054
	Aggregate	40	0.2	-	-	-	-	-
Model-V3	Mortar	23.9	0.2	4.6	3.6	1	0.39	0.01
	ITZ	12	0.2	2.3	3.6	1	0.39	0.005

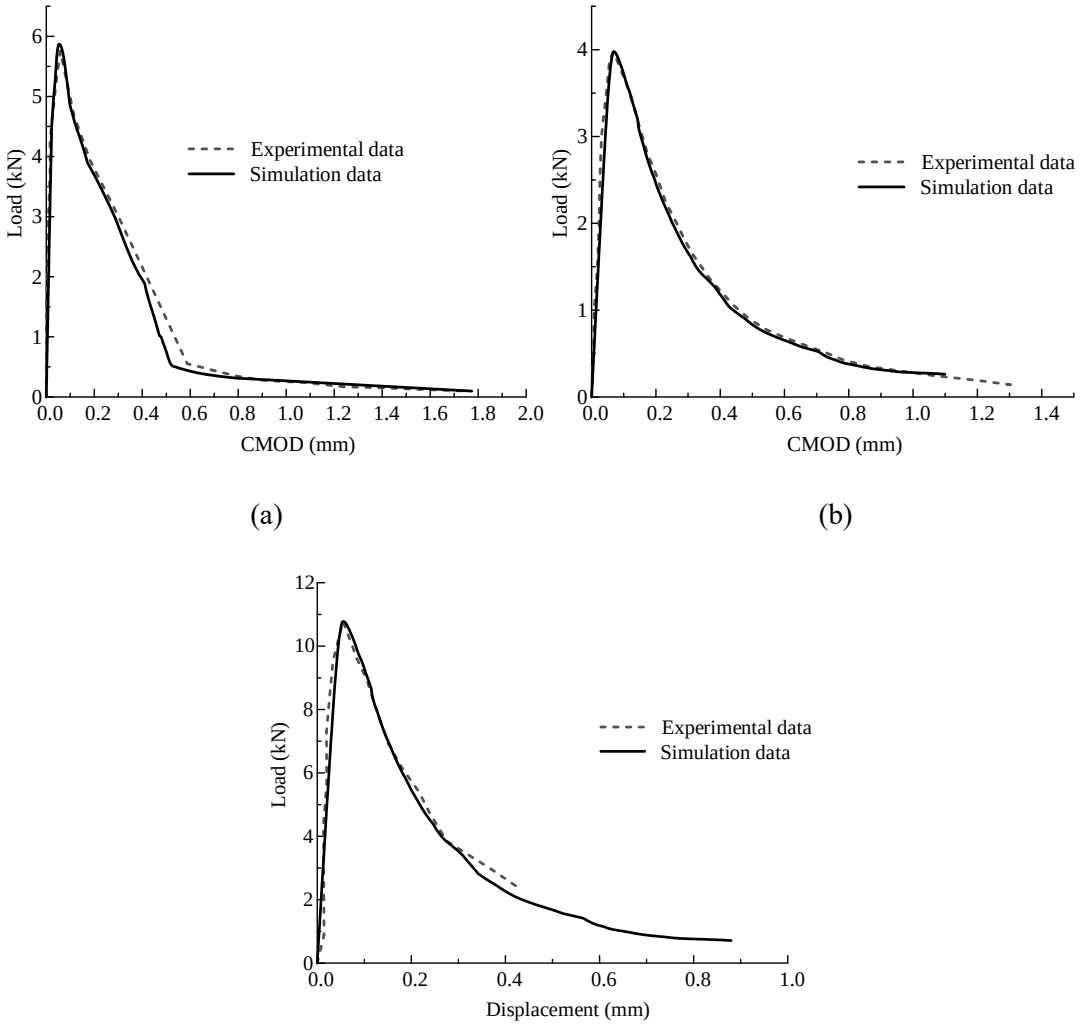

Fig. 3.24. Comparison between experimental data and numerical data: (a) Model-V1, (b) Model-V2, (c) Model-V3

3.7 Conclusions

This study presents a mesoscale phase-field model with elasto-plastic behaviour to simulate crack propagation in cementitious composites. The Drucker-Prager yield criteria is employed to capture the complex nonlinear compressive-tensile behaviour. Unlike traditional constitutive fracture models, spectral decomposition is used to regulate stress degradation, allowing for the representation of asymmetric behaviour in tension and compression. The numerical model is then verified and calibrated with independent sets of experimental data. The main conclusions are summarized as follows:

(1) Using the Monte Carlo method to generate the geometry and spatial distribution of aggregate, ITZ, and mortar, is a viable and flexible method that allows for capturing crack propagation of concrete at a mesoscale level.
(2) The phase-field model provides a good description of the crack evolution process in concrete composites at the mesoscopic level and is capable to capture the mechanical behaviour of concrete under flexural and compressive loading. The modelling results are consistent with several benchmark numerical tests from literature.
(3) The application of PTM is provides a practical and flexible approach to measure and monitor damage evolution (load-COMD) at different spatial positions of concrete or mortar samples.
(4) The spatial distribution of aggregate and the geometric property of ITZ can affect crack initiation and propagation, but does not affect significantly the overall structural response in terms of load-displacement and load-CMOD.
(5) While the model is not mesh size dependent, the choice of the length scale parameter can significantly affect the overall performance.

The mesoscale model developed in this paper will be expanded to different components with aggregate, mortar, ITZ and pores. The time-dependant effects will be incorporated with mechanical performance, such as creep and shrinkage, and provide a powerful tool to predict the long-term performance of concrete structures subjected to combined mechanical and environmental actions. Therefore, the energy dissipation between different constituents and representative mechanical properties of pores are necessary to be studied.

3.8 Appendix: Benchmark tests and numerical examples

3.8.1 Tensile test on a notched plate

The crack development of a notched plate specimen subjected to tensile loading is analysed in this section to verify the theoretical framework described in Section 3.3.2. A domain (with length L = 1 mm) includes a pre-existing crack, as shown in Fig. 3.8.1a. The mesh is refined in the anticipated crack propagation zone, as illustrated in Fig. 3.8.1b and and includes 27738 triangular elements. The mesh size in the refined region is about h_{min} = 0.001 mm and h_{max} = 0.01 mm. In this simulation, the nodes along the bottom edge are restrained in both vertical and horizontal directions. The mechanical properties of the materials are E = 210kN/mm^2 and ν = 0.3 (Miehe et al., 2010a). To compare and calibrate the theoretical model, the fracture properties reported in Miehe et al. (Miehe et al., 2010a), are implemented in this study, including the length scale parameter (l_c = 0.0075 mm) and the critical energy release rate (g_c = 0.0027 kN/mm).

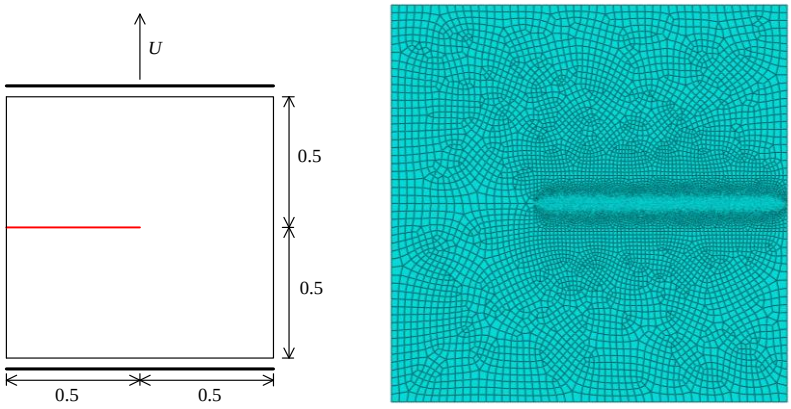

(a) (b)

Fig. 3.8.1. Geometric properties of specimen under uniaxial tension: (a) dimension and boundary conditions, (b) FEM mesh

The top edge of the plate is subjected to a tensile load in the vertical direction with an imposed displacement of 10^{-5} mm for the first 500 steps, and 10^{-6} mm for the subsequent steps. Fig. 3.8.2a and Fig. 3.8.2b shows the development of the crack path at different imposed displacements, which is in good agreement with the results from the literature (Bourdin et al., 2000). Fig. 3.8.3 shows a comparison of the vertical reaction force for the specimen under uniaxial tensile loading.

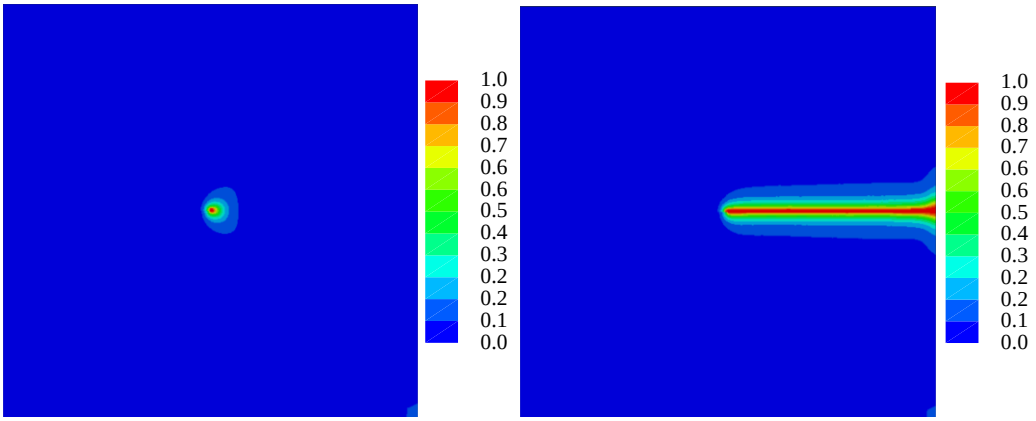

(a) (b)

Fig. 3.8.2. Crack propagation process under uniaxial tension: (a) $U = 6\times10^{-3}$ mm, (b) $U = 7.1\times10^{-3}$ mm

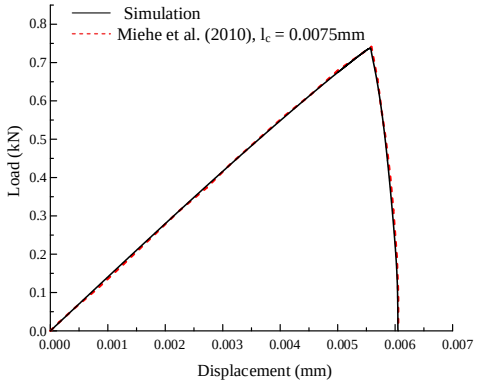

Fig. 3.8.3. Comparison of load-displacement under uniaxial tension

3.8.2 Shear test on a notched plate

The phase-field model is used to simulate the crack propagation process of the notched plate sample under shear loading as shown in Fig. 3.8.4a. In this simulation, the nodes along the bottom edge are restrained in both vertical and horizontal directions, while the nodes along the top edge are restrained only in the vertical direction. The mesh is refined within the region where crack propagation is expected to occur, as shown in Fig. 3.8.4b and includes 119998 triangular elements. A mesh size of 0.001 mm was used to model the crack propagation zone. The mechanical properties of the materials are $E = 210$ kN/mm^2 and $\nu = 0.3$ (Miehe et al., 2010a). To compare and calibrate the theoretical model, the fracture properties given in Nguyen et al. (Miehe et al., 2010a), are used, including the length scale parameter ($l_c = 0.0075$ mm) and the critical energy release rate ($g_c = 0.0027$ kN/mm).

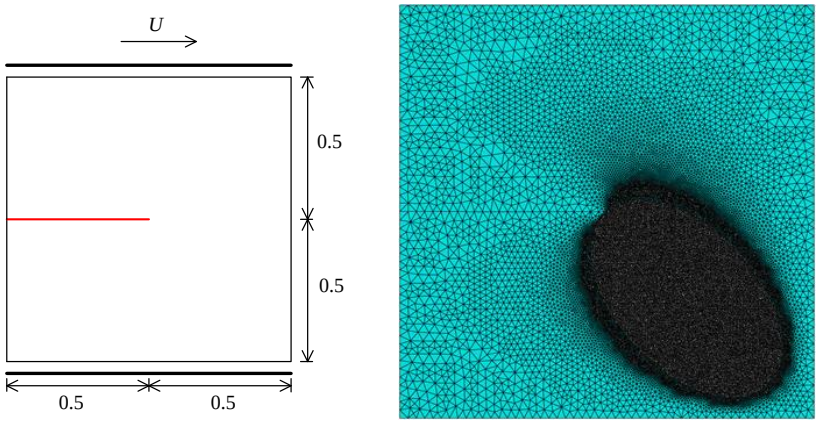

(a) (b)

Fig. 3.8.4. Geometric properties of specimen under pure shear loading: (a) dimension and boundary conditions, (b) FEM mesh

The top edge of the plate is subjected to a shear load in the horizontal direction with an imposed displacement of 10^{-4} mm for each load step. Fig. 3.8.5a and Fig. 3.8.5b indicate the crack propagation path at different displacements, which accurately reproduce the results found in the literature (Nguyen et al., 2015). Fig. 3.8.6 shows a comparison between the load-displacement curve obtained from this study and the benchmark case.

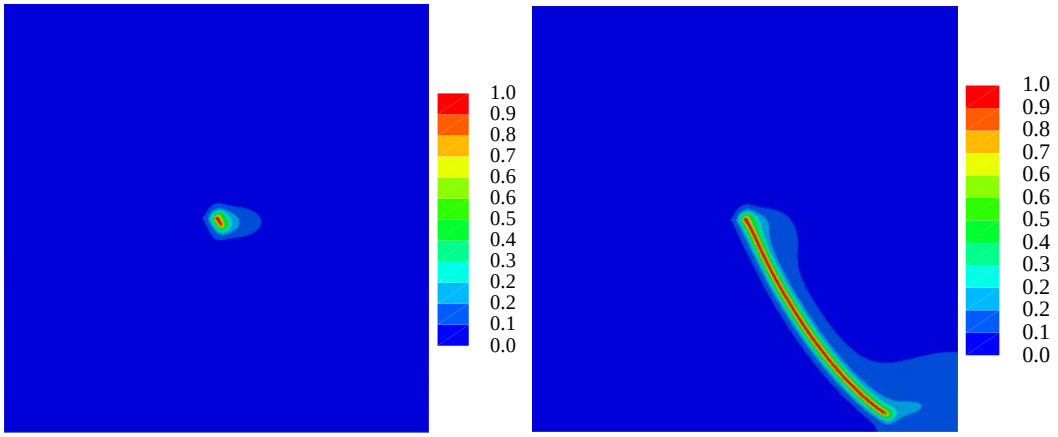

(a) (b)

Fig. 3.8.5. Crack propagation process under pure shear loading: (a) $U = 11\times10^{-3}$ mm, (b) $U = 14\times10^{-3}$ mm

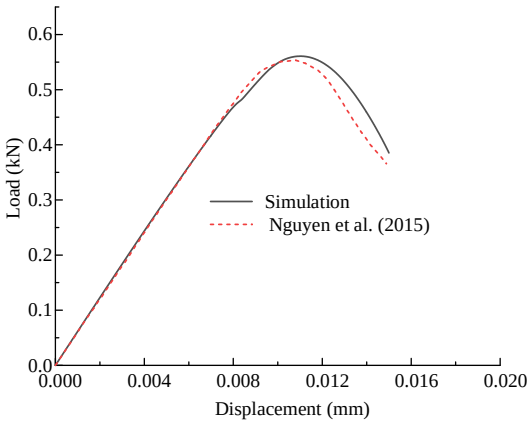

Fig. 3.8.6. Comparison of load-displacement under pure shear loading

3.8.3 Perforated asymmetric bending test

To calibrate the spectral decomposition of strain energy in tensile and compressive strain, an asymmetric bending test is analysed. This test simulates curvilinear crack development using the three-point bending configuration shown in Fig. 3.8.7a, where the location of the holes significantly influences the fracture path. As shown in the figure, the left and right sides of the specimen are treated as elastic, as suggested by Moes (Moës et al., 2011).

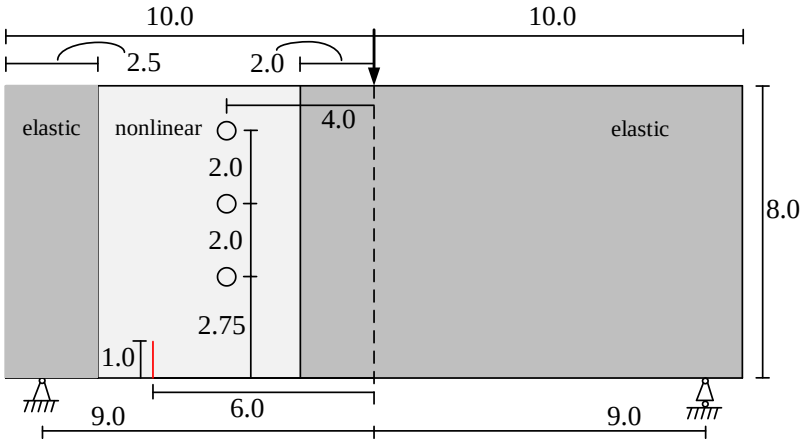

(a)

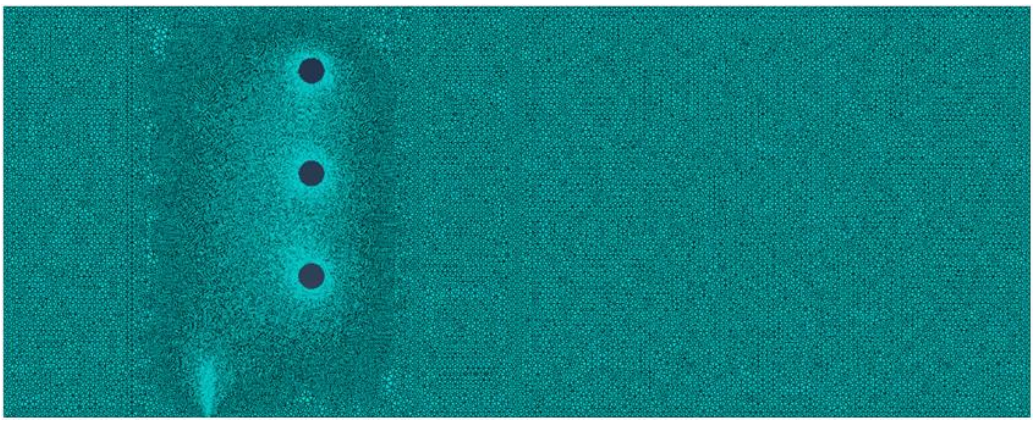

(b)

Fig. 3.8.7. Geometric properties of specimen of three-point bending test: (a) dimension and boundary conditions, (b) FEM mesh

The mechanical properties and phase-field model parameters are obtained from the tests of Bittencourt et al.(Bittencourt et al., 1996): $E = 20.8$ kN/mm^2, $\nu = 0.3$, $l_c = 0.025$ mm, $g_c = 0.001$ kN/mm. The element size is refined around the notch and holes ($h_{min} = 0.01$ mm) and a total of 94164 triangular elements are used (Fig. 3.8.7b). In this simulation, a vertical load is applied at the middle point of the top edge with an imposed displacement of 10^{-3} mm for the first 150 steps, and 10^{-4} mm for the subsequent steps. Fig. 3.8.8 illustrates that the fracture patterns obtained from the implementation of the proposed phase-field model accurately reproduce those observed experimentally.

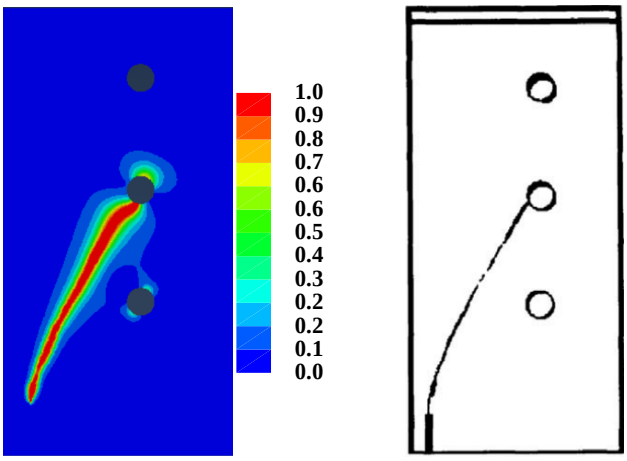

(a) (b)

Fig. 3.8.8. Crack propagation process of three-point bending test, (a) Simulation result, (b) Experimental result

Chapter 4: Multiple-phase-field Modelling for Fracture and Damage Behaviour of Concrete

Abstract

Concrete deterioration is mainly the result of progressive damage on cracks that naturally develop in concrete, either due to mechanical stress or chemical deterioration. Capturing crack propagation within concrete components is essential for determining damage fracture patterns and nonlinear failure mechanisms. This paper presents an energy dissipation theory to concrete with different components contents for homogenous and mesoscale model. A phase-field model is utilized to predict fracture development, employing Drucker-Prager yield criterion and spectral decomposition method to capture plastic behaviour and asymmetric tension-compression response of concrete. To calibrate the proposed model, three experiments from the literature with varying tests, are utilized to explore the impact of the volume content of concrete composites. Results demonstrate that the numerical models align well with experimental results, confirming its efficacy. This model will be further developed to incorporate the effects of multiple physical fields, offering a robust tool for predicting crack propagation in concrete with varying composite fractions. This study will enhance the understanding of concrete deterioration mechanisms and to new methods for mitigating them so as to achieve more durable and resilient structures.

Keywords: Concrete, Elasto-plastic phase-field model, Mesoscale model, Three-point bending test, Wedge splitting test, Multiple-phase-field

4.1 Introduction

Concrete, as a common building material, is widely utilized in various engineering facilities (Chen and Feng, 2022) due to its low cost and mouldability. In addition, concrete exhibits a broad range of mechanical responses, coupled with exceptional strength and mechanical toughness. These properties develop as a result of various failure mechanisms interacting across multiple phases, such as mortar, aggregate and interfacial transition zone (ITZ). Understanding the contribution and failure mechanisms of these phases to the overall behaviour is necessary for fabricating a composite with desired fracture properties.

In massive concrete structures, the opening and development for micro cracks among different phases, such as, can ultimately lead to macroscopic failure during both construction and operation. Cracking can attributed to thermal effects, shrinkage deformations, mechanical stress and chemical attach (Naderi et al., 2021a). Mesoscale modelling can improve the understanding of concrete's fracture mechanisms, as it can provide fundamental insights into the deterioration processes and assist the risk assessment and risk management of concrete facilities. Concrete's fracture strength and mechanical toughness are significantly influenced by the opening and evolution of cracks within each constituent phase at the mesoscale. The mechanism interactions among these components, coupled with the fracture development, lead to the formation of a non-linear process region in front of the fracture tip (Jia et al., 2022). Consequently, concrete materials exhibit complex damage and degradation mechanisms across different phases. Therefore, accurate predictive models that account for the influence of these diverse phases are essential for assessing concrete's mechanical performance and their deterioration over time due to cracking.

To understand how different phases affect crack propagation, a mesoscopic model of concrete with varying volume fractions is essential for analysing its failure mechanisms. Extensive tests have been implemented to study the mesoscopic features for concrete using different aggregate ratios (Chen et al., 2004, Amparano et al., 2000, Rozière et al., 2007). Experimental findings indicate that both the critical stress and crack energy growth with a higher content of coarse aggregates. Furthermore, the increase of coarse aggregate volume fraction leads to a larger ITZ, and a reduced fracture process zone (FPZ). In the mesoscale model, the FPZ contains interconnected fracture along interface, with paths forming inside this softening region (Huang and Li, 1989, Karihaloo et al., 1991). Based on experiments with varying aggregate ratios, a mesoscopic model of concrete can be developed to investigate its fracture mechanisms.

In constructing a mesoscale model of concrete with spatially distributed components, both indirect and direct algorithms are commonly employed. Direct algorithms are preferred for mesoscale numerical simulations because they allow for the consideration of key material features across multiple phases (Wang et al., 2015, Wu et al., 2019). Therefore, direct algorithm is utilized to achieve precise geometric properties. This method involves initially generating the various concrete's components with specific geometric properties, which are subsequently randomly located into this domain to explicitly model the meso-structures. Computational meshes are subsequently created based on these randomly generated meso-structures (Huang et al., 2016c, Ma et al., 2016).

After establishing the mesoscopic model, selecting an appropriate numerical approach is crucial for studying the failure mechanisms of concrete. For fracture computation, two common methods are the discrete (discrete element method (DEM)) and smeared approaches (finite element method (FEM)), respectively. Due to challenges such as mesh-alignment (López et al., 2008, Huang et al., 2016c, Naderi

et al., 2021b, Guo et al., 2019), high computational costs (Du et al., 2014, Patil et al., 2019, Oliver et al., 2015), smeared method is preferred for explicitly tracking crack geometry (Zhang et al., 2018b, Zhang and Mang, 2020, Zeng et al., 2019, Zhang et al., 2021, Zhang et al., 2020). FEM, rooted in continuum degradation theory, model fracture as diffused failure regions that evolve from an unbroken condition to entire stiffness loss. These methods are notably more efficient in simulating diffusive failure development compared to capturing individual fracture (Wriggers et al., 2006, Markou et al., 2013, Pulatsu et al., 2019, Huang et al., 2016b, Liu et al., 2019, Kim et al., 2011). Additionally, an parameter of crack width is needed to normalise non-local interactions of micro crack, either through integral (Pijaudier-Cabot and Bažant, 1987, Zhang et al., 2019) or gradient enhancement (Peerlings et al., 1996, Simone et al., 2004, Nguyen et al., 2018).

Developing the constitutive theory is essential to understand crack propagation in concrete across different components and is directly related to the chosen numerical method. The isotropic nature for phase-field model (Bourdin et al., 2000) often leads to unrealistic crack patterns, since it simulates identical fracture behaviour in both tension and compression. To overcome this issue, a common approach involves energy decomposition to tensile energy and compressive energy. Methods such as volumetric-deviatoric decomposition (Amor et al., 2009) and spectral (Miehe et al., 2010b) decompositions of elastic energy and strain tensor have been explored. To accurately capture the plastic fracture responses of concrete, Drucker-Prager yield theory (Drucker and Prager, 1952) is utilized. This criterion, which gradually degrades with damage, effectively accounts for plastic energy in the calculation of fracture propagation, particularly for brittle solid behaviour. However, the phase-field model with elasto-plastic property struggles to accurately track fracture response for concrete with varying aggregate content. This limitation arises because different components, such as aggregate, mortar, and the ITZ, exhibit distinct mechanical and damage responses, resulting in variations in the stiffness and energy of concrete. Consequently, analysing fracture energy dissipation between different phases is essential for understanding the mechanical response of concrete.

This paper develops a mesoscale concrete model with different components to study fracture evolution behaviour for its multi-phase composition. A multi-phase phase-field model is developed to elucidate energy dissipation of concrete. This model is conducted in ABAQUS by using the user defined element (UEL) subroutine, and multiple numerical examples are evaluated for calibration. Specifically, this proposed phase-field mesoscale modelling is applied to concrete samples subjected to three-point bending tests and splitting wedge tests, calibrating it against experimental results. This modelling allows for a detailed prediction of the influence for various features on mesoscopic fracture evolution and failure mechanisms for concrete. This is expected to lead to a better understanding in concrete deterioration along with time and allow the evolution of mitigation approaches.

4.2 Phase field model for multi-phase composites

In this theory part, phase-field degradation theory is introduced to assess the mechanical performance of concrete. Extending this theory, a multi-phase phase-field damage method is developed to analyse mechanical deformation and crack propagation within different components. Additional information on the foundational theory of the phase-field model is available in the literature (Miehe et al., 2010a). The key concepts of phase-field modelling are detailed in the following subsections.

4.2.1 Regularized representation of crack topology

The phase-field modelling introduces a concept of crack topology within a geometric context. Consider a sharp crack in a solid domain Γ subjected to distributed traction F, as depicted in Fig. 4.1a. The damage variable d ($0 \leq d \leq 1$) is used to represent the crack geometric topology, where $d = 0$ indicating an intact state and $d = 1$ indicating a completely damaged state. The cracking solid domain is represented by $\Omega \subset \mathbb{R}^D$ (with $D = 1, 2, 3$ corresponds to the spatial dimension), and its boundary is donated as $\partial\Omega$, as depicted in Fig. 4.1a. Fig. 4.1b illustrates normalised depiction of fracture surface using a diffusive fracture geometric topology to describe crack width.

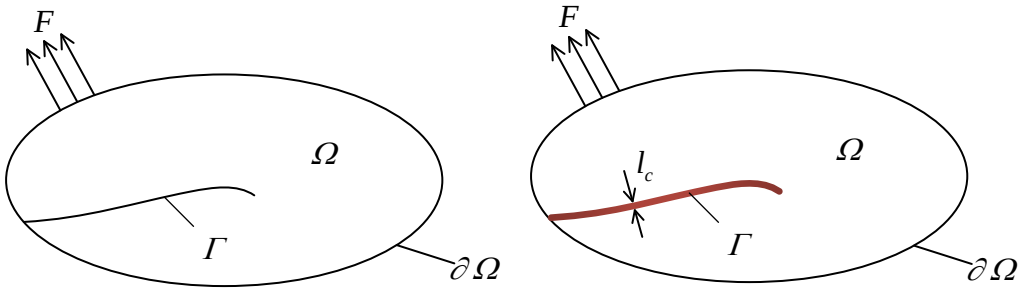

(a) (b)

Fig. 4.1. Normalised depiction for a fracture surface: (a) sharp topology, (b) diffusive topology

By approximating the discontinuous discrete crack by smearing it over the domain Ω of the solid, a continuous and diffusive method is employed. Within this region Ω, a uniform dimensionless field is used to describe crack topography. The crack surface density, γ, is introduced in research (Miehe et al., 2010a) using the following equation:

$$\gamma\left(d,\nabla d\right)=\frac{d^2}{2l_c}+\frac{l_c}{2}\left|\nabla d\right|^2 \tag{4.1}$$

where, l_c is the parameter of length scale for the diffusive fracture.

Consequently, fracture surface is associated with the crack width parameters. The regularized crack surface can thus be described as:

$$\Gamma(d)=\int_{\Omega}\gamma(d,\nabla d)d\Omega \tag{4.2}$$

Considering these equations, cracked solid with a fracture surface Γ can be considered by a dimensionless parameter.

4.2.2 Potential energy function in homogenous solid

To analyse the crack development and deformation evolution, total potential energy Π for crack region Ω is considered as the composition of strain energy and crack surface energy:

$$\Pi=E(u,d)+P(u,d)+W(d)=\int_{\Omega}\psi_{\varepsilon}\left(\varepsilon(u),d\right)d\Omega+\int_{\Gamma}g_c d\Gamma \tag{4.3}$$

where, $E(u,d)$ is elastic energy, $P(u,d)$ is plastic energy, $W(d)$ is fracture energy, u is field for displacement performance, $\varepsilon(u)$ is strain tensor, ψ_{ε} is strain energy, and g_c is the critical energy threshold.

Total energy density of displacement field $\psi_{\varepsilon}(\varepsilon(u), d)$ is described by:

$$\psi_{\varepsilon}\left(\varepsilon(u),d\right)=\psi_{\varepsilon}^{el}\left(\varepsilon(u),d\right)+\psi_{\varepsilon}^{pl}\left(\varepsilon(u),d\right) \tag{4.4}$$

where, $\psi_{\varepsilon}^{el}(\varepsilon(u), d)$ is the elastic strain energy density, $\psi_{\varepsilon}^{pl}(\varepsilon(u), d)$ is the plastic strain energy density.

Total strain tensor $\varepsilon(u)$ can be descirbed in terms of the symmetric displacement gradient $\nabla_s u$ as:

$$\varepsilon=\nabla_s u=\frac{1}{2}\left[\nabla u+\nabla^T u\right] \tag{4.5}$$

With the description of fracture surface density using phase-field variables, the crack energy is described using a region integral (Liu et al., 2016) as follows:

$$\int_{\Gamma}g_c d\Gamma\approx\int_{\Omega}g_c\left[\frac{d^2}{2l_c}+\frac{l_c}{2}|\nabla d|^2\right]d\Omega=w^0(d) \tag{4.6}$$

To propose the threshold energy in the staggered algorithm, Miehe (Miehe et al., 2016) introduces a linear term to solve the equation:

$$W(d)=\int_{\Omega}t(d)+w^0(d)d\Omega \tag{4.7}$$

where, $t(d)$ is energy threshold, $t(d)$ and $w^0(d)$ are given as:

$$\begin{cases} t(d) = \psi^c - g(d)\psi^c \\ w^0(d) = 2l_c\psi^c \left[d^2 + l_c^2 |\nabla d|^2 \right] \end{cases} \tag{4.8}$$

where, ψ_c is the specific critical fracture energy, $\psi_c = g_c/2l_c$, $g(d)$ is the degradation equation: $g(d) = (1 - d)^2 + k$, and k represents a small constant that ensures solution stability.

Therefore, the total potential energy can be described as:

$$\Pi = \int_\Omega \left[\psi_\varepsilon^{el}(\varepsilon(u), d) + \psi_\varepsilon^{pl}(\varepsilon(u), d) + W(d) \right] d\Omega \tag{4.9}$$

In elastic energy degradation, only tensile stress contributes to damage and crack development. To address this, the spectral method is used to decompose the strain energy. This decomposition allows separation of tensile and compressive components for strain energy, ensuring that only tensile stresses contribute to damage. The effect of cracks on stiffness reduction is then considered, and the elastic energy function is described as follows:

$$\psi_\varepsilon^{el}(\varepsilon(u), d) = g(d) \cdot \psi_0^{el+}(\varepsilon) + \psi_0^{el-}(\varepsilon) \tag{4.10}$$

where, ψ_0^{el+} and ψ_0^{el-} are tensile energy and compressive energy, respectively.

The elastic energy density function for tension and compression is described as follows (Liu et al., 2016):

$$\psi_0^{el\pm} = \frac{\lambda}{2} \langle tr(\varepsilon) \rangle_\pm^2 + \mu tr(\varepsilon_\pm^2) \tag{4.11}$$

where, λ and μ are the Lame's constants, $tr(\cdot)$ is the trace of strain.

The energy density of plastic strain is described as:

$$\psi_\varepsilon^{pl}(\varepsilon(u), d) = g(d)\psi_0^{pl}(\varepsilon) \tag{4.12}$$

where, $\psi_0^{pl}(\varepsilon)$ is the initial plastic strain energy.

To describe the plastic mechanical behaviour for concrete under tension and compression loads, implementation incorporates the Drucker-Prager yield theory. This criterion is well-suited for materials like concrete that exhibit different responses to tension and compression due to its ability to capture the pressure-dependent yielding behaviour (Drucker and Prager, 1952):

$$f\left(I_1, J_2\right)=\sqrt{J_2}+\beta I_1-g\left(d\right)\left[\sigma^{\lim}+H\varepsilon_{eq}^{pl}\right] \tag{4.13}$$

where, I_1 is the first invariant of the Cauchy stress tensor, J_2 is the second invariant of the deviatoric part of the Cauchy stress tensor, $\sigma^{\lim}$ is the yield stress, H is the hardening modulus and ε_{eq}^{pl} is the energy-equivalent plastic strain.

Energy history of plastic performance is represented as a formulation of yield stress and energy-equivalent plastic strain. This formulation is essential for capturing the energy dissipated during plastic behaviour of concrete. This expression for plastic energy history is given by:

$$\psi_0^{pl}\left(\varepsilon_{eq}^{pl}\left(u\right)\right)=\varepsilon_{eq}^{pl}\left(u\right)\left[\sigma^{\lim}+\frac{1}{2}H\varepsilon_{eq}^{pl}\left(u\right)\right] \tag{4.14}$$

The plastic energy function is based on the Drucker-Prager (Drucker and Prager, 1952) yield criterion and is described by flow rules, which define the association between plastic stress and plastic during plastic stage. Plastic energy function is expressed as follows (Krabbenhøft, 2002):

$$\begin{aligned}\psi_{\varepsilon}^{pl}&=g\left(d\right)\psi_0^{pl}=g\left(d\right)\left(\varepsilon_{eq}^{pl}\right)^T K_0\varepsilon_{eq}^{pl}\\ K_0&=\left(K-\frac{K\dfrac{\partial g}{\partial\sigma}\left(\dfrac{\partial f}{\partial\sigma}\right)^T K}{H+\left(\dfrac{\partial f}{\partial\sigma}\right)^T D\dfrac{\partial g}{\partial\sigma}}\right)\end{aligned} \tag{4.15}$$

where, K represents elastic constitutive matrix, K_0 represents elasto-plastic constitutive matrix, g and f are plastic potential energy.

Total potential energy function is constructed by combining elastic energy, plastic energy, and fracture energy. This comprehensive formulation accounts for the various energy contributions within the material, allowing for an in-depth analysis of deformation and damage mechanisms for concrete. Total potential energy function is given as follows:

$$\Pi=\int_{\Omega}\left\{g\left(d\right)\left[\psi_0^{el+}\left(\varepsilon\right)+\psi_0^{pl}\left(\varepsilon\right)-\psi^c\right]+\psi_0^{el-}\left(\varepsilon\right)+\psi^c+2l_c\psi_c\left[d^2+l_c^2\left|\nabla d\right|^2\right]\right\}d\Omega \tag{4.16}$$

4.2.3 Potential energy function in multi-phase solid

To analyse the muti-phase field model of concrete with individual constituents (mortar, ITZ and aggregates), the potential energy function is proposed based on a homogenous solid framework. Since

the critical crack energy for aggregates is significantly higher than that of ITZ and mortar, aggregates are considered elastic. Mortar and ITZ are treated as elasto-plastic components for crack propagation. Therefore, the crack geometry of mortar and ITZ is approximated using the diffused parameters $d_M(x)$ and $d_I(x)$, respectively, which are described as follows:

$$\begin{cases} \gamma_M\left(d_M,\nabla d_M\right)=\dfrac{{d_M}^2}{2l_c}+\dfrac{l_c}{2}\left|\nabla d_M\right|^2 \\ \gamma_I\left(d_I,\nabla d_I\right)=\dfrac{{d_I}^2}{2l_c}+\dfrac{l_c}{2}\left|\nabla d_I\right|^2 \end{cases} \tag{4.17}$$

where, γ is the fracture surface density of mortar and ITZ.

By introducing the fraction of the three phases, the total potential energy is decomposed into contributions from mortar, ITZ, and aggregates. This decomposition allows for a detailed analysis of the energy contributions from each constituent of the concrete, providing insight into the material's overall mechanical behaviour. Total potential energy function is described as:

$$\Pi=\Pi_M+\Pi_I+\Pi_A \tag{4.18}$$

where, Π_M represents potential energy of mortar, Π_{ITZ} represents the potential energy of ITZ, Π_A represents potential energy of aggregates.

By combining Eq. (4.16), the potential energy contributions from the three phases can be determined:

$$\begin{cases} \Pi_M=\int_{M\Omega}\left\{g\left(d\right)\left[\psi_{M0}^{el+}\left(\varepsilon\right)+\psi_{M0}^{pl}\left(\varepsilon\right)-\psi_M^c\right]+\psi_{M0}^{el-}\left(\varepsilon\right)+\psi_M^c+2l_c\psi_M^c\left[d^2+l_c^2\left|\nabla d\right|^2\right]\right\}d\Omega_M \\ \Pi_I=\int_{I\Omega}\left\{g\left(d\right)\left[\psi_{I0}^{el+}\left(\varepsilon\right)+\psi_{I0}^{pl}\left(\varepsilon\right)-\psi_I^c\right]+\psi_{I0}^{el-}\left(\varepsilon\right)+\psi_I^c+2l_c\psi_I^c\left[d^2+l_c^2\left|\nabla d\right|^2\right]\right\}d\Omega_I \\ \Pi_{MA}=\int_{A\Omega}\left\{\psi_{A0}^{el+}\left(\varepsilon\right)+\psi_{A0}^{el-}\left(\varepsilon\right)\right\}d\Omega_A \end{cases} \tag{4.19}$$

To regularise the integral domain of solids, the volume content of three phases are used to describe potential energy, as follows:

$$\Pi=\int_\Omega\left[V_M\psi_M+V_I\psi_I+V_A\psi_A\right]d\Omega \tag{4.20}$$

where, V_i ($i = M, I, A$) is the volume fracture of mortar, ITZ and aggregate, ψ_i ($i = M, I, A$) is the energy density function of mortar, ITZ and aggregate from the concrete domain.

Therefore, total potential energy of different parts is described as follows by combing Eq. (4.19) and Eq. (4.20):

$$\Pi=\int_{\Omega}\left\{\begin{array}{l} V_M\left(\left(\varepsilon_{eq}^{el}\right)^T\left(K_M\right)\varepsilon_{eq}^{el}+\left(\varepsilon_{eq}^{pl}\right)^T g\left(d\right)K_{M0}\varepsilon_{eq}^{pl}+\left(1-g\left(d\right)\right)\dfrac{g_M}{2l_c}+g_M\gamma\left(d,\nabla d\right)\right) \\ +V_I\left(\left(\varepsilon_{eq}^{el}\right)^T\left(K_I\right)\varepsilon_{eq}^{el}+\left(\varepsilon_{eq}^{pl}\right)^T g\left(d\right)K_{I0}\varepsilon^{eq}+\left(1-g\left(d\right)\right)\dfrac{g_I}{2l_c}+g_I\gamma\left(d,\nabla d\right)\right) \\ +V_A\left(\left(\varepsilon_{eq}\right)^T K_A\varepsilon_{eq}\right) \end{array}\right\}d\Omega \tag{4.21}$$

where, K_M, K_I and K_A are the elastic constitutive matrix of mortar, ITZ and aggregate, K_{M0} and K_{I0} are the elasto-plastic constitutive matrix of mortar and ITZ.

4.3 Staggered algorithm with FEM

4.3.1 Staggered time-integration algorithm

The phase-field model results in two fields coupling problem involving phase, *d*, and displacement, *u*, fields which is essential for tracking crack propagation paths. This coupling problem can be addressed using "monolithic" approach or "staggered" approach (Miehe et al., 2010b). The coupled equations are solved simultaneously at every time step by the monolithic algorithm, leading to non-linearity in the equations of displacement field. Therefore, this approach typically demands numerous iterations and may experience poor convergence. In contrast, staggered algorithm divides this problem into two independent minimization procedures, solving displacement field and phase field sequentially. This method effectively decouples two fields, reducing computational complexity and enhancing convergence.

With a fixed *d*, the displacement field is expressed as follows:

$$\Pi^u=\int_{\Omega}\left\{\sum_{i}^{i=1,3}\left[\psi_{\varepsilon}^{el}\left(\varepsilon\left(u\right),d\right)+\psi_{\varepsilon}^{pl}\left(\varepsilon\left(u\right),d\right)\right]\right\}d\Omega-\Pi^{ext} \tag{4.22}$$

From Eq. (4.21), the displacement field is described as follows:

$$\Pi^u=\int_{\Omega}\left\{V_M\left(\psi_{M\varepsilon}^{el}+\psi_{M\varepsilon}^{pl}\right)+V_I\left(\psi_{I\varepsilon}^{el}+\psi_{I\varepsilon}^{pl}\right)+V_A\psi_{A\varepsilon}^{el}\right\}d\Omega-\Pi^{ext} \tag{4.23}$$

where, Π^{ext} is external energy induced by force, which is formulated as follows:

$$\prod^{ext} = \int_{\Omega} \bar{\gamma} \cdot u d\Omega + \int_{\partial\Omega} \bar{t} \cdot u d\partial\Omega \tag{4.24}$$

where, $\bar{\gamma}$ and $\bar{t}$ are the body and surface forces, respectively.

By varying both energies ($\delta\Pi^u = 0$), the corresponding Eulerian equations (strong form) for displacement field is written as follows:

$$\begin{aligned} &\delta\prod^{u} = 0 \quad \forall\delta u \rightarrow \quad \nabla\sigma - \bar{\gamma} = 0 && in \quad \Omega \\ &\sigma \cdot n = \bar{t} && on \quad \Gamma_N \\ &u = \bar{u} && on \quad \Gamma_D \end{aligned} \tag{4.25}$$

Similarly, by replacing potential energy from the displacement field with history energy, the Lagrangian equation for the phase-field problem can be expressed as:

$$\prod^{d} = \int_{\Omega} \left[V_M g_M \gamma\left(d, \nabla d\right) + V_I g_I \gamma\left(d, \nabla d\right) + g\left(d\right)\left(V_M H_M + V_I H_I\right) \right] d\Omega \tag{4.26}$$

And the history field is described as:

$$\begin{aligned} &H_0 = 0 \\ &H_{n+1} = \max \begin{Bmatrix} \psi_0^{el+} + \psi_0^{pl} - \psi^{c} \\ H_n \end{Bmatrix} \end{aligned} \tag{4.27}$$

where, H_n is the history energy at step n.

Furthermore, this formulation enforces irreversibility of the damage ($\dot{d} \geq 0$). Thus, the strong form of phase field is represented as:

$$\begin{aligned} &\delta\prod^{d} = 0 \quad \forall\delta d \rightarrow \quad \frac{\boldsymbol{g}}{2l_c}\left(d - l_c^2 \Delta d\right) = \left(1 - d\right) H && in \quad \Omega \\ &\nabla d \cdot n = 0 && in \quad \Gamma \end{aligned} \tag{4.28}$$

where, $\boldsymbol{g} = \begin{bmatrix} g_m & 0 \\ 0 & g_I \end{bmatrix}$, $H = V_M H_M + V_I H_I$.

4.3.2 Staggered multi-phase algorithm

The multi-phase phase-field model results in a three-field problem, facilitating numerical solutions required for tracking the crack propagation through distinct phases. To analyse the effect of different components, energy degradation is studied for samples with varying volume fractions. Because of the non-linear property of equations of displacement field, staggered algorithm is employed to develop the energy degradation equations. Initially, the same external energy is applied to two samples to ensure the same internal potential, which are then used to compute the displacement distribution for both samples. Subsequently, the energy history is utilized to recalculate the damage field for these samples.

Based on Eq. (4.23), the displacement of two samples is described as:

$$V_M^1\psi_{M\varepsilon}+V_I^1\psi_{I\varepsilon}+V_A^1\psi_{A\varepsilon}=V_M^2\psi_{M\varepsilon}+V_I^2\psi_{I\varepsilon}+V_A^2\psi_{A\varepsilon} \tag{4.29}$$

where, V_i^1 ($i = M, I, A$) and V_i^2 represent volume fracture of mortar, ITZ, aggregate of two samples.

To simplify the function for internal potential energy density:

$$H_{\text{int}}^1=H_{\text{int}}^2 \tag{4.30}$$

The phase-field problem can be described by replacing "history energy" with "potential energy density" and incorporating the energy contributions from different parts, as follows:

$$\begin{aligned}\prod^{d1}&=\int_\Omega\left[\left(\boldsymbol{V}^1\boldsymbol{g}\right)\boldsymbol{\gamma}^1\left(d,\nabla d\right)+g\left(d^1\right)\left(H_{\text{int}}^1-V_M^1\psi_{M0}^{el-}-V_I^1\psi_{I0}^{el-}-V_A^1\psi_A^{el}\right)\right]d\Omega\\ \prod^{d2}&=\int_\Omega\left[\left(\boldsymbol{V}^2\boldsymbol{g}\right)\boldsymbol{\gamma}^2\left(d,\nabla d\right)+g\left(d^2\right)\left(H_{\text{int}}^2-V_M^2\psi_{M0}^{el-}-V_I^2\psi_{I0}^{el-}-V_A^2\psi_A^{el}\right)\right]d\Omega\end{aligned} \tag{4.31}$$

where, $\boldsymbol{V}$, $\boldsymbol{g}$ and $\boldsymbol{\gamma}$ represent tensor of volume fracture, critical energy release rate and crack surface for different phases, $\boldsymbol{V}=\begin{bmatrix}V_m & 0\\ 0 & V_I\end{bmatrix}$, $\boldsymbol{g}=\begin{bmatrix}g_m & 0\\ 0 & g_I\end{bmatrix}$, $\boldsymbol{\gamma}=\begin{bmatrix}\gamma_m\\ \gamma_I\end{bmatrix}$.

By combing Eq. (4.30) and Eq. (4.31) to Eq. (4.28), the strong form equations is described as follows:

$$\begin{cases}\boldsymbol{V}\boldsymbol{g}\Delta\boldsymbol{\gamma}\left(d,\nabla d\right)\beta=\left(1-d\right)H^1\\ \beta=\dfrac{H^1}{H^1+\Delta\psi}\\ \Delta\psi=\left(V_M^1\psi_{M0}^{el-}+V_I^1\psi_{I0}^{el-}+V_A^1\psi_A^{el}\right)-\left(V_M^2\psi_{M0}^{el-}+V_I^2\psi_{I0}^{el-}+V_A^2\psi_A^{el}\right)\end{cases} \tag{4.32}$$

where, H^l is the history energy of reference sample, β is the potential energy correction parameter.

From Eq. (4.32), the degradation evolution is influenced by potential correction parameter, which is influenced by the volume content and potential energy of different components. To simplify calculation, the mechanical property of ITZ phase are described by mortar phase, controlled by parameter α (Li et al., 2018). Additionally, the volume content of mortar is represented by the volume of aggregate, described by the parameter κ. Therefore, Eq. (4.32) can be described as:

$$\begin{cases} \boldsymbol{Vg}\Delta\gamma\left(d,\nabla d\right)\beta=\left(1-d\right)H^{1} \\ \beta=\dfrac{H^{1}}{H^{1}+\Delta\psi} \\ \psi_{I0}^{el-}=\alpha\psi_{M0}^{el-} \\ V_{M}=\kappa V_{A} \\ \Delta\psi=\left(\begin{pmatrix}\left(\alpha-\alpha V_{A}^{1}-\alpha\kappa V_{A}^{1}+\kappa V_{A}^{1}\right) \\ -\left(\alpha-\alpha V_{A}^{2}-\alpha\kappa V_{A}^{2}+\kappa V_{A}^{2}\right)\end{pmatrix}\psi_{M0}^{el-}+\left(V_{A}^{1}-V_{A}^{2}\right)\psi_{A}^{el}\right) \end{cases} \tag{4.33}$$

4.3.3 Finite element discretization in ABAQUS

By utilizing the general FEM framework, the phase field (d) and displacement field (u) can be accurately calculated. The discretized formulations for the phase field are established using FEM. According to the quantities at step t_n, the new variable of phase-field is obtained at step t_{n+1}:

$$d_{n+1}=Arg\left\{\inf_{d}\int_{\Omega}\left[g_{c}\gamma\left(d,\nabla d\right)+g\left(d\right)H\right]d\Omega\right\} \tag{4.34}$$

where, the history energy (H) is obtained based on Eq. (4.27). The associated linear equation can be solved using a Newton-Raphson nonlinear solver in the following form:

$$K_{n}^{d}d_{n+1}=-r_{n}^{d} \tag{4.35}$$

where, d_{n+1} represents unknow variable for new variable of phase-field. r_n^d represents the residual vector and K_n^d represents the tangent matrix of stiffness at step t_n.

The phase-field variable for an element is determined by interpolating the phase-field values at the nodes using the shape function,

$$d=N_{i}d_{i} \tag{4.36}$$

where, N_i represent shape function for variable of phase field ($N_i = [N_1 \ldots N_a]$CC, a = 3 or 4 for 2D with triangle or element quadrilateral), d_i represents node variable of phase field on node i.

The phase field gradient within an element is represented by a matrix, where the spatial derivatives are defined as follows:

$$\nabla d = B_i d_i \tag{4.37}$$

where, B_i is the derivative matrix of shape function.

According to Eq. (4.34), the phase-field variable is formulated by residue vector as follows:

$$r^d = \int_\Omega \left\{ \left[\frac{g_c}{l_c} - 2(1-d)H \right] (N_i)^T + g_c l_c (B_i)^T \nabla d \right\} d\Omega \tag{4.38}$$

And the tangent stiffness matrix is obatined as follows:

$$K^d = \int_\Omega \left\{ \left[\frac{g_c}{l_c} - 2H \right] (N_i)^T N_i + g_c l_c (B_i)^T B_i \right\} d\Omega \tag{4.39}$$

The displacement field variable of an element is obtained similarly and is described by external and internal components: $r^u = f^{int} - f^{ext}$, and external force encompasses both body force and boundary force:

$$f^{ext} = \int_\Omega (N_i)^T \cdot \bar{\gamma} d\Omega + \int_{\partial\Omega} (N_i)^T \cdot \bar{t} d\partial\Omega \tag{4.40}$$

The internal part is described as:

$$r^u = \int_\Omega \left\{ \left[(1-d)^2 + k \right] (B_i)^T \sigma_{i0}^{eq} \right\} d\Omega \tag{4.41}$$

The tangent stiffness matrix of displacement is obtained as follows:

$$K^u = \int_\Omega \left\{ \left[(1-d)^2 + k \right] (B_i)^T K_{i0} B_i \right\} d\Omega \tag{4.42}$$

where, K_{i0} ($i = 3$) is the elasto-plastic constitutive matrix for mortar, ITZ and elastic constitutive modulus for aggregate.

4.4 Experimental calibration of homogenous model

To calibrate the proposed energy dissipation model, crack propagation experiments on concrete with varying aggregate content were utilized, including three-point bending and wedge splitting tests. The fracture evolutions were then compared to experiments. In this section, homogenous model was conducted to investigate potential energy evolution of different samples.

4.4.1 Three-point bending test with shallow notch

This modelling was calibrated utilizing experimental results from Burcu et al. (Akcay et al., 2012). Prismatic specimens (500 mm × 100 mm × 100 mm) with varying aggregate volume fractions were cast. The aggregate volume content in the mix design were 40%, 49%, 58% and 66%. Complete details of the mix designs are available in (Akcay et al., 2012).

On testing day, a notch of depth 5 mm and width 2.5 mm was sawn at the position of mid-span. The crack mouth opening displacement (CMOD) and deflections were simultaneously measured. Load was applied a constant rate of 0.1 mm/min utilizing a closed-loop machine with the maximum capacity of 100kN.

In this calibration, a homogenous modelling for concrete was adopted to calibrate this phase-field model with different aggregate contents. In this model, the sides of the specimens are considered elastic resulting from the individuality induced by constrained nodes (Moës et al., 2011). The boundary conditions for the sample are displayed in Fig. 4.2. Load is located in y-direction on top surface of this concrete specimen while left support is fixed in both x-direction and y-direction, and right support is fixed in y-direction. The element size varies from h = 3 mm in the elastic part to h = 1 mm in the nonlinear part for this model. The potential energy correction parameter β is displayed in Fig. 4.3. Phase-field model's mechanical parameters are listed in Table 4.1.

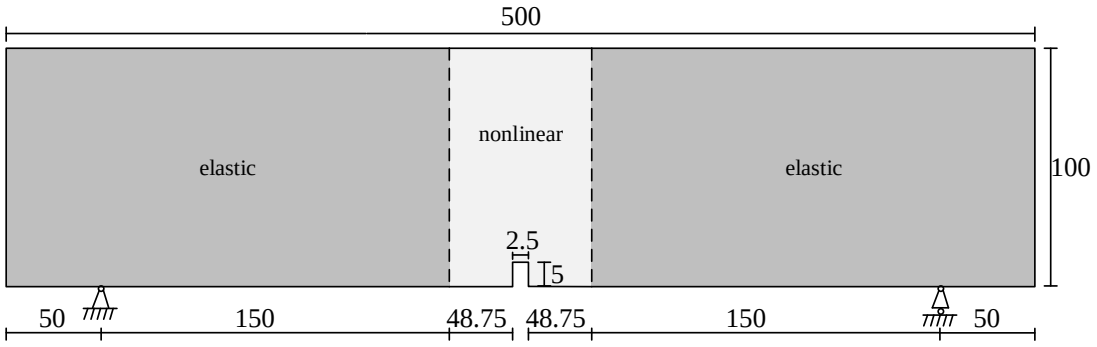

Fig. 4.2. Geometric details and boundary conditions of concrete sample with shallow notch

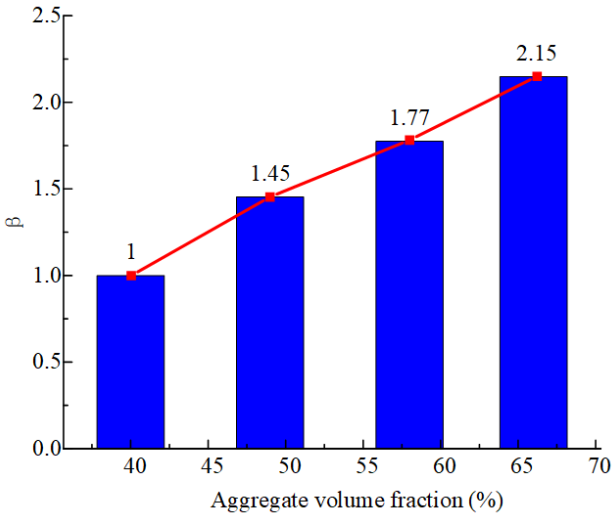

Fig. 4.3. The potential energy correction parameter β for different samples of homogenous model

Table 4.1 Parameters for concrete samples of phase field

Aggregate content (%)	E (GPa)	v	σ_y (MPa)	H (GPa)	l_c (mm)	ψ (MPa)
40	30.2	0.2	5.4	10	1	0.0078
49	30.4	0.2	6.1	11	1	0.01
58	34.1	0.2	7.3	13	1	0.013
66	39.3	0.2	7.4	15	1	0.0155

As for the homogenous model, the same mesh and element model are utilized to simulate the crack propagation for different concrete samples. Therefore, the similar fracture propagation is simulated by this elasto-plastic phase-field modelling is illustrated in Fig. 4.4. Comparison for load-deflection results between simulation results and experimental data is presented in Fig. 4.5.

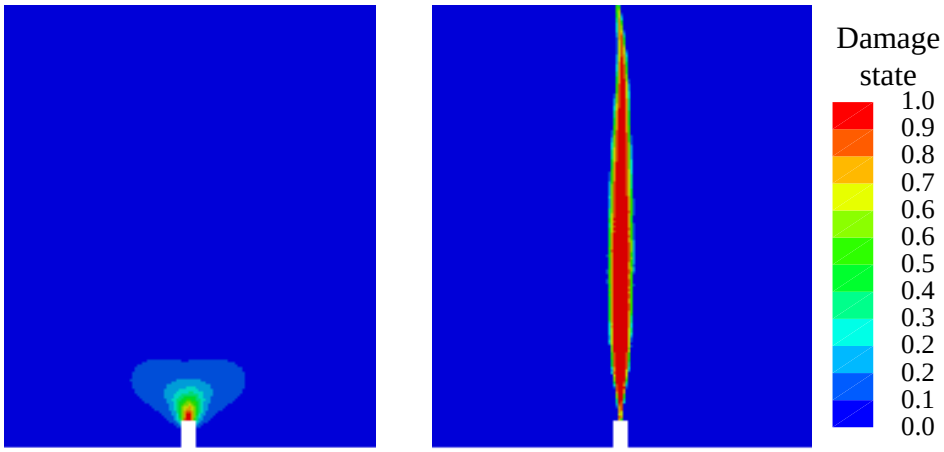

(a) (b)

Fig. 4.4. Crack propagation of concrete: (a) crack initiation, (b) crack propagation

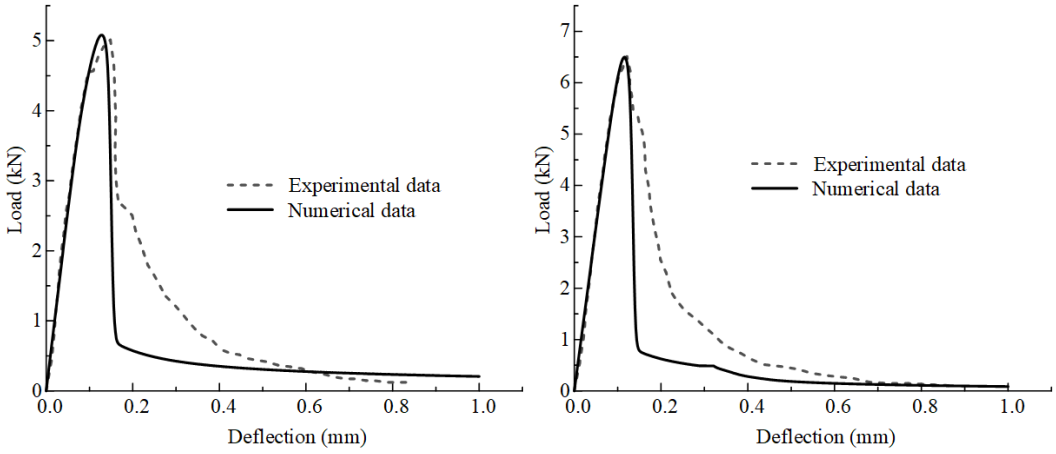

(a) (b)

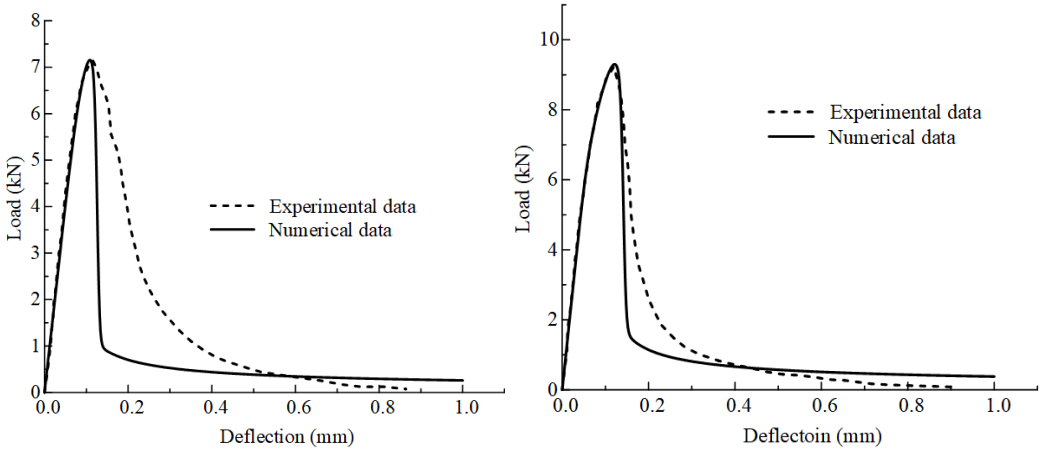

(c) (d)

Fig. 4.5. Comparison of load-deflection curves of concrete specimens with varying aggregate content: (a) 40%, (b) 49%, (c) 58%, (d) 66%

From Fig. 4.4, the concrete specimens have the same crack propagation and no crack branches resulting from the homogenous geometric properties and meshes. In Fig. 4.5, all simulation models demonstrate a good agreement before the crack initiation compared with the experimental data. However, load-deflection results exhibit sharp down associated to experiments, which results from that there is directly crack path of vertical direction without the crack propagation along with other directions.

4.4.2 Three-point bending test with deep notch

Further calibration was done on beam specimens with a deep notch, using experimental data from Burcu et al. (Akcay et al., 2012). Prismatic specimens (500 mm × 100 mm × 100 mm) with varying aggregate volume fractions were cast. These had the same concrete mix design, and aggregate volume fractions as those used in the model with the shallow notch described in Section 4.4.1. For this simulation, the mid-span notch had a depth of 50 mm and a width of 2.5 mm. The same homogenous modelling was utilized, hence, geometric properties for the sample remained consistent so as to analyse the influence of various notch configurations. Details of this sample are shown in Fig. 4.6 and Table 4.1.

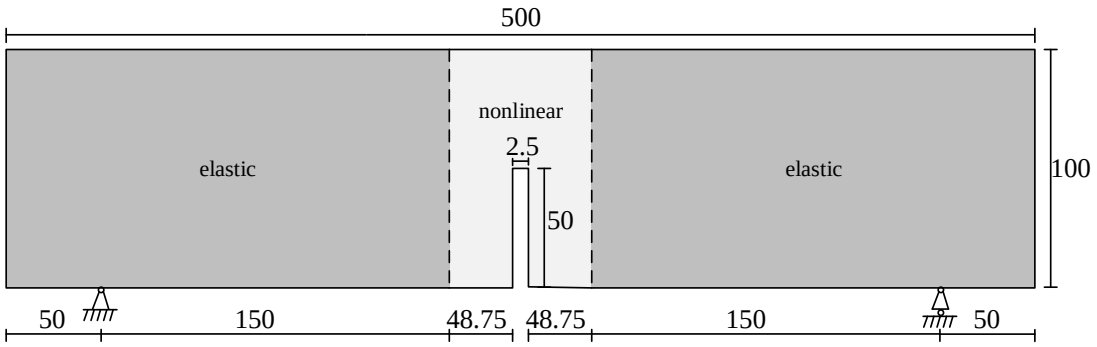

Fig. 4.6. Geometric details and boundary conditions of concrete sample with deep notch

The fracture evolution is shown in Fig. 4.7. Additionally, Fig. 4.8 presents a comparison for load-deflection curves between experimental and numerical results.

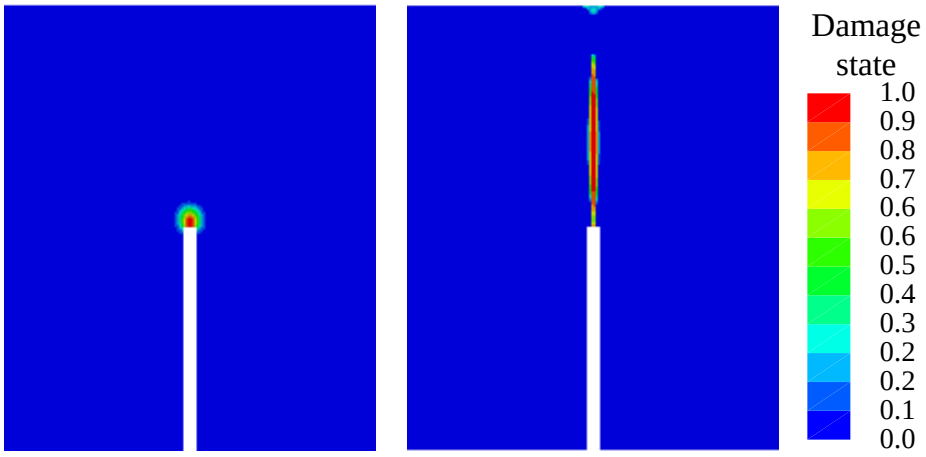

(a) (b)

Fig. 4.7. Crack propagation of concrete: (a) crack initiation, (b) crack propagation

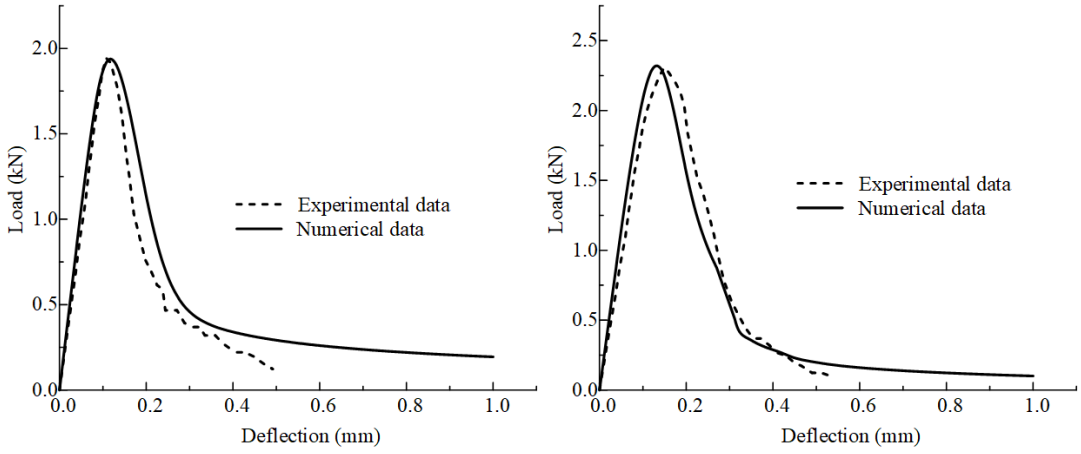

(a)

(b)

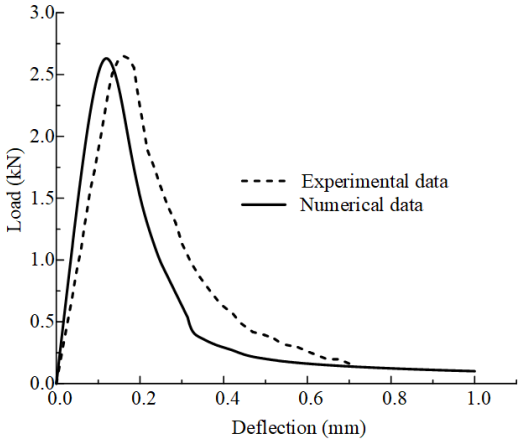

(c)

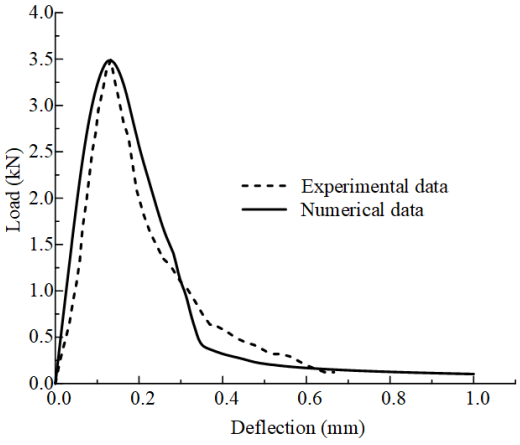

(d)

Fig. 4.8. Comparison of load-deflection curves of concrete specimens with varying aggregate content: (a) 40%, (b) 49%, (c) 58%, (d) 66%

From Fig. 4.7, the crack propagation paths have no branches resulting from the homogenous geometric properties and meshes. In Fig. 4.8, the simulation for 40% and 66% (aggregate content) closely match the experimental data, whereas simulations for 49% and 58% display discrepancies. These differences may be due to insufficient experimental control and material variabilities.

4.4.3 Wedge splitting test

This model was further verified utilizing experiments from Yanwei (Chen and Feng, 2022). Prismatic specimens with dimensions 230 mm × 200 mm × 200 mm were cast with varying aggregate volume fractions. The aggregate volume content was 19%, 25%, 31% and 37%. Full details for concrete mix design and particle distributions is available in (Chen and Feng, 2022).

The specimens for wedge splitting test were cast containing a predefined initial notch of 80 mm depth and 3 mm width. In this calibration, a homogenous modelling for concrete was adopted to calibrate this phase-field model with different aggregate contents. As in the previous models, because of individuality induced by constrained nodes, sides of specimens (50 mm) were considered elastic. The boundary conditions of this sample are depicted in Fig. 4.9.

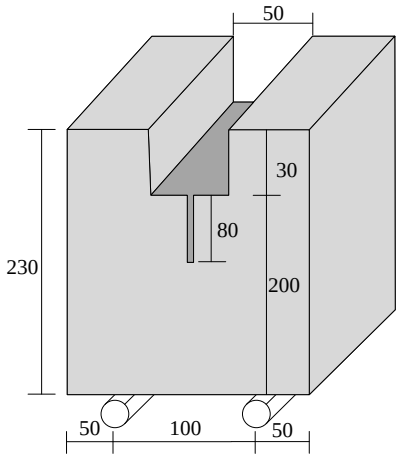

Fig. 4.9. Geometric properties and boundary conditions for concrete specimens

In the tests, the crack mouth opening displacement (CMOD) was recorded by a clip gauge fixing at top centre of preformed notches. A testing machine with the maximum capacity of 2000 kN applied the load at a constant rate of 0.1 mm/min.

In this simulation, the potential energy correction parameter β is shown in Fig. 4.10. The mechanical parameters for phase-field model are detailed in Table 4.2.

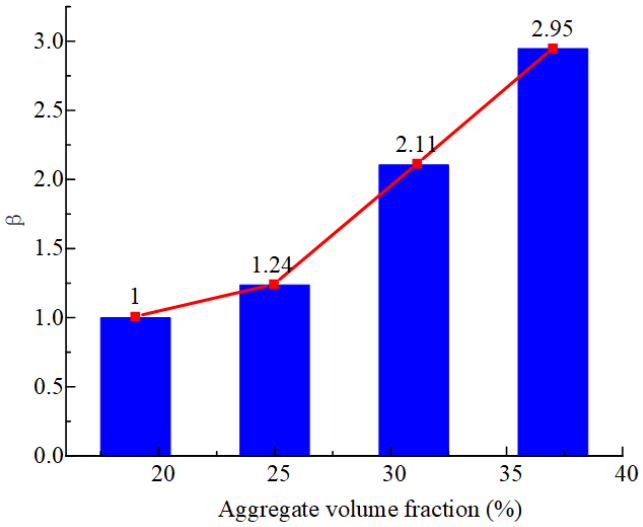

Fig. 4.10. The potential energy correction parameter β for different samples

Table 4.2 Parameters for concrete samples of phase field

Aggregate content (%)	E (GPa)	v	σ_y (MPa)	H (GPa)	l_c (mm)	ψ (MPa)
19	33.23	0.2	3.8	12	1	0.019
25	32.3	0.2	3.59	12	1	0.0235
31	34.01	0.2	4.41	12	1	0.04
37	35.26	0.2	4.85	12	1	0.056

The fracture propagation branches are indicated in Fig. 4.11, whilst the load-CMOD curves comparison between numerical results and experimental data is demonstrated in Fig. 4.12.

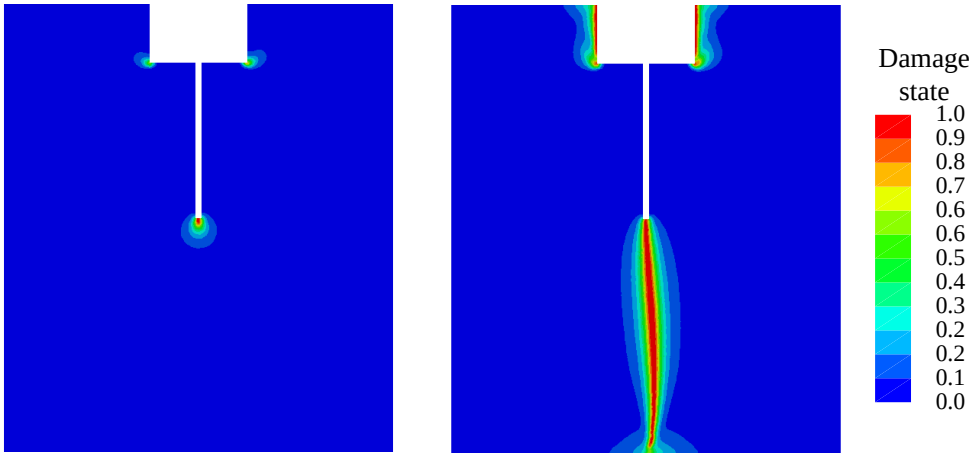

(a) (b)

Fig. 4.11. Crack propagation of concrete specimens: (a) crack initiation, (b) crack propagation

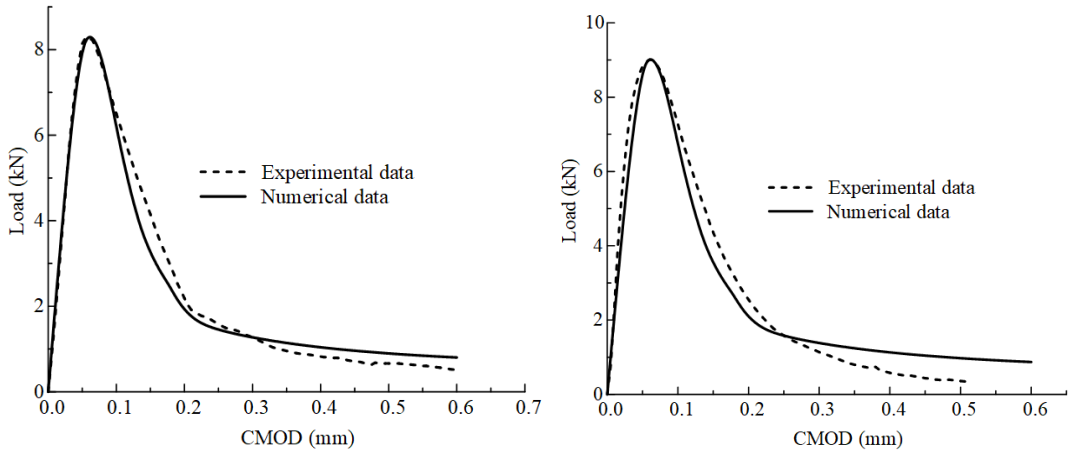

(a)

(b)

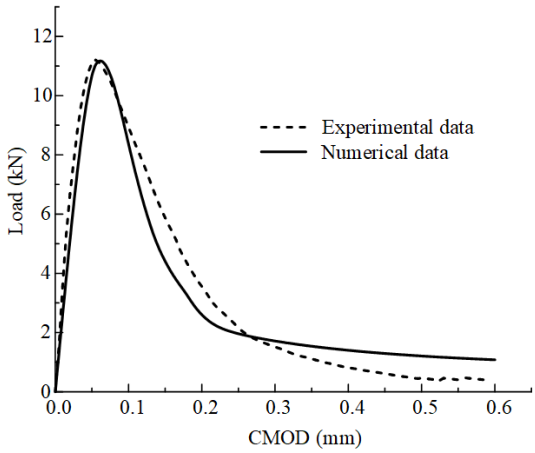

(c)

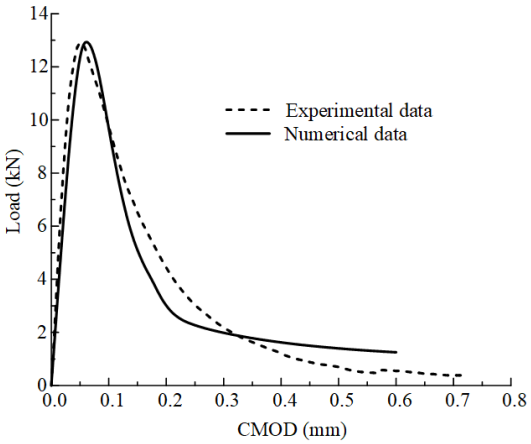

(d)

Fig. 4.12. Comparison of load-CMOD curves of concrete specimens with varying aggregate content: (a) 19%, (b) 25%, (c) 31%, (d) 37%

From Fig. 4.11 it is observed that fracture propagation paths have similar results compared to previous homogenous model. The crack propagation has no branches, will develop along with the mid-span of specimens.

From Fig. 4.12, it can be observed that all simulations align well with the experimental data. However, the load-CMOD curves also exhibit variations, which attributes to influence of spatial distribution of concrete components (mortar, aggregates and ITZ). The mechanical parameters, including elastic modulus and peak load, increase with higher aggregate content, corroborating the theoretical predictions.

4.5 Experimental calibration and calibration of mesoscale model

To verify this proposed modelling, mesoscale model of concrete was utilized to predict fracture evolution with the same experiments of Section 4.4. The crack evolutions were then compared to experimental results.

From Eq. (4.33), it is observed that the energy dissipation is influenced by volume of aggregate, potential energy of mortar and aggregate, with potential energy of aggregate being constant across different types of concrete. Therefore, the potential energy correction parameter β can be adjusted according to the volume of aggregate and potential energy of mortar.

4.5.1 Three-point bending test with shallow notch

This modelling was calibrated employing experiments from Burcu et al. (Akcay et al., 2012). Prismatic specimens (500 mm × 100 mm × 100 mm) with varying aggregate volume fractions were cast. The aggregate size ranged from 0 - 12 mm, and volume content of coarse aggregates in the mixtures were 40%, 49%, 58% and 66%. Full details of concrete mix design are available in literature (Akcay et al., 2012). Two aggregate size (diameter) ranges were used: 43% volume fraction of basalt fines (0-4 mm), and 57% volume fraction of crushed basalt (4-12 mm).

In this calibration, the direct algorithm was adopted to generate the mesoscopic model within a domain measuring 500 mm × 100mm. Polyhedral-shaped aggregates were created based on the concrete mix, with two diameter sizes range: 0 - 4 mm and 4 - 12 mm. The fraction ratio of these aggregates was 0.43:0.57.

To obtain the in-plane spatial distribution of different particles, the Monte Carlo method and Fuller distribution were used to determine the centre points, diameters, edges, and angles of polygon,

respectively. The ITZ phase is modelled as a thin layer between aggregates and cement matrix, typically with a thickness ranging from 10 to 50 μm (Shuguang et al., 2015). In this case, a thickness of 30 μm was used.

In this simulation, the sides of the specimens are considered elastic owing to the individuality induced by constrained nodes (Moës et al., 2011). The boundary conditions of concrete samples are illustrated in Fig. 4.2. Load is employed in y-direction on top surface, while left support at the bottom surface is controlled in both x-direction and y-direction, and right support is fixed in y-direction. The mesh size varies from h = 3 mm in the elastic part to h = 1 mm in the nonlinear part for all phases (aggregate, ITZ and mortar), as depicted in Fig. 4.13a. Geometric properties of the models with different aggregate content are depicted in Fig. 4.13b. Potential energy correction parameter β is shown in Fig. 4.14, and the geometric properties of all samples were shown in Fig. 4.15. The mechanical properties for this phase-field modelling are listed in Table 4.3.

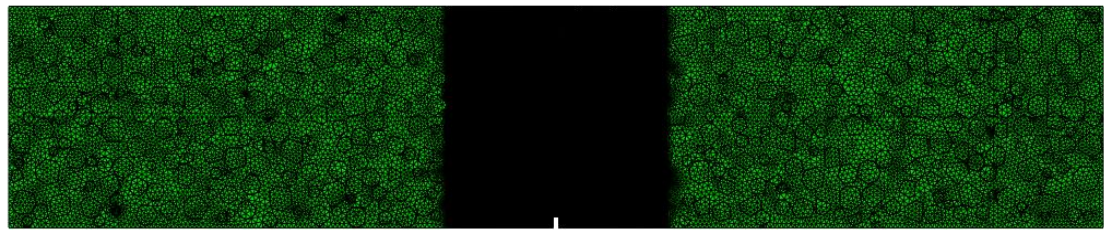

(a)

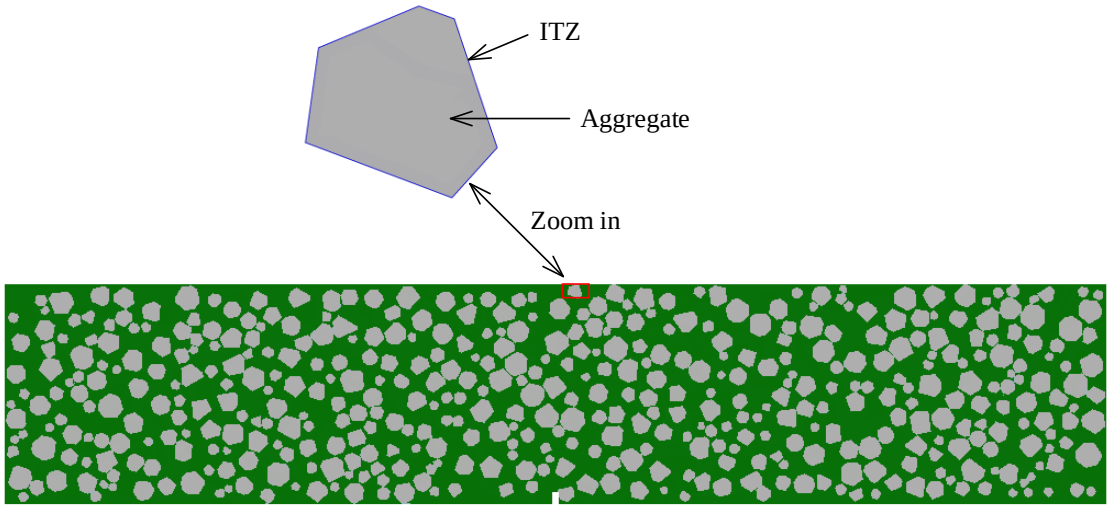

(b)

Fig. 4.13. Properties of concrete sample: (a) mesh conditions, and (b) geometric details of concrete

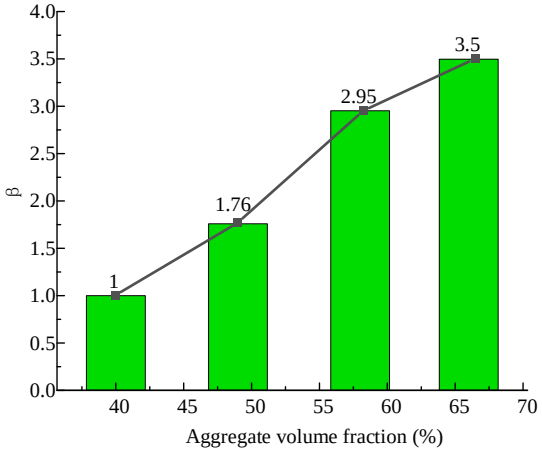

Fig. 4.14. The potential energy correction parameter β for different samples

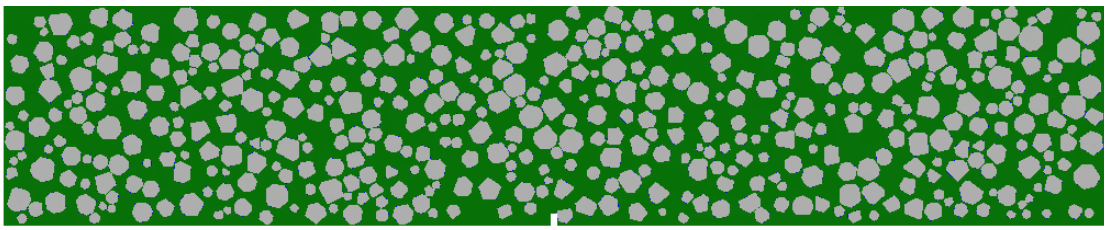

(a)

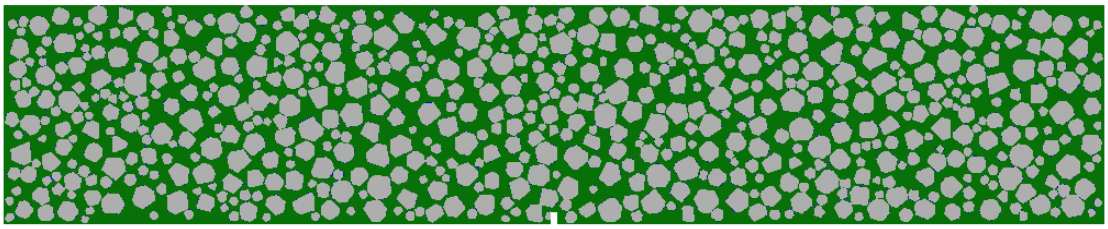

(b)

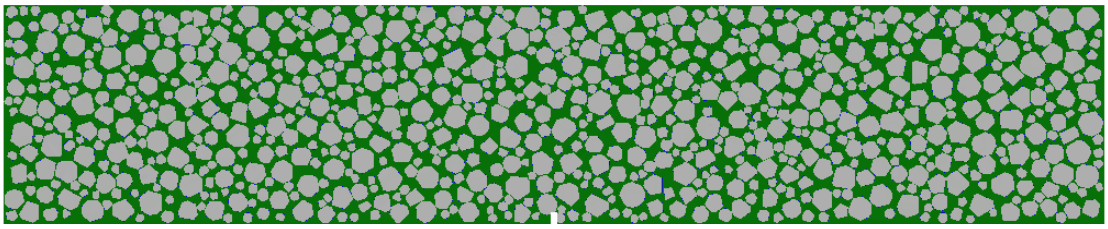

(c)

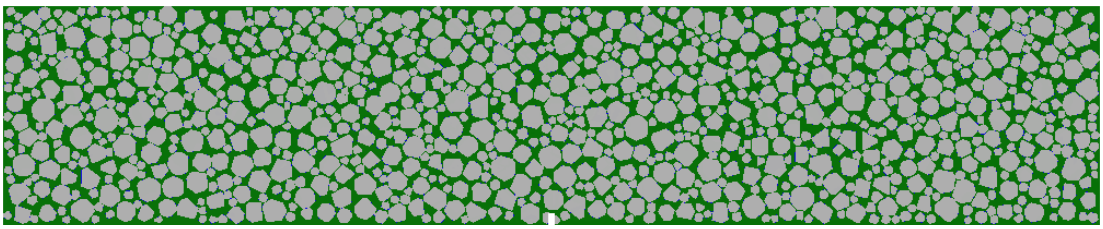

(d)

Fig. 4.15. Geometric properties of concrete specimens with different aggregate volume content: (a) 40%, (b) 49%, (c) 58%, (d) 66%

Table 4.3 Parameters for concrete samples of phase field

	E (GPa)	v	σ_y (MPa)	H (GPa)	l_c (mm)	ψ (MPa)
Aggregate	45	0.2	-	-	-	-
Mortar	28	0.2	6.2	12	1	0.0128
ITZ	14	0.2	3	6	1	0.0064

The fracture evolution branches predicted by this elasto-plastic phase-field modelling is depicted in Fig. 4.16. The comparison of load-deflection results between simulation results and experimental data is presented in Fig. 4.17. A summary of experimental results and simulation results is provided in Fig. 4.18.

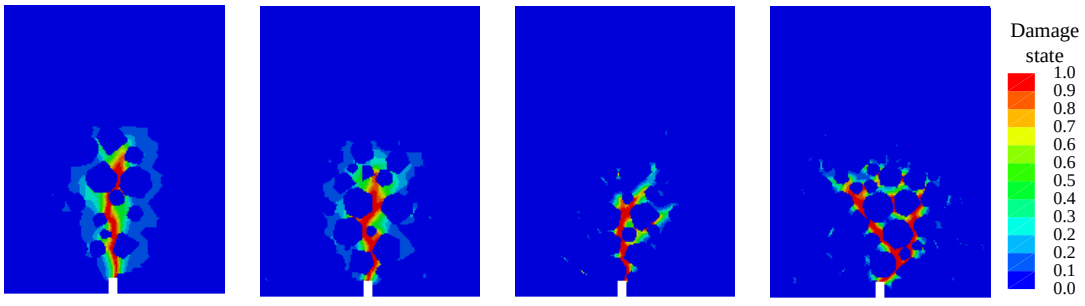

(a) (b) (c) (d)

Fig. 4.16. Crack propagation of concrete specimens with varying aggregate content: (a) 40%, (b) 49%, (c) 58%, (d) 66%

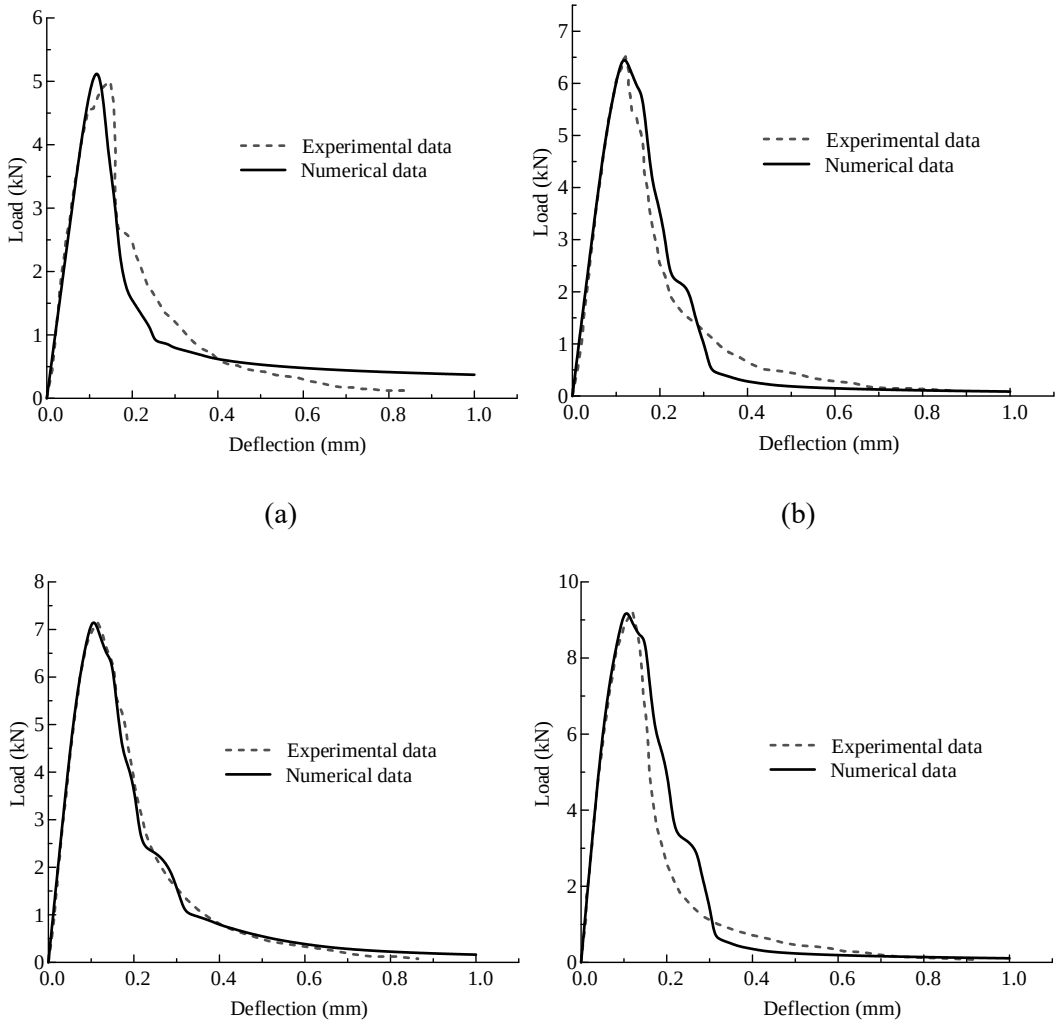

Fig. 4.17. Comparison of load-deflection results of concrete samples with varying aggregate content: (a) 40%, (b) 49%, (c) 58%, (d) 66%

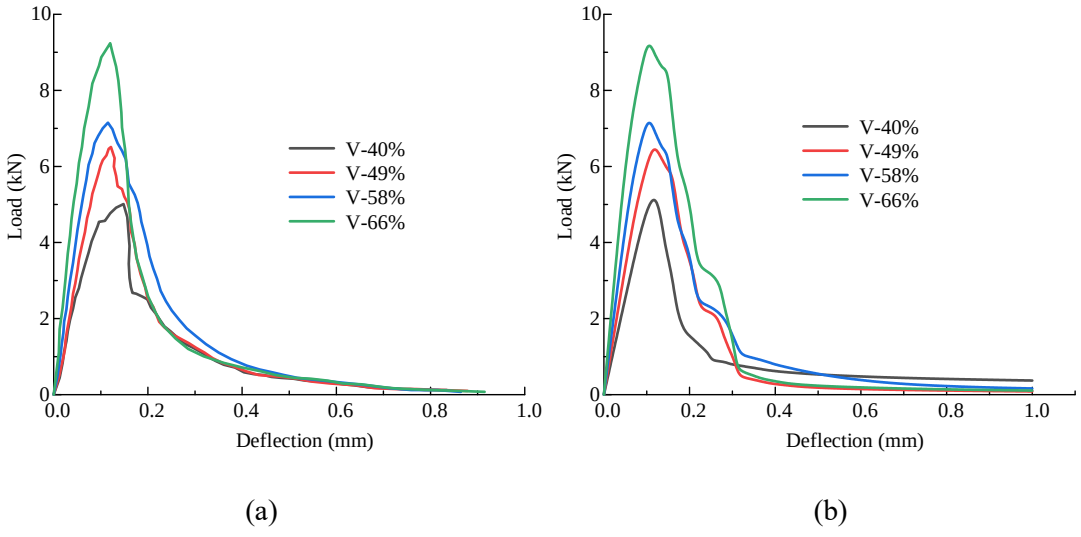

Fig. 4.18. Comparison of load-deflection results of concrete samples: (a) Experimental data, (b) numerical results

From Fig. 4.16, the crack propagation paths for different samples are captured, revealing that a higher aggregate volume fraction leads to more crack branches. This occurs because a higher aggregate volume fraction results in an increased number of ITZ, which are more susceptible to breakage compared to the mortar. Consequently, cracks tend to propagate along the ITZ. In Fig. 4.17, all simulation models demonstrate a strong alignment with experimental data. However, unloading part of the load-deflection curves exhibits different branches, influenced by the distribution of aggregate. As depicted in Fig. 4.18, the elastic properties for concrete increases with aggregate content, and peak load improves with the increasing elastic modulus.

4.5.2 Three-point bending test with deep notch

Further calibration was done on beam specimens with a deep notch, using experimental data from Burcu et al. (Akcay et al., 2012). Prismatic specimens (500 mm × 100 mm × 100 mm) with varying aggregate volume fractions were cast. These had the same aggregate size range, concrete mix design, and aggregate volume fractions as those used in the model with the shallow notch described in Section 4.5.1. For this simulation, the mid-span notch had a depth of 50 mm and a width of 2.5 mm. The same mesoscopic model was employed, hence, the geometric properties (aggregate, ITZ and mortar) of the sample remained consistent so as to assess the effect of different notch configurations. The boundary conditions of concrete are depicted in Fig. 4.6, mesh details, geometric properties of meso-model are described in Fig. 4.19 and the mechanical parameters is shown in Table 4.3.

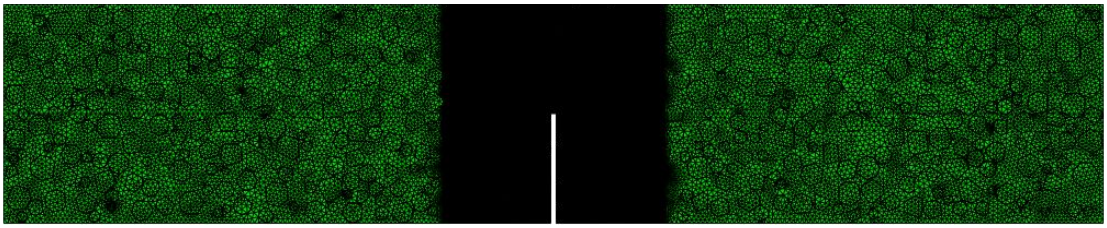

(b)

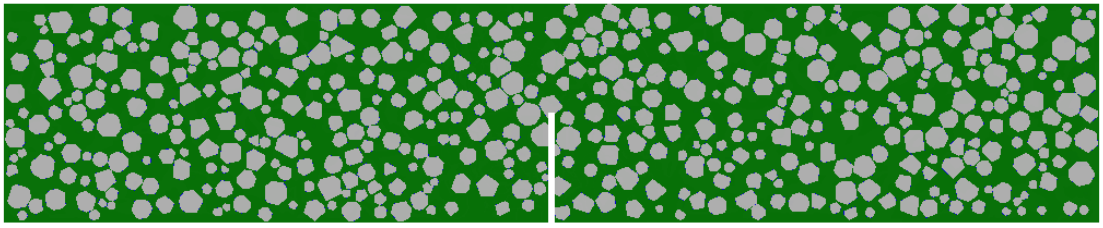

(c)

Fig. 4.19. Properties of concrete sample: (a) mesh conditions, and (b) geometric details of concrete

The fracture evolution is shown in Fig. 4.20. Additionally, Fig. 4.21 presents the comparison of load-deflection results between simulation results and experimental results. A summary of numerical and experimental results is provided in Fig. 4.22.

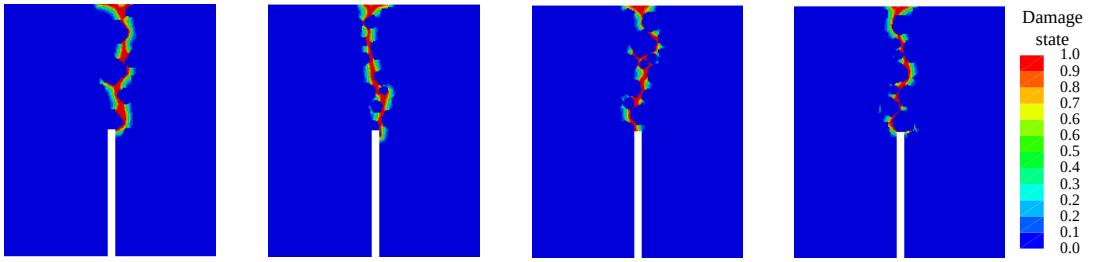

(a) (b) (c) (d)

Fig. 4.20. Crack propagation of specimens with varying aggregate content: (a) 40%, (b) 49%, (c) 58%, (d) 66%

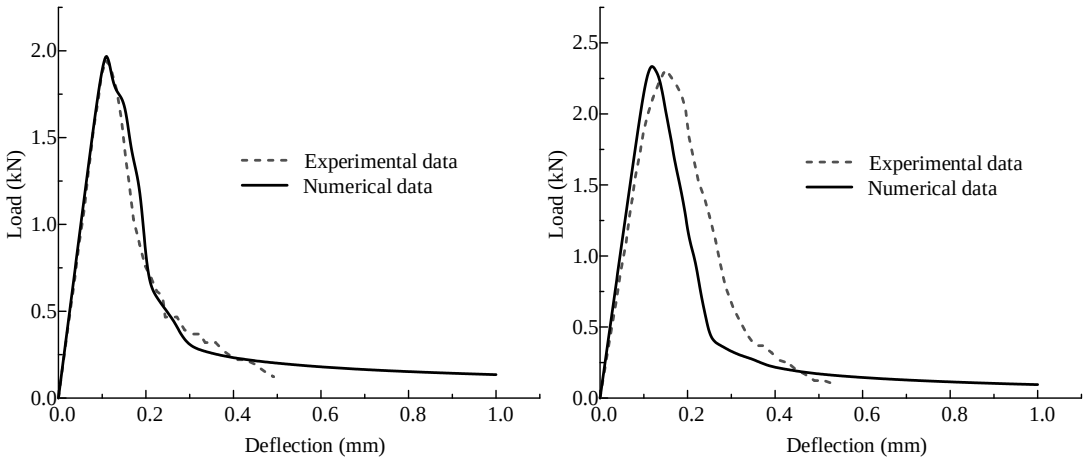

(a) (b)

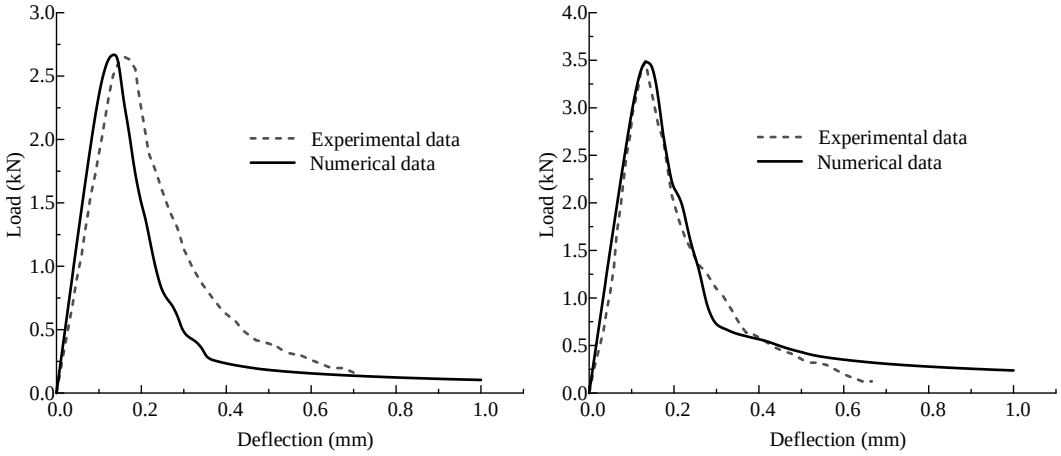

(c) (d)

Fig. 4.21. Comparison of load-deflection results of concrete samples with varying aggregate content: (a) 40%, (b) 49%, (c) 58%, (d) 66%

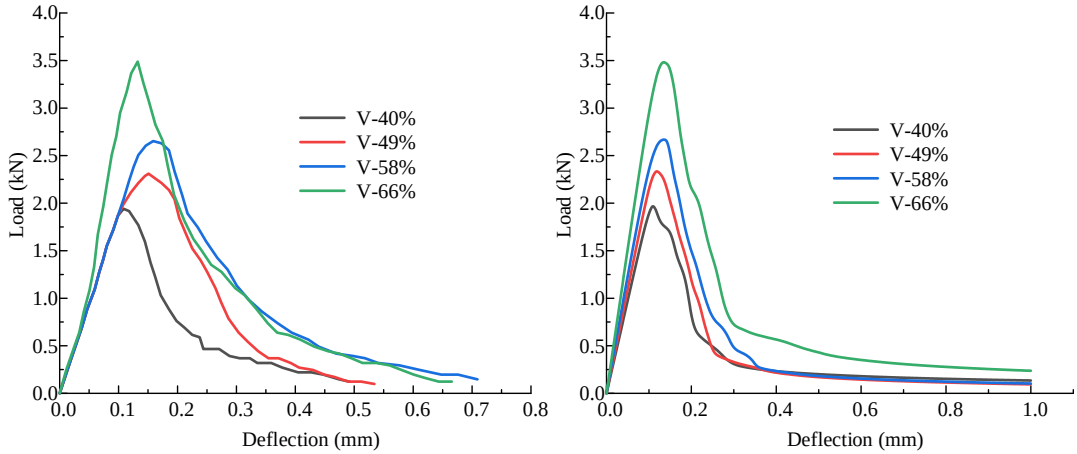

(a) (b)

Fig. 4.22. Comparison of load-deflection results of concrete samples: (a) Experimental data, (b) numerical results

From Fig. 4.20, it is observed that no additional fracture branches developed in any of the specimens. This is because the deep notch promoted single crack initiation and propagation paths. The slight variation in fracture propagation branches may attributes to the initial crack location and the distribution of aggregate and ITZ.

Fig. 4.21 shows that simulations for 40% and 66% (aggregate content) closely match the experimental data, whereas simulations for 49% and 58% display discrepancies. These differences may be due to insufficient experimental control and material variabilities. As depicted in Fig. 4.22a, the load-displacement results from experiments reveal that the elastic modulus did not increase with aggregate content, as expected numerically. Theoretically, both the elastic modulus and peak loads are expected to increase with higher aggregate volume content, as shown in Fig. 4.22b.

4.5.3 Wedge splitting test

This modelling was further verified utilizing experiments from research (Chen and Feng, 2022). Prismatic specimens with dimensions 230 mm × 200 mm × 200 mm were cast with varying aggregate volume fractions. The aggregate size ranged from 2.5 to 9.6 mm, and aggregate volume content were 19%, 25%, 31% and 37%. Full details of the concrete mixture and particle distributions are available in (Chen and Feng, 2022).

Two aggregate sizes (diameters) were used: 12% fine aggregates with diameters ranging from 2.5 to 4.8 mm, and 88% coarse aggregates with diameters ranging from 4.8 to 9.6 mm. The wedge splitting test specimens were cast with a predefined initial notch of 80 mm depth and 3 mm width. As in previous models, because of individuality induced by constrained nodes, the sides of specimens were considered elastic, as shown in Fig. 4.9, with similar meshing, as shown in Fig. 4.23a. Similarly, the direct algorithm was employed to generate the mesoscopic model within a domain measuring 230 mm × 200mm. Polyhedral-shaped aggregates were generated based on the concrete mix, with two diameter sizes ranges: 2.5 - 4.8 mm and 4.8 - 9.6 mm, matching volume fractions of 0.12 and 0.88, respectively.

To obtain the in-plane spatial location of various particles within a section measuring 230 mm × 200mm, the same methodology used previously was employed to generate the geometric properties of different phases (aggregate, ITZ and mortar). The resulting geometric properties of models, reflecting different aggregate volume fraction, are depicted in Fig. 4.23b.

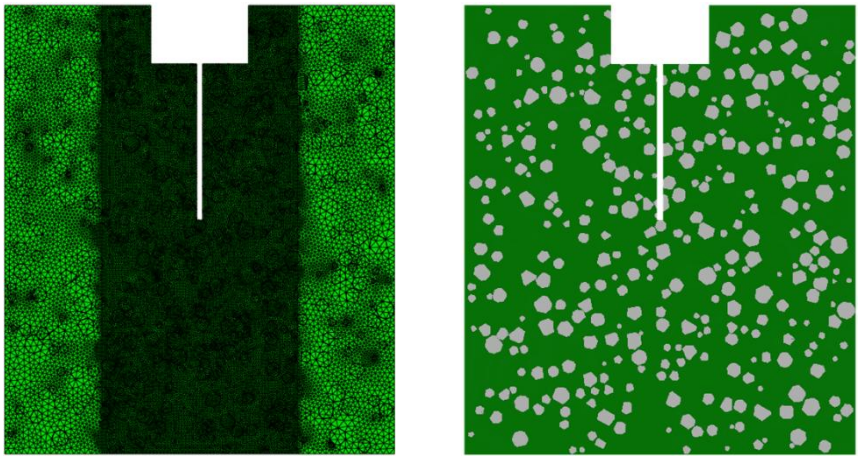

(a) (b)

Fig. 4.23. Properties of concrete sample: (a) mesh conditions, and (b) geometric details of concrete

In the experiments, the crack mouth opening displacement (CMOD) was recorded by a clip gauge fixing at top centre of preformed notches. A testing machine with a maximum capacity of 2000 kN, applied the load with a constant rate of 0.1 mm/min

In this simulation, the potential energy correction parameter β is shown in Fig. 4.24, while geometric parameters of all samples are presented in Fig. 4.25. The mechanical properties for phase-field model are detailed in Table 4.4.

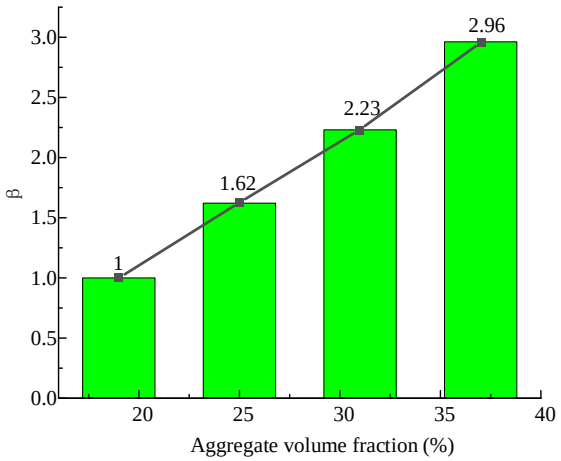

Fig. 4.24. The potential energy correction parameter β for different samples

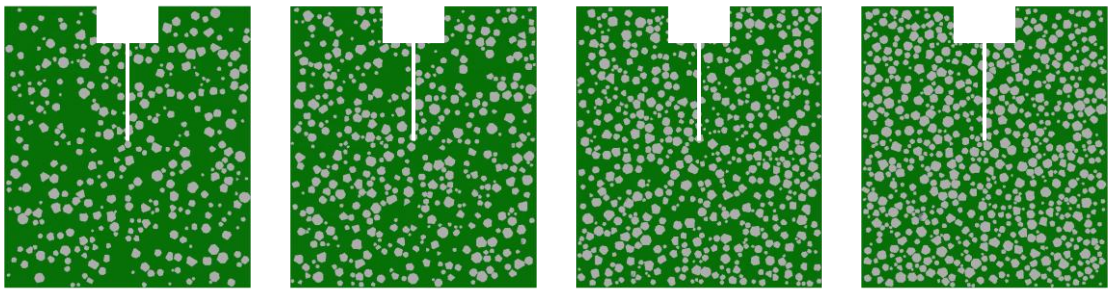

(a) (b) (c) (d)

Fig. 4.25. Geometric properties of concrete specimens with varying aggregate content: (a) 19%, (b) 25%, (c) 31%, (d) 37%

Table 4.4 Parameters for concrete samples of phase field

	E (GPa)	v	σ_y (MPa)	H (GPa)	l_c (mm)	ψ (MPa)
Aggregate	37	0.2	-	-	-	-
Mortar	30	0.2	4.2	12	1	0.0254
ITZ	15	0.2	4.2	6	1	0.0127

The fracture propagation branches are depicted in Fig. 4.26, whilst the load-CMOD curves comparison between numerical results and experimental data is given in Fig. 4.27.

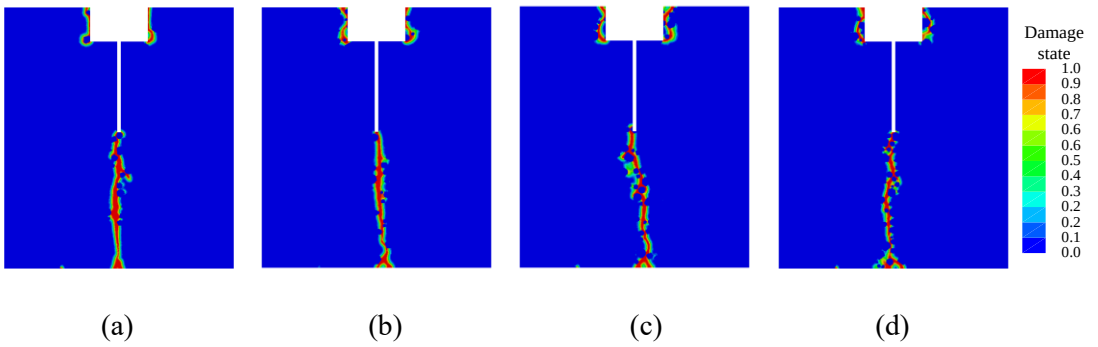

Fig. 4.26. Crack propagation of specimens with varying aggregate content: (a) 19%, (b) 25%, (c) 31%, (d) 37%

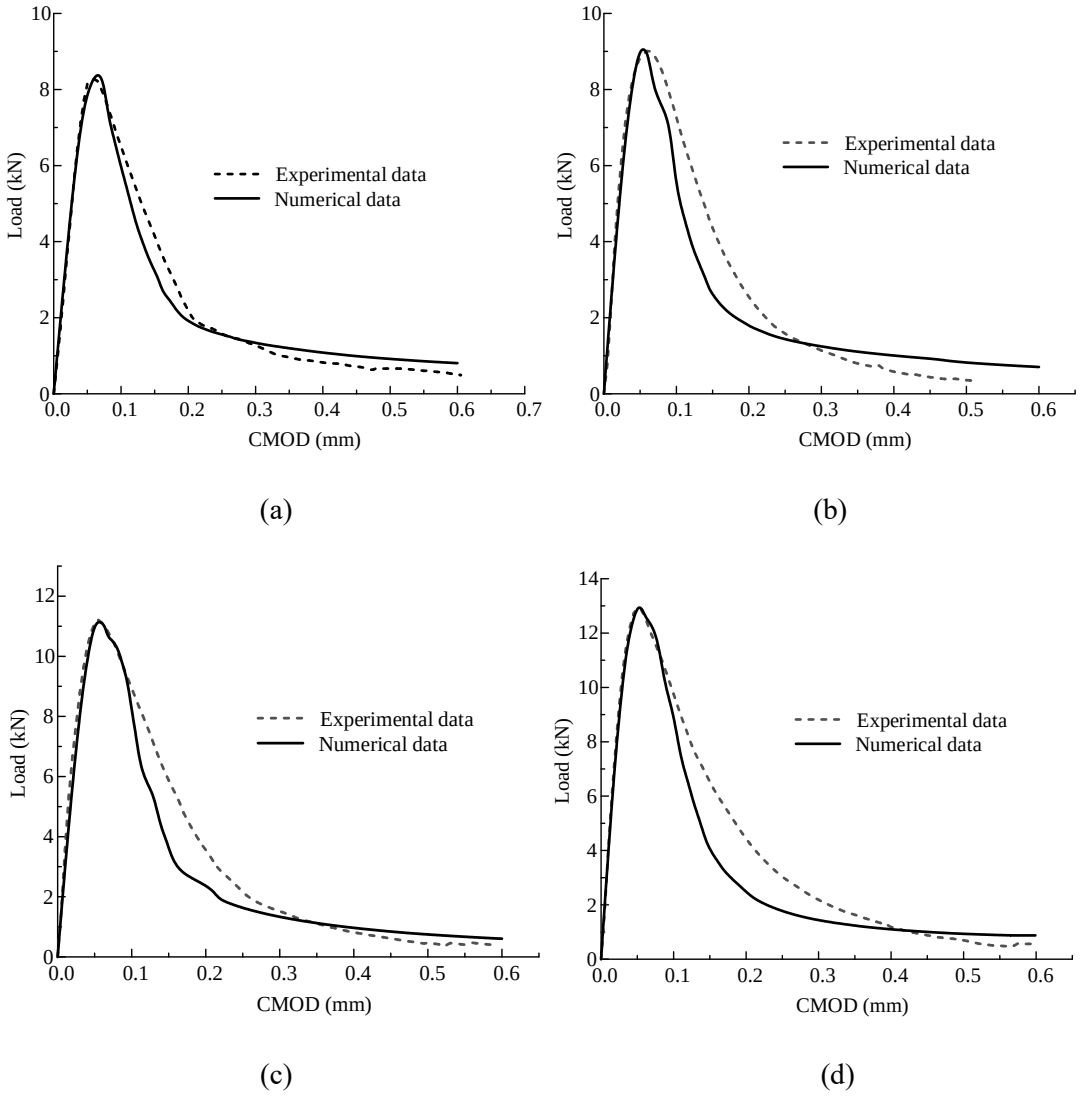

Fig. 4.27. Comparison of load-CMOD curves of concrete specimens with varying aggregate content: (a) 19%, (b) 25%, (c) 31%, (d) 37%

From Fig. 4.26 it is observed that fracture propagation paths vary slightly for different samples. It is observed that no additional crack branches appear for any of specimens. This property is attributed to the lower aggregate content and deep notch, which lead to fewer ITZ and reduced crack initiation. Consequently, the crack path evolves predominantly as a single crack, resulting in fewer branches within the concrete. Nonetheless, the distribution of aggregates and ITZ still influences the crack propagation pattern.

From Fig. 4.27, it can be observed that all simulations align well with the experimental data. However, the load-CMOD curves also exhibit variations, which can be attributed to differences in the spatial location of ITZ and aggregates. The mechanical parameters, including elastic properties and peak load, increase with higher aggregate content, corroborating the theoretical predictions.

4.6 Conclusions

Based on the Chapter 3, the multi-phase elasto-plastic phase-field model is expended by proposing the energy dissipation function within concrete is proposed to predict mechanical response and crack propagation for different concrete components. To address the complex non-linear compressive-tensile behaviour of cementitious materials, the model utilizes spectral decomposition and Drucker-Prager yield criteria. This approach allows for the degradation of stresses, capturing the asymmetric performance. The model's effectiveness is calibrated through numerical analyses of elements made of concrete with different content of aggregate phase, and compared against experimental results from three-point bending and wedge splitting tests. The key conclusions are summarized below:

(1) The phase-field model can provide a detailed representation of fracture propagation within concrete composites from the mesoscopic modelling. The modelling results align with experimental data from the literature, confirming the reliability of the proposed model.
(2) The introduced energy dissipation and the potential energy correction parameters can effectively characterise the damage response of concrete components. The mesoscale results accurately replicate crack development, with the load-deflection and load-CMOD curve comparisons confirming the numerical model's ability to match experimental observations.
(3) The proposed framework successfully captures the load-deflection and load-CMOD curves for homogeneous models. However, the simulation results display a sharp slope after crack propagation, as no more crack branching occurs in the homogeneous model.
(4) The potential energy correction parameter can capture the influence of both volume content for aggregates and potential energy for mortar phase. An increase in the potential energy of mortar phase and aggregate content induce a higher potential energy correction parameter, which can describe the increase in elastic modulus and peak load.

(5) Crack propagation is influenced by the notch depth and aggregate volume content. Shallow notches lead to more crack branches, particularly with increased aggregate content, due to a higher number of ITZ branches and uncertainties in crack initiation. Conversely, deep notches result in fewer crack branches, as they facilitate a more controlled crack propagation path.

Integrating the proposed methodology into a mix design of concrete will allow for more accurate predictions of the mechanical behaviour under load. However, it should also be noted that the mechanical properties of different phases have to be the same when the mix design is changed. In addition, tremendous elements will be generated when this method is employed to structures, the size effect and homogenous methods are necessary to be considered.

Chapter 5: A Multi-scale Poro-elasto-plastic Model for Concrete Damage and Failure Behaviour

Abstract

The complex nature of cementitious materials microstructures poses significant challenges in understanding their failure mechanisms and predicting crack generation and propagation within the different components, including mortar, aggregates, pores and interfacial transition. This paper introduces a phase-field model considering elasto-plastic performance to simulate crack propagation for concrete using a micro-meso model. Random packing and Voronoi tessellation are employed to determine the geometric properties of these four essential components. To avoid discontinuities in concrete, the Mori-Tanaka scheme and energy dissipation theory are utilized to calculate mechanical parameters for pore structure. To calibrate and calibrate this model, various specimens are subjected to compressive and three-point bending tests. By evaluating numerical predictions against experimental observations, it indicates that this proposed methodology effectively captures crack propagation in concrete. Furthermore, the modelling can be extended to include the effects of shrinkage by combining mechanical and shrinkage strains, making it a powerful tool to predict crack opening and evolution. Accurately predicting crack initiation can enhance the understanding of long-term structural performance and contribute to making structures more durable, resilient and sustainable.

Keywords: Porous material, Voronoi diagram, Elasto-plastic phase-field model, Micro-Meso model, Mesoscale parameter investigation

5.1 Introduction

Concrete is the most commonly utilized material in the construction of engineered buildings (Chen and Feng, 2022), due to its low cost, mouldability and durability. However, as a multiphase agglomerate, its complex microstructures significantly influence its mechanical performance, such as stress, toughness, and crack propagation. These properties, in turn, affect its overall structural performance, including permeability, durability (shrinkage and creep), and sustainability (Han et al., 2023). Hence, understanding the mechanical behaviour and degradation mechanisms for concrete at micro scale can offer valuable understandings for its long-term mechanical performance and facilitate innovative material designs. The mechanical properties, fracture toughness for concrete are heavily dependent on

properties and distribution of its multi-phase components, including aggregate, interfacial transition zone (ITZ), mortar, and pores (Han et al., 2023). These properties influence the opening and evolution of cracks within each constituent phase at the microstructural scale (Jia et al., 2022). The mechanical interactions among these phases, coupled with the evolution of damage, lead to the development of a non-linear mechanical process. Therefore, a multi-scale framework for predicting mechanical performance, which accounts for the influence of these phases, is essential to analyse mechanical behaviour of concrete.

To understand how varying phases affect mechanical performance and crack propagation, a multiscale model of concrete is essential for analysing its failure mechanisms. To construct micro models and obtain the mechanical properties of different phases, concurrent and hierarchical algorithms are commonly employed (Matouš et al., 2017). In concurrent algorithms, regions at various scales within concrete construction are characterized through simultaneous calculations utilizing the coupling methods, including the mesh fragmentation method (Rodrigues et al., 2018), significantly enhancing accuracy for mechanical properties (Rodrigues et al., 2021). However, this method often requires a large number of elements due to the varying scales of different phases, such as mortar (mm), aggregate (mm), ITZ (μm) and pores (nm) (Aldakheel and Mechanics, 2020). Consequently, this method is both computational consumption and time-costing. In contrast, the hierarchical approach first determine mechanical properties for different scales, and then transform the properties of micro model to a homogenization model between scales (Yu et al., 2023). This approach captures effective mechanicl properties for mesoscopic and macroscopic scales by employing microscopic governing functions on the Representative Volume Element (RVE) (Geers et al., 2010).

Several analytical methods have been developed to calculate the mechanical parameters for cementitious materials with the RVE model, such as generalized self-consistent scheme (GSCS), Mori-Tanaka (MT) scheme, and ensemble-volume average method (EVA). The EVA method incorporates the influence of different inclusions at mesoscale, including mortar, aggregates and ITZ, to study the mechanical impacts of mesoscale components of concrete (Ju and Chen, 1994, Zhang et al., 2017). However, identical shapes for all inclusions are assumed in this method. The GSCS is used to calculate the internal mechanical properties of concrete phases (Hashin et al., 2002), such as the representative modulus for concrete with recycled aggregate, considering the influence of new-generated ITZ (Dhar et al., 2018). However, because mortar is treated as a porous composite with various phases, this GSCS model tends to overvalue the influence of pore phase on mechanism performance (Zhang et al., 2018a). In contrast, the MT scheme (Mori and Tanaka, 1973) can embed inclusions within the matrix part by using a homogenization model for two-scale problem to determine effective mechanical properties for this two-scale domain (Sorelli et al., 2008). Therefore, MT method is appropriate to obtain concrete's mechanical parameters for a multiscale model.

To describe concrete's mechanical deformation under load until failure, an appropriate numerical approach and constitutive model are essential. In numerical modelling to capture fracture evolution, smeared approaches are commonly employed, corresponding to the finite element method (FEM). This smeared method necessitates prior understanding of mesh enrichment functions, along with extrinsic opening and evolution to accurately capture geometric properties of crack (Zhang et al., 2018b, Zhang and Mang, 2020, Zeng et al., 2019, Zhang et al., 2021, Zhang et al., 2020). Methods including element tracking methods (Zhang et al., 2018b, Zhang and Mang, 2020, Zeng et al., 2019, Zhang et al., 2021, Zhang et al., 2020) and particle cracking methods (Rabczuk and Belytschko, 2004, Rabczuk et al., 2010) show promise in efficiently handling embedded strong discontinuities. Smeared approaches, derived from continuum damage theory, model cracks as diffused damage regions evolving from an unbroken condition to fully damage state. These approaches are commonly effective in simulating damage evolution with a diffusive geometry comparing to sharp crack (Wriggers et al., 2006, Markou et al., 2013, Pulatsu et al., 2019, Huang et al., 2016b, Liu et al., 2019, Kim et al., 2011). An parameter of fracture width (length scale parameter) is proposed to normalise the non-local micro crack influence, through either integral (Pijaudier-Cabot and Bažant, 1987, Zhang et al., 2019) or gradient enhancement (Peerlings et al., 1996, Simone et al., 2004, Nguyen et al., 2018).

In line with the FEM, a muti-phase phase-field model considering elasto-plastic behaviour is employed to predict degradation mechanisms and crack propagation in concrete. This model introduces four phases: mortar, aggregate, ITZ and pores. To address the isotropic nature of concrete and predict identical tensile and compressive fracture behaviour (Alessi et al., 2018, Choo et al., 2018, Pise et al., 2019, Späth et al., 2021, Jiang et al., 2023, Molnár et al., 2020), spectral decomposition method is employed to decompose stored elastic energy into tensile fracture energy and compressive fracture energy (Miehe et al., 2010b). Additionally, the Drucker-Prager type plastic criterion is implemented to capture the plastic fracture responses of concrete (Drucker and Prager, 1952).

This paper presents a micro-meso model for concrete developed to analyse its fracture evolution behaviour when treated as composite with multiphase composition. A phase-field model employing elasto-plastic theory is introduced to address cracks for concrete subjected to both tensile and compressive behaviour. Two different continuous, as well as stepwise linear approximation degradation functions are employed to model the asymmetric tension and compression behaviour of mortar and concrete.

The proposed model is employed in ABAQUS using the subroutine of user defined element (UEL), with several simulation tests employed for calibration. This phase-field mesoscale modelling is utilized to simulate mortar and concrete samples for compressive test and three-point bending test, successfully calibrating the elasto-plastic multi-phase phase-field model against experimental results. Through this modelling approach, the effects of various features for mesoscopic fracture propagation and concrete's

degradation mechanisms are further predicted. Due to its enhanced predictive capabilities, the derived modelling will be utilized to investigate multi-phase coupled systems, including thermo-hygral, hygro-mechanical, and thermo-hygro-mechanical problems. Integrating the proposed methodology into existing mechanical frameworks will increase the accuracy of predicting the material's mechanical response, including shrinkage, creep and crack development effects. This, in turn, will enhance the reliability of long-term behaviour assessments, as well as facilitate the design for more durable concrete structures.

5.2 Homogenization methodology

The MT scheme is commonly utilized to determine elastic properties of concrete with varying scales. In this research, this scheme is employed to decompose pores representative elastic parameters and subsequently obtain elastic modulus for different components.

The MT scheme is commonly utilized to determine representative mechanical parameters for individual phases in concrete scale, mortar scale and cement paste scale. In the method, elastic properties are calculated by employing average stress and Eshelby's equivalent theory (Mori and Tanaka, 1973). The effective elastic modulus for isotropic materials can be calculated based on the elastic properties and the volume fractions of different components utilizing the Eshelby solution to embed the inclusion phase in a matrix phase. Therefore, MT method is appropriate for the non-dilute distribution of inclusion in cementitious materials. Further descriptions on MT scheme are available in research (Zaoui, 2002, Gao et al., 2017). The effective mechanical properties of the composite, such as bulk modulus K_{homo}, as well as shear modulus G_{homo}, can be described as:

$$K_{\mathrm{homo}} = \frac{\sum_{i=1}^{N} f_i K_i \left[1+\alpha\left(K_i / K_M - 1\right)\right]^{-1}}{\sum_{i=1}^{N} f_i \left[1+\alpha\left(K_i / K_M - 1\right)\right]^{-1}} \tag{5.1}$$

$$G_{\mathrm{homo}} = \frac{\sum_{i=1}^{N} f_i G_i \left[1+\alpha\left(G_i / G_M - 1\right)\right]^{-1}}{\sum_{i=1}^{N} f_i \left[1+\alpha\left(G_i / G_M - 1\right)\right]^{-1}} \tag{5.2}$$

where, f_i represents fraction for the i^{th} inclusion components, K_i represents bulk modulus for the i^{th} inclusion components, K_M represents bulk modulus for matrix parts, G_i represents shear modulus for the i^{th} inclusion parts, G_M represents shear modulus for matrix parts. α and β are derived from the Eshelby tensor and are shown as:

$$\alpha_i = \frac{3K_i}{3K_i + 4G_i}, \quad \beta_i = \frac{6\left(K_i + 2G_i\right)}{5\left(3K_i + 4G_i\right)} \tag{5.3}$$

At the cement paste scale, C-S-H is considered as the matrix phase, including the capillary pores and CL. Therefore, the mechanical parameters of hardened cement solid can be determined by:

$$K_{paste} = \frac{f_{CSH}K_{CSH} + \dfrac{f_{CL}K_{CL}}{1+\alpha_{CSH}\left(K_{CL}/K_{CSH}-1\right)} + \dfrac{f_{pore}K_{pore}}{1+\alpha_{CSH}\left(K_{pore}/K_{CSH}-1\right)}}{f_{CSH} + \dfrac{f_{CL}}{1+\alpha_{CSH}\left(K_{CL}/K_{CSH}-1\right)} + \dfrac{f_{pore}}{1+\alpha_{CSH}\left(K_{pore}/K_{CSH}-1\right)}} \tag{5.4}$$

$$G_{paste} = \frac{f_{CSH}G_{CSH} + \dfrac{f_{CL}G_{CL}}{1+\alpha_{CSH}\left(G_{CL}/G_{CSH}-1\right)} + \dfrac{f_{pore}G_{pore}}{1+\alpha_{CSH}\left(G_{pore}/G_{CSH}-1\right)}}{f_{CSH} + \dfrac{f_{CL}}{1+\alpha_{CSH}\left(G_{CL}/G_{CSH}-1\right)} + \dfrac{f_{pore}}{1+\alpha_{CSH}\left(G_{pore}/G_{CSH}-1\right)}} \tag{5.5}$$

At the mortar phase, the cement solid is regarded as matrix to contain fine aggregate and ITZ around fine aggregate. Therefore, the mechanical parameters of the mortar can be obatined by:

$$K_{mortar} = \frac{f_{paste}K_{paste} + \dfrac{f_{sand}K_{sand}}{1+\alpha_{paste}\left(K_{sand}/K_{paste}-1\right)} + \dfrac{f_{ITZ}K_{ITZ}}{1+\alpha_{paste}\left(K_{ITZ}/K_{paste}-1\right)}}{f_{paste} + \dfrac{f_{sand}}{1+\alpha_{paste}\left(K_{sand}/K_{paste}-1\right)} + \dfrac{f_{ITZ}}{1+\alpha_{paste}\left(K_{ITZ}/K_{paste}-1\right)}} \tag{5.5}$$

$$G_{mortar} = \frac{f_{paste}G_{paste} + \dfrac{f_{sand}G_{sand}}{1+\alpha_{paste}\left(G_{sand}/G_{paste}-1\right)} + \dfrac{f_{ITZ}G_{ITZ}}{1+\alpha_{paste}\left(G_{ITZ}/G_{paste}-1\right)}}{f_{paste} + \dfrac{f_{sand}}{1+\alpha_{paste}\left(G_{sand}/G_{paste}-1\right)} + \dfrac{f_{ITZ}}{1+\alpha_{paste}\left(G_{ITZ}/G_{paste}-1\right)}} \tag{5.6}$$

To decompose the elastic parameters for pore phase, representative elastic parameters of pores can be obtained by combining Eq. (5.4) and (5.5) as:

$$K_{pore}=\frac{\left[K_{paste}\bar{f}_{paste}-f_{CSH}K_{CSH}+\dfrac{f_{CL}K_{CL}}{1+\alpha_{CSH}\left(K_{CL}/K_{CSH}-1\right)}\right]\left(1+\alpha_{CSH}\left(K_{pore}/K_{CSH}-1\right)\right)}{f_{pore}}$$
$$\bar{f}_{paste}=f_{CSH}+\frac{f_{CL}}{1+\alpha_{CSH}\left(K_{CL}/K_{CSH}-1\right)}+\frac{f_{pore}}{1+\alpha_{CSH}\left(K_{pore}/K_{CSH}-1\right)} \tag{5.7}$$

$$G_{pore}=\frac{\left[G_{paste}\bar{f}_{paste}-f_{CSH}G_{CSH}+\dfrac{f_{CL}G_{CL}}{1+\alpha_{CSH}\left(G_{CL}/G_{CSH}-1\right)}\right]\left(1+\alpha_{CSH}\left(G_{pore}/G_{CSH}-1\right)\right)}{f_{pore}}$$
$$\bar{f}_{paste}=f_{CSH}+\frac{f_{CL}}{1+\alpha_{CSH}\left(G_{CL}/G_{CSH}-1\right)}+\frac{f_{pore}}{1+\alpha_{CSH}\left(G_{pore}/G_{CSH}-1\right)} \tag{5.8}$$

where K_{paste} and G_{paste} are bulk and shear modulus for the paste solid, which can be obtained by decomposing matrix part from mortar level based on Eq. (5.5) and (5.6).

However, the decomposing process involves numerous calculations. Additionally, the sand phase and ITZ around the sand introduce a large number of elements into the numerical modelling. To simplify geometric properties and the computation of elastic properties, mortar is treated as a pore phase (inclusion) embedded in a solid phase (matrix), which includes cement paste, sand, and ITZ. Therefore, bulk and shear modulus for hardened cement solid can be determined as follows:

$$K_{mortar}=\frac{f_{solid}K_{solid}+\dfrac{f_{pore}K_{pore}}{1+\alpha_{solid}\left(K_{pore}/K_{solid}-1\right)}}{f_{solid}+\dfrac{f_{pore}}{1+\alpha_{solid}\left(K_{pore}/K_{solid}-1\right)}} \tag{5.9}$$

$$G_{mortar}=\frac{f_{solid}G_{solid}+\dfrac{f_{pore}G_{pore}}{1+\alpha_{solid}\left(G_{pore}/G_{solid}-1\right)}}{f_{solid}+\dfrac{f_{pore}}{1+\alpha_{solid}\left(G_{pore}/G_{solid}-1\right)}} \tag{5.10}$$

5.3 Geometric properties of mesoscale modelling

To represent geometric properties for concrete modelling, combining mesoscale and microscale models, four phases including aggregate, ITZ, mortar, and pores, are generated. The following subsections outline the parameters required to define the geometry of all concrete constituents and detail the methodology used to develop the mesoscale model.

5.3.1 Distribution and shapes of aggregate

In this modelling, concrete mixture from Chapter 3 is adopted. Portland cement type CEM II 32.5R (335kg/m3) was used, and the water/cement ratio is 0.55 with a superplasticizer of 2 lt/m^3. Two size (diameter) ranges of river gravel were utilized, 5-10mm at 491kg/m^3, and 10-14mm at 532kg/m^3. River round sand was used as fine aggregate at 847kg/m^3.

The Monte Carlo method is employed for determining geometric properties for each aggregate and generate their in-plane spatial distribution (Rajamani et al., 1986, Huang et al., 2022). This method ensures that individual aggregates do not overlap and that each aggregate is located within the boundaries of the specimen. To generate the polygonal aggregates, the Fuller distribution is utilized to determine the number of edges and angles of a polygon (α). Details of this method can be found in Chapter 2. A typical two-dimensional random polygon aggregate model for the above mix design is shown in Fig. 5.1.

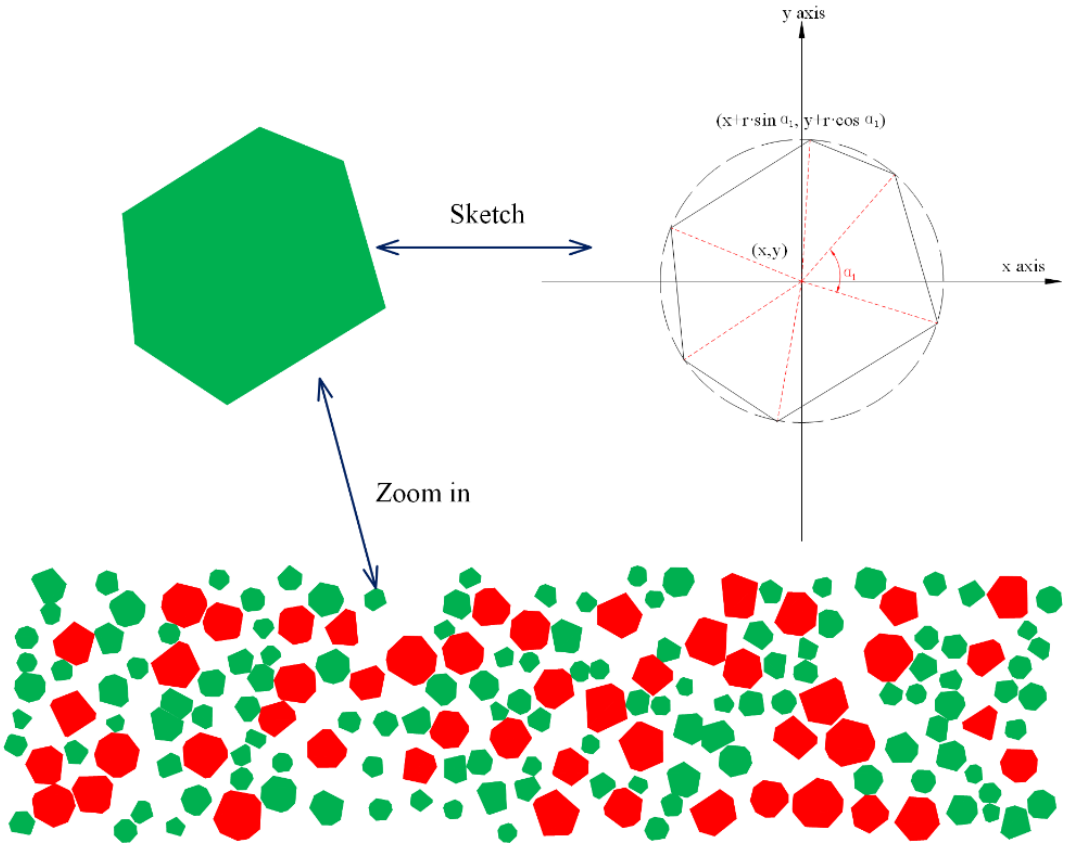

Fig. 5.1. 2-D random distribution of polygonal aggregates

5.3.2 Geometric properties of the ITZ

An important feature for concrete is the ITZ induced by the adding of aggregate. According to previous literature, the ITZ phase is modelled as a bonding layer with a thickness from 10 to 50 μm, along with the aggregates (Shuguang et al., 2015). Therefore, the ITZ is generated based on aggregate's geometric properties with a thickness *"t"* (see Fig. 5.2). In this case, a thickness of 30 μm was used.

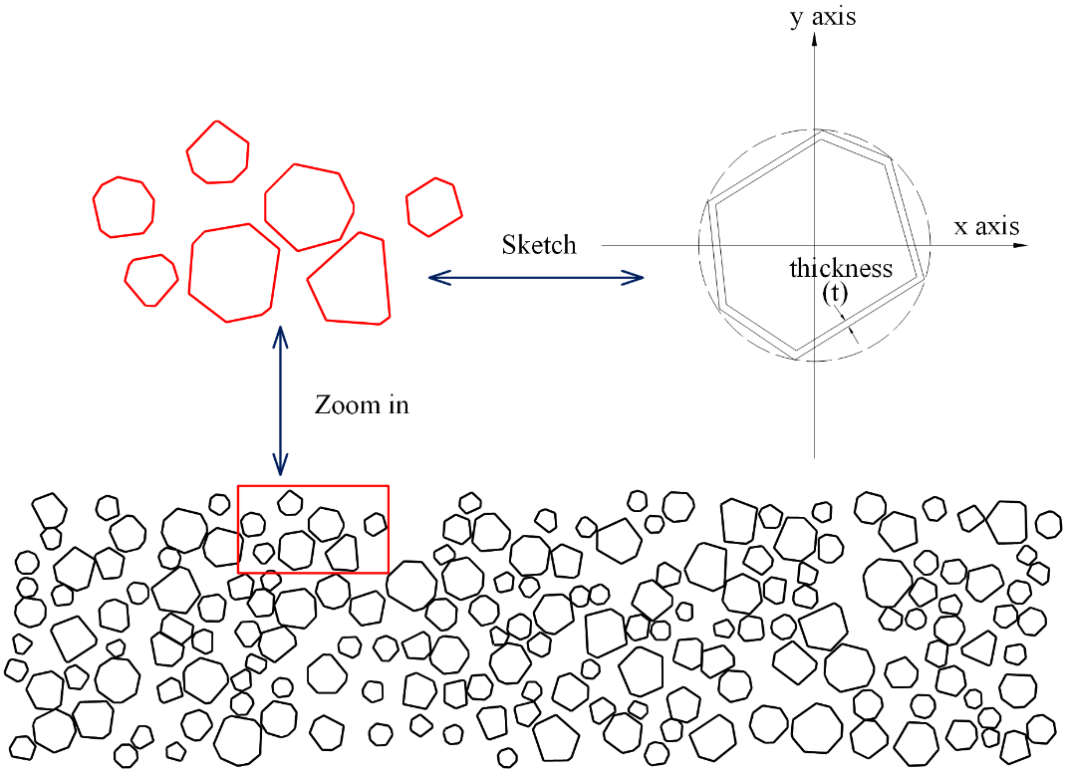

Fig. 5.2. 2-D random distribution of polygonal ITZ

5.3.3 Geometric properties of pore phase

In this study, the pore phase is considered to be embedded within the mortar phase as a network rather than as voids. Therefore, this modelling is employed not only to evaluate the mechanical behaviour for concrete but also to address multiple coupled phenomena, including thermal expansion, shrinkage, chemical corrosion, and creep, in combination Chapter 2.

To create the pore structure with a network, the Voronoi tessellation method for polygonal geometrical elements is adopted (Idiart, 2009). This method generates an array of randomly allocated nodes, located at the centroid of the Voronoi regions within the mortar. These nodes are interconnected via equidistant

segments that either intersect or meet at the ITZ, as depicted in Fig. 5.3. The total volume or area of pore network is determined by the experimentally derived porosity.

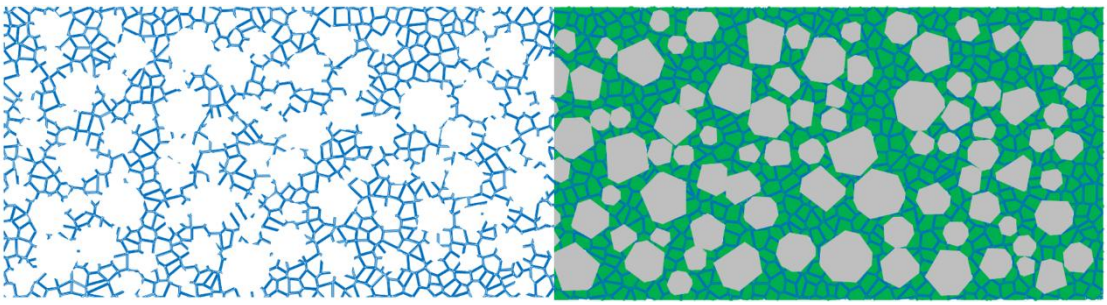

(a) (b)

Fig. 5.3. (a) Capillary structure, (b) Overall framework

5.4 Phase field model for diffusive fracture problem

In this part, main concepts for multi-phase elasto-plastic phase-field model and its finite element formulation are introduced.

5.4.1 Phase field model

5.4.1.1 Regularized representation of fracture topology

To illustrate the theory for crack topology, a sharp crack on a solid Γ is considered and subjected to a distributed traction F, as shown in Fig. 5.4a. This sharp fracture topology is described by the damage conditions d ($0 \leq d \leq 1$), which represents the damage condition ($d = 0$ indicates unbroken state, $d = 1$ indicates a fully damaged state). Let $\Omega \subset \mathbb{R}^D$ ($D = 1, 2, 3$ represents the value of space dimension) be an region describing the cracking solid, and its boundary is denoted by $\partial\Omega$, as shown in Fig. 5.4a. Fig. 5.4b defines normalised representation for fracture surface using the diffusive geomertic topology to describe crack width.

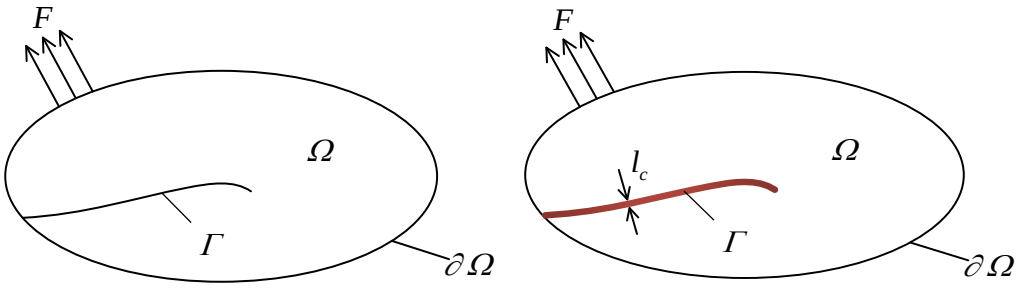

(a) (b)

Fig. 5.4. Normalised representation of a crack geometric properties: (a) sharp topology, (b) diffusive topology

By smearing out the crack over the domain Ω of the solid, the continuous and diffusion methods are utilized to approximately describe the discontinuous discrete fracture. Within this region Ω, a continuous dimensionless field is employed to capture fracture's topography. Therefore, fracture surface density γ is defined in research (Miehe et al., 2010a) using the following equation:

$$\gamma\left(d,\nabla d\right)=\frac{d^2}{2l_c}+\frac{l_c}{2}\left|\nabla d\right|^2 \tag{5.11}$$

where, l_c is the parameter of length scale.

Consequently, the crack surface is linked to crack density and width parameters. Therefore, the normalised fracture surface is expressed as:

$$\Gamma\left(d\right)=\int_{\Omega}\gamma\left(d,\nabla d\right)d\Omega \tag{5.12}$$

Considering these equations, a fracture surface Γ in the cracked region can be described by a dimensionless parameter.

5.4.1.2 Potential energy function in homogenous solid

To couple crack development with the deformation problem, total potential energy Π of cracked domain Ω can be considered as composition of fracture and strain energies. The equation is as follows:

$$\Pi=E\left(u,d\right)+P\left(u,d\right)+W\left(d\right)=\int_{\Omega}\psi_{\varepsilon}\left(\varepsilon\left(u\right),d\right)d\Omega+\int_{\Gamma}g_c d\Gamma \tag{5.13}$$

where, *E(u,d)* represents elastic energy, *P(u,d)* represents plastic energy, *W(d)* represents fracture energy, *u* represents displacement variables, *ε (u)* represents strain tensor, ψ_{ε} represents the mechanical energy, g_c is critical energy threshold.

In elastic energy degradation, only tensile stress contributes to damage and crack development. The effect of cracks on stiffness reduction is then considered. The elastic energy function can be described as follows (Liu et al., 2016):

$$\psi_{\varepsilon}^{el}\left(\varepsilon\left(u\right),d\right)=g\left(d\right)\cdot\psi_0^{el+}\left(\varepsilon\right)+\psi_0^{el-}\left(\varepsilon\right) \tag{5.14}$$

The definition of the positive and negative energy components can vary based on the implementation. For brittle materials, it is defined as follows (Amor et al., 2009, Freddi et al., 2010):

$$\psi_{\varepsilon}^{el}\left(\varepsilon(u),d\right)=\mu\sum_{i=1}^{3}\left[\left\langle\varepsilon_i\right\rangle_{-}^{2}+g(d)\left\langle\varepsilon_i\right\rangle_{+}^{2}\right]+\frac{\lambda}{2}\left[g(d)\left\langle tr(\varepsilon)\right\rangle_{+}^{2}+\left\langle tr(\varepsilon)\right\rangle_{-}^{2}\right] \tag{5.15}$$

To capture the plastic mechanical behaviour for concrete under tension and compression, this implementation employs the Drucker-Prager (Drucker and Prager, 1952) yield criterion:

$$f\left(I_1,J_2\right)=\sqrt{J_2}+\beta_{DP}I_1-g(d)\left[\sigma^{\lim}+H\varepsilon_{eq}^{pl}\right] \tag{5.16}$$

As there is no permanent volume change, the ductile component of history energy is represented as an equation of yield stress and energy-equivalent plastic strain:

$$\psi_0^{pl}\left(\varepsilon_{eq}^{pl}(u)\right)=\varepsilon_{eq}^{pl}(u)\left[\sigma^{\lim}+\frac{1}{2}H\varepsilon_{eq}^{pl}(u)\right] \tag{5.17}$$

The plastic energy function is proposed with the Drucker-Prager (Drucker and Prager, 1952) yield criterion, which is described by flow rules as follows (Krabbenhøft, 2002):

$$\begin{aligned}\psi_{\varepsilon}^{pl}&=g(d)\psi_0^{pl}=g(d)\left(\varepsilon_{eq}^{pl}\right)^{T}K_0\varepsilon_{eq}^{pl}\\ K_0&=\left(K-\frac{K\dfrac{\partial g}{\partial\sigma}\left(\dfrac{\partial f}{\partial\sigma}\right)^{T}K}{H+\left(\dfrac{\partial f}{\partial\sigma}\right)^{T}D\dfrac{\partial g}{\partial\sigma}}\right)\end{aligned} \tag{5.18}$$

where, K represents elastic constitutive matrix, K_0 represents elasto-plastic constitutive matrix, g and f are the plastic energy.

As a result, total potential energy function is constructed by combining elastic energy, plastic energy, and fracture energy, as follows:

$$\prod=\int_{\Omega}\left\{g(d)\left[\psi_0^{el+}(\varepsilon)+\psi_0^{pl}(\varepsilon)-\psi_c\right]+\psi_0^{el-}(\varepsilon)+\psi_c+2l_c\psi_c\left[d^2+l_c^2\left|\nabla d\right|^2\right]\right\}d\Omega \tag{5.19}$$

5.4.1.3 Potential energy function in multi-phase solid

To analyse the muti-phase field model of concrete, including its individual constituent (mortar, ITZ, aggregates, pores), the potential energy function is proposed based on a homogenous solid. Since the critical fracture energy is significantly higher than that for ITZ and mortar, aggregates are considered to be elastic. Mortar and ITZ are treated as elasto-plastic crack propagation components. Therefore, the crack geometry of mortar, ITZ and pores is approximated by diffused parameters $d_M(x)$, $d_I(x)$ and $d_P(x)$, respectively, which are described as follows:

$$\begin{cases} \gamma_M\left(d_M,\nabla d_M\right)=\dfrac{{d_M}^2}{2l_c}+\dfrac{l_c}{2}\left|\nabla d_M\right|^2 \\ \gamma_I\left(d_I,\nabla d_I\right)=\dfrac{{d_I}^2}{2l_c}+\dfrac{l_c}{2}\left|\nabla d_I\right|^2 \\ \gamma_P\left(d_P,\nabla d_P\right)=\dfrac{{d_P}^2}{2l_c}+\dfrac{l_c}{2}\left|\nabla d_P\right|^2 \end{cases} \tag{5.20}$$

By introducing the fraction of the three phases, the total potential energy is decomposed into energies corresponding to the mortar, ITZ, pores and aggregates:

$$\Pi=\Pi_M+\Pi_I+\Pi_P+\Pi_A \tag{5.21}$$

where, Π_M represents potential energy of mortar, Π_{ITZ} represents potential energy of ITZ, Π_P represents pores potential energy, and Π_A represents aggregates potential energy.

By combining Eq. (5.19), the potential energy of four parts is shown as:

$$\begin{cases} \Pi_M=\int_{M\Omega}\left\{g\left(d\right)\left[\psi_{M0}^{el+}\left(\varepsilon\right)+\psi_{M0}^{pl}\left(\varepsilon\right)-\psi_M^c\right]+\psi_{M0}^{el-}\left(\varepsilon\right)+\psi_M^c+2l_c\psi_M^c\left[d^2+l_c^2\left|\nabla d\right|^2\right]\right\}d\Omega_M \\ \Pi_I=\int_{I\Omega}\left\{g\left(d\right)\left[\psi_{I0}^{el+}\left(\varepsilon\right)+\psi_{I0}^{pl}\left(\varepsilon\right)-\psi_I^c\right]+\psi_{I0}^{el-}\left(\varepsilon\right)+\psi_I^c+2l_c\psi_I^c\left[d^2+l_c^2\left|\nabla d\right|^2\right]\right\}d\Omega_I \\ \Pi_P=\int_{P\Omega}\left\{g\left(d\right)\left[\psi_{P0}^{el+}\left(\varepsilon\right)+\psi_{P0}^{pl}\left(\varepsilon\right)-\psi_P^c\right]+\psi_{P0}^{el-}\left(\varepsilon\right)+\psi_P^c+2l_c\psi_P^c\left[d^2+l_c^2\left|\nabla d\right|^2\right]\right\}d\Omega_P \\ \Pi_{MA}=\int_{A\Omega}\left\{\psi_{A0}^{el+}\left(\varepsilon\right)+\psi_{A0}^{el-}\left(\varepsilon\right)\right\}d\Omega_A \end{cases} \tag{5.22}$$

To regularize the integral domain of all phases, the volume content for four components is employed to describe potential energy as follows:

$$\Pi=\int_\Omega\left[V_M\psi_M+V_I\psi_I+V_P\psi_P+V_A\psi_A\right]d\Omega \tag{5.23}$$

where, V_i ($i = M, I, P, A$) represents the mortar volume fracture, ITZ, pores and aggregates, ψ_i ($i = M, I, P, A$) represents energy density function of mortar, ITZ, pores and aggregates from the concrete domain.

Therefore, total potential energy for different phases is described as follows by combing Eq. (5.22) and Eq. (5.23):

$$\Pi=\int_{\Omega}\left\{\begin{array}{l}V_M\left(\left(\varepsilon_{eq}^{el}\right)^T\left(K_M\right)\varepsilon_{eq}^{el}+\left(\varepsilon_{eq}^{pl}\right)^T g\left(d\right)K_{M0}\varepsilon_{eq}^{pl}+\left(1-g\left(d\right)\right)\dfrac{g_M}{2l_c}+g_M\gamma\left(d,\nabla d\right)\right)\\+V_I\left(\left(\varepsilon_{eq}^{el}\right)^T\left(K_I\right)\varepsilon_{eq}^{el}+\left(\varepsilon_{eq}^{pl}\right)^T g\left(d\right)K_{I0}\varepsilon^{eq}+\left(1-g\left(d\right)\right)\dfrac{g_I}{2l_c}+g_I\gamma\left(d,\nabla d\right)\right)\\+V_P\left(\left(\varepsilon_{eq}^{el}\right)^T\left(K_P\right)\varepsilon_{eq}^{el}+\left(\varepsilon_{eq}^{pl}\right)^T g\left(d\right)K_{P0}\varepsilon^{eq}+\left(1-g\left(d\right)\right)\dfrac{g_P}{2l_c}+g_P\gamma\left(d,\nabla d\right)\right)\\+V_A\left(\left(\varepsilon_{eq}\right)^T K_A\varepsilon_{eq}\right)\end{array}\right\}d\Omega \tag{5.24}$$

where, K_M, K_I, K_P and K_A are the elastic constitutive matrix of mortar, ITZ, pores and aggregate, K_{M0}, K_P and K_{I0} are the elasto-plastic constitutive matrix of mortar, pores and ITZ.

5.4.2 Staggered algorithm with FEM

5.4.2.1 Staggered time-integration algorithm

The governing formulations of phase-field model results in two fields coupling framework involving displacement and phase fields (d and u), facilitating numerical solutions necessary to capture fracture evolution branches. To obtain the solution, "monolithic" and "staggered" methods are commonly employed (Miehe et al., 2010b). In monolithic method, the equations of the phase-field model are simultaneously calculated for each time increment. However, the strong non-linear properties of the displacement field equations often result in the monolithic method requiring numerous iterations and exhibits poor convergence. Conversely, in staggered method, this problem is divided into two independent minimization procedures. Firstly, the sharp fracture is normalised using the phase field, which is determined based on history energy. Then, the damage variable of phase field is employed to recalculate displacement field.

With a fixed d, displacement field is given as follows:

$$\Pi^u=\int_{\Omega}\left\{\sum_{i}^{i=1,4}\left[\psi_{\varepsilon}^{el}\left(\varepsilon\left(u\right),d\right)+\psi_{\varepsilon}^{pl}\left(\varepsilon\left(u\right),d\right)\right]\right\}d\Omega-\Pi^{ext} \tag{5.25}$$

From Eq. (5.24), displacement field is described as follows:

$$\Pi^u=\int_{\Omega}\left\{V_M\left(\psi_{M\varepsilon}^{el}+\psi_{M\varepsilon}^{pl}\right)+V_I\left(\psi_{I\varepsilon}^{el}+\psi_{I\varepsilon}^{pl}\right)+V_P\left(\psi_{P\varepsilon}^{el}+\psi_{P\varepsilon}^{pl}\right)+V_A\psi_{A\varepsilon}^{el}\right\}d\Omega-\Pi^{ext} \tag{5.26}$$

where, Π^{ext} is the external energy induced by body force and boundary force, which is formulated as follows:

$$\prod^{ext} = \int_{\Omega} \bar{\gamma} \cdot u d\Omega + \int_{\partial\Omega} \bar{t} \cdot u d\partial\Omega \tag{5.27}$$

where, $\bar{\gamma}$ and $\bar{t}$ are body and surface forces, respectively.

By varying both energies ($\delta\Pi^u = 0$), the corresponding Eulerian equations (strong form) can be formulated for displacement field:

$$\begin{aligned} &\delta\prod^{u} = 0 \quad \forall\delta u \rightarrow \quad \nabla\sigma - \bar{\gamma} = 0 && in \quad \Omega \\ &\sigma \cdot n = \bar{t} && on \quad \Gamma_N \\ &u = \bar{u} && on \quad \Gamma_D \end{aligned} \tag{5.28}$$

Similarly, by replacing potential energy at displacement field with history energy, Lagrangian equation for phase-field modelling is expressed as:

$$\prod^{d} = \int_{\Omega} \begin{bmatrix} V_M g_M \gamma\left(d, \nabla d\right) + V_I g_I \gamma\left(d, \nabla d\right) + V_P g_P \gamma\left(d, \nabla d\right) \\ + g\left(d\right)\left(V_M H_M + V_I H_I + V_P H_P\right) \end{bmatrix} d\Omega \tag{5.29}$$

And the history field is described as follows:

$$\begin{aligned} &H_0 = 0 \\ &H_{n+1} = \max \begin{Bmatrix} \psi_0^{el+} + \psi_0^{pl} - \psi^c \\ H_n \end{Bmatrix} \end{aligned} \tag{5.30}$$

where, H_n represents history energy at step n.

Moreover, this equation ensures irreversibility for damage condition ($\dot{d} \geq 0$). Therefore, strong form of damage field is described as follows:

$$\begin{aligned} &\delta\prod^{d} = 0 \quad \forall\delta d \rightarrow \quad \frac{\boldsymbol{g}}{2l_c}\left(d - l_c^2 \Delta d\right) = \left(1 - d\right) H \quad in \quad \Omega \\ &\nabla d \cdot n = 0 \quad in \quad \Gamma \end{aligned} \tag{5.31}$$

where, $\boldsymbol{g} = \begin{bmatrix} g_M & 0 & 0 \\ 0 & g_I & 0 \\ 0 & 0 & g_P \end{bmatrix}$, $H = V_M H_M + V_I H_I + V_P H_P$.

5.4.2.2 Staggered multi-phase algorithm

The multi-phase phase-field model results in a four-phase problem, enabling numerical solutions necessary for capturing fracture evolution branch through broken phases. To study and analyse the effect

of different components, energy degradation is proposed for samples with different volume fractions. However, due to the strong non-linear performance for displacement field, the staggered method is employed to construct energy degradation equations. Initially, the external load is applied to two samples to ensure the same internal potential and external energy, which will be used to calculate the displacement distribution of both samples. Therefore, history energy is utilized to recalculate damage field for samples.

Based on Eq. (5.26), the displacement of the two samples is described as follows:

$$V_M^1\psi_{M\varepsilon}+V_I^1\psi_{I\varepsilon}+V_P^1\psi_{P\varepsilon}+V_A^1\psi_{A\varepsilon}=V_M^2\psi_{M\varepsilon}+V_I^2\psi_{I\varepsilon}+V_P^2\psi_{P\varepsilon}+V_A^2\psi_{A\varepsilon} \tag{5.32}$$

where, ε^{eq1} and ε^{eq2} are the equivalent strains, V_i^1 ($i=M, I, A$) and V_i^2 represent volume fracture of mortar, ITZ, aggregate for two samples, respectively.

To simplify the function of internal potential energy density, Eq. (5.32) is used:

$$H_{\text{int}}^1=H_{\text{int}}^2 \tag{5.33}$$

The phase-field problem can be described by replacing history energy with potential energy density and the energy from different parts as follows:

$$\begin{aligned}\Pi^{d1}&=\int_\Omega\left[\left(\boldsymbol{V}^1\boldsymbol{g}\right)\boldsymbol{\gamma}^1\left(d,\nabla d\right)+g\left(d^1\right)\left(H_{\text{int}}^1-V_M^1\psi_{M0}^{el-}-V_I^1\psi_{I0}^{el-}-V_P^1\psi_{P0}^{el-}-V_A^1\psi_A^{el}\right)\right]d\Omega\\ \Pi^{d2}&=\int_\Omega\left[\left(\boldsymbol{V}^2\boldsymbol{g}\right)\boldsymbol{\gamma}^2\left(d,\nabla d\right)+g\left(d^2\right)\left(H_{\text{int}}^2-V_M^2\psi_{M0}^{el-}-V_I^2\psi_{I0}^{el-}-V_P^2\psi_{P0}^{el-}-V_A^2\psi_A^{el}\right)\right]d\Omega\end{aligned} \tag{5.34}$$

where, $\boldsymbol{V}$, $\boldsymbol{g}$ and $\boldsymbol{\gamma}$ represent the matrix of volume fracture, critical energy release rate, and crack surface for different phases, $\boldsymbol{V}=\begin{bmatrix}V_m & 0 & 0\\ 0 & V_I & 0\\ 0 & 0 & V_P\end{bmatrix}$, $\boldsymbol{g}=\begin{bmatrix}g_m & 0 & 0\\ 0 & g_I & 0\\ 0 & 0 & g_P\end{bmatrix}$, $\boldsymbol{\gamma}=\begin{bmatrix}\gamma_m\\ \gamma_I\\ \gamma_P\end{bmatrix}$.

By combing Eq. (5.33) and Eq. (5.34) with Eq. (5.31), the equations thus is described as follows:

$$\begin{cases}\boldsymbol{V}\boldsymbol{g}\Delta\boldsymbol{\gamma}\left(d,\nabla d\right)\beta=\left(1-d\right)H^1\\ \beta=\dfrac{H^1}{H^1+\Delta\psi}\\ \Delta\psi=\left(V_M^1\psi_{M0}^{el-}+V_I^1\psi_{I0}^{el-}+V_P^1\psi_{P0}^{el-}+V_A^1\psi_A^{el}\right)-\left(V_M^2\psi_{M0}^{el-}+V_I^2\psi_{I0}^{el-}+V_P^2\psi_{P0}^{el-}+V_A^2\psi_A^{el}\right)\end{cases} \tag{5.35}$$

where, H^l is the history energy of reference sample, β is the potential energy correction parameter.

5.5 Calibration of mechanical properties of multiple phases model

To predict fracture evolution for concrete while considering the effect induced by micro components, it is crucial to calculate the basic parameters: elastic properties (Elastic modulus and Poisson's ratio) and fracture properties (length scale parameter and critical fracture energy threshold). The plastic mechanical parameters of mortar and concrete, including yield stress (σ_y^c) and Hardening modulus (H) are obtained based on Chapter 3. Subsequently, two critical fracture energy parameters are calibrated to consider unsymmetric tension-compression behaviour of porous materials.

5.5.1 Uniaxial compressive simulation of mortar

To consider and calibrate the influence of the pore phase, mortar specimens were utilized to analyse fracture evolution applying uniaxial compressive loading. In this numerical model, a square domain (length L = 50 mm) was employed, and loading was applied on top side in y-direction. The bottom side of this sample was fixed in y-direction, as depicted in Fig. 5.5. To study and evaluate the effect of the pore phase on crack propagation, two mesoscopic components of mortar were generated with the pore width of 0.4 mm. The same mesh size of mortar model was employed, with h = 0.3 mm, and includes 96367 triangular elements. For the mechanical parameters of the pore phase, 12 GPa was used to represent the effective modulus of the pore phase instead of 0 GPa (Gao et al., 2017). Therefore, the parameters of mortar solid and pore phase were computed based on the MT scheme and experimental data, as depicted in Table 5.1.

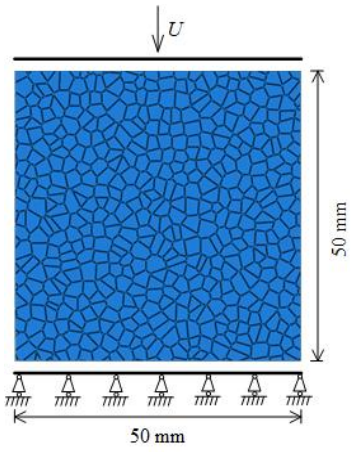

Fig. 5.5. Geometric and boundary conditions of mortar specimen

Table 5.1: Parameters for mortar samples of phase field

	E GPa	v	σ_{y1}^{c} MPa	H_1 GPa	σ_{y2}^{c} MPa	H_2 GPa	σ_{y}^{t} MPa	l_c mm	β_{DP}	ψ_{c}^{c} MPa	ψ_{c}^{c} MPa
Mortar	27	0.2	16	15	30	5	3.6	1	0.37	1.26	0.014
Pores	12	0.2	16	5.8	30	2.1	3.6	1	0.37	0.55	0.005

A compressive load is applied incrementally for 800 steps with $\Delta u = 7.5 \times 10^{-4}$mm ($\varepsilon = 10^{-5}$). Fig. 5.6 shows the fracture evolution branch, compared with test results in Fig. 5.7 (Chapter 3). The numerical model exhibits several vertical cracks similar to the experimental results, but the simulation shows a different number and length of cracks. This discrepancy results from the different spital distribution of pores and sand between the numerical model and the mortar specimen. Fig. 5.8 shows the comparison of load-displacement between the elasto-plastic phase-field model and the experimental data, which demonstrates a great agreement.

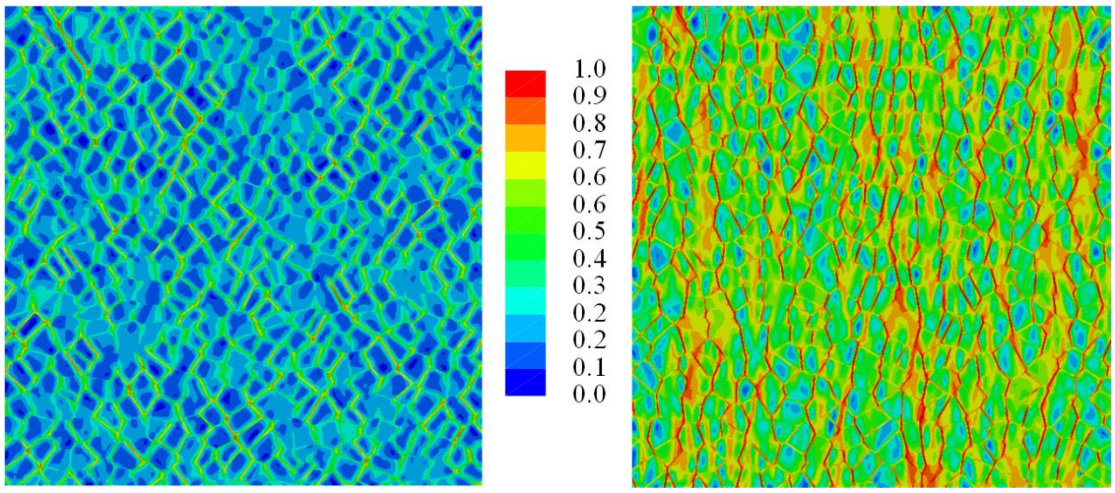

(a) (b)

Fig. 5.7. Crack propagation process over displacement, (a) $U = 0.14$ mm, (b) $U = 0.22$ mm

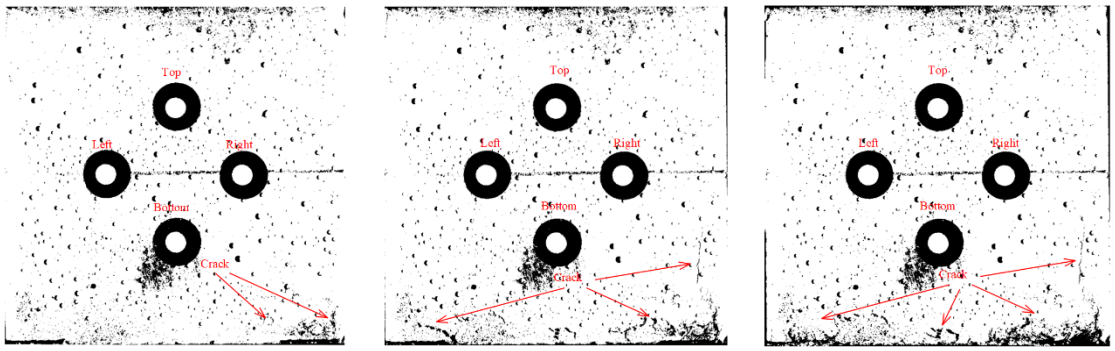

Fig. 5.8. Crack propagation of mortar specimen

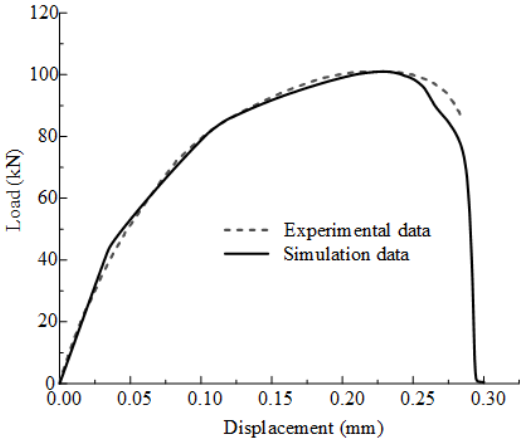

Fig. 5.9. Comparison of load-displacement result for mortar samples

5.5.2 Uniaxial compressive simulation of concrete

As for this simulation, a concrete sample was modelled to predict fracture evolution applying uniaxial compressive loading. According to concrete mix design and geometric generation method described in Section 5.3, the concrete mesoscale model was obtained. The load and boundary conditions were the same as in the mortar simulation, as demonstrated in Fig. 5.9. In concrete sample, four mesoscopic components, including mortar, ITZ, aggregate and pore phase, were generated with the ITZ thickness of 30 μm and pore width of 0.4 mm. The same element size of the concrete modelling was employed, with h = 0.3 mm for all particles (aggregate, ITZ, pores, and mortar) and includes 193984 triangular elements. The mechanical parameters for this simulation are listed in Table 5.2. To compare and verify theoretical model with experimental results, fracture evolution branch and load-displacement were analysed. The comparison shows a good agreement, as demonstrated in Fig. 5.10, Fig. 5.11 and Fig. 5.12.

Table 5.2: Parameters for concrete samples of phase field

	E GPa	v	σ_{y1}^{c} MPa	H_1 GPa	σ_{y2}^{c} MPa	H_2 GPa	σ_{y}^{t} MPa	l_c mm	β	β_{DP}	ψ_c^c MPa	ψ_c^c MPa
Aggregate	40	0.2	-	-	-	-	-	-	-	-	-	-
Mortar	27	0.2	16	15	30	5	3.6	1	1	0.37	1.26	0.014

ITZ	12	0.2	16	5.8	30	2.1	3.6	1	1	0.37	0.55	0.005
Pores	12	0.2	16	5.8	30	2.1	3.6	1	1	0.37	0.55	0.005

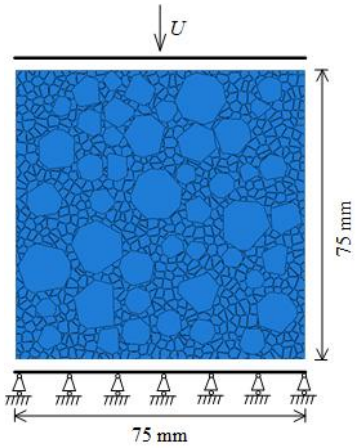

Fig. 5.9. Properties of concrete samples: (a) boundary conditions, (b) geometric details of concrete

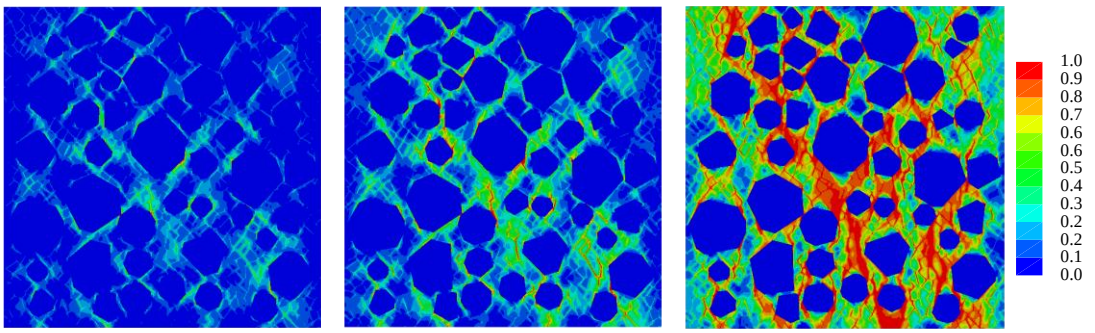

(a) (b) (c)

Fig. 5.10. Crack propagation process over displacement, (a) $U = 0.21$ mm, (b) $U = 0.29$ mm, (c) $U = 0.35$ mm

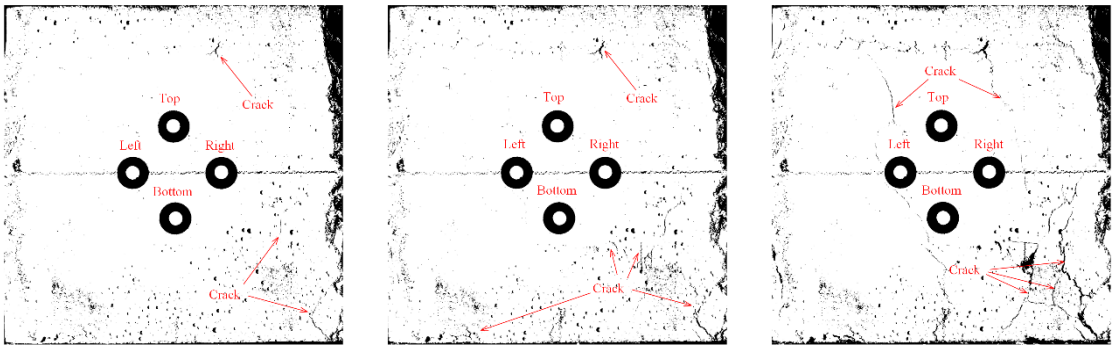

Fig. 5.11. Crack propagation of concrete specimen

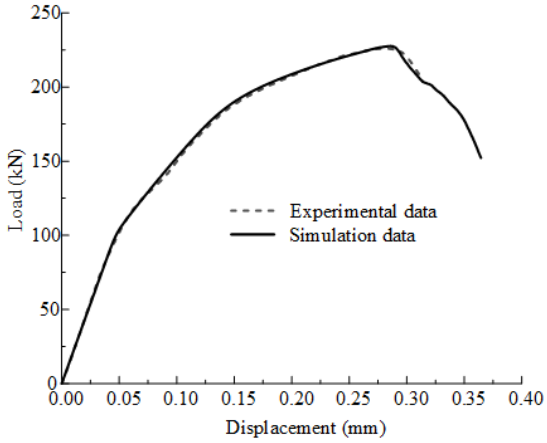

Fig. 5.12. Comparison of load-displacement result of concrete samples

5.5.3 Three-point bending modelling for concrete

As for this simulation, a concrete specimen was modelled to analyse crack propagation in flexure under a three-point bending test. Based on the mix design of concrete and geometric generation method described in Section 5.3, the concrete mesoscale model was obtained. The loading was employed at mid-span on top side in y-direction with a rate 0.045 mm/min ($\varepsilon=10^{-5}$/s). The left fulcrum at the bottom side was controlled in both x direction and y direction, and right fulcrum was controlled in y direction. The sides of specimens were considered elastic. The boundary conditions of this sample are demonstrated in Fig. 5.13. To study and evaluate the effect of the mesoscale model of concrete, four mesoscopic components, including mortar, ITZ, aggregate and pore phase, were generated with an ITZ thickness of 30 μm and a pore width of 0.4 mm. The geometric information for this model is demonstrated in Fig. 5.14. The mesh size varied from 3 mm in the elastic part to 0.5 mm in the nonlinear part for all phases (aggregate, mortar, ITZ and pores), and the model included 102846 triangular elements. The parameters are listed in Table 5.2. To compare and calibrate theoretical model and test results, crack propagation path was analysed at displacement of 0.036 mm, 0.072 mm and 0.111 mm, as obtained from experiments, as depicted in Fig. 5.15. The load-displacement results were compared, as shown in Fig. 5.16.

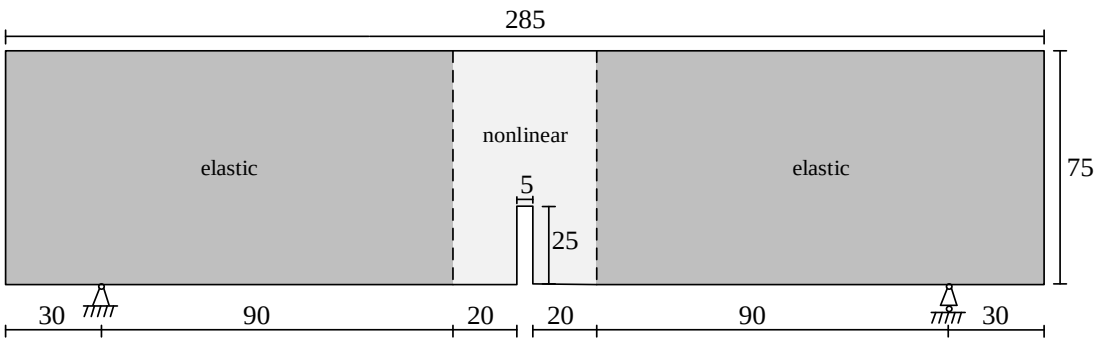

Fig. 5.13. Boundary conditions and dimension details of concrete specimen

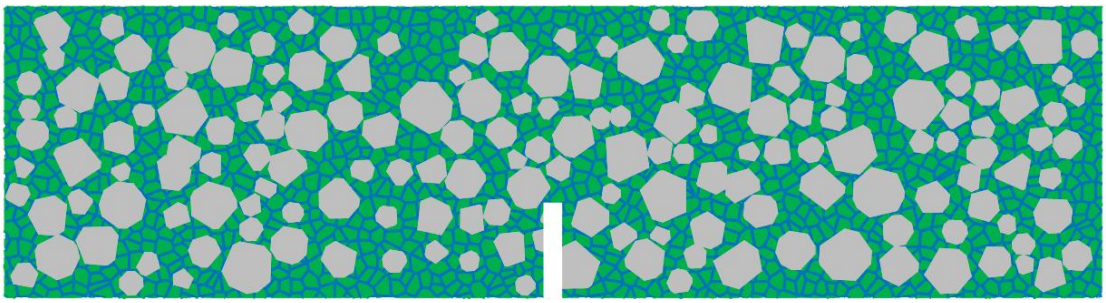

Fig. 5.14. Geometric details of meso-model of concrete specimen

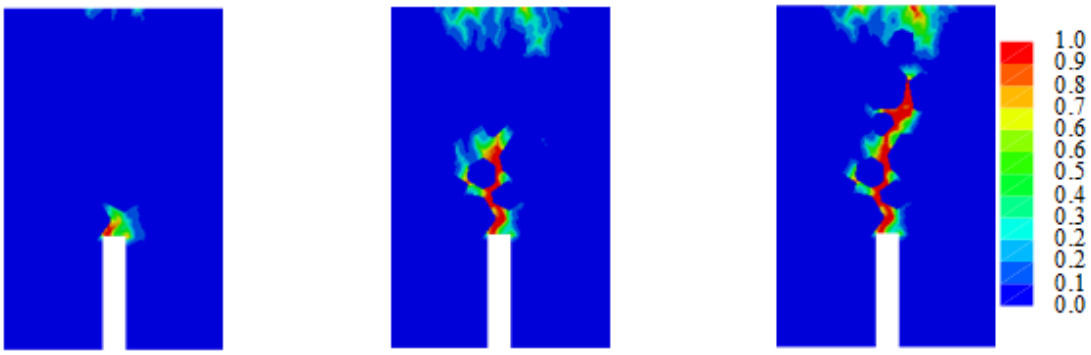

(a)

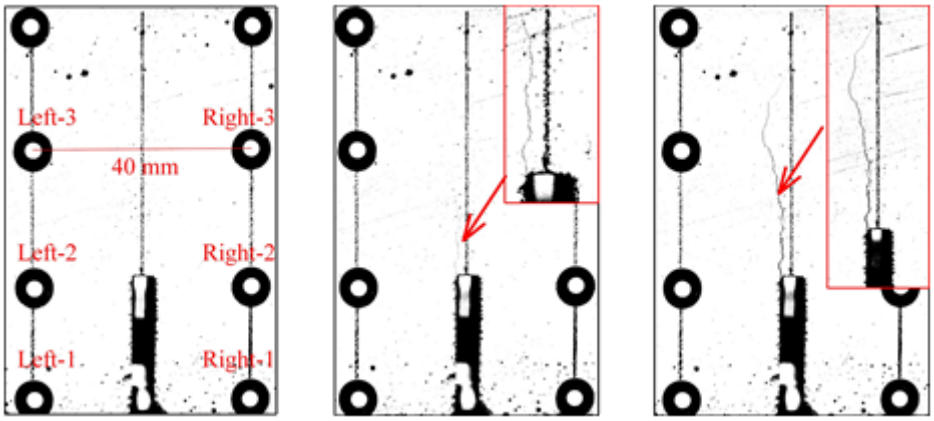

(b)

Fig. 5.15. Crack propagation process of concrete specimen with three-point bending test: (a) Simulation results, (b) experimental results

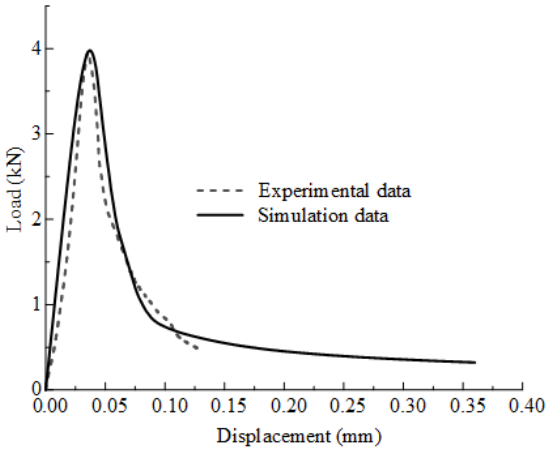

Fig. 5.16. Comparison of load-displacement result of concrete samples

From Fig. 5.16, load-displacement results between the simulation results and test data exhibit slightly different descending branches, influenced by the spatial distribution pore phase and aggregate phase. Since ITZ and pore phase are more prone to breakage compared to mortar, cracks typically propagate along ITZ and pore phases. Moreover, 2D model has limitation in representing crack propagation. To further calibrate fracture evolution in phase-field model, the load-CMOD (Crack Mouth Opening Displacement) results for the different depths are depicted in Fig. 5.17.

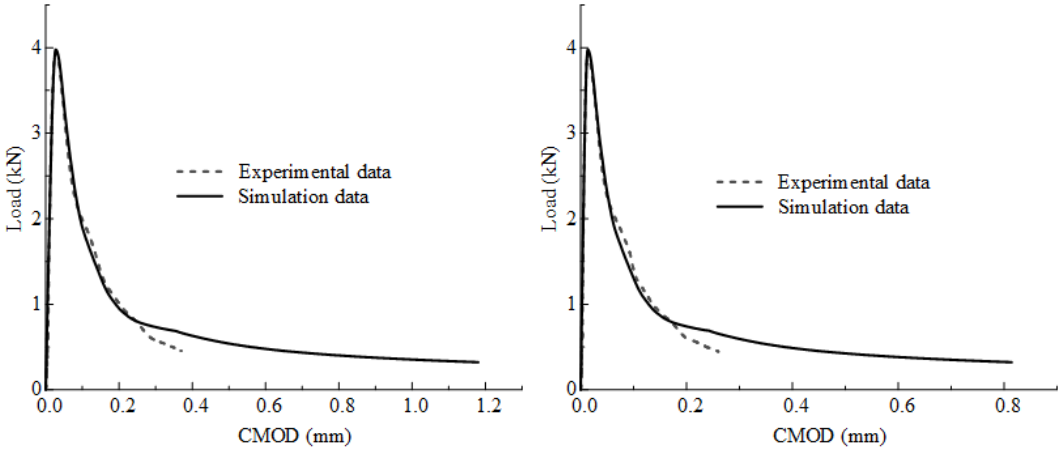

(a) (b)

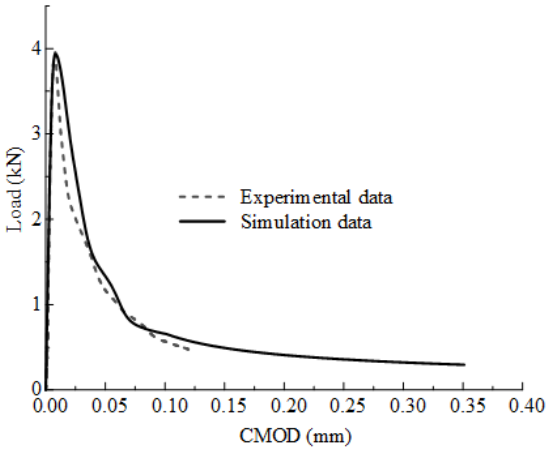

(c)

Fig. 5.17. Comparison of load-CMOD curve at different depths: (a) 0mm, (b) 25mm, (c) 50mm

According to comparison of load-CMOD at various depths, a similar trend is observed compared to the load-displacement curve. The distribution of aggregate, ITZ and pores significantly impacts crack penetration. However, overall, the elasto-plastic phase-field model is shown to effectively predict fracture evolution in flexure at the mesoscopic level in concrete.

5.6 Influence of mesoscopic properties on crack propagation

This section investigates the effects for ITZ thickness, porosity, and pore width on crack propagation in flexural tests. Various features (such as the fraction and width of pores, and the thickness of ITZ) mechanical properties for concrete are simulated using this phase-field model.

5.6.1 ITZ thickness

According to previous literature, the ITZ can be modelled as the thin bond layer with a thickness from 10 to 50 μm along aggregate particles (Shuguang et al., 2015). To analyse the influence of ITZ thickness, values of 10, 20, 40 and 50 μm are considered. The same geometric features (distribution, shape and size of pore phase and aggregate phase) for concrete are utilized to minimize the effect of other variables. To understand the mechanical effect of ITZ thickness, three-point bending tests are simulated for concrete using this elasto-plastic phase-field model. It can be observed, however, that the value of ITZ thickness affects the porosity of the ITZ phase, and in turn the total porosity, albeit slightly, as depicted in Table 5.3. From Table 5.3, fraction of various components shows a slight change within 0.2%, and

the potential energy correction parameter is thus set to 1. The phase-field parameters are listed in Table 5.2. The crack propagation with displacement of 0.111mm is depicted in Fig. 5.18, and the load-displacement result is depicted in Fig. 5.19.

Table 5.3: Fraction and size of ITZ

Model	ITZ thickness (mm)	ITZ fraction (%)	Pore width (mm)	Porosity (%)
ITZ-30	0.03	0.44	0.4	11.14
ITZ-10	0.01	0.15	0.4	11.22
ITZ-20	0.02	0.29	0.4	11.18
ITZ-40	0.04	0.58	0.4	11.10
ITZ-50	0.05	0.73	0.4	11.06

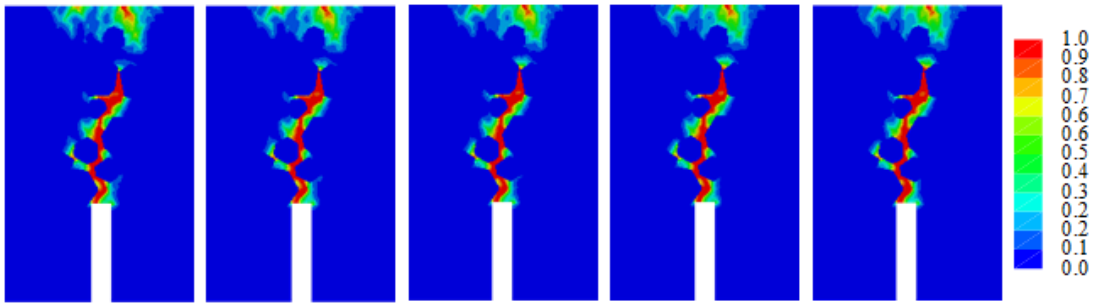

(a) (b) (c) (d) (e)

Fig. 5.18. Crack propagation with different ITZ thickness: (a) 10 μm, (b) 20 μm, (c) 30 μm, (d) 40 μm and (e) 50 μm

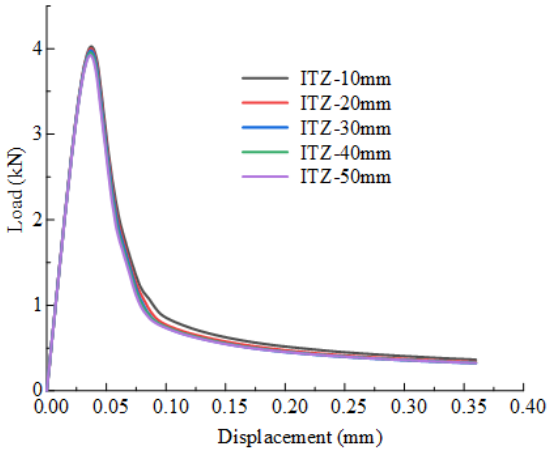

Fig. 5.19. Comparison of load-displacement curve with different thickness

From Fig. 5.18, it is clearly observed that fracture evolution branch slightly increases with the increase in ITZ thickness. Fig. 5.19 indicates that load-displacement curves exhibit the same trend due to the similar crack propagation paths. However, the peak loads decrease from 4024 N to 3923 N with increase in thickness of ITZ phase. The different ITZ thicknesses show only a slight influence for concrete mechanical behaviours. Therefore, thickness of 30 μm is considered reasonable for ITZ when studying fracture evolution and degradation mechanism of concrete.

5.6.2 Influence of porosity

To investigate the effect for different porosity levels, 9.76% and 12.86% of porosity are generated with the same pore width by increasing the tortuosity of the pore phase. To reduce computational time and minimize the number of elements, the reference pore thickness of 0.4 mm is employed. The same geometric features (distribution, shape and size of aggregate, and ITZ thickness) of concrete are utilized to minimize the effect of other variables. The feature details of the model are shown in Table 5.4. The fraction of porosity shows a change of about 2%. According to the theory in Section 5.4, the potential energy correction parameters are thus 1.1 and 0.89 for specimens with porosity of 9.76% and 12.86%, respectively. The phase-field parameters are listed in Table 5.2. The crack propagation with a displacement of 0.111 mm is depicted in Fig. 5.20, and load-displacement result is depicted in Fig. 5.21.

Table 5.4: Fraction and size of porosity

Model	ITZ thickness (mm)	ITZ fraction (%)	Pore width (mm)	Porosity (%)
Porosity-reference	0.03	0.44	0.4	11.14
Porosity-Max	0.03	0.44	0.4	12.86
Porosity-Min	0.03	0.44	0.4	9.76

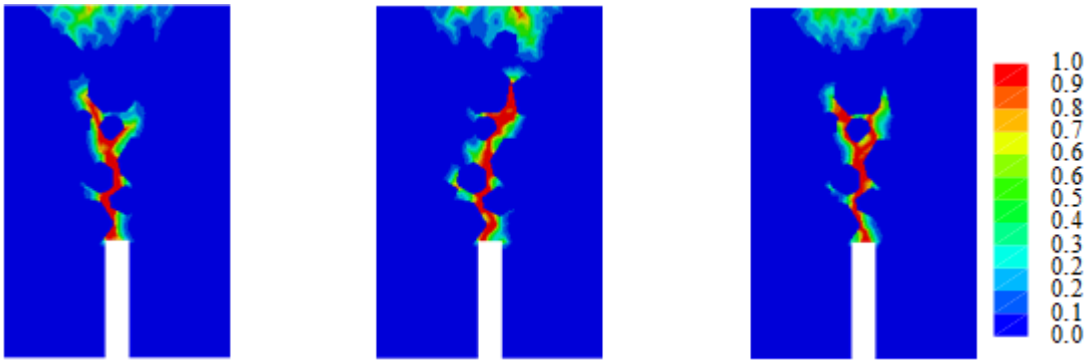

(a) (b) (c)

Fig. 5.20. Crack propagation with different porosity: (a) 9.76%, (b) 11.14%, and (c) 12.86%

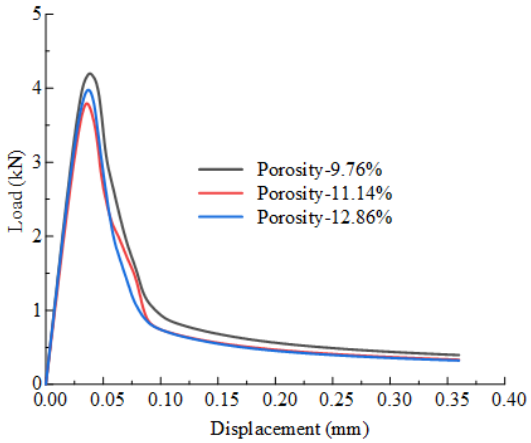

Fig. 5.21. Comparison of load-displacement curve with different porosity

From Fig. 5.20, it is observed that higher porosity induces higher tortuosity with the same pore width, resulting in significantly altered crack propagation along with the increased pore phase path. Fig. 5.21 shows that load-displacement results exhibit different branches owing to the varying fracture evolution. The peak loads decrease by around 10% from 4198 N to 3792 N with the increase in porosity.

5.6.3 Influence of pore width

To analyse the influence of different pore widths, pore thickness of 0.3 mm and 0.5 mm are generated with the same porosity by modifying the tortuosity of the pore phase. The same geometric features (distribution, shape and size of aggregate, and ITZ thickness) of concrete are utilized to minimize the effect of other variables. The feature details of the model are shown in Table 5.5. The fraction of porosity shows a slight change within 0.1%, so the potential energy correction parameter β is set to 1. The phase-field parameters are listed in Table 5.2. The crack propagation with a displacement of 0.111 mm is depicted in Fig. 5.22 and load-displacement result is depicted in Fig. 5.23.

Table 5.5: Fraction and size of porosity

Model	ITZ thickness (mm)	ITZ fraction (%)	Pore width (mm)	Porosity (%)
Width-0.4mm	0.03	0.44	0.4	11.14
Width-0.3mm	0.03	0.44	0.3	11.10
Width-0.5mm	0.03	0.44	0.5	11.12

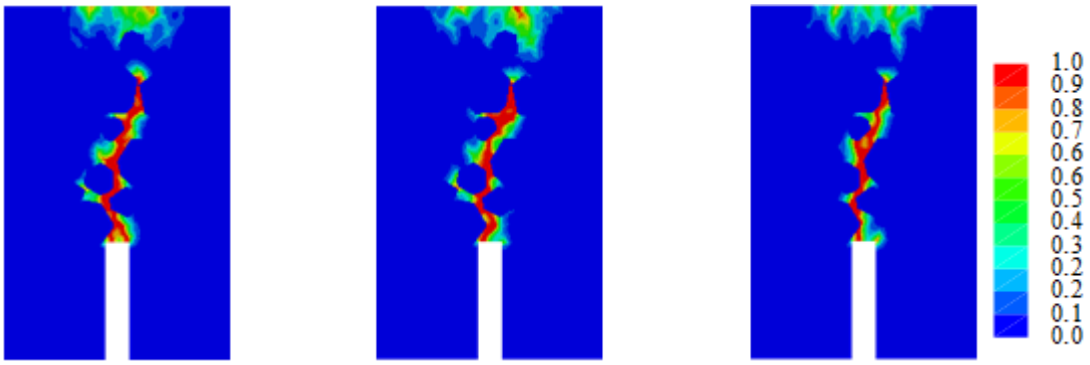

(a) (b) (c)

Fig. 5.22. Crack propagation with different porosity: (a) 0.3mm, (b) 0.4mm, and (c) 0.5mm

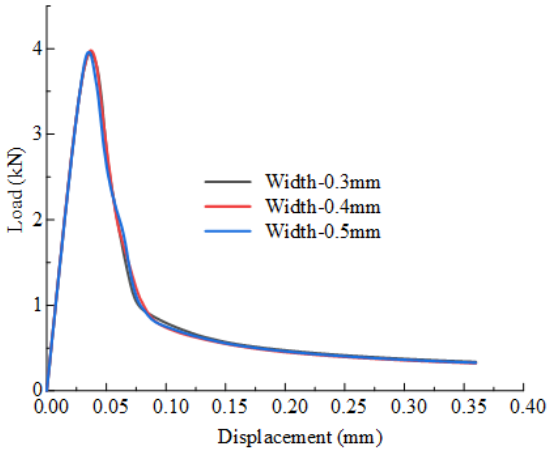

Fig. 5.23. Comparison of load-displacement curve with different pore width

From Fig. 5.22, the models with different pore widths and the same porosity exhibit slightly crack propagation branches due to different pore phase paths. However, Fig. 5.23 shows that the load-displacement curves demonstrate the same mechanical properties of elastic modulus and peak load

owing to the similar crack propagation. Therefore, pore width has a slight impact on concrete fracture evolution.

5.7 Calibration of mechanical properties of multiple phases model

In this section, the numerical modelling for three-point bending test are calibrated using results from three additional tests (Ren et al., 2023, Yang et al., 2023, Hu et al., 2018). "Model-1" prisms (experimental data by (Ren et al., 2023)) with dimensions 400 mm × 100 mm × 100 mm were stored in the curing room (20℃ and 95% RH) for 28 days. A notch, 25 mm in depth and 0.5 mm in width, was sawn at the middle of concrete sample. "Model-2" prisms (experimental data from Shutong (Yang et al., 2023)) with dimensions 400 mm × 100 mm × 100 mm were cured with temperature 20℃ and RH 95% for 60 days. After curing, specimens were also notched (30 mm depth and 3mm width). "Model-3" prisms (experimental data from (Hu et al., 2018)) with size 550 mm × 150 mm × 150 mm, the specimens were covered by wetted hessian fabric and plastic sheets after demoulding to maintain moisture during curing process, with a curing conditions (22 ± 3 ℃). After 28days for curing, all covered sheets were removed, and then specimens were exposed for drying until 90 days. Before the tests, a mid-span notch (5 mm in width and 25 mm in depth) was sawn. The loading rates were 0.05 mm/min (Model-1 and Model-3) and 0.02 mm/min (Model-2). The mechanical properties for this numerical modelling are described in Table 5.6. The numerical results are compared with experimental data, demonstrating strong agreement, as illustrated in Fig. 5.24.

Table 5.6: Parameters for calibration models of phase field

Model	Components	E (GPa)	v	H (GPa)	σ_y^t (MPa)	l_c (mm)	β_{DP}	ψ_c^t (MPa)
	Aggregate	35	0.2	-	-	-	-	-
Model-1	Mortar	23	0.2	7.2	4.19	1	0.38	0.017
	ITZ	12	0.2	3	4.19	1	0.38	0.007
	Pores	12	0.2	3	4.19	1	0.38	0.007
	Aggregate	40	0.2	-	-	-	-	-
Model-2	Mortar	34	0.2	10	4.17	1	0.37	0.012
	ITZ	12	0.2	3.4	4.17	1	0.37	0.0045
	Pores	12	0.2	3.4	4.17	1	0.37	0.0045

	Aggregate	40	0.2	-	-	-	-	-
Model-3	Mortar	25	0.2	5	3.6	1	0.39	0.012
	ITZ	12	0.2	2.3	3.6	1	0.39	0.005
	Pores	12	0.2	2.3	3.6	1	0.39	0.005

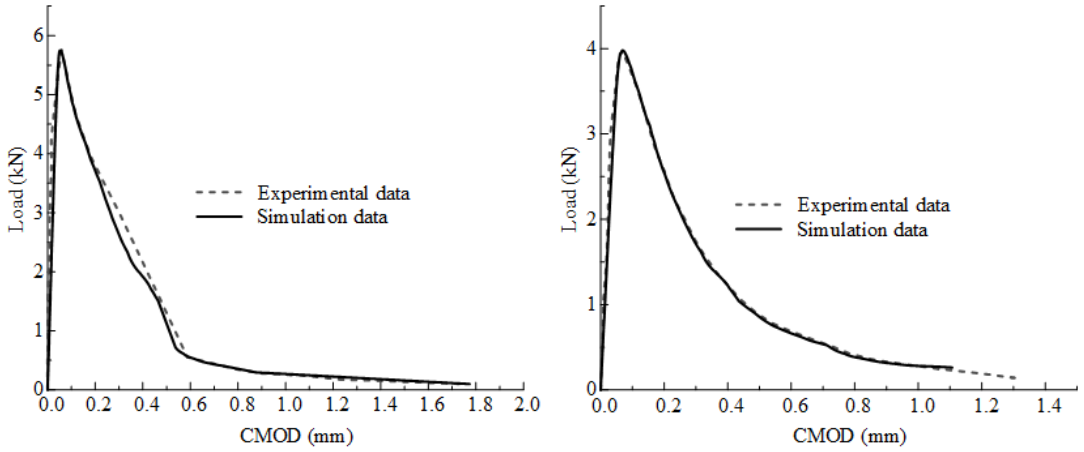

(a)

(b)

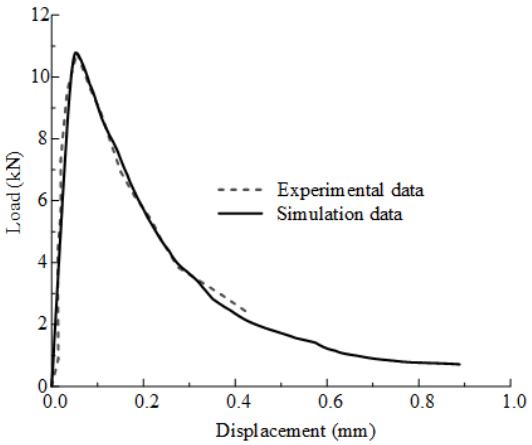

(c)

Fig. 5.24. Comparison between experimental data and numerical data: (a) Model-1, (b) Model-2, (c) Model-3

5.8 Conclusions

By combining Chapter 3 and Chapter 4, the pore phase is introduced to the phase-field model with the representative mechanical properties. The phase-field model considering plastic performance of concrete at a micro-meso structure to track crack propagation is presented. To describe complex mechanical behaviour of cementitious materials, Drucker-Prager yield criteria is employed. Compared to the traditional fracture models, spectral decomposition method is implemented to control the degradation gradient of mechanical properties, enabling the description of asymmetric tension and compression behaviours. To avoid discontinuity in concrete, the Mori-Tanaka scheme and energy dissipation theory are employed to calculate mechanical parameters of pore network. Based on this model, various simulation analyses are calibrated, simulated, and compared with experiments tested under compressive and three-point bending conditions. The influence of porosity, pore width and ITZ thickness is investigated, the primary conclusions are outlined below:

(1) MT scheme provides a reasonable estimation of mechanical behaviours of mortar solid and pore phase in micro-meso scale model for concrete. This scheme helps achieve strong alignment between the experimental data and simulation results.
(2) Monte Carlo method and Voronoi tessellation are viable and flexible techniques for generating the geometry and spatial distribution of aggregate, ITZ, pores and mortar. This geometric property allows for direct incorporation of tortuosity for concrete into the modelling process.
(3) Numerical results are compared with experimental results in terms of fracture evolution, load-displacement, as well as load-CMOD curves. The results obtained at micro-meso scale successfully reproduced the specific behaviour of crack development in concrete during compressive and three-point bending tests. The comparison for load-displacement results indicates capacity of this numerical modelling to replicate the response observed in the experiments.
(4) Investigation of ITZ thickness shows that varying ITZ thickness induces a slight impact on concrete's mechanical property. The peak loads by around 2% as the increment of ITZ thickness from 10 μm to 50 μm.
(5) Investigation of porosity demonstrates that higher porosity results in significantly altered crack propagation due to different pore paths. Increasing porosity from 9.76% to 12.86% induces a significant reduction in peak loads by about 10%.
(6) Investigation of pore widths shows that different pore widths with the same porosity induce different crack propagation branches, while causing only a slight effect on the load-displacement curve.

Integrating the proposed methodology into a fully coupled hygro-mechanical framework will allow for more accurate predictions of the mechanical behaviour under load. This in turn will enhance the

reliability of long-term performance assessments and facilitate the design of more durable concrete structures. As shown above, parameters such as shape, size of aggregate and ITZ thickness do not show an important influence on moisture diffusion. However, the effect of pores distribution requires further investigation.

Chapter 6: A Multi-scale Phase-field Model for Autogenous Shrinkage for Concrete

Abstract

Autogenous shrinkage and the resulting crack propagation in concrete are crucial factors to consider for designing large concrete structures, such as tunnels. Concrete opening microstructures presents significant challenges in understanding the hydration process, autogenous shrinkage, failure mechanisms, and predicting crack propagation paths. This paper introduces a phase-field model considering elasto-plastic behaviour to predict autogenous shrinkage and crack propagation in concrete using a micro-meso model. By combining the aggregates spatial distribution, Monte Carlo rule and Voronoi tessellation are utilized to obtain geometric details for concrete. To calibrate and calibrate this model, various specimens are subjected to autogenous shrinkage with different scales and water/cement ratios. A comparison between numerical predictions and experimental observations indicates that this proposed methodology effectively simulates autogenous shrinkage and accurately captures fracture evolution for concrete. This numerical tool will enhance reliability for long-term performance assessments and facilitate the design of more durable concrete structures.

Keywords: Porous material, Voronoi diagram, Elasto-plastic phase-field model, Micro-Meso model, Autogenous shrinkage

6.1 Introduction

Autogenous shrinkage for cementitious materials is particularly important at the early age, leading to shrinkage and stress development when the material is subjected to restrained conditions (Klausen et al., 2020, Maruyama et al., 2019, Delsaute et al., 2017). It is well established that concrete shrinkage is closely associated with the internal moisture consumption of the material (Bissonnette et al., 1999, Baroghel-Bouny et al., 1999, Wittmann, 2000, Zhang and Zhang, 2006, Zhang et al., 2010). However, evaluating shrinkage stress in a concrete structure involves understanding shrinkage deformation distribution, which, in turn, depends on the water or moisture distribution. Furthermore, the moisture distribution within pore structures directly influences stiffness, stress, creep, and thermal properties, as well as hydration degree. Crack will occur when stress caused by water loss surpasses concrete tensile stress (Wei et al., 2017, Pane et al., 2002, Shen et al., 2019, Zheng et al., 2019, Yang et al., 2021). When

cracking occurs, concrete permeability increases, leading to reduced durability (Amin et al., 2009, Sivakumar et al., 2007, Ranaivomanana et al., 2013b, Shen et al., 2021). Thus, moisture evolution and distribution, particularly at the early age, are particularly important for calculating shrinkage strain, stress, creep properties for concrete structures, as well as for predicting crack formation, durability, and lifespan.

Autogenous shrinkage, induced by volume reduction due to hydration and capillary stress from moisture loss, can be described in two stages (Zhang et al., 2010). From experimental tests, concrete internal relative humidity from casting can be divided into water saturated stage (stage I, relative humidity $RH = 1$) (Zhang et al., 2007) followed by relative humidity reduction stage (stage II, $RH < 1$) (Zhang et al., 2009). In Stage I, cement particles gradually enlarge, and neighbouring particles come into contact as portions of the surface water layer are broken. Setting occurs once the bond between solid particles becomes strong enough to support the concrete's self-weight. However, it is important to understand that hydrated cement particles connection during concrete setting will not indicate that liquid water still indicates continuity within the pore network. Consequently, internal relative humidity remains close to 1 during concrete setting process. This observation may explain why concrete's setting time occurs before internal relative humidity begins to drop from the saturation value (Zhang et al., 2012a). Chemical shrinkage induced by cement hydration continues during this process and is partially manifested as concrete macro shrinkage owing to self-restraint of hardened matrix.

In Stage II, as cement particle hydration continues, self-desiccation results in ongoing moisture loss. The curved liquid-vapor surface gradually developed inside pores to recompense for volume reduction induced by hydration process, leading to a decrease for concrete internal relative humidity. Therefore, the formation of empty capillary pores signifies the moment when concrete internal relative humidity falls below 100%, marking the transition into humidity decrease phase (Stage II). As water loss inside pores increases, due to self-desiccation, capillary stress is induced inside the pores. This stress contributes to shrinkage driven by moisture loss, which lasts until the water loss ceases.

As autogenous shrinkage results from volume reduction in a single phase for the concrete material, continuum mechanics approach cannot deal with such a problem directly. Therefore, multiscale modelling coupling moisture diffusion and failure mechanisms is necessary to fully understand autogenous shrinkage. To address this issue, numerous simulations have been carried out to analyse moisture diffusion and the failure mechanisms of concrete (Martın-Pérez et al., 2001, Samson and Marchand, 2007, de Freitas et al., 2017, Heider et al., 2020). For moisture loss, theoretical equations for liquid and vapor water based on Darcy's and Fick's second laws are widely employed to express this relationships between moisture diffusion coefficient, water saturation degree, and relative humidity (RH) (Baroghel-Bouny et al., 1999, Mounajed et al., 2004). Building upon these principles, the multi-phase modelling is developed that explicitly accounts for concrete individual phases, including mortar,

ITZ, and aggregates, as well as a homogenization phase (Caré and Hervé, 2004, Sun et al., 2011). To capture concrete's mechanical behaviour, an appropriate numerical approach and constitutive model are essential for studying its failure mechanisms. In fracture computation, smeared approaches are commonly employed, often utilizing the smeared method, which necessitates prior understanding of element enrichment theories as well as extrinsic opening and evolution standard to explicitly capture crack propagation (Zhang et al., 2018b, Zhang and Mang, 2020, Zeng et al., 2019, Zhang et al., 2021, Zhang et al., 2020). Methods includes tracking element methods (Zhang et al., 2018b, Zhang and Mang, 2020, Zeng et al., 2019, Zhang et al., 2021, Zhang et al., 2020) and fracture particle methods (Rabczuk and Belytschko, 2004, Rabczuk et al., 2010) have shown promise in efficiently handling embedded strong discontinuities.

The open and complex micro-meso structure of concrete presents a significant challenge for predicting autogenous shrinkage, particularly when considering the volume reduction of mortar and capillary stress in the pore phase. Therefore, a multiple coupling model that incorporates moisture loss, mechanical properties and crack propagation related to autogenous shrinkage with a micro-meso model, including aggregate, mortar, ITZ and pore structures, is essential for analysing and predicting these multi-physics problems in cementitious materials.

In this study, a micro-meso modelling for concrete is developed to analyse autogenous shrinkage behaviour for concrete's multiphase composition. The Monte Carlo method and Voronoi tessellation are utilized to generate the geometric properties (aggregate, mortar, ITZ, and pore structures) of concrete. The mortar solid phase is used to describe volume reduction during the hydration process, while the pore structures develop strain induced by capillary stress resulting from moisture loss. Additionally, a phase-field model with elasto-plastic mechanical behaviour is applied to predict fracture evolution for concrete under mechanical performance. This proposed model is developed based one subroutine in ABAQUS, named user-defined element (UEL). To calibrate this model, shrinkage tests on concrete cubes measuring RH and temperature are conducted, and three experiments from the relevant researches are employed to verify this proposed model. The study starts with presentation of the experimental program and results before showing the calibration and verification of this phase-field model.

Due to its enhanced predictive capabilities, the proposed modelling is also utilized to investigate multi-phase coupled systems, including thermo-hygral, hygro-mechanical, or thermo-hygro-mechanical processes. Integrating the proposed methodology into existing mechanical frameworks will increase the accuracy of predicting the material's mechanical response, including chemical shrinkage, creep, and crack development. This, in turn, will enhance the reliability of long-term performance assessments and facilitate the design of more durable concrete structures

6.2 Experimental program

6.2.1 Materials and preparation of samples

Type CEM II 32.5R of portland cement (335 kg/m³) was utilized as the cementing binder. The cement components are listed in Table 6.1. Water/cement ratio was 0.55, the superplasticizer with 2 litres per cubic meter was used in this concrete mixture. Two size ranges of river gravel were utilized: 491 kg/m³ (5-10 mm for the diameter), and 532 kg/m³ (10-14 mm for the diameter). Additionally, river sand was added as the fine aggregate with 847 kg/m³.

Table 6.1: Cement components

Oxide	Percentage (%)
Calcium Oxide (CaO)	63.87
Silicon Dioxide (SiO_2)	21.05
Aluminium Oxide (Al2O3)	4.77
Iron Oxide (Fe2O3)	3.75
Magnesium Oxide (MgO)	1.18
Sulfur Trioxide (SO3)	2.08
Sodium and Potassium Oxides (Na2O and K2O)	1.51
Other Minor Constituents	< 2

To examine the internal relative humidity (RH), as well as autogenous shrinkage, concrete cubes with size of 150 mm × 150 mm × 150 mm were cast, each sample has a hole with 60 mm depth. During casting, moulds were filled with fresh concrete, and having steel sockets centrally embedded to create voids for the sensors, as shown in Fig. 6.1. After vibration, specimens were covered by plastic sheet to retain water during curing, which was conducted at laboratory conditions (18 ± 3 °C) for 1 day. These specimens were demoulded the following day, and then sealed with aluminium foil on all surfaces, as indicated in Fig. 6.1(c).

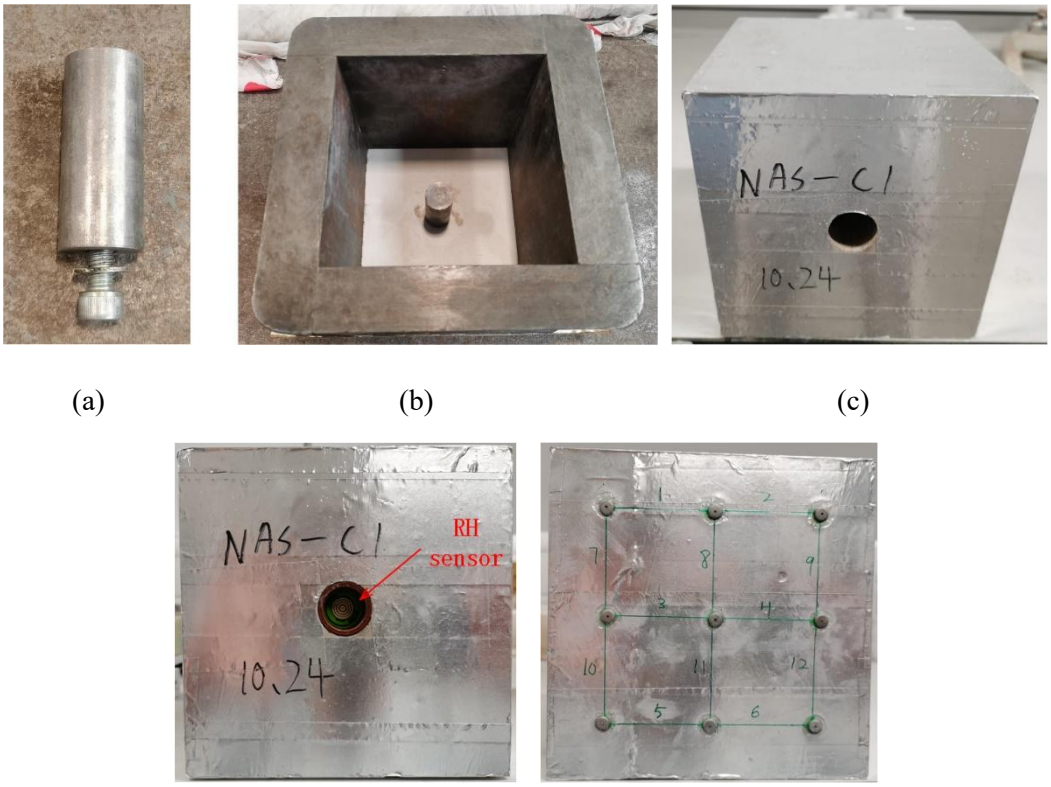

(a) (b) (c)

(d) (e)

Fig. 6.1. Moulds for concrete casting: (a) Sockets, (b) Moulds, (c) Specimen, (d) RH sensor, (e) DEMEC points

6.2.2 RH and strain measurements

Selecting an appropriate sensor for measuring the RH inside concrete is crucial, as it needs to accurately measure RH in early-age concrete (water-saturated stage) while providing reliable results. To minimize the sensor's impact on the measurement, the size of the sensor is critical, as it must effectively capture the local RH within the concrete. Considering these challenges, the Rapid RH L6 single-use sensor was selected for this study. ISO/IEC 17025 standards are employed to calibrate RH sensors. For the 0-90% RH range, the sensors have an accuracy of 1.5%. For the RH ranging from 90% to 100%, accuracy is 1.8%.

For strain measurement, DEMEC strain gauge with gauge lengths of 50 mm is utilized in this test. A typical specimen of autogenous shrinkage test is illustrated in Fig. 6.1(d) and Fig. 6.1(e). The concrete specimen has dimensions of 150 mm × 150 mm × 150 mm, with an embedded RH sensor placed in a 60 mm deep hole. DEMEC points were installed on the surface with distances of 50 mm between them. After sensor installation, specimens were stored at the room with a constant temperature (18 ± 3 ℃). The internal RH and autogenous shrinkage were measured using the embedded sensor and DEMEC points.

6.3 Results and discussion

6.3.1 Basic mechanical properties

According to BS EN 12390-3: 2009 (Standard, 2009), mortar specimens (50 mm × 50 mm × 50 mm) and plain concrete cubes (75 mm × 75 mm × 75 mm) were conducted to obtain the mechanical parameters, such as Young's modulus (E), Poisson's ratio (v) and Yield stress (σ_y), under uniaxial compressive loading with the loading rate of 0.6 N/mm^2/s. To obtain the 2D scanner marking points and camera were used to monitor and record the movement of marking points (Chapter 3). The parameters of mortar and concrete are listed in Table 6.2. And load-displacement and stress-strain results are depicted in Fig. 6.2.

Table 6.2: Basic mechanical parameters of mortar and concrete

Specimen	Compressive strength (MPa)	Peak load (kN)	Porosity (%)
Mortar A	40.9	102.3	16.8
Mortar B	40.6	101.5	17.0
Mortar C	40.3	100.8	17.2
Concrete A	41.2	231.5	11.4
Concrete B	39.4	221.6	11.0

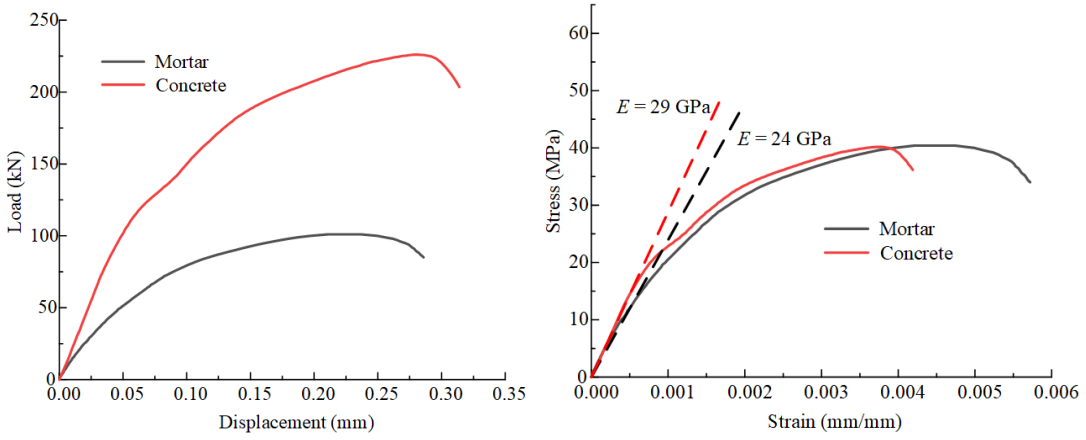

(a) (b)

Fig. 6.2. Compressive results of mortar and concrete specimens: (a) load-displacement, (b) stress-strain

6.3.2 Internal relative humidity and ambient temperature

To evaluate the effect of RH evolution on autogenous shrinkage, internal RH is measured at the pre-designed hole with the depth of 60 mm, as shown in Fig. 6.3.

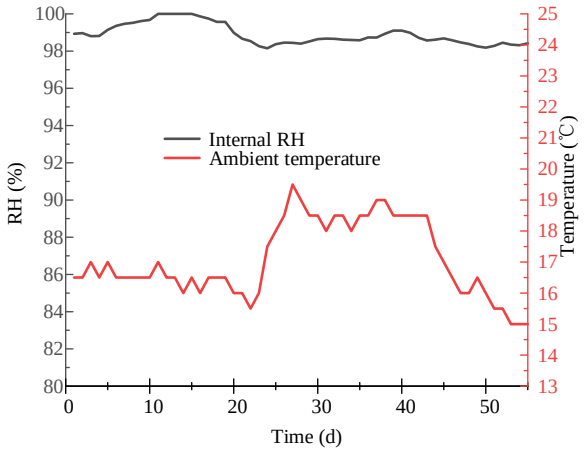

Fig. 6.3. Measured internal RH and ambient temperature

The high water/cement ratio (0.55) induces the continuity of liquid water in the network remains intact. Therefore, the internal RH remains close to 100%. At this stage, the moisture condition is still in Stage I, and the influence of capillary stress induced by water loss are negligible. Thus, at this stage volume reduction is the result of volume change in hydration products.

6.3.3 Autogenous shrinkage

Autogenous shrinkage at three depths (top, in height 125mm, mid, in height 75mm and bottom, in height 25mm) was measured over time for concrete specimens, as shown in Fig. 6.4.

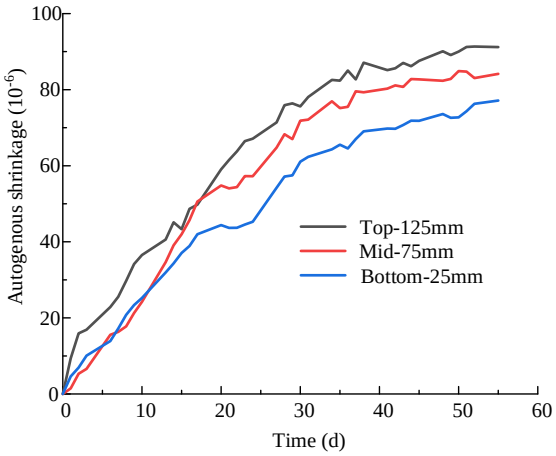

Fig. 6.4. Autogenous shrinkage of different height

From Fig. 6.4, autogenous shrinkage is shown to increase with increasing height owing to the aggregate spatial non-uniform location. As described in the study (Al-Kamyani et al., 2018), aggregate spatial distribution varies within the depth, The aggregate content increases from 35.5% at the top to 41.6% at the bottom in each quarter. More cement increases total volume reduction, while more aggregates increase the elastic modulus and self-restraint. Therefore, the bottom exhibits slightly lower autogenous shrinkage compared to the top.

6.4 Geometric properties of Micro-Meso of concrete

To correspond to the geometric properties from the concrete model, a combination of mesoscale and microscale models is used to generate four phases: aggregate, ITZ, mortar, and pores. The following sections describe the parameters necessary to ensure concrete geometry for all components and outline the methodology used to develop the mesoscale model.

6.4.1 Spatial distribution and shapes of aggregate

To account for the non-uniform aggregate spatial distribution (Al-Kamyani et al., 2018), concrete geometric properties are divided into four cross-sections along the height. Monte Carlo method is then employed for locating centroid and diameter for each aggregate and to generate their in-plane spatial distribution for each cross-section (Rajamani et al., 1986, Huang et al., 2022). This method ensures that individual aggregates do not overlap and that each aggregate is positioned within the specimen's boundaries. To generate the polygonal aggregates, the Fuller distribution is utilized to determine edge number and angles (α). Further details for this method can be found in the Chapter 2.

Based on the concrete mix design from the author's previous study, polyhedral-shaped aggregates were generated in two diameter ranges: 5-10 mm and 10-14 mm, with a volume fraction ratio of 0.48:0.52. Overall aggregate volume content was approximately 40%, determined by the mix design and the

density of aggregate (2590 kg/m³). Combining this with the spatial distribution of aggregate (Al-Kamyani et al., 2018), different volume fractions were generated along the height of the specimen: top (36.51%), mid-top (38.56%), mid-bottom (40.62%), and bottom (42.67%), as shown in Fig. 6.5.

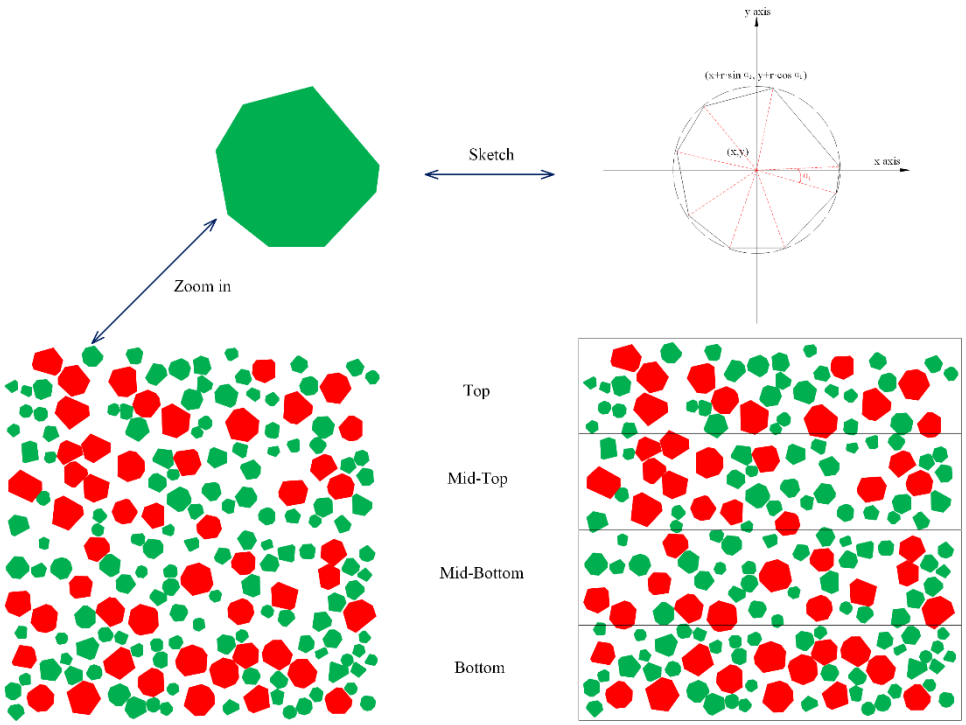

Fig. 6.5. 2-D random distribution of polygonal aggregates

6.4.2 Geometric properties of the ITZ

A key characteristic of concrete is the heterogeneity introduced by adding aggregates into the mortar solid, resulting in the ITZ. According to previous literature, ITZ phase is modelled as the thin layer with a thickness ranging from 10 to 50 μm along with aggregate particles (Shuguang et al., 2015). Therefore, the ITZ is generated based on aggregate geometry, with a thickness *"t"* (see Fig. 6.6). In this study, a thickness of 30 μm was used, following the author's previous research (Chapter 2).

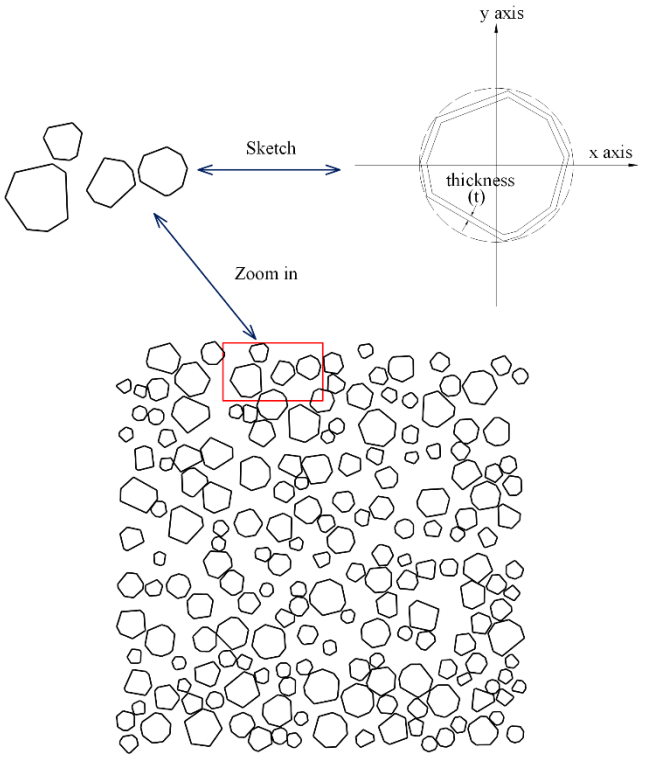

Fig. 6.6. 2-D random distribution of polygonal ITZ

6.4.3 Geometric properties of the pore structures

In this study, the pore phase is considered to be embedded within the mortar phase as a network rather than as voids. This modelling can therefore be utilized not only to predict concrete mechanical behaviour but also to address multiple coupled phenomena, including thermal expansion, shrinkage, chemical reactions, and creep (Chapter 2).

To create the pore structure as a network, the Voronoi tessellation method for polygonal geometrical elements is adopted (Idiart, 2009). This method generates an array of randomly allocated nodes, positioned at the centroids of the Voronoi regions within the mortar. These nodes are interconnected via equidistant segments that either intersect or meet at the ITZ, as depicted in Fig. 6.7(a) and Fig. 6.7(b). The total area of the pore network is determined based on experimentally derived porosity.

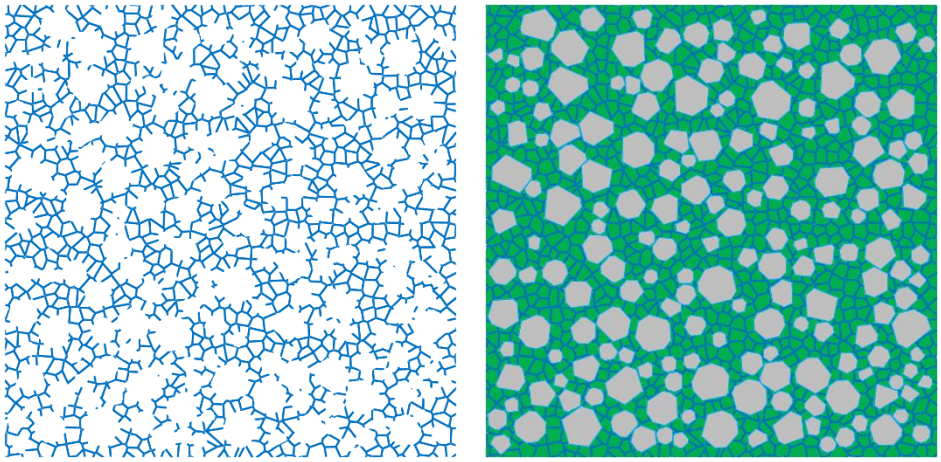

(a) (b)

Fig. 6.7. Geometric properties of specimen: (a) capillary structure, (b) overall framework

6.5 Model for autogenous shrinkage of concrete

In this part, the multi-coupling phase-field model employing elasto-plastic theory is introduced for assessing concrete mechanical behaviours at a micro-meso level. This model enables autogenous shrinkage analysis, moisture loss, and crack development. A finite element framework for this model is proposed based on this theory. Further details regarding moisture loss and the phase-field model are available in the Chapter 5.

6.5.1 Moisture loss model

Moisture loss in concrete includes self-desiccation and moisture transport, both contributing to water and vapour loss as a result of hydration and drying processes (Damrongwiriyanupap et al., 2013, Caré, 2003, Ye et al., 2006, Ding et al., 2019). Desorption occurs when concrete is exposed to an environment with relatively low RH. Liquid water diffuses due to capillary stress, while vapour water diffuses through pores that are partially unoccupied by liquid, driven by gas pressure differentials. For the purposes of this autogenous shrinkage study, moisture transport induced by the drying process is ignored.

The concrete hydration degree can be calculated as (Pang et al., 2013, Meyer and Xueyu, 2012):

$$\alpha = \frac{H(t)}{H^0} = \frac{CS(t)}{CS^0} = \frac{w_n(t)}{w_n^0} \tag{6.1}$$

where, $H(t)$, $CS(t)$, and $w_n(t)$ represent cumulative heat generation, chemical shrinkage, and non-evaporable moisture content, at time t, respectively; H^0, CS^0, and w_n^0 represent cumulative heat generation, total chemical shrinkage, and non-evaporable moisture content for a fully hydrated cement.

Based on the Eq. (6.1), the hydration degree is obtained using autogenous shrinkage, hydration degree over time can then be simulated as (Zhang et al., 2009, Wang et al., 2018):

$$\alpha = \alpha_u \exp\left[-\left(\frac{A}{t_e + t_0}\right)^B\right] \tag{6.2}$$

where, A, B and t_0 represent three materials constants. α_u represents the ultimate hydration degree, which is usually associated with water to cement ratio (w/c) as (Rastrup, 1954):

$$\alpha_u = \frac{1.031 w/c}{0.194 + w/c} \tag{6.3}$$

Power's Volumetric Model is normally employed to describe water loss due to self-desiccation (Powers and Brownyard, 1946). Primary measurements by Power and Brownyard (Powers and Brownyard, 1946), as well as later measurements by Brouwer (Brouwers and Research, 2004), demonstrated that the amount of water consumption for chemical and C-S-H gel water per gram and can be correlated with cement particles as:

$$w_t = 0.334 x_{C_3S} + 0.374 x_{C_2S} + 1.410 x_{C_3A} + 0.471 x_{C_4AF} + 0.261 x_{C\bar{S}} \tag{6.4}$$

where, w_t represents ultimate chemical and gel water consumption weight per gram cement. x represents each cement particles weight ratio.

6.5.2 Phase-field mechanical model

To capture concrete's complex mechanical properties, including elasto-plastic behaviour, unsymmetric tension-compression behaviour, stiffness degradation, and crack propagation, a micro-meso phase-field model employing elasto-plastic behaviour is utilized, incorporating spectral decomposition method (Chapter 3).

To couple crack development with the deformation problem, total potential energy Π of the fracture domain Ω is considered as a composition of mechanical and crack energies. The equation is as follows:

$$\Pi = E(u,d) + P(u,d) + W(d) = \int_\Omega \psi_\varepsilon\left(\varepsilon(u), d\right) d\Omega + \int_\Gamma g_c d\Gamma \tag{6.5}$$

where, $E(u,d)$ represents elastic energy, $P(u,d)$ represents plastic energy, $W(d)$ represents fracture energy, u represents displacement variables, $\varepsilon(u)$ represents strain tensor, ψ_ε represents mechanical energy, and g_c represents critical energy threshold, Γ represents fracture surface.

In elastic energy degradation, only tensile stress contributes to damage and crack development. The effect of cracks on stiffness reduction is then considered. Elastic energy function is given as follows (Liu et al., 2016):

$$\psi_{\varepsilon}^{el}\left(\varepsilon(u),d\right)=g\left(d\right)\cdot\psi_{0}^{el+}\left(\varepsilon\right)+\psi_{0}^{el-}\left(\varepsilon\right) \tag{6.6}$$

The definition of positive and negative energy components may differ depending on the implementation. As for brittle materials, they are defined as follows (Amor et al., 2009, Freddi et al., 2010):

$$\psi_{\varepsilon}^{el}\left(\varepsilon(u),d\right)=\mu\sum_{i=1}^{3}\left[\left\langle\varepsilon_{i}\right\rangle_{-}^{2}+g\left(d\right)\left\langle\varepsilon_{i}\right\rangle_{+}^{2}\right]+\frac{\lambda}{2}\left[g\left(d\right)\left\langle tr\left(\varepsilon\right)\right\rangle_{+}^{2}+\left\langle tr\left(\varepsilon\right)\right\rangle_{-}^{2}\right] \tag{6.7}$$

To capture concrete's nonlinear mechanical behaviour under tension and compression loads, the implementation supports the Drucker-Prager (Drucker and Prager, 1952) yield criterion:

$$f\left(I_{1},J_{2}\right)=\sqrt{J_{2}}+\beta_{DP}I_{1}-g\left(d\right)\left[\sigma^{\lim}+H\varepsilon_{eq}^{pl}\right] \tag{6.8}$$

As there is no permanent volume change, ductile component of the history energy is represented as a equation between yield stress and energy-equivalent plastic strain:

$$\psi_{0}^{pl}\left(\varepsilon_{eq}^{pl}\left(u\right)\right)=\varepsilon_{eq}^{pl}\left(u\right)\left[\sigma^{\lim}+\frac{1}{2}H\varepsilon_{eq}^{pl}\left(u\right)\right] \tag{6.9}$$

The plastic energy function is describe by using the Drucker-Prager (Drucker and Prager, 1952) yield criterion, which is described by flow rules as follows (Krabbenhøft, 2002):

$$\begin{aligned}\psi_{\varepsilon}^{pl}&=g\left(d\right)\psi_{0}^{pl}=g\left(d\right)\left(\varepsilon_{eq}^{pl}\right)^{T}K_{0}\varepsilon_{eq}^{pl}\\K_{0}&=\left(K-\frac{K\dfrac{\partial g}{\partial\sigma}\left(\dfrac{\partial f}{\partial\sigma}\right)^{T}K}{H+\left(\dfrac{\partial f}{\partial\sigma}\right)^{T}D\dfrac{\partial g}{\partial\sigma}}\right)\end{aligned} \tag{6.10}$$

where, K represents elastic constitutive matrix, K_0 represents the elasto-plastic constitutive matrix, g and f are the plastic energy.

Consequently, potential energy function is constructed by combining elastic energy, plastic energy, and fracture energy, as follows:

$$\Pi=\int_{\Omega}\left\{g\left(d\right)\left[\psi_0^{el+}\left(\varepsilon\right)+\psi_0^{pl}\left(\varepsilon\right)-\psi_c\right]+\psi_0^{el-}\left(\varepsilon\right)+\psi_c+2l_c\psi_c\left[d^2+l_c^2\left|\nabla d\right|^2\right]\right\}d\Omega \tag{6.11}$$

To analyse the multi-phase field model of concrete, including its individual constituents (mortar, ITZ, aggregates, and pores), the potential energy function is proposed based on a homogeneous solid. Since the critical fracture energy of the aggregate component is significantly higher than that of ITZ part and mortar part, the aggregate is considered to be an elastic part. Mortar and ITZ are treated as elasto-plastic crack propagation parts. Therefore, the crack geometry of mortar, ITZ and pores is described by diffused parameter $d_M(x)$, $d_I(x)$ and $d_P(x)$, respectively, which are described as follows:

$$\begin{cases}\gamma_M\left(d_M,\nabla d_M\right)=\dfrac{{d_M}^2}{2l_c}+\dfrac{l_c}{2}\left|\nabla d_M\right|^2\\ \gamma_I\left(d_I,\nabla d_I\right)=\dfrac{{d_I}^2}{2l_c}+\dfrac{l_c}{2}\left|\nabla d_I\right|^2\\ \gamma_P\left(d_P,\nabla d_P\right)=\dfrac{{d_P}^2}{2l_c}+\dfrac{l_c}{2}\left|\nabla d_P\right|^2\end{cases} \tag{6.12}$$

By introducing the potential energy correction parameter β into the total potential energy Eqs. (6.11) and (6.12), the total potential energy is decomposed into energies corresponding to the mortar, ITZ, pores and aggregates, as follows:

$$\Pi=\int_{\Omega}\begin{Bmatrix}V_M\left(\left(\varepsilon_{eq}^{el}\right)^T\left(K_M\right)\varepsilon_{eq}^{el}+\left(\varepsilon_{eq}^{pl}\right)^T g\left(d\right)K_{M0}\varepsilon_{eq}^{pl}+\left(1-g\left(d\right)\right)\dfrac{g_M}{2l_c}+g_M\gamma\left(d,\nabla d\right)\right)\\ +V_I\left(\left(\varepsilon_{eq}^{el}\right)^T\left(K_I\right)\varepsilon_{eq}^{el}+\left(\varepsilon_{eq}^{pl}\right)^T g\left(d\right)K_{I0}\varepsilon^{eq}+\left(1-g\left(d\right)\right)\dfrac{g_I}{2l_c}+g_I\gamma\left(d,\nabla d\right)\right)\\ +V_P\left(\left(\varepsilon_{eq}^{el}\right)^T\left(K_P\right)\varepsilon_{eq}^{el}+\left(\varepsilon_{eq}^{pl}\right)^T g\left(d\right)K_{P0}\varepsilon^{eq}+\left(1-g\left(d\right)\right)\dfrac{g_P}{2l_c}+g_P\gamma\left(d,\nabla d\right)\right)\\ +V_A\left(\left(\varepsilon_{eq}\right)^T K_A\varepsilon_{eq}\right)\end{Bmatrix}d\Omega \tag{6.13}$$

where, K_M, K_I, K_P and K_A are the elastic constitutive matrix of mortar, ITZ, pores and aggregate, K_{M0}, K_P and K_{I0} are the elasto-plastic constitutive matrix of mortar, pores and ITZ.

$$\begin{cases}\boldsymbol{Vg}\Delta\boldsymbol{\gamma}\left(d,\nabla d\right)\beta=\left(1-d\right)H^1\\ \beta=\dfrac{H^1}{H^1+\Delta\psi}\\ \Delta\psi=\left(V_M^1\psi_{M0}^{el-}+V_I^1\psi_{I0}^{el-}+V_P^1\psi_{P0}^{el-}+V_A^1\psi_A^{el}\right)-\left(V_M^2\psi_{M0}^{el-}+V_I^2\psi_{I0}^{el-}+V_P^2\psi_{P0}^{el-}+V_A^2\psi_A^{el}\right)\end{cases} \tag{6.14}$$

where, H^l is the history energy of reference sample, β is the potential energy correction parameter.

More details of this proposed multi-phase elasto-plastic phase-field model can be found in Chapter 5.

6.5.3 Autogenous shrinkage model

Autogenous shrinkage involves both chemical volume reduction and water consumption within the pores. In this research, high water/cement ratio results in extra free water inside the pores, meaning the hydration process remains in Stage I, and the influence of capillary stress induced by water loss are ignored. Therefore, only the volume reduction of hydration products is considered in this study.

According to test results from the literature (Powers and Brownyard, 1946, Brouwers and Research, 2004), and cement composition employed in this study, chemical shrinkage for cement matrix ranges between 0.055 and 0.057 cm^3 per gram of reacted cement. Therefore, chemical shrinkage can be determined by (Ding et al., 2019):

$$\begin{aligned} V_{cs} &= 0.056 M_c \alpha \\ \varepsilon_{cs} &= \sqrt[3]{V_{cs}} \end{aligned} \tag{6.15}$$

where, V_{cs} is chemical shrinkage, Mc represents mass of cement particles, α represents hydration degree.

Following Stage I, internal RH enters the moisture reduction phase (Stage II). Autogenous shrinkage due to water consumption is induced by the capillary stress of water loss (Mindess et al., 2003). Therefore, capillary stress mechanism can be used to calculate shrinkage due to moisture loss using Mackenzie-Bentz formulation (Mackenzie, 1950, Bentz et al., 1998):

$$\varepsilon_p = \frac{S}{3} P_{cap} \left(\frac{1}{K} - \frac{1}{K_s} \right) \tag{6.16}$$

where, S represents volumetric saturation degree, K represents bulk modulus for harden cement paste, K_s represents bulk modulus for the solid skeleton of harden cement paste (e.g., C-S-H or unreacted solids).

The capillary stress can be calculated using Kelvin-Laplace equation by surface tension, as shown below (Adamson and Gast, 1967):

$$P_{cap} = \frac{-\ln\left(RH/100\right) \square R \square T_0}{V_m} \tag{6.17}$$

where, R represents universal gas constant, RH represents internal relative humidity, T_0 represents absolute temperature, V_m represents water molar volume.

The initial mechanical strain and shrinkage strain together constitute total measured performance for concrete specimen. The total strain can be determined by employing superposition principle, as follows (Orta and Bartlett, 2014, Fisher et al., 1981):

$$\varepsilon_{total} = \varepsilon_{el} + \varepsilon_{pl} + \varepsilon_{cs} \tag{6.18}$$

where, ε_{total} is the total strain, ε_{el} represents elastic strain, ε_{pl} represents plastic strain, and ε_{cs} represents autogenous shrinkage.

Therefore, this multi-phase model of concrete is described with four phases as follows:

$$\begin{cases} \varepsilon_{total}^{M} = \varepsilon_{el}^{M} + \varepsilon_{pl}^{M} + \varepsilon_{cs}^{M} \\ \varepsilon_{total}^{ITZ} = \varepsilon_{el}^{ITZ} + \varepsilon_{pl}^{ITZ} \\ \varepsilon_{total}^{Pore} = \varepsilon_{el}^{Pore} + \varepsilon_{pl}^{Pore} + \varepsilon_{cs}^{Pore} \\ \varepsilon_{total}^{Agg} = \varepsilon_{el}^{Agg} \end{cases} \tag{6.19}$$

where, ε_{total}^{i} ($i = M, ITZ, Pore, Agg$) is the total strain of mortar, ITZ, pore and aggregate phases, ε_{el}^{i} ($i = M, ITZ, Pore, Agg$) is the elastic strain of mortar, ITZ, pore and aggregate phases, ε_{pl}^{i} ($i = M, ITZ, Pore$) is the plastic strain of mortar, ITZ and pore phases, ε_{cs}^{M} is the autogenous shrinkage of chemical volume reduction for mortar phase, ε_{cs}^{Pore} is the autogenous shrinkage of moisture loss for pore phase.

6.6 Calibration and calibration of autogenous model

6.6.1 Calibration of autogenous model

The numerical modelling is calibrated and verified in two parts: (1) autogenous shrinkage evolution over time, and (2) autogenous shrinkage prediction for different depths.

To calibrate the autogenous shrinkage model, concrete cubes were simulated for predicting both crack propagation and autogenous shrinkage, and results were evaluated using the experimental data from Section 6.3. In this simulation, a square domain (with a length L = 150 mm) was used, with bottom boundary is controlled in both x and y directions as shown in Fig. 6.8. The same element size for all phases, including mortar, ITZ, pores and aggregate, was employed with h = 0.5 mm, comprising 370448 triangular elements. The parameters used for hydration process and mechanical behaviour are depicted in Table 6.3 and Table 6.4.

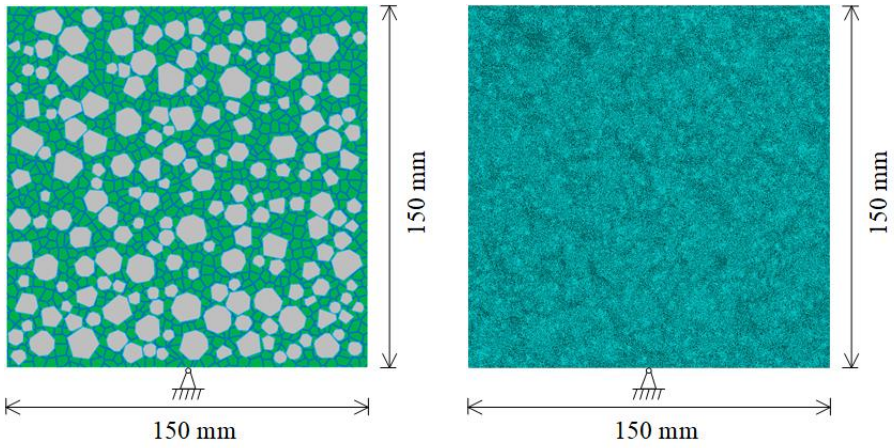

(a) (b)

Fig. 6.8. Details of model: (a) geometry and boundary condition (b) element size

Table 6.3: Parameters for hydration process

Specimen	A	B	t_0
Concrete	11610	1028	11600

Table 6.4: Parameters for concrete samples of phase field

	E GPa	v	σ_{y1}^{c} MPa	H_1 GPa	σ_{y2}^{c} MPa	H_2 GPa	σ_{y}^{t} MPa	l_c mm	β	β_{DP}	ψ_c^c MPa	ψ_c^c MPa
Aggregate	40	0.2	-	-	-	-	-	-	-	-	-	-
Mortar	23.9	0.2	16	13	30	4.6	3.6	1	1	0.37	1.1	0.0105
ITZ	12	0.2	16	6.5	30	2.3	3.6	1	1	0.37	0.55	0.0053

From this model, fracture evolution branch is analysed, as shown in Fig. 6.9. The comparison of autogenous shrinkage at different depths between numerical and experiment results is presented in Fig. 6.10.

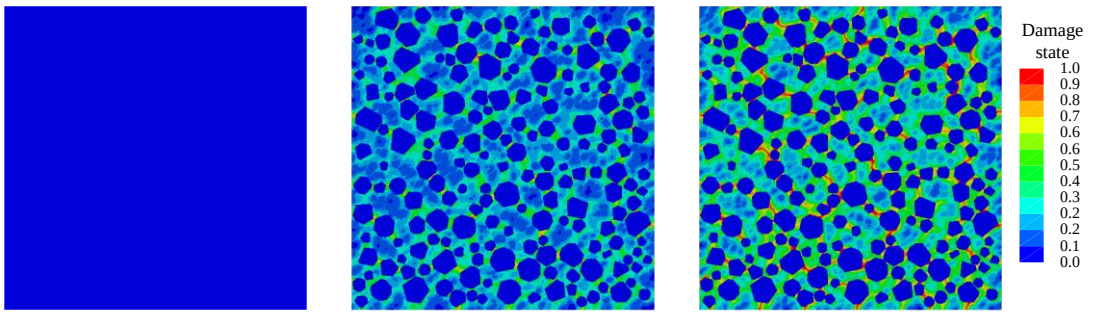

(a) (b) (c)

Fig. 6.9. Damage state at different time: (a) 3 day, (b) 25 day, (c) 50 day

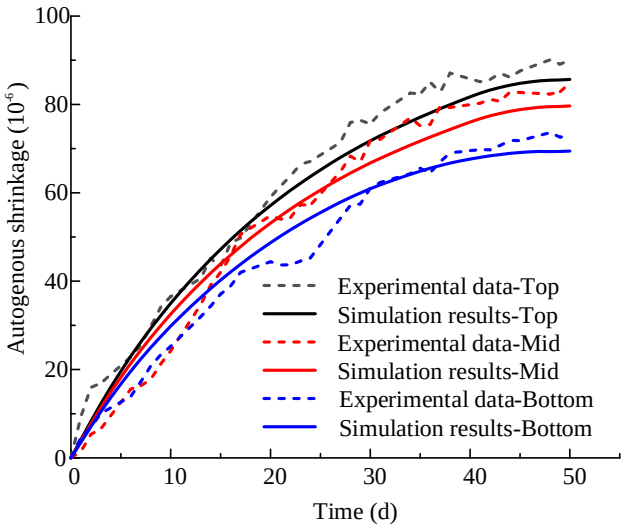

Fig. 6.10. Comparison of autogenous shrinkage between experimental data and simulation results at different depth

From Fig. 6.9, it is noted that fracture evolution paths tend to develop along ITZ and pore structures, as the ITZ and pore phases are more prone to breakage compared to the mortar. However, crack propagation begins on the 3rd day rather than the 1st, which can be attributed to gradual increment of mechanical properties over hydration degree. In this simulation, mechanical properties used were from the concrete at the 28th day, rather than varying with the hydration process. This is also evident from Fig. 6.10. where the autogenous shrinkage shows a similar trend at different depths, but the simulated shrinkage is lower than the experimental data at all depths. This discrepancy arises because higher mechanical properties lead to better resistance to deformation, resulting in lower shrinkage deformation.

6.6.2 Calibration of autogenous model with mesoscale specimen

To calibrate the proposed autogenous model and crack propagation path, an image of a concrete sample (C-0.25-SF) from X-ray μCT is used to predict autogenous shrinkage and crack propagation in early-age concrete (Mac et al., 2021a, Yio et al., 2021). The lidded plastic moulds were utilized to cast

cylindrical samples (95Ø × 65 mm) with curing 14 days. After curing process, the cores (30 mm in diameter) of cylindrical specimens were extracted from centre position to record the image using X-ray μCT. A square domain (20 mm × 20 mm) of the cylindrical core slice was zoomed in to observe crack propagation. More details regarding the experiments and concrete mix are available in research (Mac et al., 2021a, Yio et al., 2021).The concrete specimen images are depicted in Fig. 6.11(a), the greyscale images of the concrete specimen are depicted in Fig. 6.11(b).

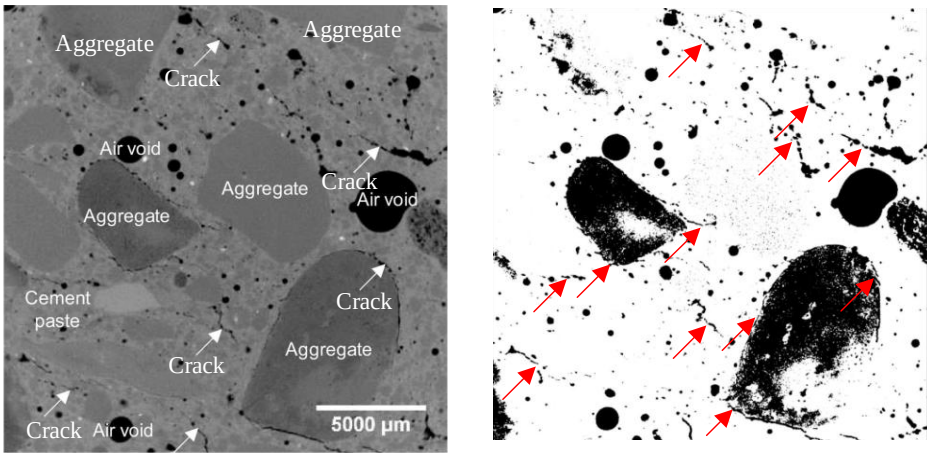

(a) (b)

Fig. 6.11. X-ray μCT image for: (a) concrete specimen, (b) grey image (Mac et al., 2021a)

In this simulation, ImageJ was utilized to determine concrete meso-model, incorporating mortar matrix, aggregate, ITZ, and pores. The geometric properties for this numerical model are depicted in Fig. 6.12(a). The element size of this specimen is h = 0.1 mm for all phases, and the specimen includes 126409 triangular elements, as depicted in Fig. 6.12(b).

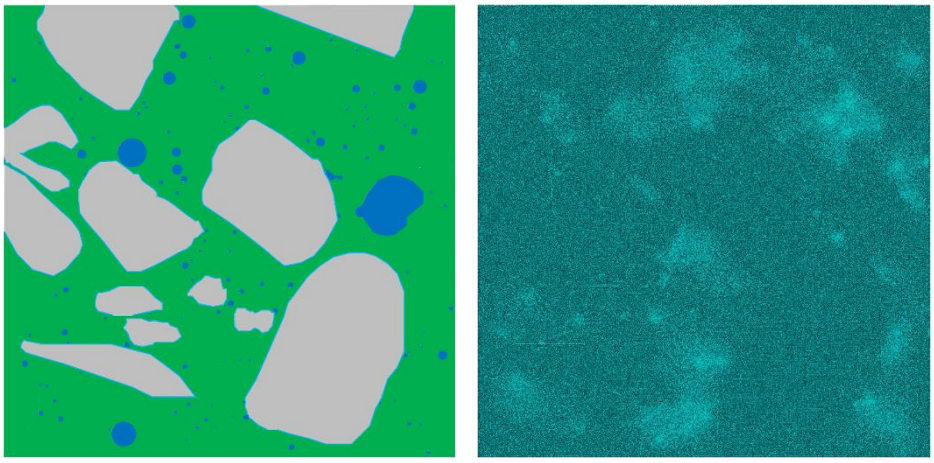

(a) (b)

Fig. 6.12. Details of model: (a) geometric properties (b) mesh size

The parameters used for hydration evolution and mechanical properties are depicted in Table 6.5 and Table 6.6. To verify theoretical modelling, autogenous shrinkage is compared between experimental and numerical results, as depicted in Fig. 6.13. To analyse fracture evolution induced by autogenous shrinkage, the crack development path is compared at 14 days, as shown in Fig. 6.14.

Table 6.5: Parameters for hydration process

Specimen	A	B	t_0
C-0.25-SF	7.58	1.05	2.77

Table 6.6: Parameters for concrete samples of phase field

	E GPa	v	σ_{y1}^{c} MPa	H_1 GPa	σ_{y}^{t} MPa	l_c mm	β	β_{DP}	ψ_c^c MPa	ψ_c^c MPa
Aggregate	50	0.2	-	-	-	-	-	-	-	-
Mortar	48	0.2	16	23	4.3	1	1	0.37	1.76	0.014
ITZ	12	0.2	16	6.5	4.3	1	1	0.37	0.55	0.0053

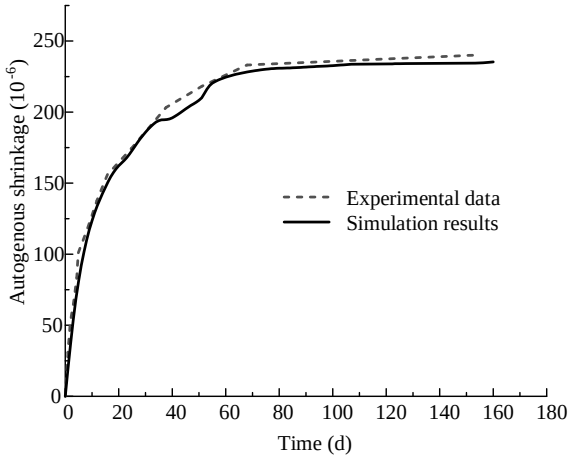

Fig. 6.13. Comparison of autogenous shrinkage between experimental data and simulation results

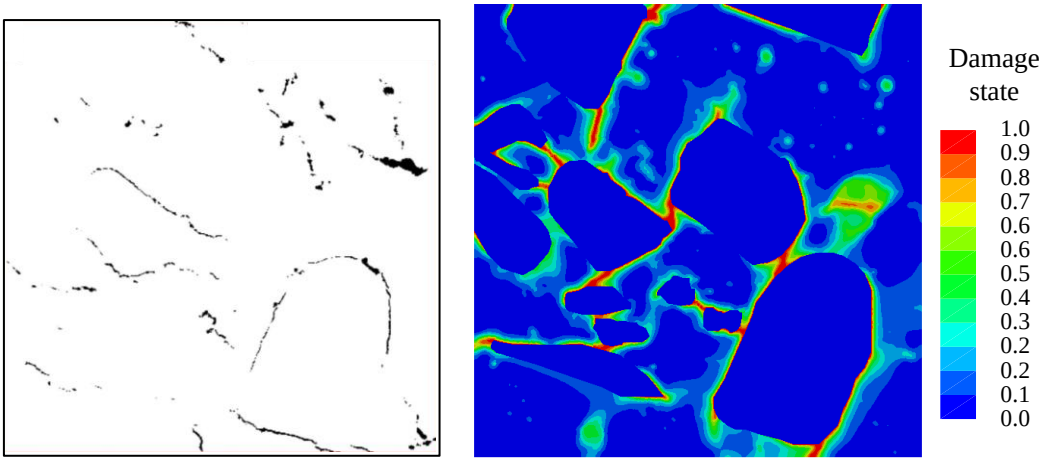

(a) (b)

Fig. 6.14. Crack propagation results of: (a) experiment (Mac et al., 2021a), (b) simulation

As observed in Fig. 6.13, a comparison for autogenous shrinkage between numerical and experimental results shows strong agreement. However, the simulation results display slightly lower autogenous shrinkage compared to the experimental data. This discrepancy arises because the mechanical properties in the simulation are calibrated as constants throughout the entire hydration process, whereas, in reality, concrete mechanical parameters increase over hydration degree. This results in a higher stiffness matrix, leading to lower shrinkage deformation. In Fig. 6.14, the crack propagation also shows strong agreement. The crack paths tend to develop along the ITZ and pore structures, as these phases are more prone to breakage compared to the mortar.

6.6.3 Calibration of autogenous model with different mix of mesoscale specimens

Cylindrical specimens (95Ø × 65 mm) with two mixes (C-AS-0.25 and C-AS-0.30) were used to calibrate the autogenous shrinkage and crack evolution in a circular domain (30 mm in diameter) (Yio et al., 2021, Mac et al., 2021b). After 14 days of curing, cylindrical cores with a diameter of 30 mm were extracted from specimen centre for every sample to record images utilizing X-ray μCT. The circular domain of the cylindrical core slice was zoomed in to observe the autogenous shrinkage microcracks. Further details of the experiments and concrete mix are available in research (Yio et al., 2021, Mac et al., 2021b). The images for concrete specimen with microcrack are depicted in Fig. 6.15.

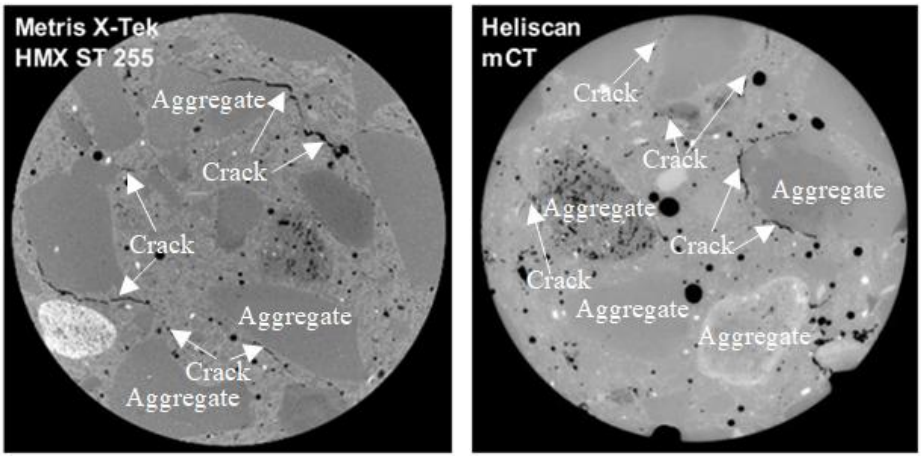

(a) (b)

Fig. 6.15. X-ray μCT images of: (a) C-AS-0.25, (b) C-AS-0.30 (Mac et al., 2021b)

In the simulations, ImageJ was utilized to obtain concrete meso model, incorporating mortar matrix, aggregate, ITZ, and pores. The geometric properties for the models are depicted in Fig. 6.16. The specimen element size is h = 0.1 mm for all phases, and the specimen includes 162897 and 160363 triangular elements.

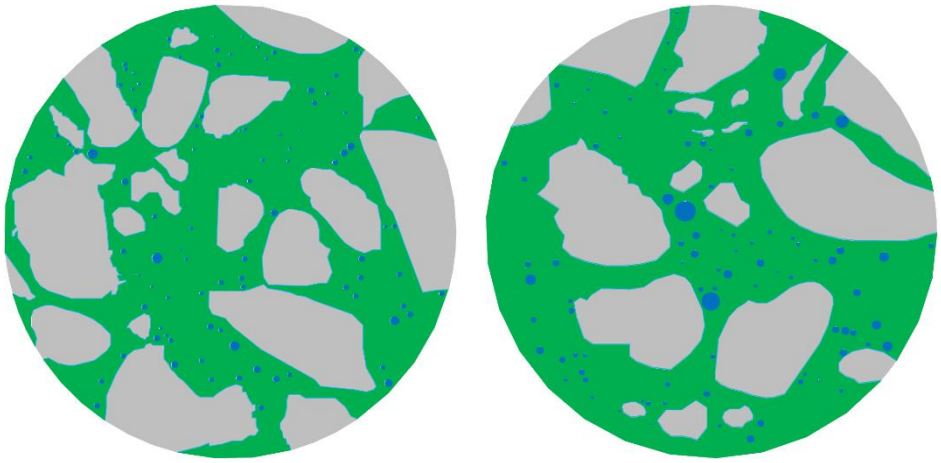

(a) (b)

Fig. 6.16. Geometric properties of models: (a) C-AS-0.25 (b) C-AS-0.30

The parameters used for the hydration process and mechanical performance are depicted in Table 6.7 and Table 6.6. The potential energy correction parameter is 0.92 for the mortar, ITZ, and pore structures of sample C-AS-0.30. To compare and calibrate the theoretical model, autogenous shrinkage is compared, as depicted in Fig. 6.17. To analyse the crack propagation induced by autogenous shrinkage, the crack development path is compared at 14 days, as shown in Fig. 6.18.

Table 6.7: Parameters for hydration process of concrete specimens

Specimen	A	B	t_0
C-AS-0.25	7.58	1.05	2.77
C-AS-0.30	6.9	1.08	1.64

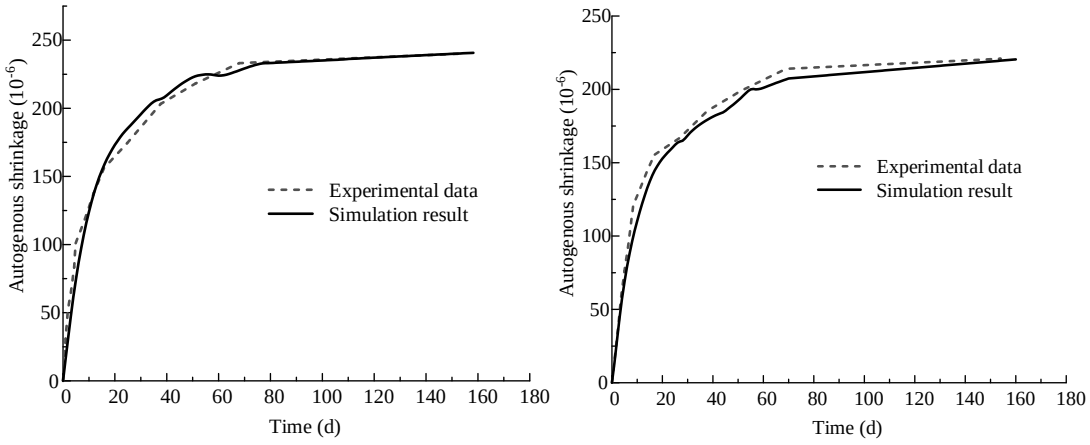

Fig. 6.17. Comparison of autogenous shrinkage of different specimens: (a) C-AS-0.25, (b) C-AS-0.30

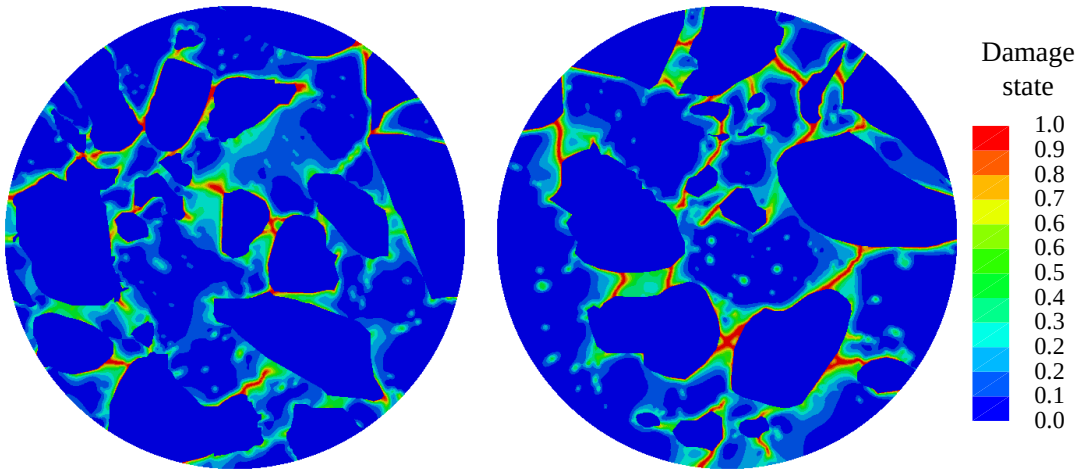

Fig. 6.18. Damage state evolution of specimens: (a) C-AS-0.25, (b) C-AS-0.30

As observed in Fig. 6.17, the autogenous shrinkage comparison between the simulation and experimental data shows strong agreement. From Fig. 6.18, fracture propagation exhibits a similar trend along the ITZ and pores, which is attributed to mechanical parameters for two phases. However, the numerical results show more crack paths than the experimental observations. This discrepancy arises

because accuracy for the images is obtained by maximum pixel resolution from the X-ray and computer imaging. More cracks are observed when the image resolution is improved in experiments (Mac et al., 2021b).

6.6.4 Calibration of autogenous model with large-scale sample

This calibration was conducted to assess crack propagation due to autogenous shrinkage in a large concrete sample. A demonstration wall (2000 mm × 50 mm × 1500 mm) was used for calibration, cast on a slab (Kheir et al., 2021). The influence of heat generation induced by hydration process was limited due to the thinness of this concrete wall. The concrete slab (2000 mm × 950 mm × 200 mm) had been cast three months prior to the wall, so the autogenous shrinkage of the slab was ignored and it was treated as an elastic component in this simulation. The concrete wall was cast on top of the slab without vibration. After demoulding, no curing was applied to the concrete wall, and aluminium foil and plastic sheets were used to retain water. DEMEC points were installed to measure autogenous shrinkage at different sections of the wall. More details of the experiment are available in (Kheir et al., 2021).

According to the concrete mixture, the geometric properties of this simulation model were obtained using the method described in Section 6.4. However, this sample consists of Ultra-High Performance Concrete (UHPC) and contains minimal porosity; therefore, the pore phase is ignored in this simulation. The ITZ thickness of 30 μm, with a volume fraction of 0.42%, was used as Chapter 3. To reduce simulation time, symmetry boundary conditions were employed to simulate half of the concrete sample. The boundary for slab bottom surface was controlled in y direction, and x direction of right node at the bottom side was fixed, as shown in Fig. 6.19.

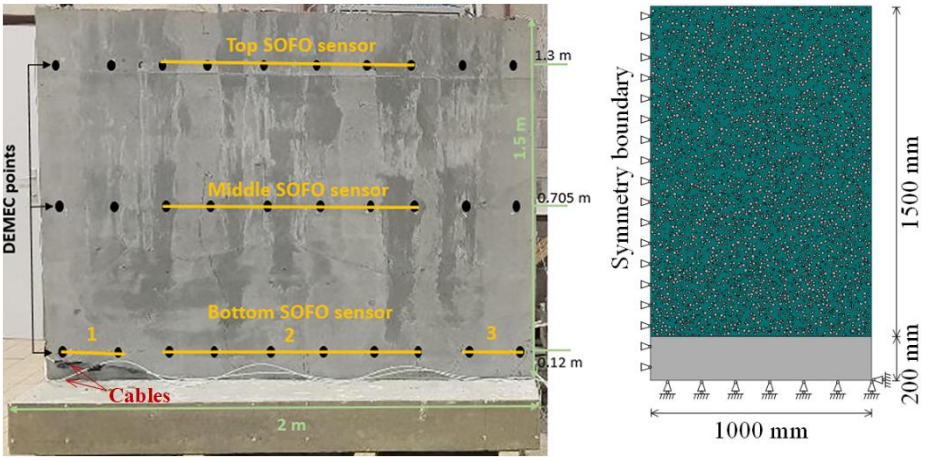

(a) (b)

Fig. 6.19. Geometric properties of sample: (a) experiment from J Kheir et al. (Kheir et al., 2021) (b) simulation

In this simulation, the elastic modulus was modelled to evolve over time using a fitted curve to capture the influence of hydration process on the mechanical parameters. To obtain elastic modulus for the mortar, Mori-Tanaka (MT) scheme was utilized, as mentioned in the author's previous work (Chapter 5), and is depicted in Fig. 6.20.

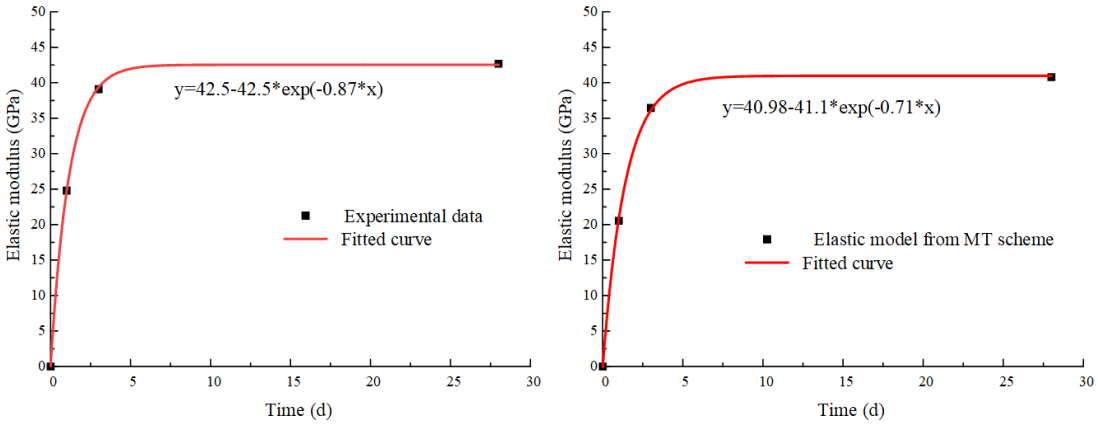

(a) (b)

Fig. 6.20. Elastic modulus varies with time: (a) concrete specimens (Kheir et al., 2021) (b) mortar phase from MT scheme

The mesh size used in this simulation ranges from h = 5 mm for the aggregate to h = 0.05 mm for the ITZ, resulting in a specimen consisting of 4325760 triangular elements. The parameters used for the hydration process and mechanical parameters are depicted in Table 6.8 and Table 6.9. To analyse the crack propagation induced by autogenous shrinkage, the crack development path is compared with experimental data at the same time point, as shown in Fig. 6.21. Additionally, to compare and calibrate the numerical model with experimental data, the autogenous shrinkage is evaluated at the same positions in the experiments (top, mid, and bottom), as shown in Fig. 6.22.

Table 6.8: Parameters for hydration process of large-scale sample

Specimen	A	B	t_0
Concrete wall	14.64	1.02	4.98

Table 6.9: Parameters for large-scale samples of phase field

	Time h	E GPa	v	σ_{y1}^{c} MPa	H_I GPa	σ_{y}^{t} MPa	l_c mm	ψ_c^c MPa	ψ_c^c MPa
Aggregate	-	50	0.2	-	-	-	-	-	-
	27	20.6	0.2	10.8	9	3.9	1	0.77	0.118
Mortar	72	36.5	0.2	19.8	16	5.7	1	1.38	0.212
	696	40.8	0.2	22.3	18	6.6	1	1.56	0.244
	27	12	0.2	10.8	4.5	3.9	1	0.37	0.06
ITZ	72	12	0.2	19.8	8	5.7	1	0.68	0.1
	696	12	0.2	22.3	9	6.6	1	0.76	0.12

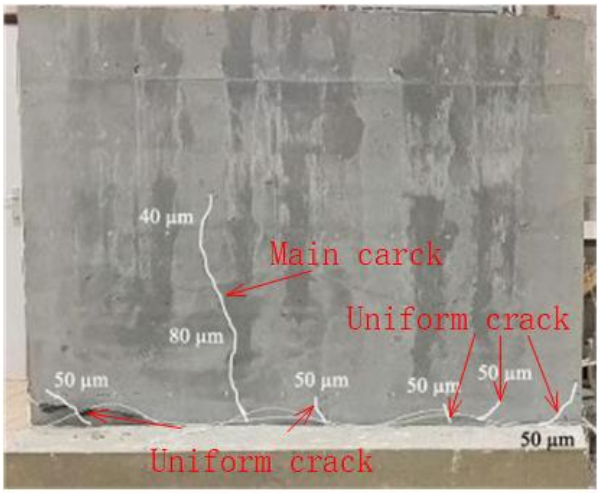

(a)

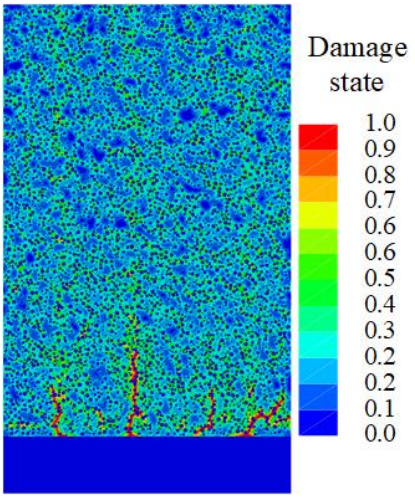

(b)

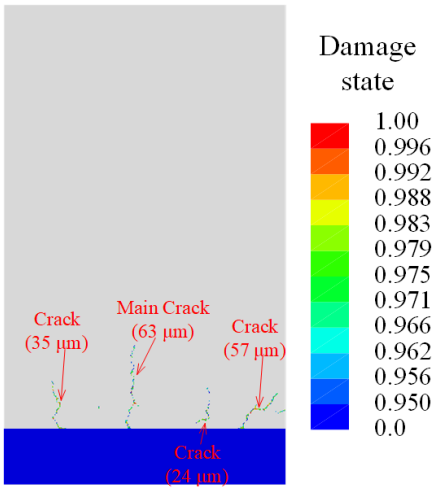

(c)

Fig. 6.21. Crack propagation: (a) experiments (Kheir et al., 2021) (b) simulation (c) crack width

As shown in Fig. 6.21, autogenous shrinkage induces several cracks, including a main crack and multiple uniformly distributed cracks originating from the bottom side of the wall. These cracks exhibit different angles and paths due to the distribution of aggregates. In the simulation, similar results are predicted, including three uniformly distributed cracks and one main crack. The diagonal crack at the boundary of the wall is also predicted. To capture the details of the cracks, the crack width was determined by limiting the damage state in the simulation ($d > 0.95$). The total crack width in the simulation (179 μm) is slightly wider than the average experimental result for half of the wall width (165 μm).

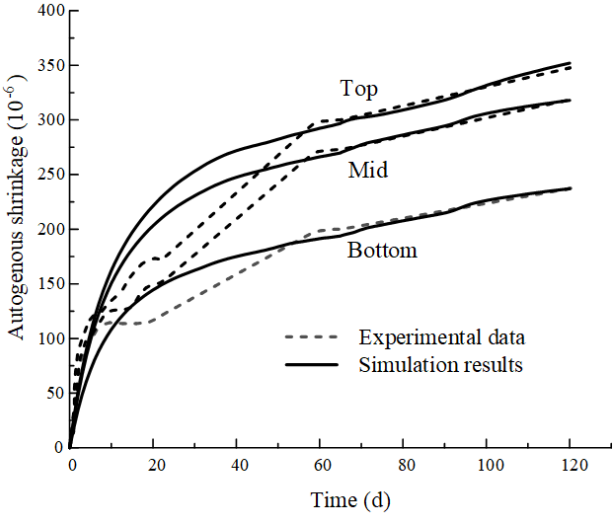

Fig. 6.22. Autogenous shrinkage Comparison of large-scale specimen of experimental data and numerical results

As observed in Fig. 6.22, autogenous shrinkage comparison between numerical and experimental data shows strong agreement. The minor variations in autogenous shrinkage are attributed to the application of the evolving mechanical properties during the hydration process in the simulation.

6.7 Autogenous simulation of influence of water/cement ratio

In this section, the influence of water/cement (W/C) ratio is studied and predicted using the proposed autogenous shrinkage model. Three experimental datasets with different mix designs and W/C ratios

(0.30, 0.45, and 0.60) from the literature are utilized to simulate autogenous shrinkage and crack propagation for early-age concrete (Wang et al., 2021).

6.7.1 Calibration of low water/cement ratio for autogenous model

Prismatic specimens were cast with size of 400 mm × 100 mm × 100 mm, and sealed on all surfaces for autogenous shrinkage measurement. The concrete mix design was based on experiments (Wang et al., 2021), using cement (180 kg/m³) with a W/C ratio of 0.3, and 6.0 kg/m³ of superplasticizer. Limestone gravel with a size ranging from 5 mm to 25 mm and a density of 2816 kg/m³ was used for coarse aggregate. River sand with a nominal diameter ranging from 0 mm to 5 mm was utilized as fine aggregates. Further details for this test procedures are available in the literature (Wang et al., 2021).

According to concrete mixture, geometric properties for this simulation model were obtained employing the approach mentioned in Section 6.4. Volume fraction of coarse aggregate is 38.4%, and an ITZ thickness of 30 μm, as used in Chapter 3, are applied with 0.42% for volume content. The total porosity with 5.8% (including free water volume after hydration and air volume) was used to model the pore structures. The geometry for this model is shown in Fig. 6.23.

In this simulation, three roller supports were used as boundary conditions. Thus, the left, middle, and right fulcrums at specimen bottom surface were fixed in y-direction, as illustrated in Fig. 6.23. The element size of h = 0.5 mm was employed for all phases (aggregate, ITZ, mortar, and pores), and the specimen includes 462,336 triangular elements. The parameters used for the hydration process and mechanical parameters are provided in Table 6.10 and Table 6.11. To verify the theoretical modelling with experimental data, autogenous shrinkage is evaluated at the same location as in the experiments (mid-span at 60 mm length), as illustrated in Fig. 6.24. To analyse fracture evolution induced by autogenous shrinkage, the crack development path is compared at different time points, as shown in Fig. 6.25.

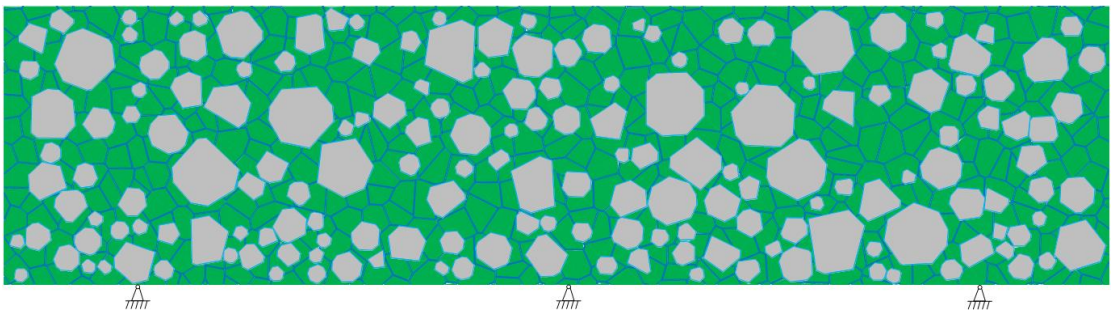

Fig. 6.23. Geometric properties of low W/C ratio concrete

Table 6.10: Parameters for hydration process of low W/C specimen

Specimen	A	B	t_0
Low W/C	6.374	0.72	0.46

Table 6.11: Parameters for concrete samples of phase field

	E GPa	v	σ_{y1}^{c} MPa	H_1 GPa	σ_{y}^{t} MPa	l_c mm	β	β_{DP}	ψ_c^c MPa	ψ_c^c MPa
Aggregate	50	0.2	-	-	-	-	-	-	-	-
Mortar	42	0.2	16	27	4.2	1	1	0.37	1.5	0.014
ITZ	12	0.2	16	7	4.2	1	1	0.37	0.55	0.0053

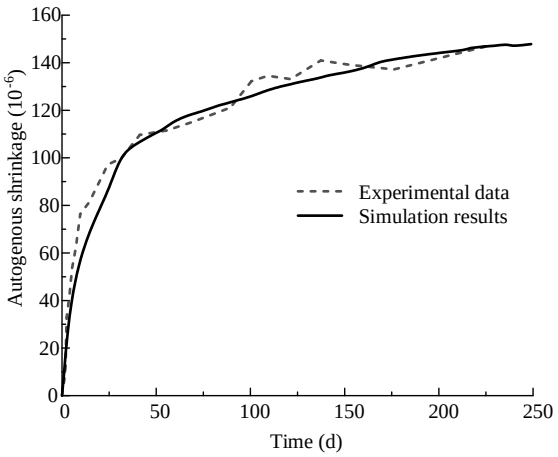

Fig. 6.24. Comparison of autogenous shrinkage between experimental data and simulation results

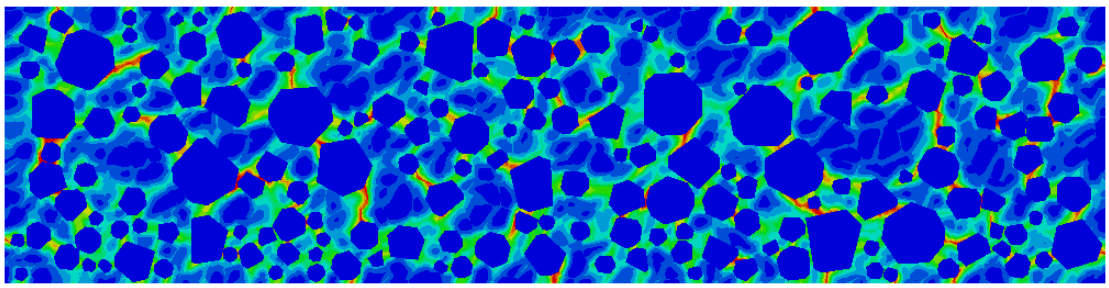

(a)

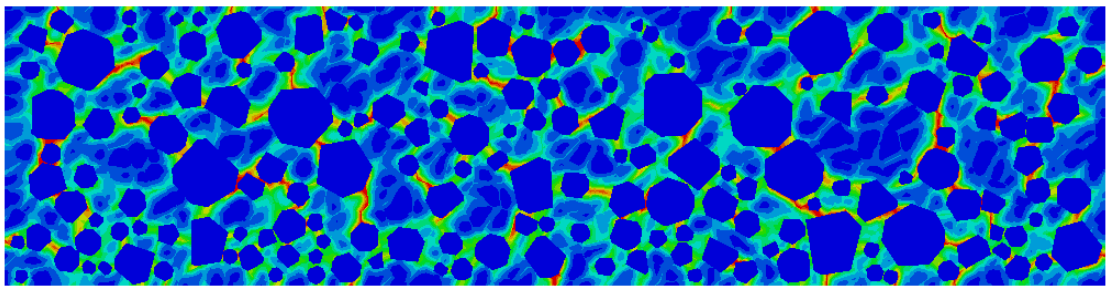

(b)

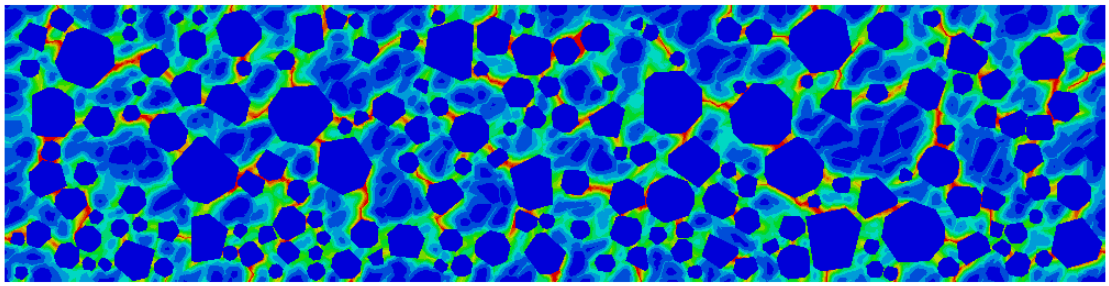

(c)

Fig. 6.25. Damage evolution at different time: (a) 28 day, (b) 60 day, (c) 250 day

As observed in Fig. 6.24, the comparison of autogenous shrinkage shows strong agreement at the mid-span for this specimen. However, at the early age of shrinkage (before 30 days), the simulated autogenous shrinkage is lower than the experimental data. This discrepancy arises because the mechanical properties used in the simulation are based on tests conducted at 28 days. Due to the hydration process progresses, concrete mechanical properties, leading to a stiffer matrix that results in lower shrinkage deformation. From Fig. 6.25, it is evident that the crack propagation paths tend to develop along the ITZ and pore structures, as these phases are more prone to breakage compared to the mortar. However, crack propagation begins on the 3rd day rather than the 1st day, which can be attributed to the gradual development of mechanical properties owing to hydration degree. Furthermore, no significant crack propagation is observed after 60 days, due to the conclusion of the hydration process and the cessation of autogenous shrinkage.

6.7.2 Calibration of mid water/cement ratio for autogenous model

A prismatic specimen with the size of 400 mm × 100 mm × 100 mm, and a medium W/C ratio was employed to calibrate this proposed autogenous shrinkage model and predict fracture evolution in early-age concrete (Wang et al., 2021). The concrete mix design included cement (180 kg/m³) using a W/C

ratio of 0.45, as well as 4.0 kg/m³ of superplasticizer. Limestone gravel with a size ranging from 5 mm to 25 mm and a density of 2816 kg/m³ was used as coarse aggregate, along with river sand as fine aggregate, using a nominal size of less than 5 mm. Further details are available in the literature (Wang et al., 2021).

The same method outlined in Section 6.4 was utilized to generate concrete geometric properties. According to concrete mixture, 41.9% coarse aggregate volume content is used and generated, and the ITZ thickness of 30 μm using 0.45% of volume content was generated. The total porosity of 10.2% was used to model the pore structures. The geometry of this model is shown in Fig. 6.26. The mesh size h = 0.5 mm was applied to all phases (aggregate, ITZ, mortar, and pores), resulting in a specimen with 503,248 triangular elements. The same mechanical properties parameters as those used for the low W/C ratio sample were applied, as shown in Table 6.11, with a potential energy correction parameter of 0.95 for the mortar, ITZ, and pore structures. The parameters for the hydration process are provided in Table 6.12. To compare and calibrate this numerical modelling with experimental recording, autogenous shrinkage was measured at the same location as in the experiments (mid-span at 60 mm length), as shown in Fig. 6.27. To analyse fracture evolution induced by autogenous shrinkage, the crack development path was compared at different time intervals, as shown in Fig. 6.28.

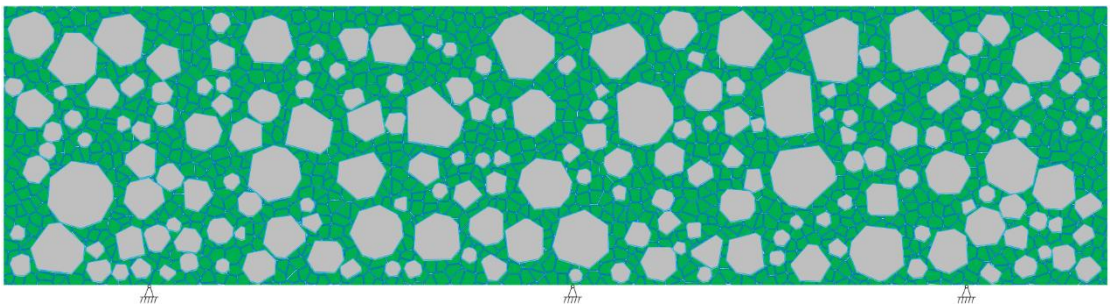

Fig. 6.26. Geometric properties of mid W/C ratio concrete

Table 6.12: Parameters for hydration process of mid W/C specimen

Specimen	A	B	t_0
Mortar A	6.726	0.545	0.4

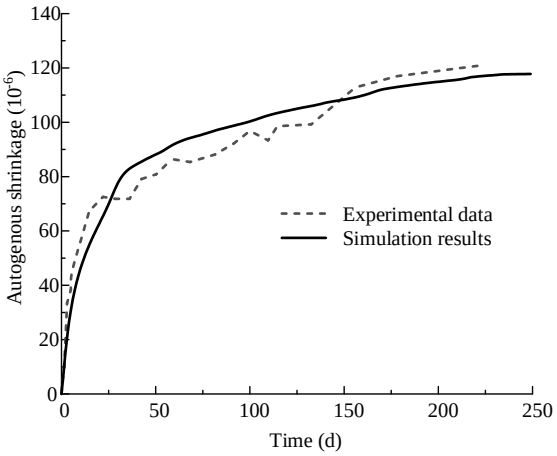

Fig. 6.27. Comparison of autogenous shrinkage between experimental data and simulation results

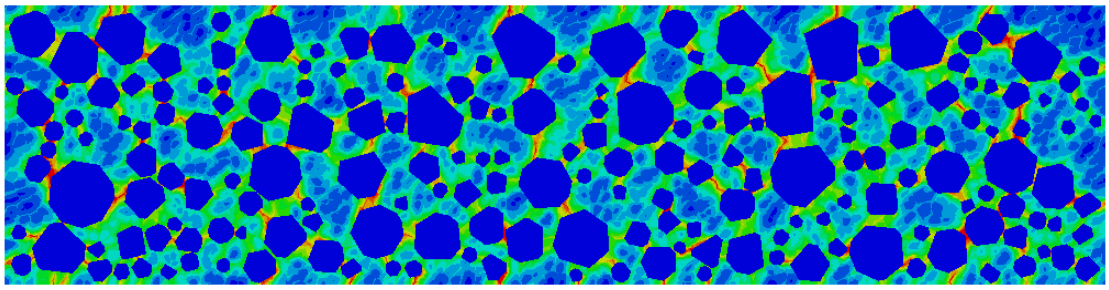

(a)

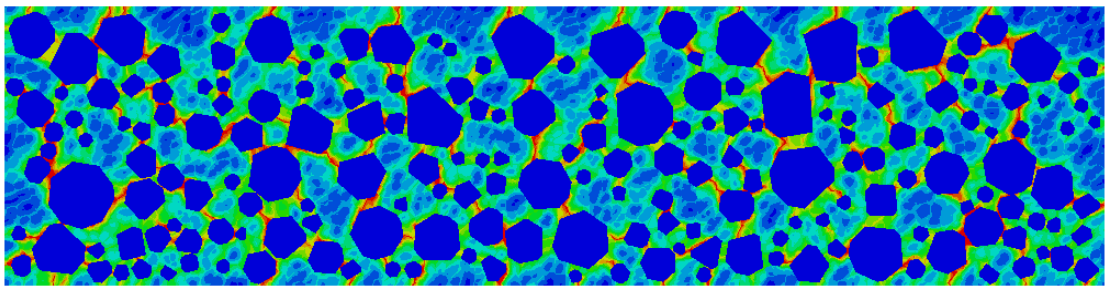

(b)

Fig. 6.28. Crack propagation at different time: (a) 60 day, (b) 250 day

As observed in Fig. 6.27, the numerical and experimental results at autogenous shrinkage shows strong agreement at the mid-span of the specimen. Similar autogenous shrinkage behaviour at the early age is noted when compared with the low W/C ratio specimen. However, the autogenous shrinkage in the experimental data is higher than that observed in the simulation results, which can be attributed to the mechanical properties being derived from tests conducted at 28 days.

As depicted in Fig. 6.28, fracture propagation branches tend to develop along the ITZ and pore structures, as these phases are more prone to breakage compared to the mortar. Compared to Fig. 6.25,

the crack propagation in this specimen starts on the 4th day, which is later than that of the low W/C ratio specimen. This delay is owing to the reduced volume of cement particles in the mixture, resulting in lower autogenous shrinkage strain. Autogenous shrinkage is driven by hydration process, and fewer cement particles lead to lower shrinkage. Additionally, the crack path shows minimal changes after 60 days, as the hydration process concludes and autogenous shrinkage diminishes.

6.7.3 Calibration of high water/cement ratio for autogenous model

A prismatic specimen with a size of 400 mm × 100 mm × 100 mm, and a high W/C ratio was employed to calibrate the proposed autogenous shrinkage model and predict fracture evolution in early-age concrete (Wang et al., 2021). The concrete mix design included cement (180 kg/m³) with a W/C ratio of 0.6, and 3.0 kg/m³ of superplasticizer. Limestone gravel with a size ranging from 5 mm to 25 mm and a density of 2816 kg/m³ was used as coarse aggregate, along with river sand as fine aggregate with a nominal size of less than 5 mm. Further details are available in literature (Wang et al., 2021).

The same method outlined in Section 6.4 was employed to generate concrete geometric properties. According to concrete mixture, 44% aggregate volume content is used, an ITZ thickness of 30 μm and 0.5% volume content were applied. The total porosity of 12.4% was used to model the pore structures. The geometric properties of this modelling are depicted in Fig. 6.29, along boundary conditions, which remain consistent with previous simulations. A element size of h = 0.5 mm was applied to all phases (aggregate, ITZ, mortar, and pores), resulting in a specimen with 564,268 triangular elements. The same mechanical property parameters as those used for the low W/C ratio sample were applied, as shown in Table 6.11, with a potential energy correction parameter of 0.93 for the mortar, ITZ, and pore structures. The parameters for the hydration process are provided in Table 6.13. To compare and calibrate the numerical modelling with experimental result, autogenous shrinkage was measured at the same location as in the experiments (mid-span at 60 mm length), as depicted in Fig. 6.30. To analyse fracture evolution induced by autogenous shrinkage, the crack development path was compared at different time intervals, as shown in Fig. 6.31.

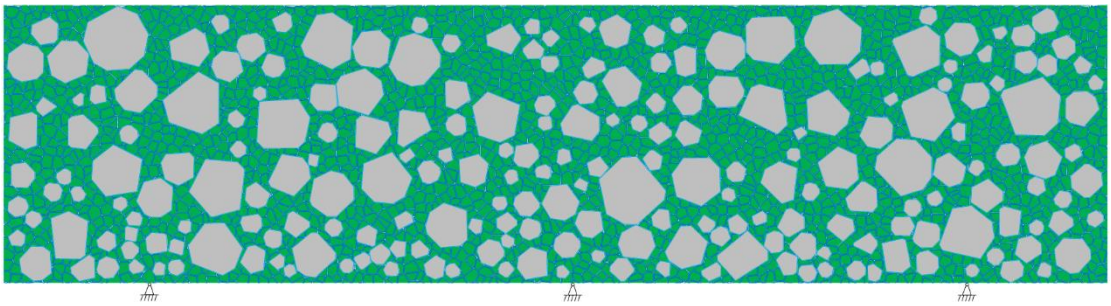

Fig. 6.29. Geometric properties of high W/C ratio concrete

Table 6.13: Parameters for hydration process of high W/C specimen

Specimen	A	B	t_0
Mortar A	8.491	2.584	0.79

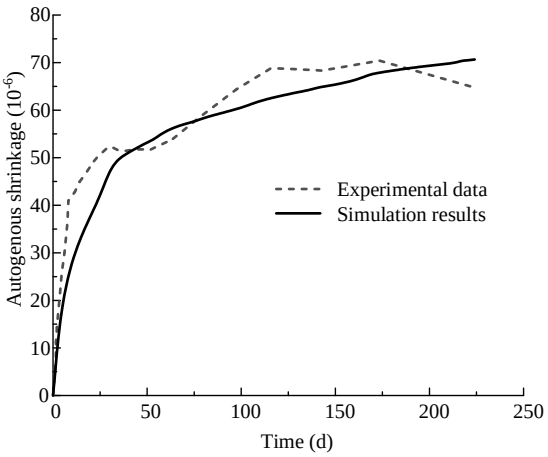

Fig. 6.30. Comparison of autogenous shrinkage between experimental data and simulation results

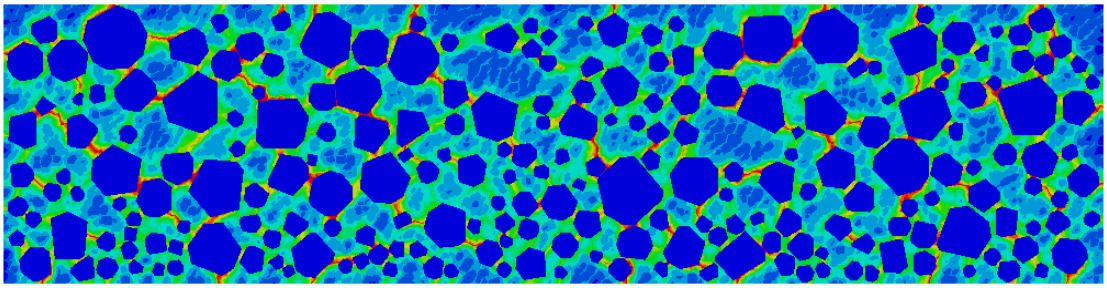

Fig. 6.31. Crack propagation at 250 day

As depicted in Fig. 6.30, autogenous shrinkage demonstrates strong agreement at the mid-span of the specimen. Similar autogenous shrinkage behaviour is observed in the early stages, comparable to that of the low and mid W/C ratio specimens.

As depicted in Fig. 6.31, fracture evolution branches tend to develop along the ITZ and pore structures, as these phases are more prone to breakage compared to the mortar. In comparison to Fig. 6.25 and Fig. 6.28, crack propagation in the high W/C ratio specimen begins on the 5th day, which is later than in the

low and mid W/C ratio specimens. The autogenous shrinkage in the high W/C ratio specimen is also lower than that observed in the other specimens.

6.8 Conclusion

According to Chapter 5, the mechanical properties of different phases are employed in this autogenous model. And comprehensive experimental and numerical studies were carried out to study the autogenous shrinkage and degradation mechanisms of early-age concrete. A meso-micro elasto-plastic phase-field model, combined with volume reduction theory, was introduced to simulate autogenous shrinkage and fracture evolution for concrete. This modelling was calibrated and calibrated against experimental results. The primary conclusions are outlined below:

(1) Monte Carlo method, combined with the volume spatial distribution of aggregate and Voronoi tessellation, was used to generate the geometry and spatial distribution of aggregate, ITZ, and pores. This method offers a viable and flexible approach for analysing autogenous shrinkage (volume reduction in the mortar phase) and drying shrinkage (capillary stress induced by water loss in the pore phase), respectively.

(2) The proposed autogenous shrinkage model demonstrates excellent agreement with the shrinkage development over time at different depths for concrete at the meso-micro level. The modelling results were calibrated through several experimental studies.

(3) The developed modelling effectively describes fracture evolution path in concrete composites across multiple experiments. The results confirm model's capacity to describe both autogenous shrinkage and mechanical behaviour of concrete.

(4) From the calibration specimens, more cement particles contribute to higher autogenous shrinkage. Less cement particles postpone crack formation and reduce the number of crack paths.

The proposed framework will provide more accurate mechanical behaviour and hygro-mechanical predictions. However, the influence of hydration process for mechanical properties requires further investigation to obtain accurate shrinkage deformation for early-age concrete. This method requires the use of numerous elements, making it resource-intensive and increasing significantly the computation cost. Further investigations into mesh topology optimization are required.

Chapter 7: A Multi-scale Phase-field Model for Drying Shrinkage for Concrete

Abstract

Drying shrinkage and the resulting cracks due to restrains are critical factors to consider in the design and durability of concrete structures. The open microstructure in concrete presents significant challenges in understanding moisture diffusion, capillary stress, drying shrinkage, failure mechanisms, and predicting crack propagation paths. This paper introduces a multi-coupled model that integrates a moisture diffusion model with a phase-field model employing elasto-plastic property to predict drying shrinkage and crack propagation in concrete using a micro-meso model. By combining the spatial distribution of aggregates, Monte Carlo method and Voronoi tessellation, concrete geometric properties are determined. Various specimens are subjected to drying shrinkage at different depths and with varying water/cement ratios to calibrate and verify this modelling. By comparing simulation predictions with experimental observations, this proposed methodology is shown to effectively predicts drying shrinkage and crack propagation in concrete. This work can enhance the reliability of long-term performance assessments and facilitate the design of more durable concrete structures.

Keywords: Porous material, Voronoi diagram, Elasto-plastic phase-field model, Micro-Meso model, Drying shrinkage

7.2 Introduction

Drying shrinkage in cementitious materials is a significant contributor to concrete deformation, often resulting in more cracks than those caused by loading, impacting structure's durability and sustainability (Nguyen et al., 2021). It is well-known that concrete shrinkage is strongly associated with water loss within the material (Bissonnette et al., 1999, Baroghel-Bouny et al., 1999, Wittmann, 2000, Zhang and Zhang, 2006, Zhang et al., 2010). However, understanding the mechanisms of drying shrinkage-induced deformation in structures requires theories for shrinkage distribution and evolution, which, in turn, necessitates an understanding for moisture diffusion and convection. As moisture evaporates, liquid-vapour menisci form, inducing capillary stress. When the stress resulting from moisture loss exceeds concrete tensile stress, cracking occurs (Wei et al., 2017, Pane et al., 2002, Shen et al., 2019, Zheng et al., 2019, Yang et al., 2021). This leads to increased permeability and reduced durability of concrete

building (Amin et al., 2009, Sivakumar et al., 2007, Ranaivomanana et al., 2013b, Shen et al., 2021). Therefore, the moisture diffusion mechanism is critical for analysing moisture transport and distribution within concrete, which is essential for predicting shrinkage induced by capillary stresses and deflections, as well as simulating crack propagation, durability, and service life.

Various numerous numerical theories have been proposed to predict moisture transport and capillary diffusion for concrete (Martın-Pérez et al., 2001, Samson and Marchand, 2007, Teixeira de Freitas et al., 2017). To accurately predict global moisture transport, it is essential to consider geometric properties of concrete's components, including aggregate phase, mortar phase, and the interfacial transition zone (ITZ) (Li and Song, 2022). A multi-scale numerical modelling is developed to incorporate the influence for pore structures, considering pore size distribution and fraction in moisture diffusion by employing the Rayleigh-Ritz (R-R) size distribution (Huang et al., 2015). Given the geometric complexity of concrete, a moisture diffusion mechanism is critical for predicting the distribution and evolution of relative humidity (RH). For this purpose, theoretical equations for liquid and vapour water transport based on Darcy's Fick's second laws are widely employed to express the relationships between moisture diffusion coefficients, water saturation degree, and RH (Baroghel-Bouny et al., 1999, Mounajed et al., 2004, Qin et al., 2009, Baker et al., 2009). Additionally, molecular, Knudsen, and surface diffusion mechanisms are considered to study moisture diffusion across different pore sizes (Dehwah et al., 2024).

Capillary pores pressure is induced due to water loss in pore phase of concrete, leading to drying shrinkage, cracking, deformation, and failure mechanisms. To address these issues, an appropriate numerical approach and constitutive model are essential for capturing the complex coupling problems involved. For fracture computation, both discrete (discrete element method (DEM)) and smeared approaches (the finite element method (FEM)) are commonly employed. In discrete approach, discontinuous displacement elements are necessary to be assigned for predicting fracture opening and evolution (Huang et al., 2016c, Naderi et al., 2021b) or inside elements (Du et al., 2014). However, the discrete method faces mesh-alignment issues and requires pre-inserting cohesive elements, resulting in high time-consuming. Conversely, the smeared method necessitates prior understanding of mesh enrichment theories and extrinsic opening and evolution standard to clearly capture crack behaviour (Zhang et al., 2018b, Zhang and Mang, 2020, Zeng et al., 2019, Zhang et al., 2021, Zhang et al., 2020). Methods including tracking element methods (Zhang et al., 2018b, Zhang and Mang, 2020, Zeng et al., 2019, Zhang et al., 2021, Zhang et al., 2020) and particle cracking methods (Rabczuk and Belytschko, 2004, Rabczuk et al., 2010) show promise in efficiently managing embedded strong discontinuities.

In line with the chosen numerical method, the phase-field constitutive modelling is employed to predict fracture mechanisms. To consider complex nonlinear behaviour for concrete, a phase-field model employing elasto-plastic behaviour has been proposed, incorporating damage evolution and distinct

mechanical behaviours under tensile loading and compressive loading (Alessi et al., 2018, Pise et al., 2019, Jiang et al., 2023). To address the isotropic nature for concrete, the decomposition method is employed to divide elastic energy into two parts: one associated with tensile energy and the other with compressive energy. Various decomposition methods, such as volumetric-deviatoric decomposition (Amor et al., 2009) and spectral decomposition of the strain tensor (Miehe et al., 2010b), have been considered. To model plastic fracture behaviour, a Drucker-Prager plastic criterion (Drucker and Prager, 1952) is implemented, which degrades gradually as damage evolves.

However, the open and complex micro-meso structure of concrete presents significant challenges in predicting drying shrinkage, particularly when accounting for the capillary stress within the pore phase. To address these complexities, a multi-coupled model is necessary to integrate moisture loss, mechanical properties, and crack propagation during drying shrinkage. This model, which incorporates the micro-meso structural components of concrete, including aggregate, mortar, ITZ and pore structures, enables a comprehensive analysis and prediction of the multi-physics interactions within cementitious materials.

In this study, a micro-meso modelling for concrete is developed to investigate drying shrinkage behaviour for its multiphase composition. The Monte Carlo method and Voronoi tessellation are employed to generate the geometric properties of concrete, including aggregates, mortar, ITZ, and pore structures. The pore structures are used to describe the strain induced by capillary stress resulting from moisture loss. Additionally, a phase-field model employing elasto-plastic performance is utilized for simulating concrete fracture evolution under mechanical load. This proposed modelling is conducted by using the subroutine in ABAQUS named User Defined Element (UEL). To calibrate this model, shrinkage tests measuring relative humidity (RH) and temperature are conducted, while other experimental results from the literature are used for calibration. Due to its enhanced predictive capabilities, this modelling will also be utilized to investigate multi-phase coupled systems, including thermo-hygral, hygro-mechanical, or thermo-hygro-mechanical interactions. Integrating this methodology into existing mechanical frameworks will improve the accuracy of predictions related to the material's mechanical response, including chemical corrections, creep, and crack development. This, in turn, will improve reliability of long-term performance assessments and support the design of more durable concrete structures.

7.2 Experimental program

7.2.1 Materials and preparation of samples

Portland cement type CEM II 32.5R (335 kg/m³) was utilized as the cementing binder. And the water/cement (W/C) ratio was 0.55. Two size ranges of river-rounded gravel were used as coarse aggregates: 491 kg/m³ with diameters ranging from 5–10 mm and 532 kg/m³ with diameters from 10–14 mm. Additionally, river-rounded sand was utilized as fine aggregate at a quantity of 847 kg/m³.

To measure internal RH and drying shrinkage of concrete, concrete cubes with size of 150 mm × 150 mm × 150 mm were cast, with two holes prepared at depths of 15 mm and 30 mm. During casting, concrete specimen was filled with fresh concrete, and steel sockets were centrally embedded, as depicted in Fig. 7.1a. After vibration, the moulds were covered by plastic sheets to retain moisture under laboratory conditions (18 ± 3 °C) for 24 hours. The samples were demoulded after 24 hours and then sealed with aluminium foil on the bottom surface, while the remaining surfaces were drying at a curing condition with a relative humidity of (76 ± 2%), as shown in Fig. 7.1 b. To control the relative humidity during the drying process, a saturated sodium chloride (NaCl) salt solution was used to provide a constant RH, with a salt-to-water ratio of 5:1. The location of specimens is shown in Fig. 7.2.

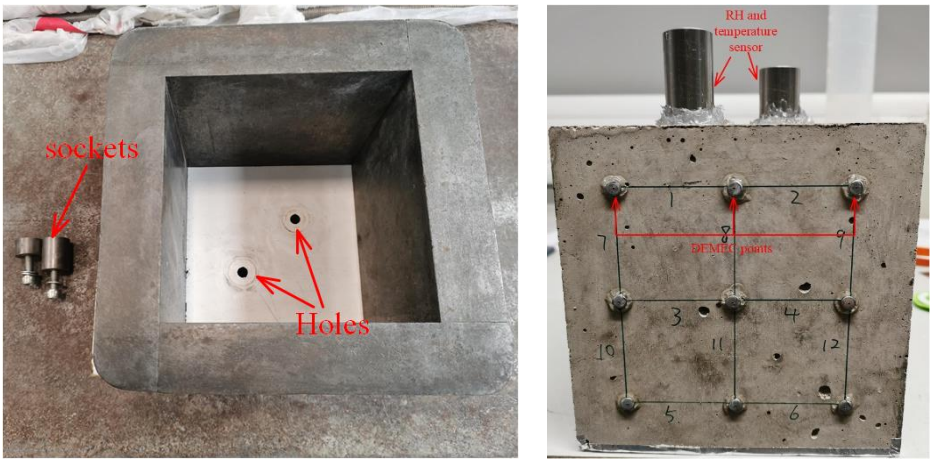

(a) (b)

Fig. 7.1. Experimental preparation: (a) Moulds and sockets, (b) sensor instalment and specimen

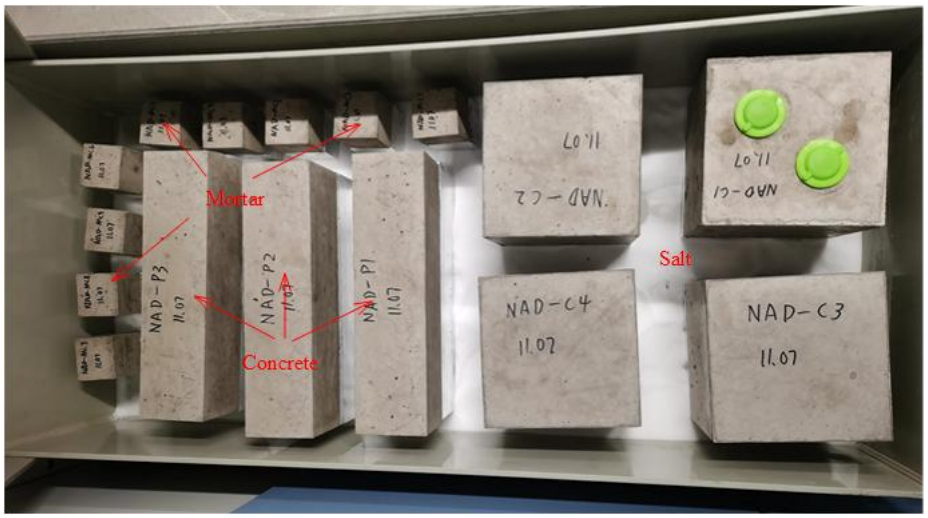

Fig. 7.2. Layout of mortar and concrete specimens

Selecting the appropriate sensor for measuring RH inside concrete is critical, particularly for early-age concrete in the water-saturated stage, to ensure accurate and reliable results. The sensor size plays a key role in minimizing its impact on local RH measurements, as capturing precise measurements inside concrete can be challenging. Based on these considerations, the Rapid RH L6 single-use sensor was chosen for this study. For strain measurements, DEMEC strain gauges of 50 mm was utilized to record shrinkage at micrometre level, as shown in Fig. 7.1 b.

7.2.2 Test methods

To ensure consistent mechanical properties, the cubes and prismatic specimens of concrete and mortar were placed in laboratory under the same conditions as the drying shrinkage specimens, as shown in Fig. 7.2. After 28 days, three-point bending and compressive tests were carried out.

The specimen for drying shrinkage measurement is shown in Fig. 7.1 b. The cube, with size of 150 mm × 150 mm × 150 mm, had embedded concrete RH sensors placed at depths of 15 mm and 30 mm. DEMEC points were installed on the surface at 50 mm and 100 mm distances. After installing the sensors, samples were stored in a box with a saturated salt solution, with a temperature of 18 ± 3 °C and relative humidity of 76 ± 2%. The internal RH and drying shrinkage were measured using the embedded sensors and DEMEC points.

7.3 Results and discussion

7.3.1 Basic mechanical properties

According to BS EN 12390-3: 2009 (Standard, 2009), mortar cubes with size of 50 mm × 50 mm × 50 mm and plain concrete cubes with size of 75 mm × 75 mm × 75 mm were subjected to uniaxial compressive loads at a rate of 0.6 N/mm²/s. To obtain Young's modulus (E), Poisson's ratio (v), and yield stress (σ_y), 2D scanner marking points and a camera were used to monitor and record the movement of the marked points (Chapter 3). The parameters for both mortar and concrete are depicted in Table 7.1. The resulting stress-strain results are presented in Fig. 7.3.

Table 7.1: Basic mechanical parameters of mortar and concrete

Specimen	Compressive strength (MPa)	Peak load (kN)	Porosity (%)
Mortar A	40.9	102.3	16.8
Mortar B	40.6	101.5	17.0
Mortar C	40.3	100.8	17.2
Concrete A	41.2	231.5	11.4
Concrete B	39.4	221.6	11.0

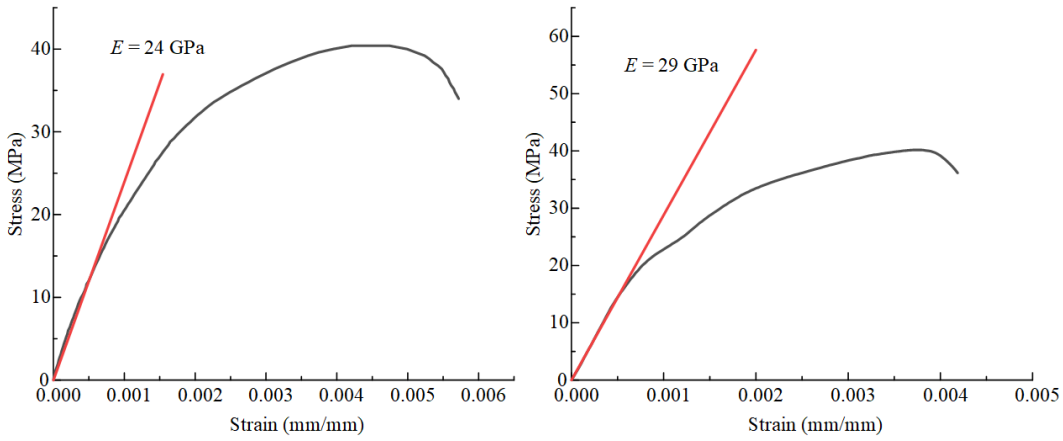

(a) (b)

Fig. 7.3. Stress-strain curve for specimens: (a) mortar, (b) concrete

7.3.2 Relative humidity and temperature

The ambient conditions of temperature and RH are depicted in Fig. 7.4a, confirming that the saturated salt solution maintains a constant ambient RH. To assess the effect of RH evolution on drying shrinkage, RH measurements were taken at depths of 15 mm and 30 mm within concrete specimen, as illustrated in Fig. 7.4b.

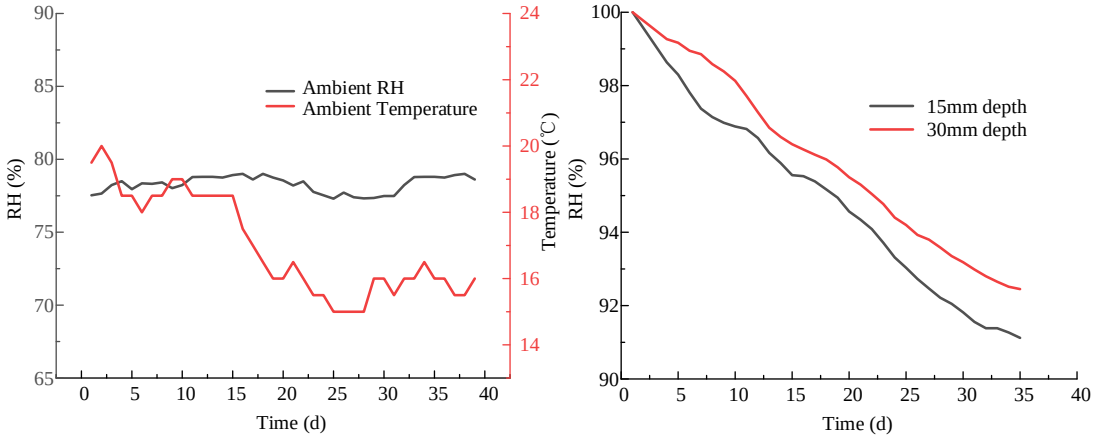

Fig. 7.4. Measured internal RH and ambient temperature

Due to the exposure of five surfaces for drying, the relative humidity (RH) evolution at depths of 15 mm and 30 mm in the concrete specimen are similar, resulting from the high moisture diffusion coefficient. The internal RH drops to around 92% at 35 days, influenced by the high ambient RH, which slows the drying process at each exposed surface.

For early age concrete, the hydration process and autogenous shrinkage must be considered. However, the continuity of liquid water remains unbroken due to the high water/cement ratio (0.55) for this concrete mixture. As a result, autogenous shrinkage related to water loss and capillary stress can be disregarded. Instead, hydration process contributes to autogenous shrinkage (Chapter 6). Consequently, moisture loss in the pore structure primarily induces drying shrinkage, which is determined by the total shrinkage and autogenous shrinkage.

7.3.3 Drying shrinkage

Drying shrinkage was recorded at three depths along with time for concrete specimens: the top at a height of 125 mm, the middle at a height of 75 mm, and the bottom at a height of 25 mm, as shown in Fig. 7.5.

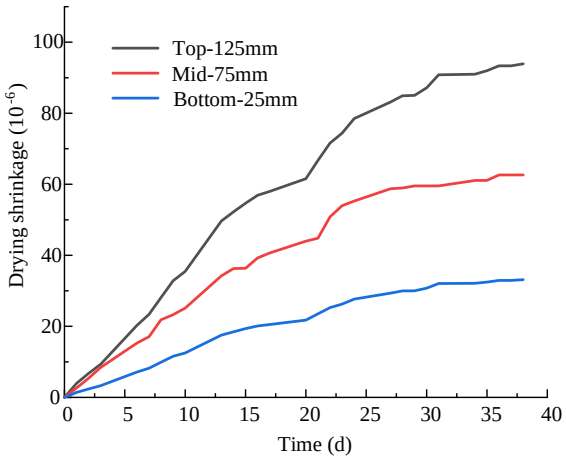

Fig. 7.5. Drying shrinkage of different height

From Fig. 7.5, it is noted that drying shrinkage increases over distance from bottom. This is induced by aggregate spatial distribution. According to literature (Al-Kamyani et al., 2018), the aggregate distribution increases from top to bottom, with 35.5% aggregate at the top quarter and 41.6% at the bottom. The lower cement content at the bottom results in reduced volume reduction, while the higher aggregate content caused the increase of elastic modulus and self-restraint. Consequently, the bottom exhibits less drying shrinkage compared to the top.

7.4 Geometric properties of Micro-Meso of concrete

To align with the geometric properties of the concrete model, a combination of mesoscale and microscale models is employed to generate four distinct phases: aggregate, ITZ, mortar, and pores. The subsequent sections detail the parameters required to determine geometry of each constituent within the concrete and outline the methodology used for the development of the mesoscale model.

The model generation approach involves the following steps: 1) Aggregate: The aggregate is represented based on its shape, distribution, and size. The spatial location of aggregates is modelled using a Monte Carlo method to ensure accurate positioning without overlap. 2) ITZ: ITZ is modelled as a thin layer over aggregate particles. The ITZ thickness is assigned based on literature values, typically ranging between 10 to 50 μm. 3) Mortar Matrix: The mortar phase acts as the continuous matrix embedding both the aggregates and the ITZ. Its geometric properties are determined by the overall concrete mixture and volume fractions of each constituent phase. 4) Pores: Pores are modelled

as a network embedded within the mortar phase, simulating the interconnected voids that occur in concrete. Voronoi tessellation method is employed to define spatial arrangement and connectivity of the pore network.

This model's geometric properties and spatial distribution are calibrated to match experimental observations, ensuring accurate representation of concrete's mechanical and physical behaviours during simulations.

7.4.1 Spatial distribution and shapes of aggregate

Based on literature (Al-Kamyani et al., 2018), concrete geometric properties are divided into four cross-sections along the height of the specimen. Monte Carlo method is utilized to locate centroid and diameter for each aggregate and generate the in-plane spatial distribution for each cross-section (Rajamani et al., 1986, Huang et al., 2022). This method guarantees that individual aggregates do not overlap and remain within the boundaries of the specimen. To generate polygonal-shaped aggregates, the Fuller distribution is employed to determine the edge number and angles (α). Further details for this method are available Chapter 2.

Based on the mix design from the author's previous study, polyhedral-shaped aggregates were generated in two diameter size ranges: 5-10 mm and 10-14 mm, with a volume fraction ratio of 0.48:0.52. The overall aggregate volume fraction was approximately 40%, determined by the mix design and the density of 2590 kg/m³ for the aggregates. When combined with the spatial distribution of aggregates from literature (Al-Kamyani et al., 2018), the volume fractions varied along the height direction. The top section had a volume fraction of 36.51%, mid-top 38.56%, mid-bottom 40.62%, and bottom 42.67%, as depicted in Fig. 7.6.

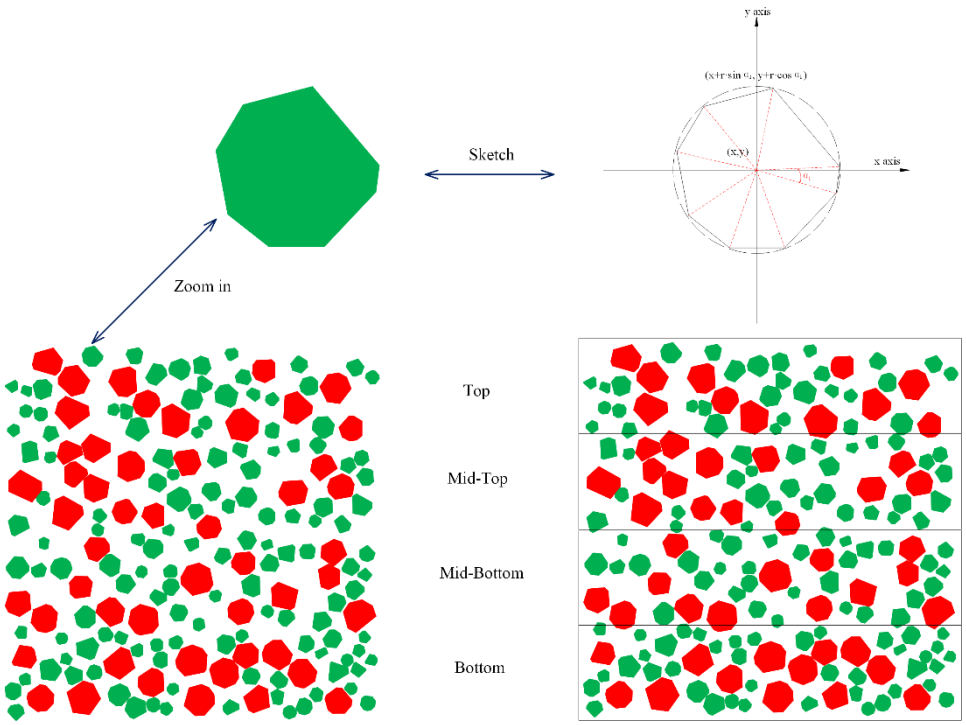

Fig. 7.6. 2-D random distribution of polygonal aggregates

7.4.2 Geometric properties of the ITZ

One of the key characteristics of concrete is its inherent heterogeneity, which arises from the incorporation of aggregate into the mortar matrix. This process induces the ITZ formation. Previous studies describe the ITZ as a thin layer, with a typical thickness ranging from 10 to 50 μm (Shuguang et al., 2015). Consequently, the ITZ can be modelled based on the aggregate's geometric properties, with a designated thickness *"t"* (see Fig. 7.7). In this study, a thickness of 30 μm was applied, consistent with findings from Chapter 3.

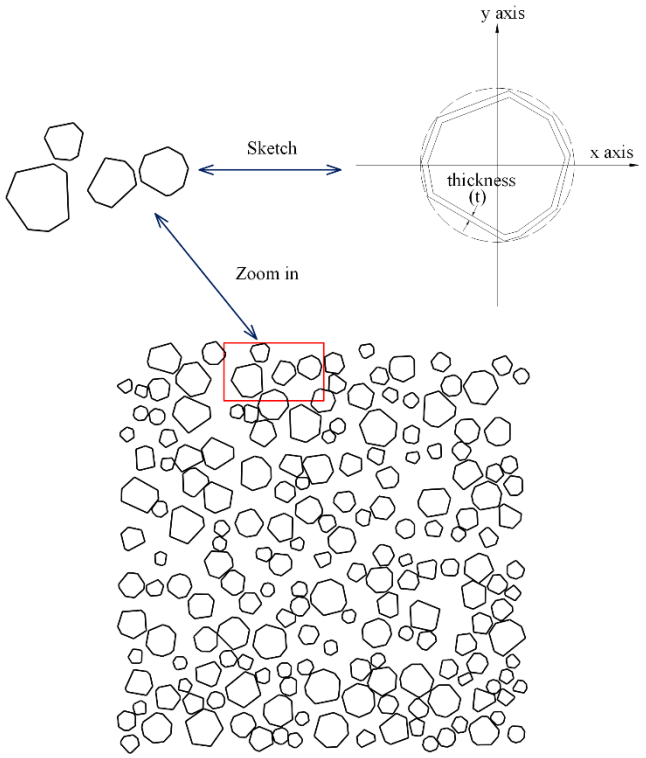

Fig. 7.7. 2-D random distribution of polygonal ITZ

7.4.3 Geometric properties of the pore structures

In this study, the pore phase is embedded within the mortar phase as a network rather than being treated as voids. This modelling approach allows for this simulation of not only concrete mechanical behaviour but also the integration of multiple coupled phenomena, such as thermal expansion, shrinkage, chemical degradation, and creep. These phenomena are addressed in conjunction with Chapter 5 and 6.

The pore structure, represented as a network, is generated using the Voronoi tessellation method for polygonal geometrical elements (Idiart, 2009). This approach creates an array of randomly distributed nodes, each positioned at the centroid of the corresponding Voronoi regions within the mortar. These nodes are connected by equidistant segments that either intersect or converge at the ITZ, as illustrated in Fig. 7.8a and Fig. 7.8b. Total area of pore network is calculated based on experimentally measured porosity.

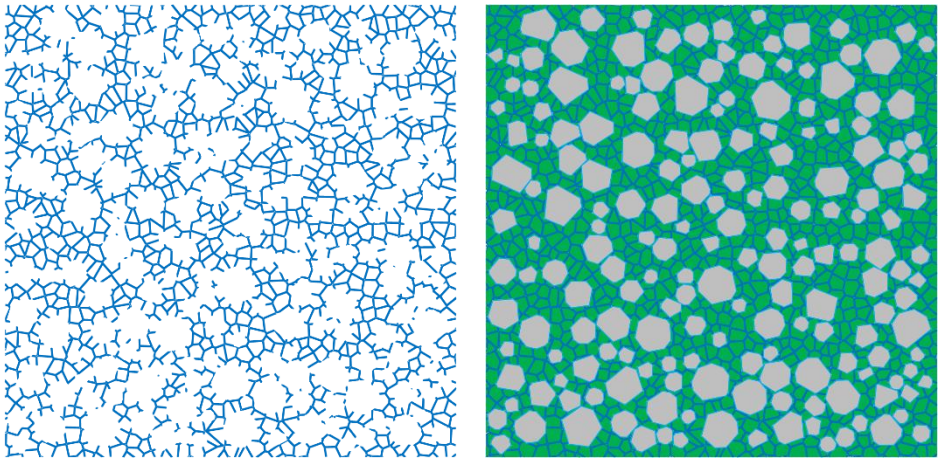

(a) (b)

Fig. 7.8. Geometric properties of specimen: (a) capillary structure, (b) overall framework

7.5 Model for drying shrinkage of concrete

In this part, the multi-coupled elasto-plastic phase-field model is introduced to predict concrete mechanical properties at a micro-meso scale. This model facilitates the investigation of drying shrinkage, moisture transport, water loss, and crack development. A finite element theory of this proposed model is proposed based on this framework. For further details on the underlying theory of moisture loss and the phase-field model, refer to the Chapter 2, 5 and 6.

7.5.1 Moisture diffusion and convection model

Moisture diffusion in concrete is driven by both vapour and liquid water, resulting in desorption and adsorption processes (Damrongwiriyanupap et al., 2013, Caré, 2003, Ye et al., 2006). According to the extended Darcy's and Fick's laws, moisture diffusion is described as follows (Chapter 2):

$$\frac{\partial w}{\partial h}\frac{\partial h}{\partial t} = \frac{\partial}{\partial x}\left(K_L \frac{\rho_L RT}{M_W h}\frac{\partial h}{\partial x} + K_V p_{VS}\frac{\partial h}{\partial x} \right) \tag{7.1}$$

where $\partial w/\partial h$ represents slope of the desorption isotherm, w and h are water content and RH due to moisture diffusion ($w = w_a - \Delta w_s$, $h = h_a - \Delta h_s$), w_a and h_a are total water content and RH in concrete, Δw_s water loss by hydration process, Δh_s is the RH reduction due to hydration process.

To determine the diffusion coefficients for vapour and liquid water, the diameter and proportion of each pore type must be considered. The Rayleigh-Ritz size distribution is employed to describe and calculate the distribution of each pore type (Maekawa et al., 2008).

$$\phi = \phi_t \sum_{1}^{4} \phi_i \left(1 - \exp\left(-\frac{r}{B_i} \right) \right) \tag{7.2}$$

where ϕ_t represents concrete porosity, and ϕ_i represents ratio between the porosity of pore type i and the overall porosity. B_i is pore radius corresponding to the peak of the differential porosity for each pore type on a logarithmic scale.

To derive the analytical solution for Rayleigh-Ritz (R-R) scheme, the well-established water saturation degree model by Brunauer-Skalny-Bodor is utilized, along with the empirical functions developed by Xi et al. (Xi et al., 1994) to obtain parameters for R-R size distribution model. Further details can be found in (Chapter 2).

Knudsen's theory is applied to describe collisions between water molecules and their interactions with pore walls during vapour diffusion. The mean free path of water molecules, l_m, is used to express vapour diffusion within a pore. Consequently, the diffusion coefficient for vapour water is derived by integrating over the entire pore size range (Maekawa et al., 2008):

$$K_V = \int_{r_c}^{\infty} \frac{k_V}{\tau} \left(\frac{r - t_a}{r} \right)^2 f_d(r)\, dr \tag{7.3}$$

where τ is a parameter representing pore tortuosity and it is taken as $\tau = (\pi/2)^2$ (Maekawa et al., 2008, Ishida et al., 2007).

The moisture diffusion coefficient for liquid water is determined through moisture flux balance, utilizing Hagen-Poiseuille formulation, as follows (Ishida et al., 2007):

$$K_L = \frac{\rho_L}{8\tau^2 \eta} \left(\int_0^{r_c} r f_d(r)\, dr \right)^2 \tag{7.4}$$

where ρ_L represents density for liquid water, η represents the viscosity of liquid water.

Considering mass balance between ambient conditions and concrete surface, the convection process at the exposed surface is considered. The diffusion flux to the air is expressed as follows:

$$J = -\frac{D_{va} M_w p_{vs}}{RT} \cdot \frac{h_b - h_e}{\delta} \tag{7.5}$$

where h_b and h_e represent the relative humidity on concrete surface and ambient air, respectively. The parameter δ is effective thickness for concrete boundary, which can be taken to be about 25 mm (Xi et al., 1994).

7.5.2 Phase-field mechanical model

To describe complex mechanical behaviours for concrete, including elasto-plastic behaviour, asymmetric tension-compression response, stiffness degradation, and crack propagation, a micro-meso elasto-plastic phase-field model is employed. This model incorporates spectral decomposition method (Chapter 5).

To couple crack development with deformation, total potential energy Π for fracture domain Ω is proposed as the sum of crack and strain energies. The equation is as follows:

$$\Pi = E(u,d) + P(u,d) + W(d) = \int_{\Omega} \psi_{\varepsilon}\left(\varepsilon(u),d\right) d\Omega + \int_{\Gamma} g_c d\Gamma \tag{7.6}$$

where, *E(u,d)* represents elastic energy, *P(u,d)* represents plastic energy, *W(d)* represents fracture energy, u represents displacement variables, $\varepsilon(u)$ is strain tensor, ψ_{ε} is mechanical energy, g_c is critical energy threshold, Γ is fracture surface.

In degradation of elastic energy, only tensile stress contributes to damage and crack development. The impact of cracks on stiffness reduction is also accounted for. Elastic energy function is described as follows (Liu et al., 2016):

$$\psi_{\varepsilon}^{el}\left(\varepsilon(u),d\right) = g(d)\cdot\psi_0^{el+}(\varepsilon) + \psi_0^{el-}(\varepsilon) \tag{7.7}$$

The definition of the positive and negative energy components can differ based on the implementation. For brittle materials, it is described as follows (Amor et al., 2009, Freddi et al., 2010):

$$\psi_{\varepsilon}^{el}\left(\varepsilon(u),d\right) = \mu\sum_{i=1}^{3}\left[\langle\varepsilon_i\rangle_-^2 + g(d)\langle\varepsilon_i\rangle_+^2\right] + \frac{\lambda}{2}\left[g(d)\langle tr(\varepsilon)\rangle_+^2 + \langle tr(\varepsilon)\rangle_-^2\right] \tag{7.8}$$

To describe the nonlinear mechanical behaviour under tensile and compressive loads, the implementation utilizes the Drucker-Prager yield criterion (Drucker and Prager, 1952):

$$f(I_1,J_2) = \sqrt{J_2} + \beta_{DP} I_1 - g(d)\left[\sigma^{\lim} + H\varepsilon_{eq}^{pl}\right] \tag{7.9}$$

As there is no permanent volume change, ductile component of the history energy is represented as a equation between yield stress and energy-equivalent plastic strain:

$$\psi_0^{pl}\left(\varepsilon_{eq}^{pl}(u)\right) = \varepsilon_{eq}^{pl}(u)\left[\sigma^{\lim} + \frac{1}{2}H\varepsilon_{eq}^{pl}(u)\right] \tag{7.10}$$

The plastic energy function is derived from the Drucker-Prager yield criterion (Drucker and Prager, 1952) and can be described using the following flow rules (Krabbenhøft, 2002):

$$\psi_{\varepsilon}^{pl} = g(d)\psi_0^{pl} = g(d)\left(\varepsilon_{eq}^{pl}\right)^T K_0 \varepsilon_{eq}^{pl}$$
$$K_0 = \left(K - \frac{K\frac{\partial g}{\partial \sigma}\left(\frac{\partial f}{\partial \sigma}\right)^T K}{H + \left(\frac{\partial f}{\partial \sigma}\right)^T D \frac{\partial g}{\partial \sigma}} \right) \tag{7.11}$$

where, K represents elastic constitutive matrix, K_0 represents elasto-plastic constitutive matrix, g and f are the plastic potential energy.

Therefore, the total potential energy function is developed by combining elastic energy, plastic energy, and crack energy, as follows:

$$\prod = \int_{\Omega} \left\{ g(d)\left[\psi_0^{el+}(\varepsilon) + \psi_0^{pl}(\varepsilon) - \psi_c\right] + \psi_0^{el-}(\varepsilon) + \psi_c + 2l_c\psi_c\left[d^2 + l_c^2\left|\nabla d\right|^2\right] \right\} d\Omega \tag{7.12}$$

To analyse the muti-phase field model of concrete, including its individual constituent (mortar, ITZ, aggregates, pores), the potential energy function is proposed based on the homogenous solid. Since the critical fracture energy is significantly higher than that of mortar and ITZ, aggregate is considered as an elastic part. Mortar and ITZ are treated as elasto-plastic crack propagation parts. Therefore, the crack geometry of mortar, ITZ and pores is described by $d_M(x)$, $d_I(x)$ and $d_P(x)$, respectively, which are described as follows:

$$\begin{cases} \gamma_M(d_M, \nabla d_M) = \dfrac{d_M^{\,2}}{2l_c} + \dfrac{l_c}{2}\left|\nabla d_M\right|^2 \\ \gamma_I(d_I, \nabla d_I) = \dfrac{d_I^{\,2}}{2l_c} + \dfrac{l_c}{2}\left|\nabla d_I\right|^2 \\ \gamma_P(d_P, \nabla d_P) = \dfrac{d_P^{\,2}}{2l_c} + \dfrac{l_c}{2}\left|\nabla d_P\right|^2 \end{cases} \tag{7.13}$$

By introducing the potential energy correction parameter β into the total potential energy Eqs (7.11) and (7.12), the total potential energy is decomposed into energies corresponding to the mortar, ITZ, pores and aggregates, as:

$$\Pi=\int_{\Omega}\left\{\begin{array}{l}V_M\left(\left(\varepsilon_{eq}^{el}\right)^T\left(K_M\right)\varepsilon_{eq}^{el}+\left(\varepsilon_{eq}^{pl}\right)^T g\left(d\right)K_{M0}\varepsilon_{eq}^{pl}+\left(1-g\left(d\right)\right)\dfrac{g_M}{2l_c}+g_M\gamma\left(d,\nabla d\right)\right)\\+V_I\left(\left(\varepsilon_{eq}^{el}\right)^T\left(K_I\right)\varepsilon_{eq}^{el}+\left(\varepsilon_{eq}^{pl}\right)^T g\left(d\right)K_{I0}\varepsilon^{eq}+\left(1-g\left(d\right)\right)\dfrac{g_I}{2l_c}+g_I\gamma\left(d,\nabla d\right)\right)\\+V_P\left(\left(\varepsilon_{eq}^{el}\right)^T\left(K_P\right)\varepsilon_{eq}^{el}+\left(\varepsilon_{eq}^{pl}\right)^T g\left(d\right)K_{P0}\varepsilon^{eq}+\left(1-g\left(d\right)\right)\dfrac{g_P}{2l_c}+g_P\gamma\left(d,\nabla d\right)\right)\\+V_A\left(\left(\varepsilon_{eq}\right)^T K_A\varepsilon_{eq}\right)\end{array}\right\}d\Omega \tag{7.14}$$

where, K_M, K_I, K_P and K_A are the elastic constitutive matrix of mortar, ITZ, pores and aggregate, K_{M0}, K_P and K_{I0} are the elasto-plastic constitutive matrix of mortar, pores and ITZ.

$$\left\{\begin{array}{c}\boldsymbol{Vg}\Delta\boldsymbol{\gamma}\left(d,\nabla d\right)\beta=\left(1-d\right)H^1\\\beta=\dfrac{H^1}{H^1+\Delta\psi}\\\Delta\psi=\left(V_M^1\psi_{M0}^{el-}+V_I^1\psi_{I0}^{el-}+V_P^1\psi_{P0}^{el-}+V_A^1\psi_A^{el}\right)-\left(V_M^2\psi_{M0}^{el-}+V_I^2\psi_{I0}^{el-}+V_P^2\psi_{P0}^{el-}+V_A^2\psi_A^{el}\right)\end{array}\right. \tag{7.15}$$

where, H^l is the history energy of reference sample, β is the potential energy correction parameter.

The more details of this proposed multi-phase elasto-plastic phase-field model can be found in Chapter 5.

7.5.3 Drying shrinkage model

Moisture loss within pores induces capillary stress, leading to concrete drying shrinkage. At thermodynamic equilibrium at the vapor-water interface, the difference between vapor pressure and liquid pressure determines the capillary pressure (P_{cap}). Consequently, capillary stress mechanism is employed to calculate shrinkage due to moisture loss using Mackenzie-Bentz formulation (Mackenzie, 1950, Bentz et al., 1998):

$$\varepsilon_p=\frac{S}{3}P_{cap}\left(\frac{1}{K}-\frac{1}{K_s}\right) \tag{7.16}$$

where, S represents volumetric saturation degree, K represents bulk modulus for harden cement paste, K_s represents bulk modulus for solid skeleton of harden cement paste.

Capillary pressure can be calculated using the Kelvin-Laplace theory based on the surface tension, as follows (Adamson and Gast, 1967):

$$P_{cap} = \frac{-\ln(RH/100)RT_0}{V_m} \tag{7.17}$$

where, R represents universal gas constant, RH represents internal relative humidity, T_0 represents absolute temperature, V_m represents water molar volume.

The total measured concrete deformation consists of both shrinkage and initial mechanical strain. The total strain is obtained utilizing the rule of superposition (Orta and Bartlett, 2014, Fisher et al., 1981):

$$\varepsilon_{total} = \varepsilon_{el} + \varepsilon_{pl} + \varepsilon_{ds} \tag{7.18}$$

where, ε_{total} represents total strain, ε_{el} represents elastic strain, ε_{pl} represents plastic strain, and ε_{ds} represents drying shrinkage.

Therefore, this multi-phase model of concrete is described by four phases as follows:

$$\begin{cases} \varepsilon_{total}^{M} = \varepsilon_{el}^{M} + \varepsilon_{pl}^{M} \\ \varepsilon_{total}^{ITZ} = \varepsilon_{el}^{ITZ} + \varepsilon_{pl}^{ITZ} \\ \varepsilon_{total}^{Pore} = \varepsilon_{el}^{Pore} + \varepsilon_{pl}^{Pore} + \varepsilon_{ds}^{Pore} \\ \varepsilon_{total}^{Agg} = \varepsilon_{el}^{Agg} \end{cases} \tag{7.19}$$

where, ε_{total}^{i} (i = *M*, *ITZ*, *Pore*, *Agg*) are the total strain of mortar, ITZ, pore and aggregate phases, ε_{el}^{i} (i = *M*, *ITZ*, *Pore*, *Agg*) are the elastic strain of mortar, ITZ, pore and aggregate phases, ε_{pl}^{i} (i = *M*, *ITZ*, *Pore*) are the plastic strain of mortar, ITZ and pore phases ε_{ds}^{Pore} is the drying shrinkage of moisture loss for pore phase.

7.6 Calibration and calibration of drying model

7.6.1 Calibration of drying shrinkage model

In this part, this developed modelling is calibrated and verified from three aspects: (1) the RH evolution at different depths, (2) the drying shrinkage prediction over time, and (3) the drying shrinkage estimation at various depths.

To calibrate the drying model, concrete specimens were simulated to predict moisture diffusion, drying shrinkage, and crack propagation, were compared with test results in Section 7.3. In this simulation, a square domain with the length of L = 150 mm was used, with bottom boundary controlled in both the x direction and y direction, as illustrated in Fig. 7.9. A same element size of h = 0.5 mm was applied across all phases, including aggregate, mortar, ITZ and pores, comprising 370,448 triangular elements.

The parameters used for R-R model and mechanical parameters are depicted in Table 7.2 and Table 7.3, and Fig. 7.10 shows the moisture diffusivity based on the methodology detailed in Section 7.5.

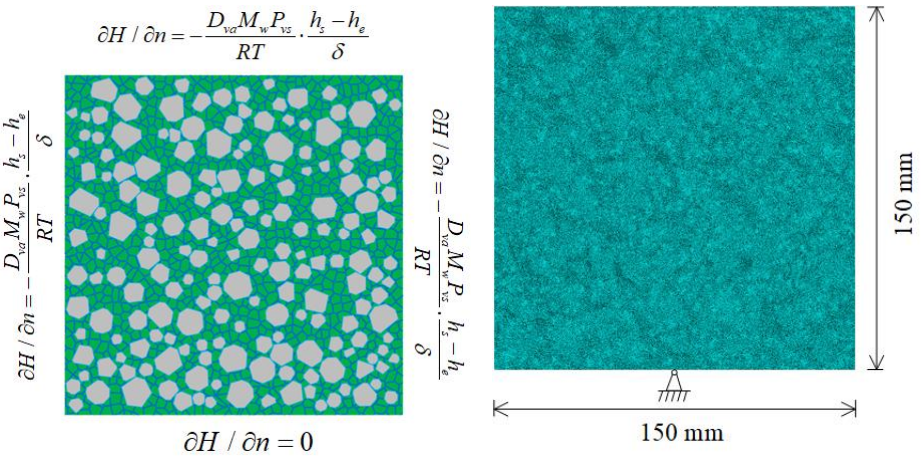

Fig. 7.9. Details of model: (a) geometry and boundary condition (b) mesh size

Table 7.2: Parameter for R-R model

	ϕ_1	B_1 (nm)	ϕ_2	B_2 (nm)	ϕ_3	B_3 (nm)	ϕ_4	B_4 (nm)
sample	0.021	1.03	0.032	6.55	0.024	72.9	0.027	554.80

Table 7.3: Parameters for concrete samples of phase field

	E GPa	v	σ_{y1}^c MPa	H_1 GPa	σ_{y2}^c MPa	H_2 GPa	σ_y^t MPa	l_c mm	β	β_{DP}	ψ_c^c MPa	ψ_t^c MPa
Aggregate	40	0.2	-	-	-	-	-	-	-	-	-	-
Mortar	23.9	0.2	16	13	30	4.6	3.6	1	1	0.37	1.1	0.0105
ITZ	12	0.2	16	6.5	30	2.3	3.6	1	1	0.37	0.55	0.0053

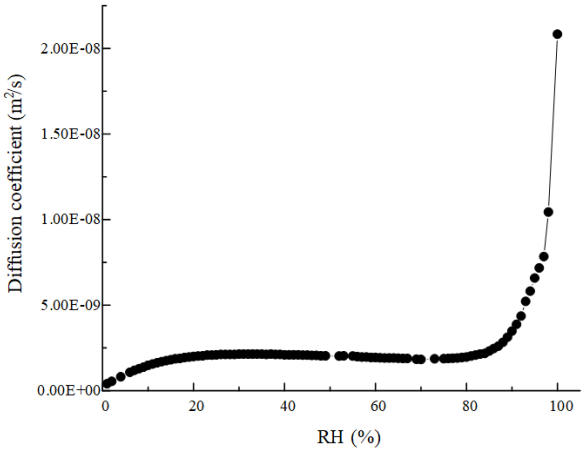

Fig. 7.10. Diffusion coefficient versus RH

The RH distribution within the sample can be predicted using this drying shrinkage model, incorporating the parameters from the R-R model. Fig. 7.11a presents the finite element method (FEM) model developed, accounting for ITZ and pore structures, as well as approach mentioned in Section 7.5 and initial boundary conditions. A comparison between numerical predictions and experimental results at 40 days is shown in Fig. 7.11b, demonstrating overall good agreement between the two.

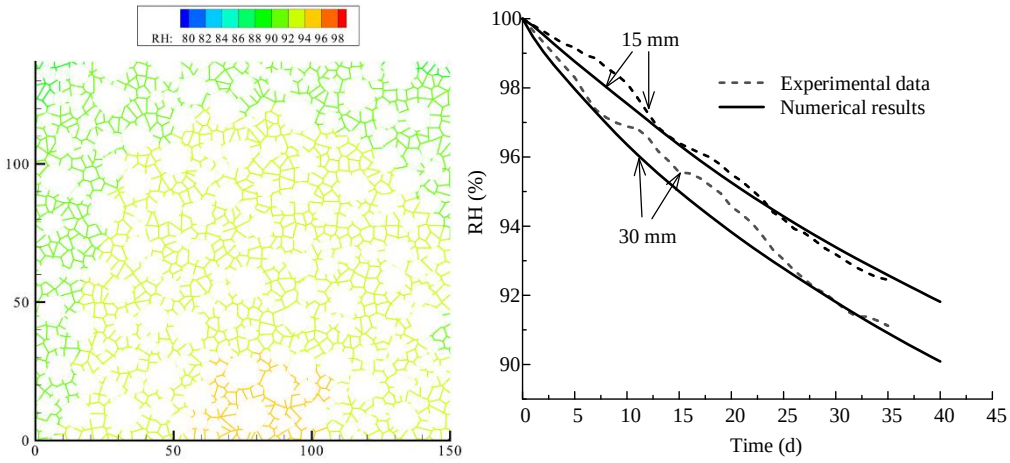

(a) (b)

Fig. 7.11. FEM RH results: (a) RH distribution at 40 days (b) comparison between experimental data and simulation results

To analyse the moisture drying process at three surfaces, the relative humidity (RH) evolution within the pore network of the specimen at various time intervals (i.e., 3, 7, 28, and 40 days) is illustrated in Fig. 7.12. As anticipated, RH decreases rapidly near the boundaries, while the central area of the bottom surface remains nearly fully saturated, retaining 96% RH.

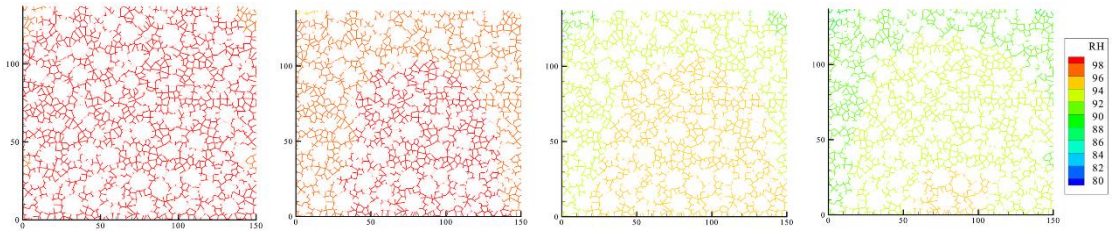

(a) (b) (c) (d)

Fig. 7.12. Moisture diffusion evolution at different time: (a) 3 day, (b) 7 day, (c) 28 day, (d) 40 day

The multiple coupling model also allows of this analysis of fracture evolution branches, as depicted in Fig. 7.13. A comparison between test results and numerical results for drying shrinkage at varying depths is presented in Fig. 7.14.

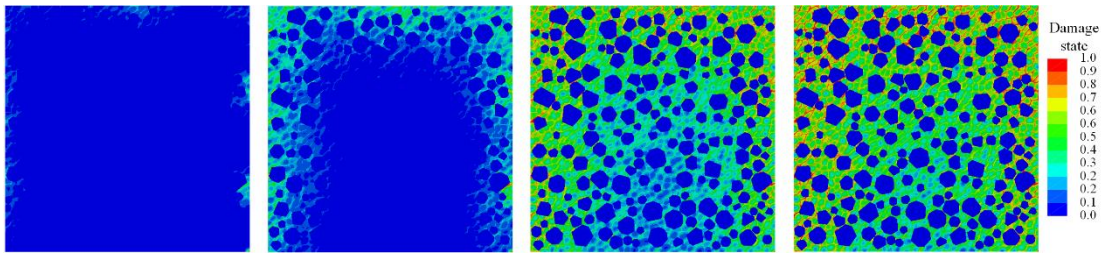

(a) (b) (c) (d)

Fig. 7.13. Crack propagation at different time: (a) 3 day, (b) 7 day, (c) 28 day, (d) 40 day

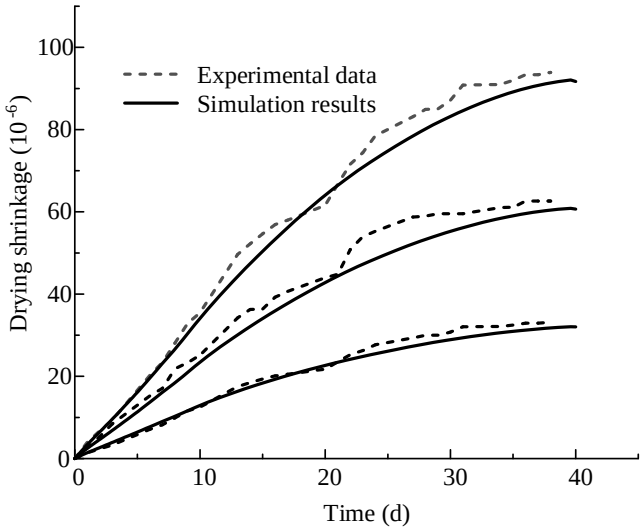

Fig. 7.14. Comparison of drying shrinkage between experimental data and simulation results at different depth

As depicted in Fig. 7.13, fracture evolution paths originate from the drying surface due to moisture loss and tend to follow the ITZ and pore structures, as these regions are more susceptible to breakage

compared to the mortar. Crack propagation begins on the 3rd day rather than the 1st, which can be attributed to mechanical properties development during hydration process. In this simulation, the mechanical properties are based on concrete at the 28th day, rather than evolving with hydration. This observation is also reflected in Fig. 7.14, where the drying shrinkage follows a similar trend at different depths. However, the simulated shrinkage is consistently lower than the experimental observation across various depths, likely owing to higher mechanical properties used in the model, which result in reduced shrinkage deformation.

7.6.2 Calibration of different water/cement ratio for drying shrinkage model

To calibrate the developed drying model, experimental data from two mortar samples with different mix designs and water/cement (W/C) ratios from the literature are utilized to predict the drying shrinkage and crack propagation in early-age mortar overlays (Beushausen et al., 2013). The overlay mortar (1000 mm × 150 mm × 30 mm) was cast on a pre-existing concrete beam for calibration (Beushausen et al., 2013). Due to the thinness of the mortar overlay, the impact of heat generation from hydration process was minimal. The concrete beam (1000 mm × 150 mm × 200 mm) had been cast three months prior to the overlay, allowing the hydration process of the beam to be disregarded. After casting the overlay and demoulding, no curing was applied. The samples were removed to a curing room (18 ± 3 °C and 76 ± 2% RH), where all surfaces were exposed to air. For this calibration, W/C ratios of 0.45 and 0.60, without curing, were employed to assess the model's ability to predict drying shrinkage. Further details are available in literature (Beushausen et al., 2013).

To simulate the drying process and crack propagation at the top surface, three key aspects are considered: (1) the RH evolution at the side surface, (2) the elastic modulus during the hydration process, and (3) the estimation of crack propagation.

To calibrate this drying model, mortar specimens were simulated to predict moisture diffusion at the side surface, while drying process on top surface was applied to forecast drying shrinkage and crack propagation. To reduce computational time, a half-specimen domain (500 mm × 30 mm) was used for the moisture diffusion process at the side surface, and a domain of (500 mm × 150 mm) was employed for drying shrinkage and crack propagation analysis. The geometric properties for moisture diffusion are illustrated in Fig. 7.15. The same element size of h = 0.5 mm was employed across all phases, including mortar and pores, resulting in 220,748 triangular elements for specimen with a W/C ratio of 0.45 and 247,088 triangular elements for specimen with a W/C ratio of 0.60. The parameters for the R-R model are listed in Table 7.4, and Fig. 7.16 shows the moisture diffusivity and average RH evolution at the top surface, based on the methodology depicted in Section 7.5.

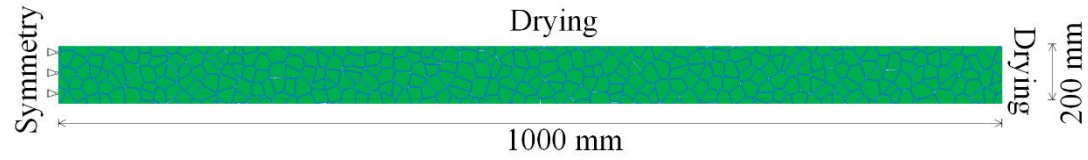

(a)

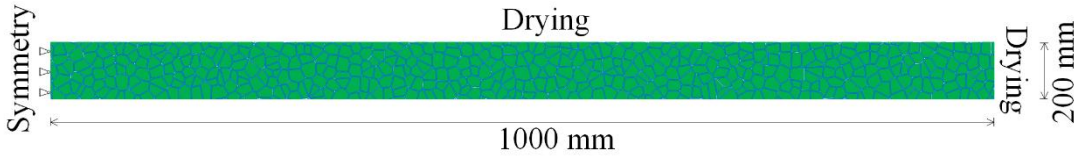

(b)

Fig. 7.15. Geometric properties for moisture diffusion model with different W/C ratio: (a) 0.45 (b) 0.60

Table 7.4: Parameter for R-R model

W/C	ϕ_1	B_1 (nm)	ϕ_2	B_2 (nm)	ϕ_3	B_3 (nm)	ϕ_4	B_4 (nm)
0.45	0.042	0.99	0.041	6.59	0.034	73.2	0.015	557.62
0.60	0.051	1.09	0.055	6.71	0.043	74.4	0.019	560.41

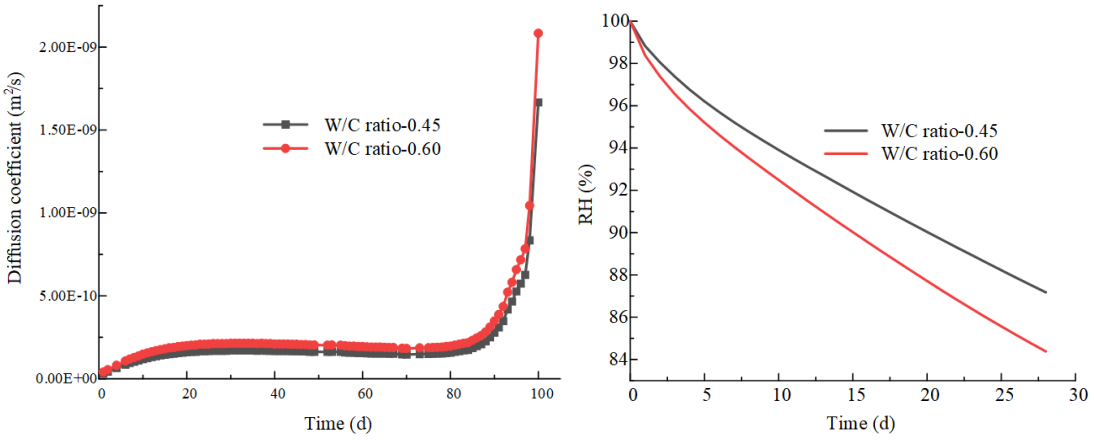

(a) (b)

Fig. 7.16. Moisture diffusion parameter and results: (a) diffusion coefficient (b) average RH evolution

In this simulation, the elastic modulus was modelled to evolve over time using a fitted curve to account for the influence of hydration process on mechanical parameters. To determine elastic modulus for mortar matrix, the Mori-Tanaka (MT) scheme was employed, as outlined in the authors' previous work (Chapter 5), and is illustrated in Fig. 7.17.

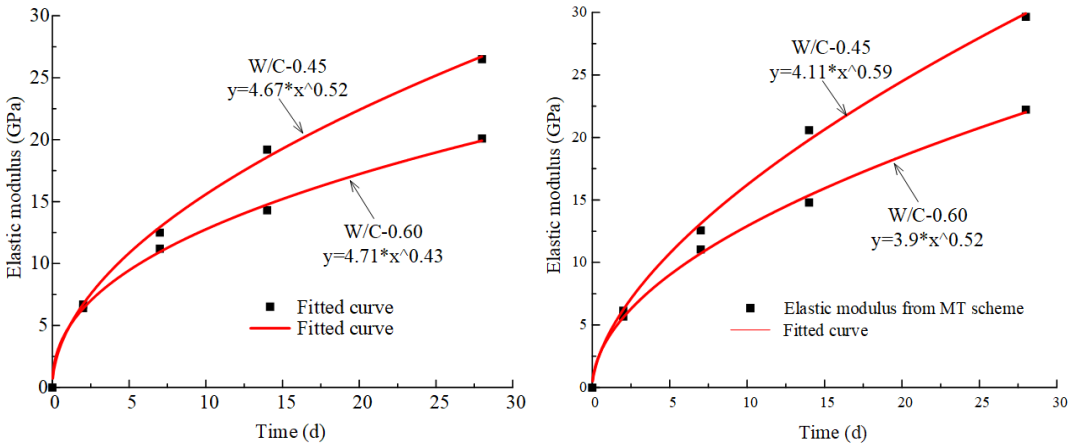

(a) (b)

Fig. 7.17. Elastic modulus varies with time: (a) mortar specimens (Kheir et al., 2021) (b) mortar solid phase from MT scheme

To predict crack propagation and drying shrinkage, the top surface of the overlay, including pores and the mortar solid phase, was simulated. In the deformation simulation, a domain of 500 mm × 150 mm was used for the investigation of shrinkage and crack development. The geometric properties of the shrinkage model are depicted in Fig. 7.18. A uniform mesh size of h = 1 mm was employed across all phases, including mortar and pores, resulting in 1,114,924 triangular elements for the specimen with a W/C ratio of 0.45 and 1,254,152 triangular elements for the specimen with a W/C ratio of 0.60. The parameters used for the mechanical properties of the mortar solid and pores for both types of specimens are given in Table 7.5, Additionally, the specimen with a W/C ratio of 0.60 has a potential energy correction parameter of 0.968 for the mortar and pore structures.

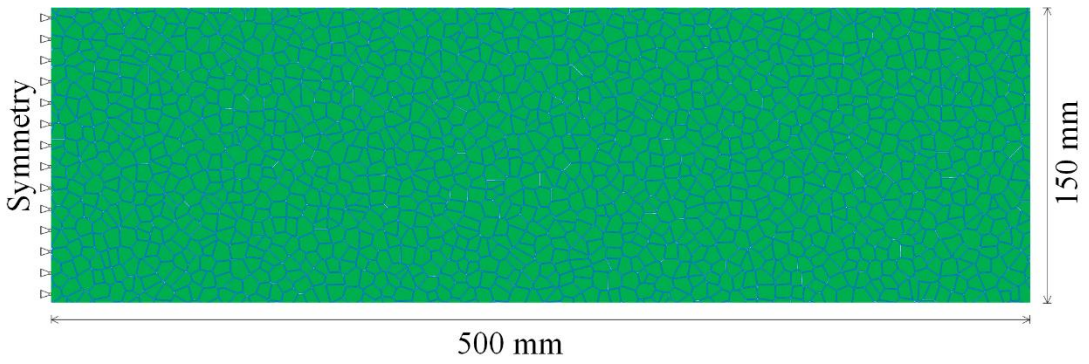

(a)

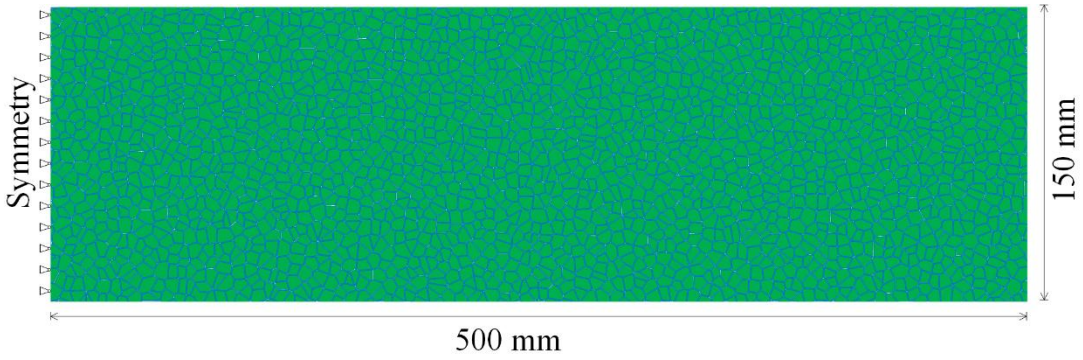

(b)

Fig. 7.18. Geometric properties for shrinkage model with different W/C ratio: (a) 0.45 (b) 0.60

Table 7.5: Parameters for concrete samples of phase field

	Time d	E GPa	v	σ_{y1}^{c} MPa	H_1 GPa	σ_{y}^{t} MPa	l_c mm	ψ_c^c MPa	ψ_t^c MPa
Mortar	2	6.15	0.2	3.3	4	2.2	1	0.24	0.002
	7	12.57	0.2	6.8	9.3	2.6	1	0.48	0.0045
	14	20.58	0.2	11.3	13.6	3.7	1	0.78	0.0074
	28	29.65	0.2	16	16	4.3	1	1.13	0.011
Pores	2	12	0.2	3.3	2	2.2	1	0.12	0.001
	7	12	0.2	6.8	4.7	2.6	1	0.24	0.0045
	14	12	0.2	11.3	6.8	3.7	1	0.39	0.0074
	28	12	0.2	16	8	4.3	1	0.56	0.0055

To analyse crack propagation induced by drying shrinkage, the crack development path at the top surface is compared with experimental data, as depicted in Fig. 7.19.

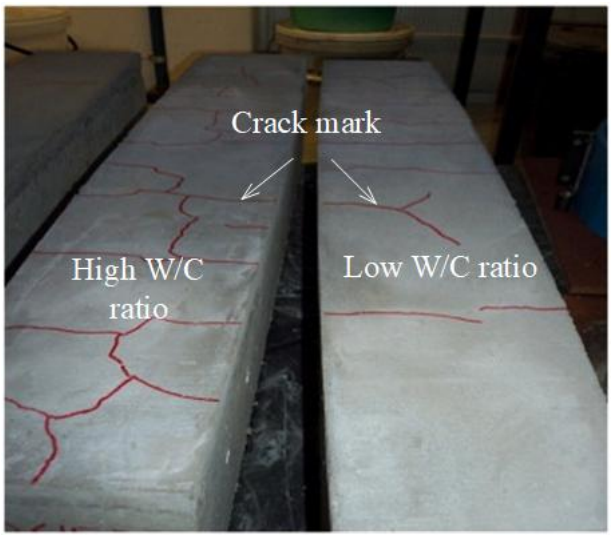

(a)

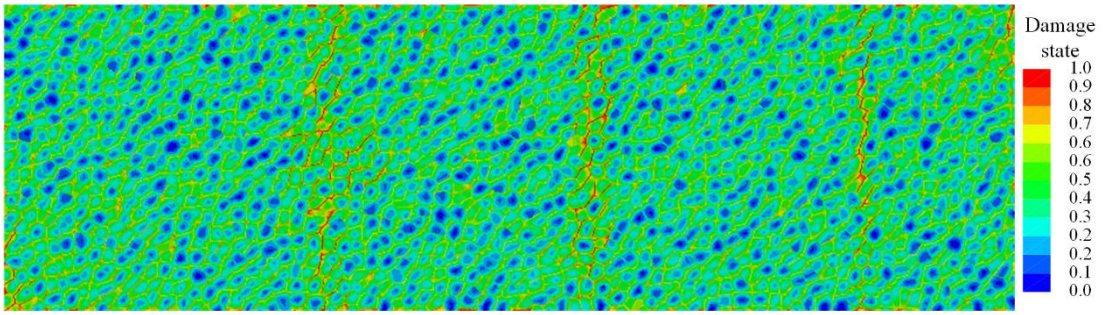

(b)

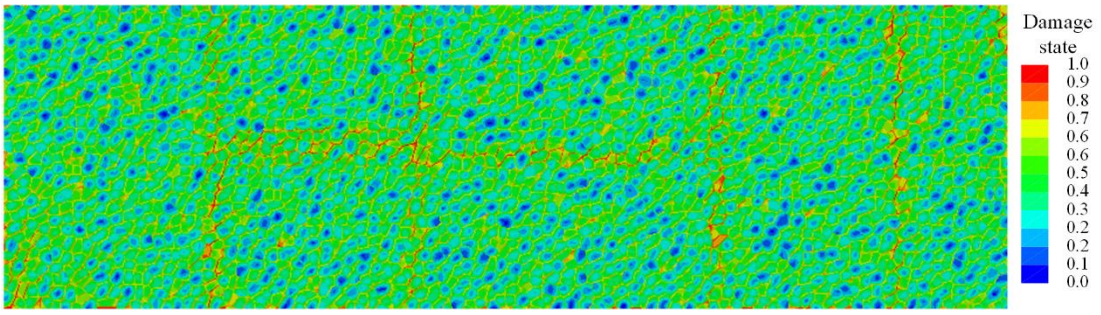

(c)

Fig. 7.19. Crack propagation: (a) experiments (Beushausen et al., 2013) (b) W/C ratio 0.45 (c) W/C ratio 0.60

As seen in Fig. 7.19, the crack propagation paths induced by the drying process due to moisture loss tend to follow the pore structures, as the pore phase is more susceptible to breakage compared to the mortar solid. Additionally, a higher W/C ratio induces increased crack propagation because the higher

ratio leads to greater porosity and weaker mechanical properties in the simulation. At the crack branches, the numerical results exhibit the same trends as experimental findings.

To further investigate the details of the cracks, the crack width was determined by constraining the damage state in the simulation to $d > 0.95$, as depicted in Fig. 7.20.

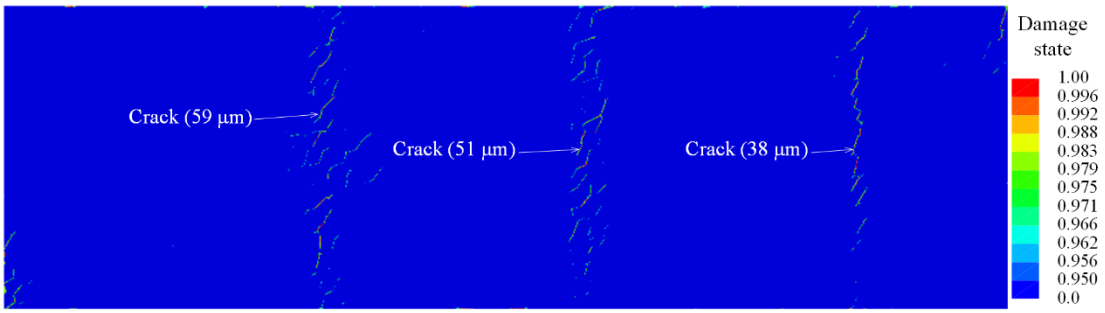

(a)

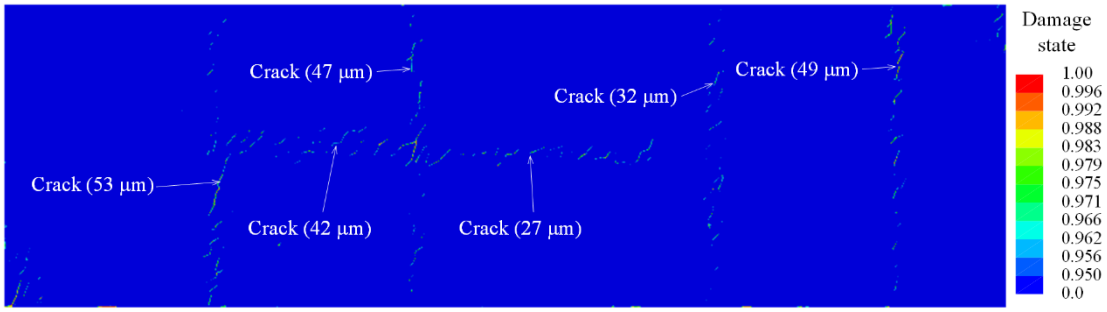

(b)

Fig. 7.20. Crack width for different specimens: (a) W/C ratio 0.45, (b) W/C ratio 0.60

As shown in Fig. 7.20, drying shrinkage induces varying crack propagation in the different specimens, primarily due to the differences in porosity within the mortar. A higher W/C ratio results in more free moisture in mortar, leading to an increased formation of pore structures and, consequently, more crack branches when moisture is lost to ambient conditions. The crack widths were analysed for both specimens in Fig. 7.20. The specimen with a W/C ratio of 0.45 primarily developed vertical cracks, with a total fracture width of 148 μm at 28 days. Similarly, the sample with a W/C ratio of 0.60 also produced vertical cracks but with a wider total crack width of 181 μm. Additionally, horizontal cracks were induced by the drying process due to the high porosity, with widths of 42 μm and 27 μm for the samples with W/C ratios of 0.45 and 0.60, respectively.

7.7 Conclusion

According to Chapter 5 and Chapter 6, the drying shrinkage is investigated by employing the mechanical performance and autogenous shrinkage. And the comprehensive numerical modelling was proposed to study drying shrinkage and failure mechanisms of early-age concrete. The meso-micro elasto-plastic phase-field model, along with volume reduction theory, was incorporated into the drying shrinkage modelling to simulate drying shrinkage and fracture evolution in cementitious materials. The model was calibrated and calibrated against experimental results. The primary conclusions are outlined below:

(1) Monte Carlo method and Voronoi tessellation are employed to generate the geometry of aggregate, ITZ, and pore structures. This approach offers a viable and flexible method for separately analysing drying shrinkage (capillary stress induced by water loss in the pore phase).
(2) The proposed drying shrinkage model demonstrates strong agreement with the evolution of shrinkage over time at various depths of concrete on the meso-micro scale. The modelling results are verified through comparison with multiple experimental results.
(3) This proposed model accurately describes the crack propagation path in cementitious composites across multiple experiments. The results confirm the model's capability to capture both drying shrinkage and the associated mechanical behaviour.
(4) Calibration of the specimens shows that higher W/C ratio induces the increased porosity due to the presence of free water after hydration process. This leads to greater drying shrinkage, more crack branching, and wider crack widths.

The proposed model enables more accurate predictions of mechanical behaviour and the hygro-mechanical framework in concrete. However, the method generates numerous elements, resulting in high time-consuming. Therefore, further research is necessary to propose algorithms that reduce the number of mesh elements and improve computational efficiency.

Chapter 8: Conclusions and Discussion for Future Research

8.1 Conclusions

This research aimed to quantify the moisture loss (self-desiccation and drying process), shrinkage development and crack propagation at the meso-micro scale for concrete. A wide range of research studies were reviewed to investigate and analyse the theories and parameters that induce moisture evolution in concrete. Based on the moisture diffusion theories for liquid and vapour water, an innovative method for modelling moisture diffusion inside concrete was proposed by combining Voronoi tessellation and the Rayleigh-Ritz (R-R) distribution. To describe the mechanical and failure performance of concrete, a multiple-phase elasto-plastic phase-field model was proposed to predict the degradation process of concrete. The spectral decomposition of the strain tensor and the Drucker-Prager yield criterion were employed to model the asymmetric tension-compression behaviour and plastic performance of concrete. Combining the moisture diffusion and mechanical model, the autogenous and drying shrinkage were predicted at different components (pore or mortar phases). The main conclusions are summarised as follows:

(1) Using the Monte Carlo method and Voronoi tessellation to generate the geometry and spatial distribution of aggregate, ITZ, and pores, leads to a viable and flexible numerical method that allows for the tortuosity of concrete to be taken into account directly in the moisture diffusion modelling process.
(2) Moisture diffuses slightly faster with decreasing ITZ thickness and decreasing fine aggregate fractions. The shape of coarse aggregate has a minor effect on moisture diffusion.
(3) Comparisons of numerical predictions and experimental results show that the RH evolution can be adequately predicted for early age concrete, hardened concrete and concretes with different W/C ratios.
(4) The phase-field model is calibrated using independent experimental results in terms of crack propagation and load-displacement behaviour. The results confirm the ability of the model to capture the mechanical behaviour of concrete in flexure and compression.
(5) The introduced energy dissipation and the potential energy correction parameters can effectively characterise the damage response of concrete components. The mesoscale results accurately replicate crack development behaviour, with the load-deflection and load-CMOD curve comparisons confirming the numerical model's ability to match experimental observations.
(6) Crack propagation is influenced by the notch depth and aggregate volume content. Shallow notches lead to more crack branches, particularly with increased aggregate content, due to a

higher number of ITZ branches and uncertainties in crack initiation. Conversely, deep notches result in fewer crack branches, as they facilitate a more controlled crack propagation path.

(7) The MT scheme provides a reasonable estimation of the mechanical properties of mortar solid and pore phase in the micro-meso scale model of concrete. This scheme contributes to a good agreement between experimental data and simulation results.

(8) The proposed autogenous shrinkage model demonstrates excellent agreement with the shrinkage development over time at different depths of concrete at the meso-micro scale. The modelling results were calibrated through several experimental studies.

(9) The proposed drying shrinkage model demonstrates strong agreement with the development of shrinkage over time at various depths of concrete on the meso-micro scale. The modelling results are calibrated through comparison with multiple experimental data sets.

8.2 Discussion and Future Work

This study focused on the multiple-coupling problems in concrete at a meso-micro scale level by employing moisture diffusion model, phase-field model, M-T scheme and spatial distribution of concrete. This method can simulate and predict shrinkage in each phase, but this also induces some problems. At this mesoscale level, the random spatial distribution was employed to generate aggregates in the horizontal direction. For the vertical direction, it is not enough to predict the real spatial distribution even if the different aggregate content was considered from the vertical direction. Furthermore, as the ITZ thickness is fixed with one value, this will affect the crack initiation and propagation. The spatial distribution of pore structure is considered as a random phase, which also affects the moisture diffusion and mechanical properties.

For the mesoscale model, the small mesh size results in a very large number of elements and it is computationally expensive and resource intensive. To predict the crack propagation by using the phase-field method in real structures a tremendous number of elements need to be generated to capture the overall behaviour and crack development. Obviously, this scale cannot be used to simulate large concrete structures such as bridges, tunnels and buildings.

To complement this work, the homogenous method should be introduced. This method can be used to translate the mesoscale model to the homogenous model with a suitable mesh size for concrete structures. To meet this requirement, analytical homogenous and numerical homogenous methods need to be employed to describe the moisture diffusion and mechanical properties with a consideration of the different components of concrete.

To investigate the spatial distribution of pores, aggregate and the thickness of ITZ, more experiments need to be conducted for conventional concrete.

However, Experimental findings can differ significantly between types of concrete, particularly when comparing high-performance concrete (HPC) and lightweight concrete (LWC). These differences arise primarily due to variations in material composition, density, microstructure, and intended application. Experimental tests consistently show that HPC exhibits higher compressive and tensile strength, greater resistance to cracking, and lower rates of permeability than conventional concrete. These properties make HPC ideal for structures requiring long-term durability and exposure to harsh environments. However, HPC often shows increased autogenous shrinkage due to its low water-to-cement ratio, which may lead to early-age cracking if not properly managed.

In contrast, lightweight concrete is designed with lower density to reduce structural dead loads, which is advantageous in high-rise buildings and bridge decks. Experimental results indicate that while LWC typically has lower compressive strength and higher porosity than HPC, it provides better thermal insulation and acceptable performance in structural applications where reduced weight is prioritized. However, LWC tends to have greater variability in strength and workability due to the characteristics of lightweight aggregates and their sensitivity to moisture. As a result, it may require tighter control during mixing and placement to ensure consistent performance.

Therefore, the methods proposed by this research will be expanded to investigate the mechanical and physical performance of HPC and LWC in the future.

In addition, environmental factors such as freeze-thaw cycles and chemical exposure can further influence the long-term behaviours of both concrete types. HPC, with its dense microstructure, generally performs well in freeze-thaw environments, especially when air-entraining admixtures are used. However, its low permeability can trap internal moisture, which may contribute to internal cracking under repeated freeze-thaw action if not adequately cured or vented. LWC is more susceptible to freeze-thaw damage due to its higher porosity and moisture absorption, making proper air entrainment and protective measures essential for durability in cold climates.

When it comes to chemical attack, HPC tends to exhibit better resistance due to its dense matrix and often includes supplementary cementitious materials (SCMs) like fly ash or silica fume, which enhance chemical durability. Sulfate and chloride attacks are less likely to penetrate HPC, making it suitable for marine or industrial environments. On the other hand, LWC may allow faster ingress of aggressive agents due to its porous nature and the reactivity of some lightweight aggregates, potentially leading to faster deterioration if not treated with sealants or protective coatings.

Additional long-term concerns include carbonation and alkali-silica reaction (ASR). HPC's dense matrix slows down carbonation, helping to protect embedded reinforcement, though the risk of ASR still exists if reactive aggregates are used. LWC, with its more open pore structure, may experience faster carbonation, increasing the risk of steel corrosion over time, especially if concrete cover is

inadequate. These environmental and chemical influences emphasize the importance of selecting the right concrete mix for the specific application and expected exposure conditions.

Therefore, the methods proposed by this research also will be expanded to investigate different types of long-term effects of HPC, LWC and conventional concrete.

Reference

ADAMSON, A. W. & GAST, A. P. 1967. *Physical chemistry of surfaces*, Interscience publishers New York.

AKCAY, B., AGAR-OZBEK, A. S., BAYRAMOV, F., ATAHAN, H. N., SENGUL, C., TASDEMIR, M. A. J. C. & MATERIALS, B. 2012. Interpretation of aggregate volume fraction effects on fracture behavior of concrete. 28**,** 437-443.

AL-KAMYANI, Z., GUADAGNINI, M. & PILAKOUTAS, K. J. E. S. 2018. Predicting shrinkage induced curvature in plain and reinforced concrete. 176**,** 468-480.

ALDAKHEEL, F. J. T. & MECHANICS, A. F. 2020. A microscale model for concrete failure in poro-elasto-plastic media. 107**,** 102517.

ALESSI, R., AMBATI, M., GERASIMOV, T., VIDOLI, S. & DE LORENZIS, L. J. A. I. C. P. A. B. I. H. O. D. R. J. O. 2018. Comparison of phase-field models of fracture coupled with plasticity. 1-21.

AMIN, M. N., KIM, J.-S., LEE, Y., KIM, J.-K. J. C. & RESEARCH, C. 2009. Simulation of the thermal stress in mass concrete using a thermal stress measuring device. 39**,** 154-164.

AMOR, H., MARIGO, J.-J., MAURINI, C. J. J. O. T. M. & SOLIDS, P. O. 2009. Regularized formulation of the variational brittle fracture with unilateral contact: Numerical experiments. 57**,** 1209-1229.

AMPARANO, F. E., XI, Y. & ROH, Y.-S. J. E. F. M. 2000. Experimental study on the effect of aggregate content on fracture behavior of concrete. 67**,** 65-84.

ANDERBERG, A. & WADSö, L. 2008. Method for simultaneous determination of sorption isotherms and diffusivity of cement-based materials. *Cement and Concrete Research,* 38**,** 89-94.

BAKER, P. H., GALBRAITH, G. H., MCLEAN, R. C. J. B. S. E. R. & TECHNOLOGY 2009. Temperature gradient effects on moisture transport in porous building materials. 30**,** 37-48.

BARENBLATT, G. I. J. A. I. A. M. 1962. The mathematical theory of equilibrium cracks in brittle fracture. 7**,** 55-129.

BAROGHEL-BOUNY, V., MAINGUY, M., LASSABATERE, T., COUSSY, O. J. C. & RESEARCH, C. 1999. Characterization and identification of equilibrium and transfer moisture properties for ordinary and high-performance cementitious materials. 29**,** 1225-1238.

BARY, B. & BéJAOUI, S. 2006. Assessment of diffusive and mechanical properties of hardened cement pastes using a multi-coated sphere assemblage model. *Cement and Concrete Research,* 36**,** 245-258.

BASHEER, L., KROPP, J., CLELAND, D. J. J. C. & MATERIALS, B. 2001. Assessment of the durability of concrete from its permeation properties: a review. 15**,** 93-103.

BAŽANT, Z. J. C. & RESEARCH, C. 1972. Thermodynamics of hindered adsorption and its implications for hardened cement paste and concrete. 2**,** 1-16.

BENTZ, D. P., GARBOCZI, E. J., QUENARD, D. A. J. M., SCIENCE, S. I. M. & ENGINEERING 1998. Modelling drying shrinkage in reconstructed porous materials: application to porous Vycor glass. 6**,** 211.

BEUSHAUSEN, H., CHILWESA, M. J. C. & RESEARCH, C. 2013. Assessment and prediction of drying shrinkage cracking in bonded mortar overlays. 53**,** 256-266.

BISSONNETTE, B. T., PIERRE, P., PIGEON, M. J. C. & RESEARCH, C. 1999. Influence of key parameters on drying shrinkage of cementitious materials. 29**,** 1655-1662.

BITTENCOURT, T. N., WAWRZYNEK, P. A., INGRAFFEA, A. R. & SOUSA, J. J. E. F. M. 1996. Quasi-automatic simulation of crack propagation for 2D LEFM problems. 55**,** 321-334.

BOURDIN, B., FRANCFORT, G. A. & MARIGO, J.-J. J. J. O. E. 2008. The variational approach to fracture. 91**,** 5-148.

BOURDIN, B., FRANCFORT, G. A., MARIGO, J.-J. J. J. O. T. M. & SOLIDS, P. O. 2000. Numerical experiments in revisited brittle fracture. 48**,** 797-826.

BRIFFAUT, M., BENBOUDJEMA, F. & D'ALOIA, L. 2016. Effect of fibres on early age cracking of concrete tunnel lining. Part II: Numerical simulations. *Tunnelling and Underground Space Technology,* 59**,** 221-229.

BROUWERS, H. J. C. & RESEARCH, C. 2004. The work of Powers and Brownyard revisited: Part 1. 34**,** 1697-1716.

CARé, S. 2003. Influence of aggregates on chloride diffusion coefficient into mortar. *Cement and Concrete Research,* 33**,** 1021-1028.

CARé, S. & HERVé, E. J. T. I. P. M. 2004. Application of an-phase model to the diffusion coefficient of chloride in mortar. 56**,** 119-135.

CEN 2005. Test method for metallic fibre concrete-Measuring the flexural tensile strength (limit of proportionality (LOP), residual). BSI London, UK.

CHEN, B., LIU, J. J. C. & MATERIALS, B. 2004. Effect of aggregate on the fracture behavior of high strength concrete. 18**,** 585-590.

CHEN, D., MIAO, C., LIU, J. & TANG, M. J. I. J. O. C. E. 2015. Advances in multi-scale simulation of hygro-thermo-mechanical deformation behavior of structural concrete. 13**,** 267-277.

CHEN, Y. & FENG, J. J. J. O. A. C. T. 2022. Experimental study on effect of coarse aggregate volume fraction on Mode I and Mode II fracture behavior of concrete. 20**,** 57-71.

CHOO, J., SUN, W. J. C. M. I. A. M. & ENGINEERING 2018. Coupled phase-field and plasticity modeling of geological materials: From brittle fracture to ductile flow. 330**,** 1-32.

CHRISTENSEN, R. M. 2012. *Mechanics of composite materials*, Courier Corporation.

COLERI, E., HARVEY, J. T., YANG, K., BOONE, J. M. J. M. & STRUCTURES 2013. Investigation of asphalt concrete rutting mechanisms by X-ray computed tomography imaging and micromechanical finite element modeling. 46**,** 1027-1043.

COUSSY, O., EYMARD, R. & LASSABATèRE, T. J. J. O. E. M. 1998. Constitutive modeling of unsaturated drying deformable materials. 124**,** 658-667.

DAMRONGWIRIYANUPAP, N., LI, L., XI, Y. J. C. & CONCRETE, A. I. J. 2013. Coupled diffusion of multi-component chemicals in nonsaturated concrete. 11**,** 201-222.

DE FREITAS, J. T., CUONG, P., FARIA, R. J. C. & STRUCTURES 2017. Hybrid finite elements for nonlinear thermal and hygral problems. 182**,** 14-25.

DEHWAH, O. H., XI, Y. J. C. & RESEARCH, C. 2024. Theoretical model for the coupling effect of moisture transport on chloride penetration in concrete. 177**,** 107431.

DELAGRAVE, A., BIGAS, J., OLLIVIER, J., MARCHAND, J. & PIGEON, M. J. A. C. B. M. 1997. Influence of the interfacial zone on the chloride diffusivity of mortars. 5**,** 86-92.

DELSAUTE, B., TORRENTI, J.-M., STAQUET, S. J. C. & COMPOSITES, C. 2017. Modeling basic creep of concrete since setting time. 83**,** 239-250.

DHAR, A., RAJASANKAR, J., ANANDAVALLI, N. J. C. & MATERIALS, B. 2018. A mathematical formulation to find effective bulk and shear moduli of recycled aggregate concrete. 168**,** 747-757.

DIAMOND, S. J. C. & RESEARCH, C. 2000. Mercury porosimetry: an inappropriate method for the measurement of pore size distributions in cement-based materials. 30**,** 1517-1525.

DING, X., ZHANG, J. & WANG, J. 2019. Integrative modeling on self-desiccation and moisture diffusion in concrete based on variation of water content. *Cement and Concrete Composites,* 97**,** 322-340.

DRUCKER, D. C. & PRAGER, W. J. Q. O. A. M. 1952. Soil mechanics and plastic analysis or limit design. 10**,** 157-165.

DU, X., JIN, L. & MA, G. J. I. J. O. D. M. 2014. Numerical modeling tensile failure behavior of concrete at mesoscale using extended finite element method. 23**,** 872-898.

ESPINOSA, R. M. & FRANKE, L. 2006. Inkbottle Pore-Method: Prediction of hygroscopic water content in hardened cement paste at variable climatic conditions. *Cement and Concrete Research,* 36**,** 1954-1968.

FELDMAN, R. & SEREDA, P. J. E. J. 1970. A new model for hydrated Portland cement and its practical implications. 53**,** 53-59.

FISHER, L. R., ISRAELACHVILI, J. N. J. J. O. C. & SCIENCE, I. 1981. Experimental studies on the applicability of the Kelvin equation to highly curved concave menisci. 80**,** 528-541.

FRANCFORT, G. A., MARIGO, J.-J. J. J. O. T. M. & SOLIDS, P. O. 1998. Revisiting brittle fracture as an energy minimization problem. 46**,** 1319-1342.

FREDDI, F., ROYER-CARFAGNI, G. J. J. O. T. M. & SOLIDS, P. O. 2010. Regularized variational theories of fracture: a unified approach. 58**,** 1154-1174.

GALLUCCI, E., SCRIVENER, K., GROSO, A., STAMPANONI, M., MARGARITONDO, G. J. C. & RESEARCH, C. 2007. 3D experimental investigation of the microstructure of cement pastes using synchrotron X-ray microtomography (μCT). 37**,** 360-368.

GAO, X., WEI, Y., HUANG, W. J. C. & MATERIALS, B. 2017. Effect of individual phases on multiscale modeling mechanical properties of hardened cement paste. 153**,** 25-35.

GARBOCZI, E. J. & BENTZ, D. P. J. A. C. B. M. 1998. Multiscale analytical/numerical theory of the diffusivity of concrete. 8**,** 77-88.

GEERS, M. G., KOUZNETSOVA, V. G., BREKELMANS, W. J. J. O. C. & MATHEMATICS, A. 2010. Multi-scale computational homogenization: Trends and challenges. 234**,** 2175-2182.

GEORGET, F., WILSON, W., SCRIVENER, K. L. J. C. & RESEARCH, C. 2021. edxia: Microstructure characterisation from quantified SEM-EDS hypermaps. 141**,** 106327.

GRIFFITH, A. A. J. P. T. O. T. R. S. O. L. S. A., CONTAINING PAPERS OF A MATHEMATICAL OR PHYSICAL CHARACTER 1921. VI. The phenomena of rupture and flow in solids. 221**,** 163-198.

GUO, H., OOI, E., SAPUTRA, A., YANG, Z., NATARAJAN, S., OOI, E. & SONG, C. J. E. F. M. 2019. A quadtree-polygon-based scaled boundary finite element method for image-based mesoscale fracture modelling in concrete. 211**,** 420-441.

HAN, T.-S., EUM, D., KIM, S.-Y., KIM, J.-S., LIM, J.-H., PARK, K., STEPHAN, D. J. C. & COMPOSITES, C. 2023. Multi-scale analysis framework for predicting tensile strength of cement paste by combining experiments and simulations. 139**,** 105006.

HANSEN, W. J. J. O. T. A. C. S. 1987. Drying shrinkage mechanisms in Portland cement paste. 70**,** 323-328.

HASHIN, Z., MONTEIRO, P. J. C. & RESEARCH, C. 2002. An inverse method to determine the elastic properties of the interphase between the aggregate and the cement paste. 32**,** 1291-1300.

HEIDER, Y., SUN, W. J. C. M. I. A. M. & ENGINEERING 2020. A phase field framework for capillary-induced fracture in unsaturated porous media: Drying-induced vs. hydraulic cracking. 359**,** 112647.

HOU, D., JIA, Y., YU, J., WANG, P. & LIU, Q. 2018. Transport Properties of Sulfate and Chloride Ions Confined between Calcium Silicate Hydrate Surfaces: A Molecular Dynamics Study. *The Journal of Physical Chemistry C,* 122**,** 28021-28032.

HU, H., PAPASTERGIOU, P., ANGELAKOPOULOS, H., GUADAGNINI, M., PILAKOUTAS, K. J. C. & MATERIALS, B. 2018. Mechanical properties of SFRC using blended recycled tyre steel cords (RTSC) and recycled tyre steel fibres (RTSF). 187**,** 553-564.

HU, H., WANG, Z., FIGUEIREDO, F. P., PAPASTERGIOU, P., GUADAGNINI, M. & PILAKOUTAS, K. J. S. C. 2019. Postcracking tensile behavior of blended steel fiber-reinforced concrete. 20**,** 707-719.

HUANG, J. & LI, V. C. J. C. 1989. A meso-mechanical model of the tensile behaviour of concrete. Part II: modelling of post-peak tension softening behaviour. 20**,** 370-378.

HUANG, Q.-H., LI, C.-Z. & SONG, X.-B. 2022. Spatial distribution characteristics of ellipsoidal coarse aggregates in concrete considering wall effect. *Construction and Building Materials,* 327.

HUANG, Q., JIANG, Z., GU, X., ZHANG, W. & GUO, B. 2015. Numerical simulation of moisture transport in concrete based on a pore size distribution model. *Cement and Concrete Research,* 67**,** 31-43.

HUANG, Y., YAN, D., YANG, Z. & LIU, G. J. E. F. M. 2016a. 2D and 3D homogenization and fracture analysis of concrete based on in-situ X-ray Computed Tomography images and Monte Carlo simulations. 163**,** 37-54.

HUANG, Y., YANG, Z., CHEN, X. & LIU, G. J. I. J. O. I. E. 2016b. Monte Carlo simulations of meso-scale dynamic compressive behavior of concrete based on X-ray computed tomography images. 97**,** 102-115.

HUANG, Y., YANG, Z., LIU, G. & CHEN, X. J. C. M. 2016c. An efficient FE–SBFE coupled method for mesoscale cohesive fracture modelling of concrete. 58**,** 635-655.

HUSSAIN, R. R. & ISHIDA, T. 2010. Development of numerical model for FEM computation of oxygen transport through porous media coupled with micro-cell corrosion model of steel in concrete structures. *Computers & Structures,* 88**,** 639-647.

IDIART, A. E. 2009. *Coupled analysis of degradation processes in concrete specimens at the meso-level*, Universitat Politècnica de Catalunya.

IRWIN, G., KRAFFT, J., PARIS, P. & WELLS, A. J. N. R. 1967. Basic aspects of crack growth and fracture. 6598**,** 9-10.

ISHIDA, T., MAEKAWA, K. & KISHI, T. 2007. Enhanced modeling of moisture equilibrium and transport in cementitious materials under arbitrary temperature and relative humidity history. *Cement and Concrete Research,* 37**,** 565-578.

JENNINGS, H. M. J. C. & RESEARCH, C. 2008. Refinements to colloid model of CSH in cement: CM-II. 38**,** 275-289.

JIA, M., WU, Z., YU, R. C. & ZHANG, X. J. J. O. E. M. 2022. Experimental and numerical study on mixed mode I-II fatigue crack propagation in concrete. 148**,** 04022044.

JIANG, Y., LI, C., WU, C., RABCZUK, T., FANG, J. J. C. M. I. A. M. & ENGINEERING 2023. A double-phase field method for mixed mode crack modelling in 3D elasto-plastic solids with crack-direction-based strain energy decomposition. 405**,** 115886.

JIN, H., FAN, X., LI, Z., ZHANG, W., LIU, J., ZHONG, D. & TANG, L. 2022. An experimental study on the influence of continuous ambient humidity conditions on relative humidity changes, chloride diffusion and microstructure in concrete. *Journal of Building Engineering,* 59.

JU, J. & CHEN, T. J. A. M. 1994. Effective elastic moduli of two-phase composites containing randomly dispersed spherical inhomogeneities. 103**,** 123-144.

KARIHALOO, B., FU, D. & HUANG, X. J. M. O. M. 1991. Modelling of tension softening in quasi-brittle materials by an array of circular holes with edge cracks. 11**,** 123-134.

KHEIR, J., KLAUSEN, A., HAMMER, T. A., DE MEYST, L., HILLOULIN, B., VAN TITTELBOOM, K., LOUKILI, A. & DE BELIE, N. J. E. F. M. 2021. Early age autogenous shrinkage cracking risk of an ultra-high performance concrete (UHPC) wall: Modelling and experimental results. 257**,** 108024.

KIM, H.-T., SZILáGYI, V., KIS, Z., SZENTMIKLóSI, L., GLINICKI, M. A., PARK, K. J. C. & RESEARCH, C. 2021. Reconstruction of concrete microstructure using complementarity of X-ray and neutron tomography. 148**,** 106540.

KIM, J.-K., LEE, C.-S. J. C. & RESEARCH, C. 1999. Moisture diffusion of concrete considering self-desiccation at early ages. 29**,** 1921-1927.

KIM, S.-M., AL-RUB, R. K. A. J. C. & RESEARCH, C. 2011. Meso-scale computational modeling of the plastic-damage response of cementitious composites. 41**,** 339-358.

KLAUSEN, A. E., KANSTAD, T., BJøNTEGAARD, Ø., SELLEVOLD, E. J. J. C. & COMPOSITES, C. 2020. The effect of curing temperature on autogenous deformation of fly ash concretes. 109**,** 103574.

KRABBENHøFT, K. J. U. O. D. 2002. Basic computational plasticity.

LARRARD, F. J. S. P. 1990. Creep and shrinkage of high-strength field concretes. 121**,** 577-598.

LéGER, P., CôTé, P., TINAWI, R. J. C. & STRUCTURES 1996. Finite element analysis of concrete swelling due to alkali-aggregate reactions in dams. 60**,** 601-611.

LI, C.-Z. & SONG, X.-B. 2022. Mesoscale modeling of chloride transport in unsaturated concrete based on Voronoi tessellation. *Cement and Concrete Research,* 161.

LI, D., JIN, L., DU, X. & LIU, J. J. E. F. M. 2018. A theoretical method to determine the tortuous crack length and the mechanical parameters of concrete in direct tension—a particle size effect analysis. 197**,** 128-150.

LIU, C. & ZHANG, M. 2023. Microstructure-based modelling of chloride diffusivity in non-saturated cement paste accounting for capillary and gel pores. *Cement and Concrete Research,* 168.

LIU, G., LI, Q., MSEKH, M. A. & ZUO, Z. J. C. M. S. 2016. Abaqus implementation of monolithic and staggered schemes for quasi-static and dynamic fracture phase-field model. 121**,** 35-47.

LIU, H., SUN, Z., YANG, J., JI, Y. J. C. & RESEARCH, C. 2021. A novel method for semi-quantitative analysis of hydration degree of cement by 1H low-field NMR. 141**,** 106329.

LIU, J., WENXUAN, Y., XIULI, D., ZHANG, S. & DONG, L. J. I. J. O. I. E. 2019. Meso-scale modelling of the size effect on dynamic compressive failure of concrete under different strain rates. 125**,** 1-12.

LóPEZ, C. M., CAROL, I., AGUADO, A. J. M. & STRUCTURES 2008. Meso-structural study of concrete fracture using interface elements. I: numerical model and tensile behavior. 41**,** 583-599.

MA, H., XU, W., LI, Y. J. C. & STRUCTURES 2016. Random aggregate model for mesoscopic structures and mechanical analysis of fully-graded concrete. 177**,** 103-113.

MAC, M., YIO, M., WONG, H., BUENFELD, N. J. C. & RESEARCH, C. 2021a. Analysis of autogenous shrinkage-induced microcracks in concrete from 3D images. 144**,** 106416.

MAC, M. J., YIO, M. H., DESBOIS, G., CASANOVA, I., WONG, H. S., BUENFELD, N. R. J. C. & RESEARCH, C. 2021b. 3D imaging techniques for characterising microcracks in cement-based materials. 140**,** 106309.

MACKENZIE, J. J. P. O. T. P. S. S. B. 1950. The elastic constants of a solid containing spherical holes. 63**,** 2.

MAEKAWA, K., ISHIDA, T. & KISHI, T. 2008. *Multi-scale modeling of structural concrete*, Crc Press.

MARKOU, G., PAPADRAKAKIS, M. J. C. & CONCRETE 2013. Computationally efficient 3D finite element modeling of RC structures. 12**,** 443-498.

MARTıN-PéREZ, B., PANTAZOPOULOU, S. J., THOMAS, M. J. C. & STRUCTURES 2001. Numerical solution of mass transport equations in concrete structures. 79**,** 1251-1264.

MARUYAMA, I., LURA, P. J. C. & RESEARCH, C. 2019. Properties of early-age concrete relevant to cracking in massive concrete. 123**,** 105770.

MATOUŠ, K., GEERS, M. G., KOUZNETSOVA, V. G. & GILLMAN, A. J. J. O. C. P. 2017. A review of predictive nonlinear theories for multiscale modeling of heterogeneous materials. 330**,** 192-220.

MCDONALD, P. J., RODIN, V. & VALORI, A. 2010. Characterisation of intra- and inter-C–S–H gel pore water in white cement based on an analysis of NMR signal amplitudes as a function of water content. *Cement and Concrete Research,* 40**,** 1656-1663.

MENU, B., JACOB-VAILLANCOURT, T., JOLIN, M. & BISSONNETTE, B. J. A. M. J. 2020. Influence of Curing Methods on Moisture Loss and Drying Shrinkage of Shotcrete at Early Age. 117.

MEYER, C. & XUEYU, P. J. I. C. 2012. Cement chemical shrinkage as measure of hydration kinetics and its relationship with nonevaporable water. 109**,** 341-352.

MIEHE, C., ALDAKHEEL, F. & RAINA, A. J. I. J. O. P. 2016. Phase field modeling of ductile fracture at finite strains: A variational gradient-extended plasticity-damage theory. 84**,** 1-32.

MIEHE, C., HOFACKER, M., WELSCHINGER, F. J. C. M. I. A. M. & ENGINEERING 2010a. A phase field model for rate-independent crack propagation: Robust algorithmic implementation based on operator splits. 199**,** 2765-2778.

MIEHE, C., WELSCHINGER, F. & HOFACKER, M. 2010b. Thermodynamically consistent phase-field models of fracture: Variational principles and multi-field FE implementations. *International Journal for Numerical Methods in Engineering,* 83**,** 1273-1311.

MINDESS, S., YOUNG, J. & DARWIN, D. J. U. S. R., NJ 2003. Concrete, 2nd edPrentice Hall.

MOëS, N., STOLZ, C., BERNARD, P. E. & CHEVAUGEON, N. J. I. J. F. N. M. I. E. 2011. A level set based model for damage growth: the thick level set approach. 86**,** 358-380.

MOLNáR, G., GRAVOUIL, A., SEGHIR, R., RéTHORé, J. J. C. M. I. A. M. & ENGINEERING 2020. An open-source Abaqus implementation of the phase-field method to study the effect of plasticity on the instantaneous fracture toughness in dynamic crack propagation. 365**,** 113004.

MORA, C., KWAN, A., CHAN, H. J. C. & RESEARCH, C. 1998. Particle size distribution analysis of coarse aggregate using digital image processing. 28**,** 921-932.

MORI, T. & TANAKA, K. J. A. M. 1973. Average stress in matrix and average elastic energy of materials with misfitting inclusions. 21**,** 571-574.

MOUNAJED, G., OBEID, W. J. M. & STRUCTURES 2004. A new coupling FE model for the simulation of thermal-hydro-mechanical behaviour of concretes at high temperatures. 37**,** 422-432.

MUALEM, Y. J. W. R. R. 1976. A new model for predicting the hydraulic conductivity of unsaturated porous media. 12**,** 513-522.

MULTON, S. & SELLIER, A. 2016. Multi-scale analysis of alkali–silica reaction (ASR): Impact of alkali leaching on scale effects affecting expansion tests. *Cement and Concrete Research,* 81**,** 122-133.

MUMFORD, D. B., SHAH, J. J. C. O. P. & MATHEMATICS, A. 1989. Optimal approximations by piecewise smooth functions and associated variational problems.

NADERI, S., TU, W., ZHANG, M. J. C. & RESEARCH, C. 2021a. Meso-scale modelling of compressive fracture in concrete with irregularly shaped aggregates. 140**,** 106317.

NADERI, S., ZHANG, M. J. C. & COMPOSITES, C. 2021b. Meso-scale modelling of static and dynamic tensile fracture of concrete accounting for real-shape aggregates. 116**,** 103889.

NGUYEN, D.-B., LIN, W.-S. & LIAO, W.-C. J. M. 2021. Long-term creep and shrinkage behavior of concrete-filled steel tube. 14**,** 295.

NGUYEN, T.-T., WALDMANN, D. & BUI, T. Q. 2019. Computational chemo-thermo-mechanical coupling phase-field model for complex fracture induced by early-age shrinkage and hydration heat in cement-based materials. *Computer Methods in Applied Mechanics and Engineering,* 348**,** 1-28.

NGUYEN, T. H., BUI, T. Q., HIROSE, S. J. C. M. I. A. M. & ENGINEERING 2018. Smoothing gradient damage model with evolving anisotropic nonlocal interactions tailored to low-order finite elements. 328**,** 498-541.

NGUYEN, T. T., YVONNET, J., ZHU, Q.-Z., BORNERT, M. & CHATEAU, C. J. E. F. M. 2015. A phase field method to simulate crack nucleation and propagation in strongly heterogeneous materials from direct imaging of their microstructure. 139**,** 18-39.

NIELSEN, E. P., GEIKER, M. R. J. C. & RESEARCH, C. 2003. Chloride diffusion in partially saturated cementitious material. 33**,** 133-138.

NIZOVTSEV, M. I., STANKUS, S. V., STERLYAGOV, A. N., TEREKHOV, V. I. & KHAIRULIN, R. A. 2008. Determination of moisture diffusivity in porous materials using gamma-method. *International Journal of Heat and Mass Transfer,* 51**,** 4161-4167.

OLIVER, J., CAICEDO, M., ROUBIN, E., HUESPE, A. E., HERNáNDEZ, J. J. C. M. I. A. M. & ENGINEERING 2015. Continuum approach to computational multiscale modeling of propagating fracture. 294**,** 384-427.

ORTA, L. & BARTLETT, F. M. J. A. M. J. 2014. Free shrinkage strains in concrete overlays. 111**,** 263.

PANE, I., HANSEN, W. J. M. & STRUCTURES 2002. Early age creep and stress relaxation of concrete containing blended cements. 35**,** 92-96.

PANG, X., BENTZ, D. P., MEYER, C., FUNKHOUSER, G. P., DARBE, R. J. C. & COMPOSITES, C. 2013. A comparison study of Portland cement hydration kinetics as measured by chemical shrinkage and isothermal calorimetry. 39**,** 23-32.

PARROTT, L. & YOUNG, J. 1982. Shrinkage and swelling of two hydrated alite pastes. *Fundamental research on creep and shrinkage of concrete.* Springer.

PATEL, R. A., PERKO, J., JACQUES, D., DE SCHUTTER, G., YE, G. & VAN BRUEGEL, K. 2018. Effective diffusivity of cement pastes from virtual microstructures: Role of gel porosity and capillary pore percolation. *Construction and Building Materials,* 165**,** 833-845.

PATIL, R., MISHRA, B., SINGH, I. V. J. T. & MECHANICS, A. F. 2019. A multiscale framework based on phase field method and XFEM to simulate fracture in highly heterogeneous materials. 100**,** 390-415.

PEERLINGS, R. H., DE BORST, R., BREKELMANS, W. M. & DE VREE, J. J. I. J. F. N. M. I. E. 1996. Gradient enhanced damage for quasi‐brittle materials. 39**,** 3391-3403.

PIJAUDIER-CABOT, G. & BAŽANT, Z. P. J. J. O. E. M. 1987. Nonlocal damage theory. 113**,** 1512-1533.

PIPILIKAKI, P. & BEAZI-KATSIOTI, M. 2009. The assessment of porosity and pore size distribution of limestone Portland cement pastes. *Construction and Building Materials,* 23**,** 1966-1970.

PISE, M., BLUHM, J. & SCHRöDER, J. J. I. J. F. M. C. E. 2019. Elasto-plastic phase-field model of hydraulic fracture in saturated binary porous media. 17.

PIVONKA, P., HELLMICH, C. & SMITH, D. 2004. Microscopic effects on chloride diffusivity of cement pastes—a scale-transition analysis. *Cement and Concrete Research,* 34**,** 2251-2260.

POLLMANN, N., LARSSON, F., RUNESSON, K., LUNDGREN, K., ZANDI, K. & JäNICKE, R. 2021. Modeling and computational homogenization of chloride diffusion in three-phase meso-scale concrete. *Construction and Building Materials,* 271.

POWERS, T. C. 1960. Physical properties of cement paste.

POWERS, T. C. & BROWNYARD, T. L. Studies of the physical properties of hardened Portland cement paste. Journal Proceedings, 1946. 101-132.

PULATSU, B., ERDOGMUS, E., LOURENçO, P. B. & QUEY, R. J. I. J. O. F. 2019. Simulation of uniaxial tensile behavior of quasi-brittle materials using softening contact models in DEM. 217**,** 105-125.

QIN, M., BELARBI, R., AïT-MOKHTAR, A. & NILSSON, L.-O. 2009. Coupled heat and moisture transfer in multi-layer building materials. *Construction and Building Materials,* 23**,** 967-975.

QUENARD, D., SALLEE, H. J. M. & STRUCTURES 1992. Water vapour adsorption and transfer in cement-based materials: a network simulation. 25**,** 515-522.

RABCZUK, T. & BELYTSCHKO, T. J. I. J. F. N. M. I. E. 2004. Cracking particles: a simplified meshfree method for arbitrary evolving cracks. 61**,** 2316-2343.

RABCZUK, T., ZI, G., BORDAS, S., NGUYEN-XUAN, H. J. C. M. I. A. M. & ENGINEERING 2010. A simple and robust three-dimensional cracking-particle method without enrichment. 199**,** 2437-2455.

RAJAMANI, K., PATE, W. T., KINNEBERG, D. J. J. I. & FUNDAMENTALS, E. C. 1986. Time-driven and event-driven Monte Carlo simulations of liquid-liquid dispersions: a comparison. 25**,** 746-752.

RANAIVOMANANA, H., VERDIER, J., SELLIER, A. & BOURBON, X. 2011. Toward a better comprehension and modeling of hysteresis cycles in the water sorption–desorption process for cement based materials. *Cement and Concrete Research,* 41**,** 817-827.

RANAIVOMANANA, H., VERDIER, J., SELLIER, A. & BOURBON, X. 2013a. Prediction of relative permeabilities and water vapor diffusion reduction factor for cement-based materials. *Cement and Concrete Research,* 48**,** 53-63.

RANAIVOMANANA, N., MULTON, S., TURATSINZE, A. J. C. & MATERIALS, B. 2013b. Basic creep of concrete under compression, tension and bending. 38**,** 173-180.

RASTRUP, E. J. M. O. C. R. 1954. Heat of hydration in concrete. 6**,** 79-92.

REN, H., LI, T., NING, J., SONG, S. J. C. & MATERIALS, B. 2023. Bending damage and fractal characteristics of steel fiber-reinforced concrete under three-point bending test. 409**,** 134053.

REZVANI, M., PROSKE, T. & GRAUBNER, C.-A. 2019. Modelling the drying shrinkage of concrete made with limestone-rich cements. *Cement and Concrete Research,* 115**,** 160-175.

RODRIGUES, E. A., GIMENES, M., BITENCOURT JR, L. A., MANZOLI, O. L. J. C. & MATERIALS, B. 2021. A concurrent multiscale approach for modeling recycled aggregate concrete. 267**,** 121040.

RODRIGUES, E. A., MANZOLI, O. L., BITENCOURT JR, L. A., BITTENCOURT, T. N., SáNCHEZ, M. J. C. M. I. A. M. & ENGINEERING 2018. An adaptive concurrent multiscale model for concrete based on coupling finite elements. 328**,** 26-46.

ROY, D. M. 2004. Water Transport in Brick, Stone and Concrete. *Cement and Concrete Research,* 34.

ROZIèRE, E., GRANGER, S., TURCRY, P., LOUKILI, A. J. C. & COMPOSITES, C. 2007. Influence of paste volume on shrinkage cracking and fracture properties of self-compacting concrete. 29**,** 626-636.

SAMSON, E. & MARCHAND, J. 2007. Modeling the transport of ions in unsaturated cement-based materials. *Computers & Structures,* 85**,** 1740-1756.

SHEN, D., LIU, C., FENG, Z., ZHU, S., LIANG, C. J. C. & MATERIALS, B. 2019. Influence of ground granulated blast furnace slag on the early-age anti-cracking property of internally cured concrete. 223**,** 233-243.

SHEN, D., LIU, C., KANG, J., YANG, Q., LI, M., LI, C., ZENG, X. J. C. & COMPOSITES, C. 2022. Early-age autogenous shrinkage and tensile creep of hooked-end steel fiber reinforced concrete with different thermal treatment temperatures. 131**,** 104550.

SHEN, D., LIU, X., ZHOU, B., ZENG, X. & DU, J. J. M. O. C. R. 2021. Influence of initial cracks on the frequency of a 60-year-old reinforced-concrete box beam. 73**,** 121-134.

SHUGUANG, L., QINGBIN, L. J. F. E. I. A. & DESIGN 2015. Method of meshing ITZ structure in 3D meso-level finite element analysis for concrete. 93**,** 96-106.

SIMONE, A., ASKES, H., SLUYS, L. J. J. I. J. O. S. & STRUCTURES 2004. Incorrect initiation and propagation of failure in non-local and gradient-enhanced media. 41**,** 351-363.

SIVAKUMAR, A., SANTHANAM, M. J. C. & COMPOSITES, C. 2007. A quantitative study on the plastic shrinkage cracking in high strength hybrid fibre reinforced concrete. 29**,** 575-581.

SONG, Y., DAVY, C., TROADEC, D., BOURBON, X. J. C. & RESEARCH, C. 2019. Pore network of cement hydrates in a High Performance Concrete by 3D FIB/SEM—Implications for macroscopic fluid transport. 115**,** 308-326.

SORELLI, L., CONSTANTINIDES, G., ULM, F.-J., TOUTLEMONDE, F. J. C. & RESEARCH, C. 2008. The nano-mechanical signature of ultra high performance concrete by statistical nanoindentation techniques. 38**,** 1447-1456.

SPäTH, M., HERRMANN, C., PRAJAPATI, N., SCHNEIDER, D., SCHWAB, F., SELZER, M. & NESTLER, B. J. C. G. 2021. Multiphase-field modelling of crack propagation in geological materials and porous media with Drucker-Prager plasticity. 25**,** 325-343.

STANDARD, B. J. C. S. O. T. S., BS EN 2009. Testing hardened concrete. 12390-3.

SUN, G., ZHANG, Y., SUN, W., LIU, Z. & WANG, C. 2011. Multi-scale prediction of the effective chloride diffusion coefficient of concrete. *Construction and Building Materials,* 25**,** 3820-3831.

TADA, S. & WATANABE, K. 2005. Dynamic determination of sorption isotherm of cement based materials. *Cement and Concrete Research,* 35**,** 2271-2277.

TAERWE, L. & MATTHYS, S. 2013. Fib model code for concrete structures 2010. Ernst & Sohn, Wiley.

TAZAWA, E.-I. 1999. *Autogenous shrinkage of concrete*, CRC Press.

TEIXEIRA DE FREITAS, J. A., CUONG, P. T. & FARIA, R. 2017. Hybrid finite elements for nonlinear thermal and hygral problems. *Computers & Structures,* 182**,** 14-25.

TERHEIDEN, K. 2008. Simultaneous measurement of vapor and liquid moisture transport in porous building materials. *Building and Environment,* 43**,** 2188-2192.

THERMOU, G. E. & HAJIRASOULIHA, I. 2018. Design-oriented models for concrete columns confined by steel-reinforced grout jackets. *Construction and Building Materials,* 178**,** 313-326.

THOMAS, J. J., ALLEN, A. J., JENNINGS, H. M. J. C. & RESEARCH, C. 2012. Density and water content of nanoscale solid C–S–H formed in alkali-activated slag (AAS) paste and implications for chemical shrinkage. 42**,** 377-383.

TORTORELLI, L. A.-V. & AMBROSIO, L. J. C. P. A. M. 1990. Approximation of functionals depending on jumps by elliptic functionals via Gamma-convergence. 43**,** 999-1036.

VAN MIER, J. G. 2012. *Concrete fracture: a multiscale approach*, CRC press.

WANG, J., ZHANG, J. & ZHANG, J. J. J. A. C. T. 2018. Study on cement hydration rate of normal and internal cured concretes. 16**,** 306-316.

WANG, L.-C., UEDA, T. J. W. S. & ENGINEERING 2009. Meso-scale modeling of chloride diffusion in concrete with consideration of effects of time and temperature. 2**,** 58-70.

WANG, Q., WANG, Y.-Y., GENG, Y. & ZHANG, H. 2021. Experimental study and prediction model for autogenous shrinkage of recycled aggregate concrete with recycled coarse aggregate. *Construction and Building Materials,* 268.

WANG, X., YANG, Z. J., YATES, J., JIVKOV, A., ZHANG, C. J. C. & MATERIALS, B. 2015. Monte Carlo simulations of mesoscale fracture modelling of concrete with random aggregates and pores. 75**,** 35-45.

WEI, Y., HUANG, J. & LIANG, S. 2019. Measurement and modeling concrete creep considering relative humidity effect. *Mechanics of Time-Dependent Materials,* 24**,** 161-177.

WEI, Y., LIANG, S., GUO, W., HANSEN, W. J. C. & COMPOSITES, C. 2017. Stress prediction in very early-age concrete subject to restraint under varying temperature histories. 83**,** 45-56.

WITTMANN, F. Material properties influencing early cracking of concrete. International Workshop on Control of Cracking in Early Age of Concrete, Sendai, 2000, 2000.

WRIGGERS, P., MOFTAH, S. J. F. E. I. A. & DESIGN 2006. Mesoscale models for concrete: Homogenisation and damage behaviour. 42**,** 623-636.

WU, Z., CUI, W., FAN, L., LIU, Q. J. C. & MATERIALS, B. 2019. Mesomechanism of the dynamic tensile fracture and fragmentation behaviour of concrete with heterogeneous mesostructure. 217**,** 573-591.

XI, Y., BAŽANT, Z. P. & JENNINGS, H. M. J. A. C. B. M. 1994. Moisture diffusion in cementitious materials adsorption isotherms. 1**,** 248-257.

XIA, Y., WU, W., YANG, Y. & FU, X. 2021. Mesoscopic study of concrete with random aggregate model using phase field method. *Construction and Building Materials,* 310.

YANG, G., WU, Y., LI, H., GAO, N., JIN, M., HU, Z., LIU, J. J. C. & COMPOSITES, C. 2021. Effect of shrinkage-reducing polycarboxylate admixture on cracking behavior of ultra-high strength mortar. 122**,** 104117.

YANG, S., WANG, M., LAN, T., LIU, S., SUN, Z. J. C. & MATERIALS, B. 2023. Fracture model for predicting tensile strength and fracture toughness of concrete under different loading rates. 365**,** 129978.

YANG, Z.-J., LI, B.-B. & WU, J.-Y. J. E. F. M. 2019. X-ray computed tomography images based phase-field modeling of mesoscopic failure in concrete. 208**,** 151-170.

YANG, Z., REN, W., MOSTAFAVI, M., MCDONALD, S. A. & MARROW, T. J. Characterisation of 3D fracture evolution in concrete using in-situ X-ray computed tomography testing and digital volume correlation. VIII international conference on fracture mechanics of concrete and concrete structures, 2013. Toledo, Spain CIMNE, 1-7.

YANG, Z., REN, W., SHARMA, R., MCDONALD, S., MOSTAFAVI, M., VERTYAGINA, Y., MARROW, T. J. C. & COMPOSITES, C. 2017. In-situ X-ray computed tomography characterisation of 3D fracture evolution and image-based numerical homogenisation of concrete. 75**,** 74-83.

YANG, Z., SU, X., CHEN, J. F., LIU, G. J. I. J. O. S. & STRUCTURES 2009. Monte Carlo simulation of complex cohesive fracture in random heterogeneous quasi-brittle materials. 46**,** 3222-3234.

YE, G., LURA, P. & VAN BREUGEL, K. 2006. Modelling of water permeability in cementitious materials. *Materials and Structures,* 39**,** 877-885.

YE, H., JIN, X., FU, C., JIN, N., XU, Y. & HUANG, T. 2016. Chloride penetration in concrete exposed to cyclic drying-wetting and carbonation. *Construction and Building Materials,* 112**,** 457-463.

YIO, M., MAC, M., YEOW, Y., WONG, H., BUENFELD, N. J. C. & RESEARCH, C. 2021. Effect of autogenous shrinkage on microcracking and mass transport properties of concrete containing supplementary cementitious materials. 150**,** 106611.

YU, P., REN, Z., CHEN, Z., BORDAS, S. P. A. J. F. E. I. A. & DESIGN 2023. A multiscale finite element model for prediction of tensile strength of concrete. 215**,** 103877.

ZAOUI, A. J. J. O. E. M. 2002. Continuum micromechanics: survey. 128**,** 808-816.

ZENG, Y., LI, M., ZHOU, Y., LI, N. J. T. & MECHANICS, A. F. 2019. Development of a new method for estimating the fatigue life of notched specimens based on stress field intensity. 104**,** 102339.

ZHANG, J., DONGWEI, H. & WEI, S. J. M. O. C. R. 2010. Experimental study on the relationship between shrinkage and interior humidity of concrete at early age. 62**,** 191-199.

ZHANG, J., HOU, D., HAN, Y. J. C. & MATERIALS, B. 2012a. Micromechanical modeling on autogenous and drying shrinkages of concrete. 29**,** 230-240.

ZHANG, J., HUANG, Y. & QI, K. J. J. T. U. 2007. Development of internal humidity in concrete at early age. 473**,** 309-312.

ZHANG, J., QI, K. & HUANG, Y. J. J. O. E. M. 2009. Calculation of moisture distribution in early-age concrete. 135**,** 871-880.

ZHANG, M., YE, G. & VAN BREUGEL, K. 2012b. Modeling of ionic diffusivity in non-saturated cement-based materials using lattice Boltzmann method. *Cement and Concrete Research,* 42**,** 1524-1533.

ZHANG, Y., GAO, Z., LI, Y., ZHUANG, X. J. F. E. I. A. & DESIGN 2020. On the crack opening and energy dissipation in a continuum based disconnected crack model. 170**,** 103333.

ZHANG, Y., HUANG, J., YUAN, Y., MANG, H. A. J. F. E. I. A. & DESIGN 2021. Cracking elements method with a dissipation-based arc-length approach. 195**,** 103573.

ZHANG, Y., JU, J. W., ZHU, H., GUO, Q., YAN, Z. J. C. & MATERIALS, B. 2018a. Micromechanics based multi-level model for predicting the coefficients of thermal expansion of hybrid fiber reinforced concrete. 190**,** 948-963.

ZHANG, Y. & MANG, H. A. J. I. J. F. N. M. I. E. 2020. Global cracking elements: a novel tool for Galerkin-based approaches simulating quasi-brittle fracture. 121**,** 2462-2480.

ZHANG, Y., YAN, Z.-G., JU, J. W., ZHU, H.-H., CHEN, Q. J. C. & MATERIALS, B. 2017. A multi-level micromechanical model for elastic properties of hybrid fiber reinforced concrete. 152**,** 804-817.

ZHANG, Y. & YE, G. 2019. A model for predicting the relative chloride diffusion coefficient in unsaturated cementitious materials. *Cement and Concrete Research,* 115**,** 133-144.

ZHANG, Y., ZHUANG, X. J. F. E. I. A. & DESIGN 2018b. Cracking elements: A self-propagating strong discontinuity embedded approach for quasi-brittle fracture. 144**,** 84-100.

ZHANG, Z.-B. & ZHANG, J. J. J. C. X. 2006. Experimental study on relationship between shrinkage strain and environmental humidity of concrete. 9**,** 720-723.

ZHANG, Z., LIU, Y., DISSANAYAKE, D. D., SAPUTRA, A. A. & SONG, C. J. E. A. W. B. E. 2019. Nonlocal damage modelling by the scaled boundary finite element method. 99**,** 29-45.

ZHENG, X., JI, T., EASA, S. M., ZHANG, B., JIANG, Z. J. C. & MATERIALS, B. 2019. Tensile basic creep behavior of lightweight aggregate concrete reinforced with steel fiber. 200**,** 356-367.

ZHOU, S., RABCZUK, T. & ZHUANG, X. J. A. I. E. S. 2018. Phase field modeling of quasi-static and dynamic crack propagation: COMSOL implementation and case studies. 122**,** 31-49.

ZHU, X., ZI, G., CAO, Z. & CHENG, X. 2016. Combined effect of carbonation and chloride ingress in concrete. *Construction and Building Materials,* 110**,** 369-380.